



**HAL**  
open science

# Synthèse d'une solution GNC basée sur des capteurs de flux optique bio-inspirés adaptés à la mesure des basses vitesses pour un atterrissage lunaire autonome en douceur

Guillaume Sabiron

## ► To cite this version:

Guillaume Sabiron. Synthèse d'une solution GNC basée sur des capteurs de flux optique bio-inspirés adaptés à la mesure des basses vitesses pour un atterrissage lunaire autonome en douceur. Physique de l'espace [physics.space-ph]. ISAE - Institut Supérieur de l'Aéronautique et de l'Espace, 2014. Français. NNT: . tel-01096458

**HAL Id: tel-01096458**

**<https://hal.science/tel-01096458>**

Submitted on 17 Dec 2014

**HAL** is a multi-disciplinary open access archive for the deposit and dissemination of scientific research documents, whether they are published or not. The documents may come from teaching and research institutions in France or abroad, or from public or private research centers.

L'archive ouverte pluridisciplinaire **HAL**, est destinée au dépôt et à la diffusion de documents scientifiques de niveau recherche, publiés ou non, émanant des établissements d'enseignement et de recherche français ou étrangers, des laboratoires publics ou privés.



Université  
de Toulouse

# THÈSE

En vue de l'obtention du

## DOCTORAT DE L'UNIVERSITÉ DE TOULOUSE

Délivré par : *l'Institut Supérieur de l'Aéronautique et de l'Espace (ISAE)*

---

---

Présentée et soutenue le 18/11/2014 par :

**Guillaume SABIRON**

**Synthèse d'une Solution GNC basée sur des Capteurs de Flux Optique  
Bio-inspirés adaptés à la mesure des basses vitesses pour un Atterrissage  
Lunaire Autonome en Douceur**

---

---

### JURY

F. CHAUMETTE	DR INRIA	IRISA	Président du Jury
I. FANTONI	DR CNRS	Heudiasyc	Rapporteur
N. MARCHAND	DR CNRS	GIPSA-lab	Rapporteur
P. MORIN	Prof. UPMC	ISIR	Examineur
L. BURLION	Ingénieur de recherche Onera	DCSD	Examineur
T. RAHARIJAONA	Maître de conférence AMU	ISM	Examineur
P. MOUYON	Ingénieur de recherche Onera	DCSD	Directeur de thèse
F. RUFFIER	CR HDR CNRS	ISM	Co-Directeur de thèse

---

**École doctorale et spécialité :**

*EDSYS : Automatique 4200046*

**Double mention :**

*EDSYS : Systèmes embarqués 4200046*

**Unité de Recherche :**

*Commande des Systèmes et Dynamique du Vol — Onera - The French Aerospace Lab*

**Directeur(s) de Thèse :**

*Philippe MOUYON et Franck RUFFIER*

**Rapporteurs :**

*Isabelle FANTONI et Nicolas MARCHAND*



INSTITUT SUPÉRIEUR DE L'AÉRONAUTIQUE ET DE L'ESPACE  
ONERA - SYSTEMS CONTROL AND FLIGHT DYNAMICS DEPT.

# DOCTORAL THESIS

submitted in fulfillment of the requirements for the degree of Doctor of  
Philosophy in Control Theory and Embedded Systems

by

Guillaume Sabiron

## DESIGN OF A GNC SOLUTION BASED ON BIO-INSPIRED OPTIC FLOW SENSORS ADAPTED TO LOW SPEED MEASUREMENT FOR AN AUTONOMOUS SOFT LUNAR LANDING

Thesis defended on November 18th, 2014, in front of the jury composed of :

F. CHAUMETTE	DR INRIA	IRISA	Rennes	Pres. of the Jury
I. FANTONI	DR CNRS	Heudiasyc	Compiègne	Reviewer
N. MARCHAND	DR CNRS	GIPSA-lab	Grenoble	Reviewer
P. MORIN	Prof. UPMC	ISIR	Paris	Examinator
L. BURLION	Research engineer	ONERA/DCSD	Toulouse	Examinator
T. RAHARIJAONA	Associate Prof. AMU	ISM	Marseille	Examinator
P. MOUYON	Research engineer	ONERA/DCSD	Toulouse	Advisor
F. RUFFIER	CR HDR CNRS	ISM	Marseille	Advisor



*To my parents, to my brother*



# ACKNOWLEDGEMENTS

**E**N me retournant sur ces trois dernières années, je me rends compte du chemin parcouru. Je me souviens de mes premiers pas dans le monde de la robotique bio-inspirée à Marseille où l'idée de s'inspirer du monde animal pour améliorer les capacités d'autonomie des systèmes robotisés m'a immédiatement fasciné.

En premier lieu je souhaite exprimer toute ma gratitude à mon co-directeur de thèse Franck Ruffier. Je le remercie pour avoir su partager et me communiquer sa passion tant pour les insectes ailés que pour la robotique, pour m'avoir accordé sa confiance, pour sa grande disponibilité et ses conseils francs et avisés tout au long de cette thèse, et ce, malgré la distance.

Je tiens à remercier l'ensemble des membres du jury pour avoir accepté d'expertiser mes travaux. Merci à Isabelle Fantoni, Nicolas Marchand, François Chaumette et Pascal Morin pour leur temps et leurs remarques constructives sur ces travaux.

Ce projet n'aurait pu voir le jour sans la confiance et le support de MM. Leopold Summerer et Patrick Fabiani qui ont su croire en l'idée innovante de poser des robots sur la lune grâce à la vision des insectes. Je ne saurais aussi assez remercier les nombreux encadrants et collègues qui m'auront suivi, guidé et beaucoup appris durant ces trois années, je pense notamment à mon directeur de thèse Philippe Mouyon de l'Onera, Eric Bornschlegl de l'ESA et Erwan Kervendal et Grégory Jonniaux d'Airbus Defence and Space.

Un grand merci également à Laurent Burlion pour son support technique et avec qui j'ai passé de très bons moments à l'Onera ainsi que durant notre dernière mission à Leiden.

Je tiens à remercier tout particulièrement Thibaut Raharijaona avec qui j'ai travaillé durant trois ans et demi et qui m'a poussé à faire cette thèse et dont le soutien technique et humain a été une des clés de la réussite de cette thèse.

Je garderai le souvenir du temps passé à Marseille au sein de l'équipe biorobotique de l'ISM pour l'accueil et la collaboration de ces différents membres. Je remercie pour cela Stéphane Viollet, Nicolas Franceschini, Julien Dipéri, Jessica Blanc et Marc Boyron pour leurs expertises respectives ainsi que les doctorants que j'y ai côtoyés: Fabien Expert, Frédéric Roubieu, Raphael Juston, Fabien Colonnier, Stefano Mafrica et Augustin Manecy.

Let's switch to English to thank all the fascinated and fascinating people I met during my six months in the Netherlands at ESTEC. First of all, I would like to express all my gratitude to Alain Benoit and Guillermo Ortega for their warm welcome in TEC-ECN. I also thank all the staff members I met and worked with, especially Alvaro, Antonio and Olivier. I spent a great moments surrounded many by European trainees

and YGTs. Last but not least I thank my office mate Julien Chaudenson for sharing many discussions about control theory, aerospace technologies and also a little bit of fun and laughter.

Suite à cela j'ai posé mes valises à l'Onera de Toulouse où j'ai passé 18 mois fort intéressants. L'équipe drone du DCSD mérite largement toute ma reconnaissance pour leur expertise méthodologique et leur bonne humeur, je remercie ainsi Vincent, Paul, Alexandre, Pierre, Yoko, Henry et Alain. A nouveau je tiens à féliciter l'équipe des doctorants pour m'avoir supporté soit dans leur bureau: Jérémy V., Emmanuel, Jérémy L. et Moumoune, soit tout le reste du temps: Elodie, Pierre, Razvan, Yann, Adrien, Nicolas et tous ceux que j'aurais pu oublier. Merci également à Valérie Cassagnol pour m'avoir si souvent rendu service avec la logistique parfois complexe de cette thèse.

Enfin, je remercie et félicite ma famille, mes colocataires ainsi que tous mes amis pour leur soutien sans faille, leur intérêt dans mes travaux et le fait d'avoir toujours cru en moi bien que je ne leur rendais pas visite aussi souvent qu'ils l'auraient voulu (tout comme moi d'ailleurs).

Finalement, je souhaite témoigner toute mon affection pour Hélène qui malgré la distance a su me motiver au quotidien pour terminer ce que j'avais entrepris depuis son petit bout de caillou au milieu de l'Océan Indien.

Merci à tous!

# PUBLICATIONS

## Journal Papers

- [1] **Sabiron G.**, Raharijaona T., Burlion L., Kervendal E., Bornschlegl E., Ruffier F. (2014) **In revision.**  
Sub-optimal lunar landing GNC using Non-Gimbaled Optic Flow sensors,  
IEEE Transaction on Aerospace and Electronic Systems.
- [2] Roubieu F. L., Expert F., **Sabiron G.**, Ruffier F. (2013)  
A two-directional 1-gram visual motion sensor inspired by the fly's eye,  
IEEE Sensors Journal, 13(3): pp. 1025-1035, 2013.

## Peer-reviewed proceedings

- [3] **Sabiron G.**, Burlion L., Raharijaona T., and Ruffier F. (2014) **In press**  
Optic Flow-Based Nonlinear Control and Sub-Optimal Guidance for Lunar Landing,  
IEEE International Conference on Robotics and Biomimetics (ROBIO) 2014.
- [4] **Sabiron G.**, Burlion L., Jonniaux G., Kervendal E., Bornschlegl E., Raharijaona T., and Ruffier F. (2014)  
Backup state observer based on optic flow applied to lunar landing,  
IEEE/RSJ International Conference on Intelligent Robots and Systems (IROS), pp 2325-2332, Chicago, USA, 14-18 September 2014.
- [6] **Sabiron G.**, Chavent P., Raharijaona T., Fabiani P., Ruffier F. (2013)  
Low-speed optic-flow sensor onboard an unmanned helicopter flying outside over fields,  
IEEE Int. Conf. Robot. Autom. (ICRA), pp. 1734-1741, Karlsruhe, Germany, 6-10 May 2013.
- [5] **Sabiron G.**, Chavent P., Burlion L., Kervendal E., Bornschlegl E., Fabiani P., Raharijaona T., Ruffier F. (2013)  
Toward an autonomous lunar landing based in low-speed optic flow sensors,  
EuroGNC 2013, 2nd CEAS Specialist Conference on Guidance, Navigation & Control, pp. 993-1011, Delft, The Netherlands, 10-12 April 2013.

## Book Chapters

- [7] Raharijaona T., **Sabiron G.**, Viollet S., Franceschini N., Ruffier F. (2013)  
Bio-inspired Landing Approaches and Their Potential Use on Extraterrestrial Bodies, Asteroids. Prospective Energy and Material Resources, Springer-Verlag, pp. 221-246, 2013.
- [8] **Sabiron G.**, Chavent P., Burlion L., Kervendal E., Bornschlegl E., Fabiani P., Raharijaona T., Ruffier F. (2013)

Toward an autonomous lunar landing based in low-speed optic flow sensors,  
Advances in Aerospace Guidance, Navigation and Control, Springer , pp. 681-699 Selected Papers of the Second CEAS Specialist Conference on Guidance, Navigation & Control, Springer, 2013.

## Other Conference and Workshop

- **Sabiron G.**, Burlion L., Kervendal E., Bornschlegl E., Raharijaona T., Ruffier F. (2014)  
Autonomous Lunar Landing Based on Bio-inspired Visual Motion sensors tested in flight,  
9th International ESA Conference on Guidance, Navigation & Control Systems, Oporto, Portugal, 2-6 June 2014.
- **Sabiron G.**, Chavent P., Raharijaona T., Fabiani P., Ruffier F. (2013)  
Capteur mesurant de faibles Flux Optique testé en extérieur et en vol libre sur le drone ReSSAC,  
GT UAV meeting, ENSAM, Paris, France 21 June 2013.

## Posters

- **Sabiron G.**, Raharijaona T., Burlion L., Kervendal E., Ruffier F.  
Toward a Bio-inspired Autopilot for Safe and Soft Lunar Landing,  
ESA Technology and Innovation Days, ESTEC, Noordwijk, The Netherlands, 2011.
- **Sabiron G.**, Chavent P., Raharijaona T., Fabiani P., Ruffier F.  
Bio-inspired low-speed optic flow sensor tested flying over fields,  
Workshop Curvace, Compound Eyes: from Biology to Technology, Tübingen, Germany, 26-28 March, 2013.

# RÉSUMÉ

**D**ANS cette thèse, nous nous intéressons au problème de l'atterrissage lunaire autonome et nous proposons une méthode innovante amenant une alternative à l'utilisation de capteurs classiques qui peuvent se révéler encombrants, énergivores et très onéreux.

La première partie est consacrée au développement et à la construction de capteurs de mouvement inspirés de la vision des insectes volants et mesurant le flux optique. Le flux optique correspond à la vitesse angulaire relative de l'environnement mesurée par la rétine d'un agent. Dans un environnement fixe, les mouvements d'un robot génèrent un flux optique contenant des informations essentielles sur le mouvement de ce dernier. En utilisant le principe du « temps de passage », nous présentons les résultats expérimentaux obtenus en extérieur avec deux versions de ces capteurs.

Premièrement, un capteur mesurant le flux optique dans les deux directions opposées est développé et testé en laboratoire. Deuxièmement un capteur adapté à la mesure des faibles flux optiques similaires à ceux pouvant être mesurés lors d'un alunissage est développé, caractérisé et enfin testé sur un drone hélicoptère en conditions extérieures.

Dans la seconde partie, une méthode permettant de réaliser le guidage, la navigation et la commande (GNC pour Guidance Navigation and Control) du système est proposée. L'innovation réside dans le fait que l'atterrissage en douceur est uniquement assuré par les capteurs de flux optique. L'utilisation des capteurs inertiels est réduite au maximum. Plusieurs capteurs orientés dans différentes directions de visée, et fixés à la structure de l'atterrisseur permettent d'atteindre les conditions finales définies par les partenaires industriels. Les nombreuses informations décrivant la position et l'attitude du système contenues dans le flux optique sont exploitées grâce aux algorithmes de navigation qui permettent d'estimer les flux optiques ventraux et d'expansion ainsi que le tangage.

Nous avons également montré qu'il est possible de contrôler l'atterrisseur planétaire en faisant suivre aux flux optiques estimés une consigne optimale au sens de la consommation d'énergie. Les simulations réalisées durant la thèse ont permis de valider le fonctionnement et le potentiel de la solution GNC proposée en intégrant le code du capteur ainsi que des images simulées du sol de la lune.



# ABSTRACT

**I**N this PhD thesis, the challenge of autonomous lunar landing was addressed and an innovative method was developed, which provides an alternative to the classical sensor suites based on RADAR, LIDAR and cameras, which tend to be bulky, energy-consuming and expensive.

The first part is devoted to the development of a sensor inspired by the fly's visual sensitivity to optic flow (OF). The OF is an index giving the relative angular velocity of the environment sensed by the retina of a moving insect or robot. In a fixed environment (where there is no external motion), the self-motion of an airborne vehicle generates an OF containing information about its own velocity and attitude and the distance to obstacles. Based on the "Time of Travel" principle we present the results obtained for two versions of 5 LMSs based optic flow sensors.

The first one is able to measure accurately the OF in two opposite directions. It was tested in the laboratory and gave satisfying results. The second optic flow sensor operates at low velocities such as those liable to occur during lunar landing was developed. After developing these sensors, their performances were characterized both indoors and outdoors, and lastly, they were tested onboard an 80-kg helicopter flying in an outdoor environment.

The Guidance Navigation and Control (GNC) system was designed in the second part on the basis of several algorithms, using various tools such as optimal control, non-linear control design and observation theory. This is a particularly innovative approach, since it makes it possible to perform soft landing on the basis of OF measurements and as less as possible on inertial sensors. The final constraints imposed by our industrial partners were met by mounting several non-gimbaled sensors oriented in different gaze directions on the lander's structure. Information about the lander's self-motion present in the OF measurements is extracted by navigation algorithms, which yield estimates of the ventral OF, expansion OF and pitch angle.

It was also established that it is possible to bring the planetary lander gently to the ground by tracking a pre-computed optimal reference trajectory in terms of the lowest possible fuel consumption. Software-in-the-loop simulations were carried out in order to assess the potential of the proposed GNC approach by testing its performances. In these simulations, the sensor firmware was taken into account and virtual images of the lunar surface were used in order to improve the realism of the simulated landings.

# CONTENTS

<b>Acknowledgements</b>	<b>v</b>
<b>Publications</b>	<b>vii</b>
<b>Résumé</b>	<b>ix</b>
<b>Abstract</b>	<b>xi</b>
<b>Contents</b>	<b>xii</b>
<b>Acronyms</b>	<b>xvii</b>
<b>Notations</b>	<b>xix</b>
<b>Preface</b>	<b>xxi</b>
<b>1 Introduction</b>	<b>1</b>
1.1 PLANETARY LANDING: A BRIEF HISTORY . . . . .	3
1.1.1 PAST EXPLORATION MISSIONS IN THE SOLAR SYSTEM . . . . .	3
1.1.2 LUNAR LANDINGS GOALS AND STRATEGY . . . . .	4
1.1.3 ESA'S LUNAR LANDER MISSION . . . . .	6
1.2 GUIDANCE NAVIGATION AND CONTROL CHALLENGES IN SOFT LANDINGS . .	9
1.2.1 GUIDANCE SCHEMES . . . . .	10
1.2.2 CONTROL ALGORITHMS . . . . .	12
1.2.2.1 Control of airborne vehicles . . . . .	12
1.2.2.2 Vision based control . . . . .	13
1.2.3 NAVIGATION APPROACHES . . . . .	14
1.2.3.1 Navigation sensors . . . . .	15
1.2.4 VISION-BASED TERRAIN RELATIVE NAVIGATION . . . . .	17
1.2.4.1 Absolute Visual Navigation . . . . .	18
1.2.4.2 Relative Visual Navigation . . . . .	18
1.2.4.3 Validation of TRN solutions . . . . .	20
1.3 BIO-INSPIRED ROBOTICS . . . . .	21
1.3.1 DEFINITION OF THE OPTIC FLOW VISUAL CUE . . . . .	23
1.3.2 THE COMPOUND EYE OF THE FLYING INSECTS . . . . .	26
1.3.3 OTHER SENSORY SYSTEMS OBSERVED IN FLYING INSECTS . . . . .	31
1.3.4 FLYING INSECT USE VISUAL RELATIVE MOTION FOR FLIGHT CONTROL . . . .	32
1.3.5 DETERMINING THE OPTIC FLOW AS INSECTS DOES: THE "TIME OF TRAVEL SCHEME" . . . . .	36
1.3.5.1 Presentation of the "Time of travel scheme" . . . . .	36
1.3.5.2 Evolution of the LMS . . . . .	38

1.3.5.3	Other optic flow sensors technologies . . . . .	38
1.3.6	DEVELOPING ROBOTS INSPIRED BY FLYING INSECTS' VISION BASED CONTROL . . . . .	39
1.4	OPTIC FLOW BASED LUNAR LANDING . . . . .	47
	OBJECTIVES OF THE THESIS . . . . .	51
	THESIS OVERVIEW . . . . .	52
<b>2</b>	<b>Development and characterization of bio-inspired optic flow sensors</b>	<b>53</b>
<b>2.1</b>	<b>Article 1: A two-directional 1-gram visual motion sensor inspired by the fly's eye</b>	<b>55</b>
	ABSTRACT . . . . .	59
	I INTRODUCTION . . . . .	59
	II DESCRIPTION OF THE DEVICE . . . . .	60
	III EXPERIMENT . . . . .	62
	IV RESULTS . . . . .	63
	V ESTIMATION OF THE DIRECTION AND MAGNITUDE OF THE VISUAL MOTION . . . . .	63
	VI CONCLUSION . . . . .	66
	ACKNOWLEDGMENT . . . . .	68
	REFERENCES . . . . .	68
<b>2.2</b>	<b>Article 2: Low-speed optic-flow sensor onboard an unmanned helicopter flying outside over fields</b>	<b>71</b>
	ABSTRACT . . . . .	75
	I INTRODUCTION . . . . .	75
	II DEFINITION OF THE GROUND-TRUTH OPTIC FLOW . . . . .	76
	III PRESENTATION OF THE LOW-SPEED VISUAL MOTION SENSOR . . . . .	76
	IV EXPERIMENTAL RESULTS . . . . .	78
	V CONCLUSION . . . . .	81
	VI ACKNOWLEDGMENT . . . . .	81
	REFERENCES . . . . .	81
<b>2.3</b>	<b>Conclusion</b>	<b>83</b>
<b>3</b>	<b>Guidance Navigation and Control based on minimalistic optic flow sensors</b>	<b>85</b>
<b>3.1</b>	<b>Introduction</b>	<b>87</b>
<b>3.2</b>	<b>Article 3: Sub-optimal Lunar Landing GNC using Non-gimbaled Bio-inspired Optic Flow Sensors</b>	<b>91</b>
	ABSTRACT . . . . .	97
	I INTRODUCTION . . . . .	97
	II SCENARIO DEFINITION AND ITS FULL GNC SOLUTION . . . . .	99
	III LUNAR LANDER DYNAMIC MODEL AND OPTIC FLOW EQUATIONS . . . . .	100
	IV SIMULATED VISUAL ENVIRONMENT: PANGU SOFTWARE AND OF SENSOR MODEL . . . . .	101
	V OPTIMAL FUEL-EFFICIENT OF REFERENCE TRAJECTORY DESIGN . . . . .	102
	VI CONTROL LAW DESIGN . . . . .	104
	VII NON-GIMBALED OF SENSOR SET-UP . . . . .	106

VIII COMPLETE GNC SIMULATION USING PANGU . . . . .	110
IX CONCLUSION . . . . .	110
ACKNOWLEDGMENT . . . . .	113
REFERENCES . . . . .	113
<b>3.3 Article 4: OF-based Nonlinear control and Sub-Optimal Guidance for lunar landing</b>	<b>119</b>
ABSTRACT . . . . .	123
I INTRODUCTION . . . . .	123
II LUNAR LANDER DYNAMIC MODELING AND OPTIC FLOW EQUATIONS . . . . .	123
III SUB-OPTIMAL GUIDANCE STRATEGY . . . . .	124
IV LYAPUNOV-BASED NONLINEAR CONTROL DESIGN . . . . .	125
V SIMULATION RESULTS . . . . .	127
VI CONCLUSION . . . . .	128
ACKNOWLEDGMENT . . . . .	129
REFERENCES . . . . .	129
<b>3.4 Article 5: Backup State Observer Based on Optic Flow Applied to Lunar Landing</b>	<b>131</b>
ABSTRACT . . . . .	135
I INTRODUCTION . . . . .	135
II LUNAR LANDER DYNAMICS AND OPTIC FLOW EQUATIONS . . . . .	136
III OPTIC FLOW FUSION AND LPV MODEL DEFINITION . . . . .	137
IV OBSERVER DESIGN FOR A CLASS OF LPV SYSTEMS AND APPLICATION TO A LUNAR LANDING SCENARIO . . . . .	138
V SIMULATION RESULTS WITH 3 OF SENSORS . . . . .	138
VI CONCLUSIONS . . . . .	141
ACKNOWLEDGMENT . . . . .	142
REFERENCES . . . . .	142
<b>3.5 Conclusion</b>	<b>143</b>
<b>4 Discussion and outlook</b>	<b>145</b>
4.1 ACCOMPLISHED WORK . . . . .	147
4.1.1 OF-BASED GNC STRATEGY DESIGN . . . . .	148
4.1.2 OPTIC FLOW SENSORS DEVELOPMENT AND CHARACTERIZATION . . . . .	150
4.1.3 SUMMARY OF THE MAIN CONTRIBUTIONS . . . . .	151
4.2 NEW LIMITS TO EXCEED . . . . .	151
4.2.1 FLAT TERRAIN HYPOTHESIS . . . . .	151
4.2.2 ILLUMINATION CONDITIONS . . . . .	152
4.2.3 6-DOF MOTION . . . . .	153
4.2.4 EVENT BASED CONTROL DESIGN . . . . .	153
4.2.5 ROBUSTNESS OF THE GNC STRATEGY TO INITIAL UNCERTAINTIES . . . . .	153
4.2.6 LINEARIZATION AROUND A REFERENCE TRAJECTORY . . . . .	154
4.3 FUTURE WORK . . . . .	155
4.3.1 FUTURE WORK ON THE OPTIC FLOW SENSORS . . . . .	155
4.3.2 FUTURE WORK ON THE GNC DESIGN . . . . .	156
<b>Bibliography</b>	<b>159</b>

<b>Résumé de thèse en français</b>	<b>180</b>
1 INTRODUCTION . . . . .	185
2 DÉVELOPPEMENT ET CARACTÉRISATION DE CAPTEURS DE FLUX OPTIQUE . . .	192
2.1 DÉVELOPPEMENT D'UN CAPTEUR DE FLUX OPTIQUE BIDIRECTIONNEL . . .	192
2.2 DÉVELOPPEMENT D'UN CAPTEUR DE FLUX OPTIQUE DÉDIÉ AUX BASSES VITESSES ET TESTÉ EN VOL . . . . .	196
3 SYNTHÈSE D'ALGORITHMES DE GUIDAGE NAVIGATION ET COMMANDE POUR UN ATERRISSAGE LUNAIRE EN DOUCEUR . . . . .	201
3.1 DÉFINITION DU SCÉNARIO DE RÉFÉRENCE . . . . .	201
3.2 DÉFINITION D'UN STRATÉGIE GNC INNOVANTE . . . . .	202
3.3 LIMITES ET AMÉLIORATIONS DE LA STRATÉGIE GNC . . . . .	208
4 CONCLUSION . . . . .	214
BIBLIOGRAPHIE . . . . .	216



# ACRONYMS

ACS	:	Attitude Control System,
AGL	:	Above Ground Level,
AI	:	Artificial Intelligence,
ALHAT	:	Autonomous Landing Hazard Avoidance Technology,
AP	:	Approach Phase,
ASI	:	Agenzia Spaziale Italiana,
ATV	:	Automated Transfer Vehicle,
AVN	:	Absolute Visual Navigation,
CCD	:	Charge-Coupled Device,
CNSA	:	China National Space Administration,
CNRS	:	French National Centre for Scientific Research,
COU	:	Central Processing Unit,
DEM	:	Digital Elevation Model,
DOI	:	Descent Orbit Initiation,
DOF	:	Degree Of Freedom,
EAM	:	European Apogee Motor,
EDL	:	Entry Descent and Landing,
EMD	:	Elementary Motion Detector,
ESA	:	European space Agency,
ESTEC	:	European Space Research and Technology Centre,
FoE	:	Focus of Expansion,
FoV	:	Field of View,
GNC	:	Guidance Navigation and Control,
GNSS	:	Global Navigation Satellite System,
GPS	:	Global Positioning System,
HG	:	High Gate,
I <sub>2</sub> A	:	Image Interpolation Algorithm,
IBVS	:	Image Based Visual Servoing,
IMU	:	Inertial Measurement Unit,
IR	:	InfraRed,
JAXA	:	Japan Aerospace Exploration Agency,
LASER	:	Light Amplification by Stimulated Emission of Radiation,
LG	:	Low Gate,
LIDAR	:	LIght Detection And Ranging,
LLO	:	Low Lunar Orbit,
LMS	:	Local Motion Sensor,
LOLA	:	Lunar Orbiter Laser Altimeter,
LORA	:	Lateral Optic flow Regulation Autopilot,
LPTC	:	Lobula Plate Tangential Cell,
LROC	:	Lunar Reconnaissance Orbiter Camera,
LPV	:	Linear Parameter Varying,
LQG	:	Linear Quadratic Gaussian,
LQR	:	Linear Quadratic Regulator,
MAV	:	Micro Aerial Vehicle,

MER	:	Mars Exploration Rover,
MPC	:	Model Predictive Control,
MPF	:	Mars Pathfinder,
MSL	:	Mars Science Laboratory,
NAC	:	Narrow Angle Camera,
NASA	:	National Aeronautics and Space Administration,
OCTAVE	:	Optic flow Control sysTem for Aerial VEHicles,
OF	:	Optic Flow,
PANGU	:	Planet and Asteroid Natural scene Generation Utility,
BBVS	:	Position Based Visual Servoing,
PID	:	Proportional-Integral-Derivative,
PDI	:	Powered Descent Initiation,
RAD	:	Rocket Assisted Descent,
RADAR	:	RAdio Detection And Ranging,
ReSSAC	:	Recherche et Sauvetage par Système Autonome Coopérant,
RVN	:	Relative Visual Navigation,
Rx	:	Receiver,
SIL	:	Software-In-the-Loop,
SNR	:	Signal-to-Noise Ratio,
STD	:	Standard Deviation,
TD	:	Touchdown,
TRL	:	Technology Readiness Levels ,
TRN	:	Terrain Relative Navigation,
TTC	:	Time-To-Contact,
UAV	:	Unmanned Aerial Vehicle,
VLSI	:	Very Large Scale Integration,
VMS	:	Visual Motion Sensor,
WAC	:	Wide Angle Camera,
WFI	:	Wide Field Integration,

# NOTATIONS

$g_{Moon}$	Moon gravity
$I_{sp}$	Duration of specific impulse
$V_{x,z}$	Horizontal or Vertical velocity
$m$	Spacecraft mass
$h$	Local ground height
$\theta$	Spacecraft pitch angle
$I$	Spacecraft moment of inertia
$R$	Spacecraft radius
$D$	Distance from the ground in the gaze direction (sensor's optical axis)
$\gamma$	Flight Path Angle (angle between the velocity vector and the local horizontal)
$\Phi$	Elevation angle (angle between the velocity vector and the gaze direction)
$\omega$	Optic flow
$u_{th}$	Main thrusters control signal
$u_{\theta}$	ACS thrusters control signal
$F$	Main thrusters force
$L$	Vertical lift
$a$	Lander's acceleration
$\Omega_j$	Angular speed around $j$ axis
$\lambda$	Elevation angle between the gaze direction and the lander's axis of rotation
$\Delta\varphi$	Interreceptor angle
$\Delta\rho$	Acceptance angle
$f_{refresh}$	Refresh rate
$\Delta t$	Time of travel
$f_{c_{HP}}$	Cutoff frequency of high pass filter
$f_0$	Center frequency of the notch filter
$Q$	Q-factor,
$f_s$	Sampling frequency,
$\Delta\omega$	Full width at a level
$f_t$	Temporal frequency
$f_{spatial}$	Spatial frequency
$Ph_i$	$i^{th}$ photodiode
$Ph_{filt}$	$3^{rd}$ photodiode after filtering
$\omega_{median}$	Median of the 5 OF measurements
$K_{filter}$	Programmable gain of the VMS
$grd - trh$	Ground-truth



# PREFACE

**T**HIS PhD study was funded through the Network/Partnering Initiative (NPI) of the European Space Agency (ESA) by ONERA, Institute of Movement Science, Airbus Defense and Space and ESA-ESTEC.

ONERA is a French laboratory for applied aerospace research. This activity involved the Systems Control and Flight Dynamics Department (DCSD) in Toulouse, France.

Institute of Movement Science is a joint research unit attached to Aix-Marseille University and the French National Centre for Scientific Research (CNRS): the ISM includes the birobotic team in Marseille, France.

Airbus Defense and Space (previously ASTRIUM - EADS) is an industrial company of the Airbus Group. It is located in Toulouse, France.

ESA's European Space Research and TEchnology Centre (ESTEC) is the main technology development and test centre in Europe. It is located in Noordwijk, The Netherlands.

This thesis report is composed of a scientific paper collection. The peer-reviewed papers published or submitted during the thesis duration, or currently in revision, are presented along with a general introduction and conclusion. In accordance with French regulation regarding PhD thesis, a self-contained French summary of the thesis is attached after the English part.



## **Part 1**

# **Introduction**



**T**HIS introductory part aims at guiding the reader through the specific challenges addressed during this thesis via the presentation of the context and background that made us strongly believe that insect-inspired visual motion sensors could bring a reliable backup solution to perform safe emergency lunar landing. Section 1.1 presents a brief history of planetary landing and points out different challenges to be addressed for such complex robotic task. This history is intentionally non exhaustive since many previous works give very interesting and complete history time-line of this fascinating field (see Ulivi and Harland (2007), Ball et al. (2007), Harvey (2007), Ulivi and Harland (2008), and Ulivi and Harland (2012)). Section 1.2 describes Guidance Navigation and Control (GNC) background to provide the reader with necessary technical tools for the following chapters. Section 1.3 focuses on bio-inspired robotics and presents its interest for landing applications. The visual cue used in the sensors developed here called optic flow is presented and defined. Previous versions of optic flow sensors are presented and several applications are discussed. Finally, the general objectives of the thesis are stated along with the main assumptions taken in all this work.

### 1.1 Planetary landing: a brief history

#### 1.1.1 Past exploration missions in the solar system

Since the 4th of October 1957, day of Sputnik 1 launch, the eagerness of scientists to explore the surroundings of our planet never faded away. Many exploration missions were launched and many successfully landed on the expected target (see table 1). These missions usually have two separates but complementary objectives; scientific study of other celestial bodies and validation of key enabling technologies for future space exploration. Many different technologies have been tested and validated to perform such landings depending both on the objectives of the mission and on the atmospheric density of the targeted celestial body. Landing on the Moon or on an asteroid is quite different than landing on Mars or Venus due to the lack of atmosphere preventing the use of aeroshells or even parachutes which helps greatly reducing the entry velocity. Such technologies have been validated several times on Mars and Venus.

Although numerous space exploration missions were successful and provided scientists with extremely valuable results, space is far from well-known and many challenges remain unsolved. Teams of engineer who gathered priceless experience from past missions are often required to start over from scratch depending on the mission requirements. If we have a look at the landing systems developed and validated by NASA (National Aeronautics and Space Administration, USA) for Mars landing, we can see that very different innovative technologies were used ( $V_{x_f}$  is the horizontal ve-

locity at touchdown,  $V_{z_f}$  is the vertical velocity at touchdown, and  $m_f$  is the mass at touchdown,):

- Viking (1976,  $m_f = 590\text{kg}$ ,  $V_{z_f} < 2.4\text{m/s}$ ,  $V_{x_f} < 1\text{m/s}$ ) and Phoenix (2004) landers used retro-engines to control their descents until touchdown (Desai et al., 2011),
- Mars Pathfinder (MPF) (1997,  $m_f = 360\text{kg}$ ,  $V_{z_f} < 12.5\text{m/s}$ ,  $V_{x_f} < 20\text{m/s}$ ) used inflated airbags to allow higher velocities at touchdown with improved safety for the lander and thus reduced fuel consumption and overall cost (Spencer et al., 1999),
- Mars Exploration Rovers (MER) (2004,  $m_f = 539\text{kg}$ ,  $V_{z_f} < 8\text{m/s}$ ,  $V_{x_f} < 11.5\text{m/s}$ ) was based on previous technology but with an improvement which came from the use of three rocket-assisted descent (RAD) motors and a camera to further reduce the impact velocity of these much heavier rovers (Cheng et al., 2004),
- MSL (2012,  $m_f = 1541\text{kg}$ ,  $V_{z_f} < 0.75\text{m/s}$ ,  $V_{x_f} < 0.5\text{m/s}$ ) had to use a completely new technology due to its size and weight which prevented the use of airbag technology. NASA's developed the Sky-crane descent and landing architecture which dropped the rover gently onto the surface (Steltzner et al., 2006; Grotzinger et al., 2012).

A comprehensive study of NASA's Mars landing was presented by Braun and Manning (2007).

One can conclude that depending on many parameters (mission requirements at touchdown, size of the payload, reduced costs, elevation of the landing site, atmospheric density of the planet, ...) a lot of innovative efforts have to be performed for each space exploration mission to ensure successful landing at each attempt.

### 1.1.2 Lunar landings goals and strategy

Several kinds of landings might be described: safe, soft and precision landing.

- Soft landing is opposed to hard landing and is often required to ensure integrity of the science equipment, the communication instruments and the lander. The goal is to land on the surface with residual velocities small enough to use landing pads or the rover's wheels.
- Safe landing requires to land on a clean landing site without any direct threats for the lander such as boulders, craters or highly inclined ground. A landing site selection algorithm coupled to a hazard avoidance algorithm might be used to perform safe landing.

Table 1 – Successful soft landings (or failure at landing) on other celestial bodies than Earth in chronological order. NASA, ESA, ASI, JAXA and CNSA are respectively the US, European, Italian, Japanese and Chinese space agencies. Philae is expected to perform a soft landing on Churyumov-Gerasimenko on November the 11th of 2014. Updated from Delaune (2013)

Program	Target	Agency	Successful landings	Dates
Mars program	Mars	USSR	1	1960 - 1973
Luna	Moon	USSR	6	1966 - 1976
Surveyor	Moon	NASA	5	1966 - 1968
Apollo	Moon	NASA	6	1969 - 1972
Venera	Venus	USSR	8	1970 - 1982
Viking	Mars	NASA	2	1976 - 1976
Vega	Venus	USSR	2	1966 - 1985
Mars Pathfinder	Mars	NASA	1	Jul, 1997
NEAR Shoemaker	Eros	NASA	1	Feb, 2001
Beagle 2	Mars	ESA/UK	0	Jun 2003
MER	Mars	NASA	2	Jan, 2004
Cassini-Huygens	Titan	ESA, ASI, NASA	1	Jan, 2005
Hayabusa	Itokawa	JAXA	1	Nov, 2005
Phoenix	Mars	NASA	1	May, 2008
MSL (Curiosity)	Mars	NASA	1	Aug, 2012
Chang'e	Moon	CNSA	1	Dec, 2013
Philae (Rosetta)	Churyumov-Gerasimenko	ESA		Nov, 2014

- Finally, precision landing focus on reducing uncertainties on the knowledge of the landing site prior to landing. Indeed, high scientific interest areas might be located in regions filled with many hazards which increases *de facto* the requirement for precision.

Current missions might require safe, soft and precision landing capabilities at the same time which results in even more complex problems. Specific difficulties of each kind for landing adds up. For example:

- Selecting a hazard-free landing site and retargeting maneuvers possible complications. For example, pilots of the Apollo 11 mission had to avoid obstacles on the landing site few moments before landing and landed with about 25 seconds of fuel left,
- Landing gently in an energy efficient way without complete knowledge of the current position and attitude,
- Tracking accurately the reference trajectory to land at a specific landing site even if accumulated errors brought states deviations.

When addressing lunar landing, one has to mention the tremendous achievement brought by the Apollo program. The Apollo missions are somehow the foundations for planetary exploration science as it contributed to our understanding of the Moon on both the fundamental planetary science knowledge and the capabilities related to landing on our natural satellite (Crawford et al., 2012).

A much more complete description of hazards and challenges can be found in a very nice study of the six Apollo lunar landings by Brady and Paschall (2010). Another paper worth mentioning describes the complete strategies for trajectory design from Earth-launch to Lunar landing was presented by Loucks et al. (2005).

Following the enthralling era of Apollo landings, interest of the space community for Moon exploration started to decrease. Recently several missions such as Lunar Reconnaissance Orbiter (LRO) (Chin et al., 2007) (launched in 2009), Chang'e 1, 2 and 3 (Ouyang et al., 2010) (launched in 2007, 2010 and 2013 respectively), SELENE (Kato et al., 2008) (launched in 2007) or even Chandrayaan-1 (Goswami and Annadurai, 2009) (launched in 2008) showed a regain of interest of the scientific community for lunar landing which offer numerous untackled challenges. Lunar exploration could be of interest for a large number of sciences such as planetary science, geology, plasma physics, astronomy, and fundamental physics and so on.

### 1.1.3 ESA's Lunar Lander mission

In order to be part of this incoming prosperous lunar exploration era, ESA defined a new lunar landing mission called "Lunar Lander" which was selected as reference test scenario in this thesis.

- The first objective of the Lunar Lander mission is to demonstrate European safe, soft and precision landing capabilities (an extensive presentation of the mission was proposed by Carpenter et al. (2012)). Indeed Moon exploration is a stepping stone to explore further planets and validate at a lower cost such advanced technologies.
- The second objective of this mission concerns on-surface scientific experiments to ensure sustainable exploration programs such as robotic manipulation of payloads or lunar boulders.

Objectives and priorities of lunar exploration from ESA point of view are listed and described by Carpenter et al. (2010). Intended landing sites are located in the lunar South Pole Region ( $-85^\circ$  to  $-90^\circ$  latitude) because of the long duration of illuminated areas. These favorable conditions due to low sun elevation makes the use of solar energy possible during both the landing and science tasks performed on the ground (De Rosa

et al., 2012). The major drawback of Polar Regions is that irregularities on the local horizon creates very large shadows and thus reduce the number and the size of safe landing sites candidates. Precision landing capabilities are thus consequently required to ensure an accuracy of 100 meters in diameter at touchdown (Delaune, 2013).

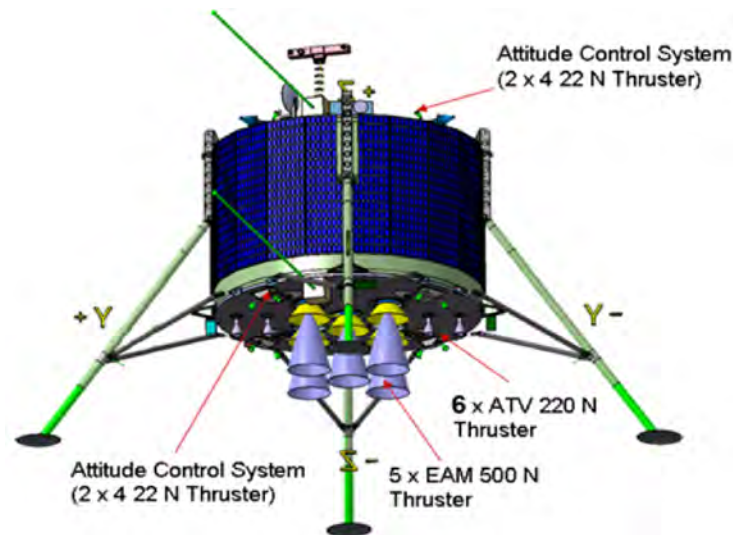


Figure 1 – Illustration of the configuration of thrusters for the lunar lander (Phase B1). Courtesy of Airbus Defence and Space (ex ASTRIUM). The ACS is composed of 4 clusters of  $4 \times 22$  N thrusters situated at the top and bottom of the lunar module to create torque (yaw pitch and roll control). The propulsion system is made up of  $5 \times 500$  N Bipropellant EAM (European Apogee Motor) and 6 ATV (Automated Transfer Vehicle) 220N.

Before it was put on hold at the 2012 ESA Ministerial Council, the Lunar Lander mission was intended to be launched not later than 2018. The lander was supposed to reach a 100km low lunar orbit (LLO) after Earth-to-Moon transfer. From this position, it would have wait until perfect illumination conditions occur while performing check-out procedures as well as position and velocity determination. The spacecraft then would have begun its descent procedure over the North Pole region with the Descent Orbit Initiation burn (DIO) toward the South Pole. When it reached a 15 km altitude, the Powered Descent Initiation (PDI) is performed. A precise DOI position and duration of burn is crucial to keep the intended landing site reachable. A small error at 100km of altitude may result in large errors at touchdown and thus unnecessary fuel expenditure. From DOI to PDI, Absolute Visual Navigation (AVN) is realized: images captured by the spacecraft are processed to extract landmarks which are then compared with on-board Digital Elevation Model<sup>1</sup> (DEM) database. These landmark databases could come from previous missions based on lunar imagers such as LRO or Kaguya missions. This matching helps improving the absolute knowledge of the lander's position during this high altitude phase. PDI is mainly a braking phase where Terrain Relative Navi-

---

<sup>1</sup>A DEM corresponds to a referenced map indicating longitude, latitude, and elevation with respect to a reference level.

gation (TRN) is performed to extract lander's state from the visual environment thanks to advanced feature tracking techniques. This thesis addresses the Approach Phase (AP) defined from the High Gate (HG) where the landing site becomes visible to the Low Gate (LG) where the dust raised by the thrust prevents the use of visual sensors. During that phase, the thrusters are used in pulsed mode to control the trajectory in a precise and energy-efficient way. Figure 1 presents the thruster configuration of the lunar lander with 3820 N of braking force (5 main and 6 assist engines) oriented along the vertical axis of the body fixed frame and 8 clusters of attitude thrusters delivering a 44 N force on each rotation axis. During the last tens of seconds, the landing site is scanned by on-board remote sensors to identify potential unpredicted hazards. If so, the autopilot initiates a retargeting procedure to select a safer target. The landing ends with a vertical descent at low speed until TouchDown (TD). See Fig. 2 for an illustration of a similar EDL (Entry Descent and Landing) strategy presented by NASA. The lunar lander mission nominal duration is 4 to 6 month depending on the actual landing site illumination conditions.

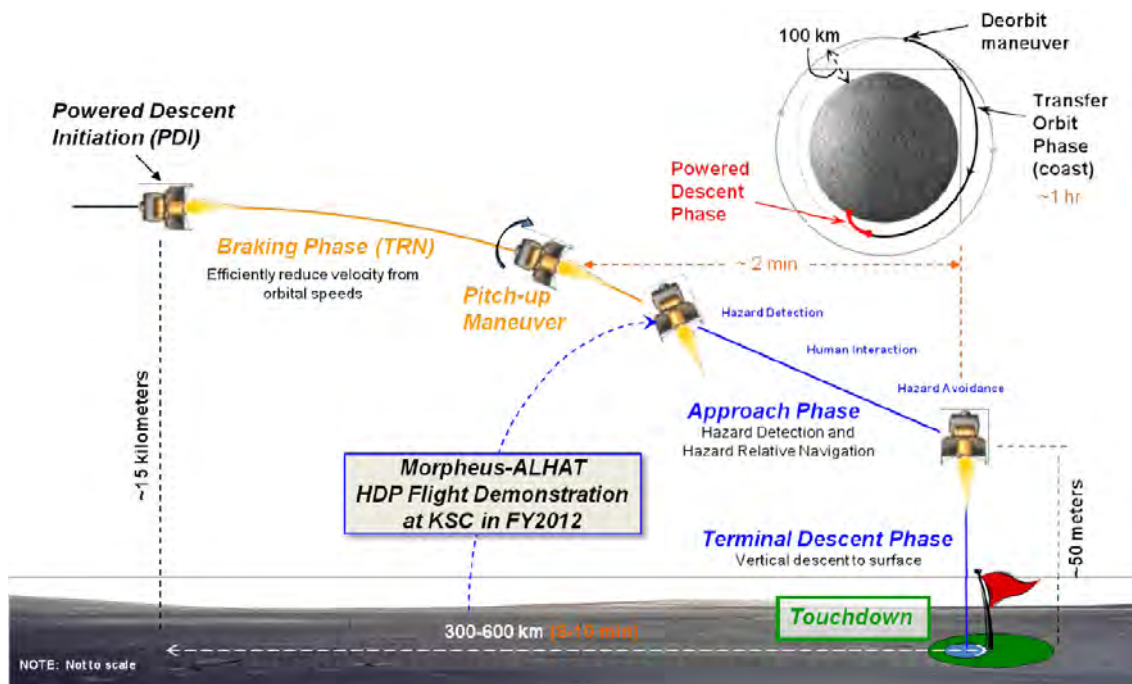


Figure 2 – Representative lunar Entry Descent and Landing trajectory profile from the deorbit maneuver to the terminal descent phase. During the test campaigns for ALHAT performed from 2012, the Morpheus prototype took off and reached the beginning of the approach phase where ALHAT was initialized. Reprinted from Rutishauser, Epp, and Robertson (2012).

## 1.2 Guidance navigation and Control challenges in soft landings

The main challenge of GNC for EDL is that it has to be fully autonomous due to the transmission time from the lander to Earth. This time delay cannot be compressed and is often longer than the EDL duration itself. EDL sequence of the Mars Science Laboratory (MSL) mission is referred to as the "6 minutes of terror". As soon as ground control station received the information that the EDL started: the robot had already landed on the martian surface (see Steltzner et al. (2006) and Burkhart and Casoliva (2012) for a description of EDL sequence for MSL). During this short lap of time a complex series of time triggered actions had to take place autonomously to perform a successful landing. Even if the Moon is way closer than Mars<sup>2</sup>, an embedded advanced GNC algorithm running at a sufficient rate is required to control the high dynamics associated with the lander's self-motion. Sensors availability is another pitfall associated with planetary EDL. Thanks to the wide satellite cover around Earth, GNSS (Global Navigation Satellite System) provides high precision positioning allowing impressive achievement regarding flying robots or airplanes on Earth. Of course these kinds of sensor suites are not available on other planets which increases the challenge of safe EDL. On top of that, one should say that landing on the Moon is quite particular in terms of control due to the lack of atmosphere. Numerous challenges have yet to be addressed and tackled regarding GNC algorithm for planetary EDL which is a critical and complex phase.

A Guidance Navigation and Control subsystem have to answer in real time the three following questions:

### Guidance

Which reference path should I follow to get to the target from my current position?

### Navigation

Where am I and how can I use available sensors outputs (and embedded knowledge of my surroundings (sky map and DEM)) to know that information?

### Control

What orders should I give to the actuators to follow the reference trajectory computed by the guidance using information provided by the navigation?

The brief overview presented in this section is not an exhaustive presentation of guidance, control and navigation techniques. It is limited to those encountered in this thesis or in the optic flow based GNC literature. We will mainly be interested in optimal

---

<sup>2</sup>Distance from Earth to Mars is greater than 50 million of kilometers meanwhile the Moon is located at a mean distance of 385000 km (Williams, Newhall, and Dickey, 1996)

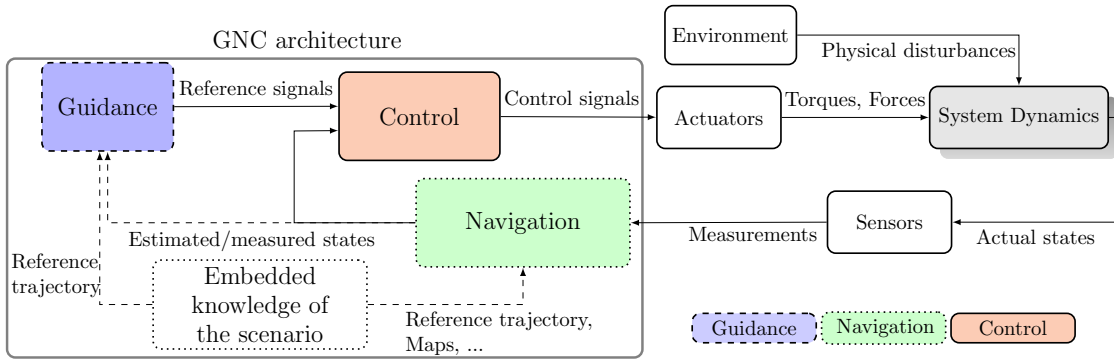


Figure 3 – Guidance Navigation and Control system sketch. The system dynamics described by a set of differential equations, is actuated through external physical inputs such as gravity, wind gust and also its own actuators (usually thrusters for braking and thrusters or inertial wheels for attitude control). The sensor suite measures several physical quantities depending on the setup (see section 1.2.3.1), for instance it could be velocities, attitude, position, and many different visual cues. Regarding GNC, one can see that the navigation filters are fed with measurements from sensors; the navigation block then estimates states of the dynamic system. It is worth noting that the entire state vector is not necessarily entirely measured. Eventually the estimation step is used to feed the control laws with signals in accordance with the designed control. For instance, for a velocity/attitude control architecture the navigation uses all the available information to estimate velocity and attitude parameters. Lastly, the guidance scheme delivers the path to follow to the control laws. Optionally, some on-board memory might be used to store knowledge of the scenario such as pre-computed trajectories, Digital Elevation Model (DEM) of the terrain, system dynamics, waypoints and so on. Dashed lines represent optional connections.

control, classical linear control and Lyapunov based nonlinear control and observation theory. Technical tools used for GNC designs mostly rely on control theory. More information about control can be found in many reference books covering linear control (Åström and Murray, 2010), nonlinear control (Isidori, 1995; Sontag, 1998; Kokotović and Arcak, 2001; Khalil and Grizzle, 2002; Coron, 2009), robust control (Zhou, Doyle, Glover, et al., 1996), optimal control (Bryson, 1975; Boyd and Vandenberghe, 2009) and observation theory (Gauthier and Kupka, 2001; Besançon, 2007; Anderson and Moore, 2012).

The general GNC structure along with its interconnections to the system dynamics are presented on Fig. 3. A detailed example of a complete GNC system with human in the loop interactions that flew on Apollo missions is presented on Fig. 4. It is worth noting that such division in three main blocks was already formalized as GNC in the 60s.

### 1.2.1 Guidance schemes

Guidance is used for generating a reference trajectory in terms of lander's states (position, velocity and attitude) that allows the landing site to be reached. It has to take into account the inherent systems dynamics, the initial states, and the final objectives along

## 1.2. Guidance navigation and Control challenges in soft landings

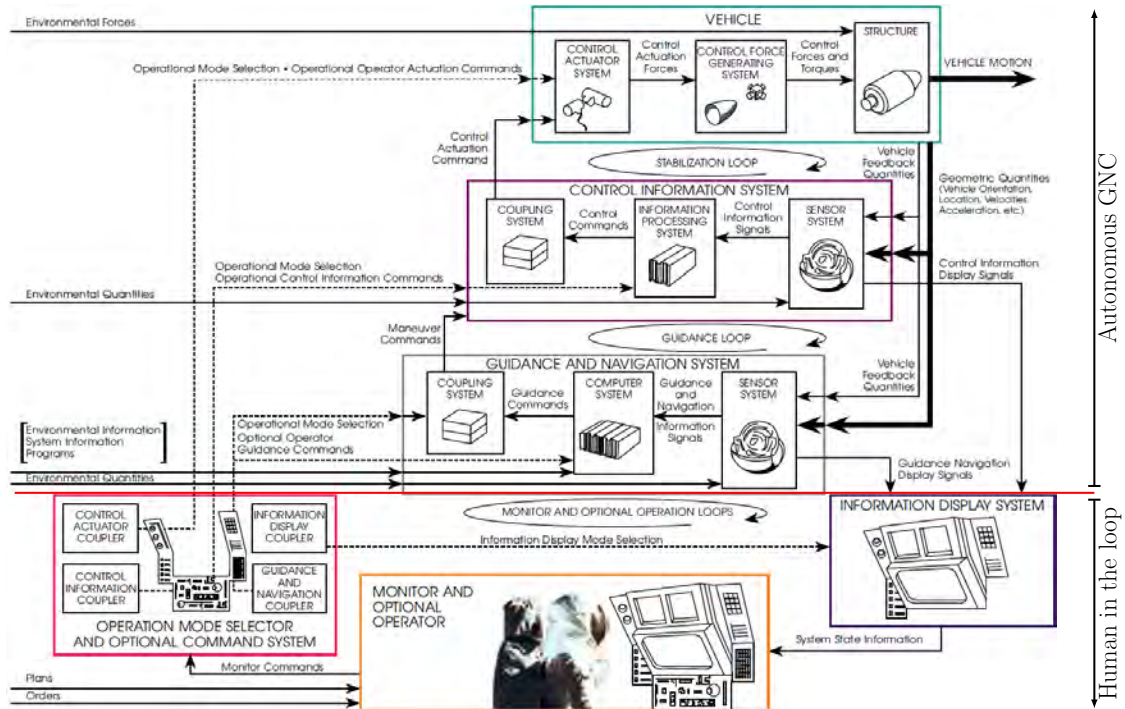


Figure 4 – Control and guidance system with Ground Based Monitor. Autonomous GNC and human in the loop interactions for the Apollo missions. In the 60s, with the Apollo program for example, the GNC framework was already formalized and complex GNC structures were developed and implemented in space. Modified from Forest, Kessler, and Homer (2007) and original version from Draper (1965).

with actuation capabilities of the system. The guidance system can take as input the current state estimates and embedded knowledge of the scenario. This is implemented either as fixed reference trajectory (or trajectories) or as a dynamic algorithm in the GNC computer. The three main objectives of the guidance design are:

1. Optimizing the trajectory to minimize the fuel consumption of the proposed landing scenario (Hargraves and Paris, 1987; Acikmese and Ploen, 2007; Liu, Duan, and Teo, 2008),
2. Providing a reference trajectory achievable from the system dynamics point of view,
3. Delivering the reference signals to the control scheme autonomously,
4. Initiating hazard avoidance maneuvers in the case of a non-hazard-free landing site (Johnson et al., 2002; Wang, Huang, and Guan, 2008).

Numerous techniques can be used to design a guidance algorithm for planetary landing. Delaune (2009) studied various fuel optimal guidance strategies to perform lunar landing from circular parking orbit to touchdown along with a trajectory optimization method to determine optimal descent gates conditions. Several solutions to this optimal

control problem were proposed in literature (Ramanan and Lal, 2005; Ploen, Acikmese, and Wolf, 2006; Guo and Han, 2009; Cho et al., 2009).

## 1.2.2 Control algorithms

### 1.2.2.1 Control of airborne vehicles

Control is used to compute and deliver to the actuators the required amount of actuation so that the current states of the system can reach the desired states. In other words, control theory describes how the actuators should be used to cancel the reference tracking errors (difference between the guidance reference signals and the actual states provided by the sensors). Even so control theory is still a young field, it is promised to a great future since it cuts across most of the classical engineering sciences (aeronautical, chemical, mechanical, electrical, economics). Two very interesting papers by Åström give a wide overview of control theory history, applications and perspectives (Åström, 1996; Åström and Kumar, 2014). In flying robots, typical control schemes are often decomposed in two parts thanks to the time-scale separation between the translation dynamics (slow time-scale) and the orientation dynamics (fast time-scale) (Bertrand, Hamel, and Piet-Lahanier, 2008). The first one concerns the attitude stabilization which controls the orientation of the system in flight (hovering for a UAV, orientation of the main thrust on a lander, high accuracy pointing toward a specific area for geostationary satellites, ...). This inner-loop usually relies on inertial measurements of angular rates and/or angular position. The second part corresponds to the so-called outer-loop which controls translational velocities and position. The control laws have to ensure performances, and robustness to initial uncertainties, modeling errors, external disturbances. Mahony, Kumar, and Corke (2012) presented the fundamentals of the dynamics, estimation and control of multirotor aerial vehicles, widely studied in literature. In complex landings such as in the South Polar Region, these external disturbances are composed of abundant boulders, shadows, slopes, and various illumination conditions. A well-known control strategy is to align the thrust vector force with the velocity vector to follow a pre-programmed velocity magnitude profile as a function of the altitude. This strategy was called the gravity turn and was for example validated on Surveyor landings by NASA (Cheng, 1966). Thanks to the gravitational acceleration, the flight path is aligned with the local vertical over time. Indeed, if the lander starts with a pure translational velocity, the braking forces will keep reducing this velocity while gravity will add a vertical downward component. This kind of strategy requires knowledge of the vehicle attitude and linear velocities. In gravity turn strategy the guidance would provide the pre-programmed velocity magnitude profile as a function of altitude and the navigation

estimate the velocity and altitude measurements. It could be noted that from a control theory point of view, a planetary lander is a quite interesting underactuated nonlinear dynamic systems (Fantoni and Lozano, 2002; Hua et al., 2009; Hua et al., 2013). Indeed, the translational dynamics have to be controlled despite the nonlinear coupling existing between the braking thrust and the attitude control thrust. It can be compared, in some sense, with unmanned aerial vehicles which often feature the same kind of challenges with different type of actuators.

Another key feature of such complex system often addressed in literature concerns the saturations on the control signals (Marchand and Hably, 2005; Marchand, Hably, and Chemori, 2007; Guerrero-Castellanos et al., 2009; Rifaï, Marchand, and Poulin-Vittrant, 2012; Rifaï et al., 2013). Physical actuators are always bounded, for instance thrusters available on the lunar lander can only produce a positive and limited force.

### 1.2.2.2 Vision based control

One focus of this thesis concerns vision based control which has a long history in robotics since Shirai and Inoue (1973) when authors first described the potential of visual feedback. These kinds of approaches are intended to control a robot based on the information contained in the output signal of a camera.

Two cameras configurations are possible, the so-called “eye-in-hand” and “stand-alone”. “Eye-in-hand” implementation consist in a camera mounted on the robot and giving images directly related to the pose<sup>3</sup> and motion of the later. In contrast, “stand-alone” configurations consider cameras either fixed in the workspace, providing image of the target independent of the robot motion or mounted on a gyro-stabilized system called gimbal system on the robot. Regarding planetary landing, vision sensors are, of course, necessarily mounted on the lander and often considered to be implemented on a gimbaled system as further discussed in section 1.4.

Firstly, open-loop solutions called “Static look and move” approaches (observation, computation of the motion to realize, motion, observation and so on) were distinguished from “dynamic look and move” where observation and motion are performed simultaneously (Weiss, 1984). Then, the term of visual servoing was introduced by Weiss, Sanderson, and Neuman (1987) where authors categorized two main approaches: **Image Based Visual Servoing (IBVS)** and **Position Based Visual Servoing (PBVS)**. IBVS and PBVS using modern control theory allow robots to move and use vision at the same time, improving response time and transient trajectories. In PBVS, features are extracted from the images and used to estimate the pose of the target with respect to the camera. Using these values, an error between the current and the desired pose of

---

<sup>3</sup>In computer vision, pose denotes the position and orientation of an object

the robot is defined in the task space and the control signals are computed. In IBVS, the control task is only defined in terms of features contained in images thus avoiding the state estimation step. Once IBVS or PBVS strategy is chosen the controller have to be design. With PBVS, the determination of the vehicle's states allow the use of classical control techniques. However, in the case of nonlinear systems, we have to ensure that the designed nonlinear observer do not deteriorate the control performances. Indeed, it is well known that the separation principle usually does not hold for nonlinear systems. Even though IBVS schemes might use the same background control theory, they are merely based on image features and thus they might be used for systems where all the states are not measured or estimated. Very nice tutorial paper can be found on visual servo control of robotic manipulators by Hutchinson, Hager, and Corke (1996), and a more recent study nicely presents advances of this theory in robotics by Chaumette and Hutchinson (2006) for basic principles and by Chaumette, Hutchinson, et al. (2007) for advance approaches. In 2014, Henry de Plinval's drew in his PhD thesis the timeline of vision based control with an extensive state-of-the-art (de Plinval, 2014). Optic flow based control studied in this thesis are discussed in the next section where the mathematical and biological background are defined.

### 1.2.3 Navigation approaches

Navigation is used to assess the current states of a dynamic system on the basis of available sensors, knowledge of the system dynamics, and configuration of the environment. The usual states of a flying vehicle are the position  $\xi = (x, y, z) \in \mathcal{I}$ , the velocity  $V = (V_x, V_y, V_z) \in \mathcal{I}$ , the attitude  $\eta = (\Omega_{roll}, \theta, \psi) \in \mathcal{I}$  and angular rates  $\omega = (p, q, r) \in \mathcal{B}$  and the mass  $m$ . Usually, the roll is noted  $\varphi$  but since this notation is already used in optic flow equation, the roll will be noted  $\Omega_{roll}$ . Figure 5 presents the various notations and the reference frames used in this work. This determination is realized either directly if the states are measured with dedicated sensors or indirectly thanks to more or less complex navigation filters. Using model of the system dynamics or fusion methods, the available measurements are used to estimate non measured states. For lunar landers, various sensors could be used including usual sensors such as Inertial Measurement Units (IMU), star-trackers, as well as Terrain Relative Navigation (TRN) systems, including cameras, lidars and altimeter/velocimeters. Various navigation solutions might be implemented depending on the current EDL phase and on the intrinsic capabilities of the embedded sensors.

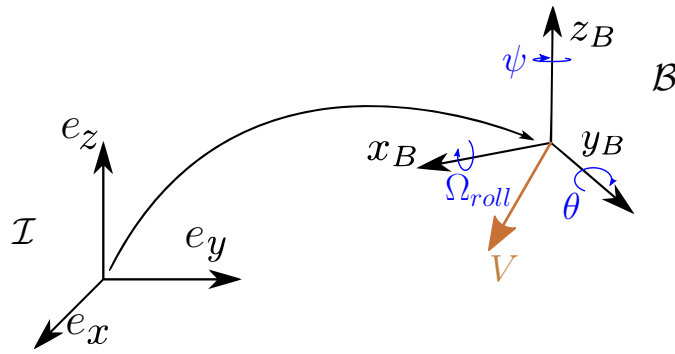


Figure 5 – Notations of position  $(x, y, z)$ , velocity  $(V_x, V_y, V_z)$ , and attitude  $(\Omega_{roll}, \theta, \psi)$ , inertial  $\mathcal{I}$  and body fixed  $\mathcal{B}$  reference frames.

### 1.2.3.1 Navigation sensors

One can sort sensors into two categories. **Proprioceptive sensors** are used to assess the knowledge of the own motion of the vehicle. For instance IMU, compass and star trackers inform on the current pose (position and orientation). **Exteroceptive Sensors** are used to sense to surrounding environment. These sensors keep the robot from colliding with hazards and provide information to proximity of obstacles. For instance vision based sensors, Global Positioning System (GPS), radars (RAdio Detection And Ranging) and lidars (LIght Detection And Ranging) can be used to analyze the targeted landing site and switch to a safer location if necessary. Among exteroceptive sensors for robotics applications one can also find contact sensors (e.g. force sensors, tactile sensors), and even olfactory sensors. Another classification could be done with passive and active sensors. Passive sensors measure ambient environmental information reaching the sensors like cameras or IMUs. Active sensors such as radar, laser, sonar emit energy into the environment and measure its reaction. Active sensors are usually more accurate than passive sensors but imply higher energy requirements, furthermore, emitted sensor's signals may suffer from interferences. Here we present briefly the different sensing devices which are mentioned in the planetary exploration literature.

**Altimeter** Laser altimeter and radar technology are used to assess the local altitude.

The laser emits an amplified light signal (ultraviolet, visible or near-infrared wavelength) which is reflected by the surface in the line of sight. The determination of the time delay between the emission and the reception of the signal gives a measure of the current height. Radar altimeters send radio signals. If an on-board database is present, the altitude with respect to a reference level can then be computed using position measurements. Doppler radar could also be used to compute ground relative velocity. Once the reflected signal is received by the Doppler radar, the frequency difference between the emitted signal and the received one is

computed and is called the Doppler shift. This shift is directly proportional to the lunar lander velocity with respect to the lunar surface (Rozas and Cunningham, 1972; Pollard and Sadowy, 2005).

**IMU** Inertial Measurement Unit includes accelerometers and gyroscopes on each axis to produce measurement of linear accelerations and angular rates. Thanks to an integration step, attitude, velocity, and position estimates can be obtained at rates ranging from 100 to 1000 Hz. Those estimates are relative measurement between the current state and the initialization states (or last calibration). The major drawback of the integration procedure is that it suffers from accumulative errors which lead to large drifts. The higher the refresh rate, the larger the accumulated bias could be.

**Lidar** Lidar is able to generate a range map of the region under the vehicle in order to assess its topography by raster scanning a pulsed laser beam across the targeted surface. It therefore ensures the suitability of a landing site, before committing to a possibly hazardous site. The output of the lidar is a cloud of 3-D points that convey the topography of the scanned surface. Correlation techniques could be used for feature matching navigation based on lidar measurements (Hamel, Neveu, and Lafontaine, 2006).

**Star tracker** A star tracker provides the absolute 3-axis attitude of a spacecraft based on star observations. A camera associated with processing electronics performs star identification using an internal database. The attitude quaternion is then computed autonomously (Liebe, 2002).

**Cameras** Cameras are passive sensors and may thus be used at any distance (altimeter range  $< 25\text{km}$  and lidar range  $< 5\text{km}$ ) on any kinds of terrain (altimeter and lidar are incompatible with flat terrain since no reflected signal can be received) as long as it is illuminated. Images acquired by cameras provide a lot of useful information on self-motion and on the absolute pose (if a feature matching algorithm is used with an on-board database). The baseline for the ESA lunar lander mission, is a camera with  $1024 \times 1024$  pixels, covering a field of view of 70 deg, at a 20 Hz frame rate. It is intended to be lightweight (500g), small-sized  $13\text{cm} \times 13\text{cm} \times 8\text{cm}$  and energy efficient (2W) (Frapard and Mancuso, 2006). Drawback often associated with vision based navigation concerns the need for a scene with a sufficient illumination as constant as possible. Regarding the Lunar Lander mission this is not an issue thank to favorable illumination condition at South Pole of the Moon. On top of that, it requires high computational cost due to large amount of data to

process in order to extract useful information from images. Finally, a fine camera calibration is required for some applications such as object recognition and tracking. Despite these pitfalls vision based planetary landing was already successfully achieved by NASA for MER missions where velocity estimation was performed to fire the RAD rockets (Johnson et al., 2007).

Delaune (2013) presented the following table 2 containing comparison of update rate and accuracy of main sensors used for planetary landings:

Table 2 – Comparison of update rate and accuracy of main sensors used for planetary landings. Reprinted from Delaune (2013)

Sensor	Measured signal	Update rate (Hz)	Accuracy
Accelerometer	Linear acceleration	100-1000	300 $\mu\text{g}$
Gyroscopes	Angular rate	100-1000	0.5 $\text{deg.h}^{-1}$
Star tracker	Attitude	1-20	0.01 deg
Altimeter	Height	1-70	10 cm
Lidar	Range image	1-30	5 cm
Camera	Intensity image	10-100	$\text{SNR} \approx 205(\sigma)$

As already stated, no GNSS were deployed around the Moon yet. We thus need to use other kinds of information embedded on the lander to steer it safely toward its landing site. Autonomous navigation in GPS denied environment such as cluttered environment or indoor flying area is an active field of research in robotics. In contrast with usual navigation sensors, such as IMU or GPS which delivers respectively self-motion and absolute positioning with respect to the inertial frame, vision sensors bring rich information which takes into account all the complexity of the surrounding environment.

#### 1.2.4 Vision-based terrain relative navigation

As explained in 1.2.3.1, inertial navigation alone is not sufficient to ensure safe landing due to the accumulative errors related to the dead reckoning type of measurements. That is why the use of Terrain Relative Navigation (TRN) in addition to inertial measurements is currently extensively studied in literature. Using remote sensing of imaging, TRN provides position or bearing measurements relative to known or unknown surface. Among the various navigation solutions studied currently, we saw that the vision based navigation seems to be of particular interest for future exploration missions. Two different kinds of vision-based navigation have to be presented.

#### 1.2.4.1 Absolute Visual Navigation

The first one concerns **Absolute Visual Navigation** (AVN). The main objective is to match images taken by on-board cameras with embedded terrain map in order to estimate the absolute current states of the vehicle in real time. For instance image-to-map registration for absolute position calculation were presented by Gianpaolo and Patrick (2009). Trawny et al. (2007) proposed a solution based on a priori mapped landmarks detection and matching techniques. More recently, Delaune (2013) proposed an absolute vision-based navigation system for planetary descent and landing with pinpoint accuracy on any terrain relief using image-to-map matching. Validation was assessed via experimental demonstration of the pinpoint landing performances on a lunar-representative optical test bench. On top of the computational requirements of AVN, one other major drawback is that it can be performed only where reference maps exist, and accuracy of estimation depends strongly on the resolution of the map. For example, Clementine mission provided 100m/px resolution with large uncovered area around the polar regions which is not precise enough to handle precision landing. Lunar Reconnaissance Orbiter (LRO) was launched in 2009 with principal objectives to produce accurate maps and high-resolution images of feasible landing sites, assess potential resources and characterize the radiation environment (Chin et al., 2007; Robinson et al., 2010). LRO features the LROC (LRO Camera) composed of two Narrow-Angle Cameras (NAC) and one Wide-Angle Camera (WAC). The NACs provide 0.5 m/px image resolution for latitudes above 85° while the WAC covers the entire surface with a reduce resolution of 100 m/px images. The Lunar Orbiter Laser Altimeter (LOLA) allowed for example the creation of DEM of the lunar surface with vertical accuracy of about 1 m (Mazarico et al., 2012).

#### 1.2.4.2 Relative Visual Navigation

The second kind of visual navigation is called **Relative Visual Navigation** (RVN) and focuses on estimating current states of the vehicle relative to the lunar surface (Mourikis et al., 2009). It might be used for example for hazard avoidance since unpredicted obstacles may be seen even if they are not on an embedded map of the terrain previously recorded. It is also very useful where no reference maps are available or if the resolution is not precise enough for GNC requirements. RVN provides state estimates by calculating the self-motion on the basis of successive images. The main advantage of RVN comes from the local processing on the images (for example feature tracking techniques) which reduces greatly the computational requirements and allow higher

update rates than AVN. However, this dead reckoning process cannot compensate for initial errors as for inertial measurement devices.

Two extensive reviews were presented by Johnson and Montgomery (2008) regarding terrain relative navigation for pinpoint landing and Bonin-Font, Ortiz, and Oliver (2008) for vision-based navigation systems for mobile robots.

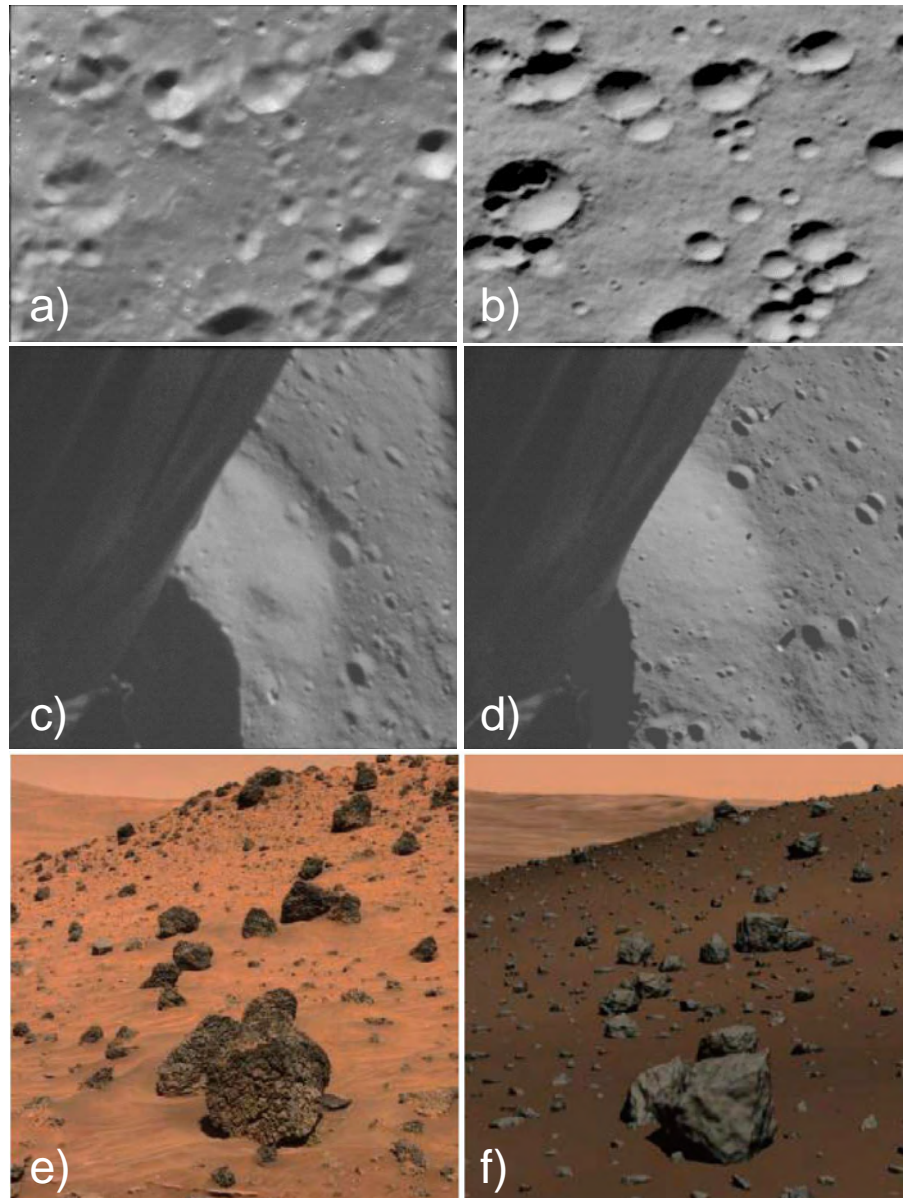


Figure 6 – Comparison between real images and PANGU generated images. Sub-figures a. was taken from the clementine mission (joint space project between the Ballistic Missile Defense Organization (BMDO) and NASA) and b. was generated with LunarSim the ancestor of PANGU. Sub-figures c., illustrating a near surface scene, was taken from Apollo 11 mission. The aim was to create synthetic images, similar in form to the real images to support the critical evaluation of the PANGU tool: PANGU generated images are showed in sub-figure d. Finally sub-figures e. and f. show rock model comparison on Mars. Real image from the Spirit Mars Exploration Rover (left) and PANGU generated image (right). Sub figures a-b modified from Parkes, Martin, and Dunstan (2003), b-c Parkes and Martin (1999) and d-e McCrum et al. (2010).

### 1.2.4.3 Validation of TRN solutions

Design of GNC systems is usually followed by a validation phase. When dealing with planetary landings, accessing representative data (descent images) or performing closed loop experiments is often a challenging part and is not always possible. The flight experiment on the intended platform could be extremely expensive and images of landing areas that have been targeted before unavailable. Various solutions exist to extend validation beyond pure numerical simulations. Firstly the cheapest one and thus the most used is to render them virtually from DEM, surface and camera models. PANGU (Planet and Asteroid Natural scene Generation Utility) is developed for ESA by the University of Dundee (Parkes, Martin, and Dunstan, 2004). PANGU is a tool used to simulate visual environments on planetary surfaces. The GNC simulator provides the position and orientation of a spacecraft above the planet's surface to PANGU which responds by producing an image of the surface from that view point. PANGU creates surface models either from scratch using fractal techniques and requirements for terrain topography and illumination (craters and boulders size and density distribution, surface roughness, sun elevation, sand dunes) or from an existing DEM e.g. MOLA (Mars Orbiting Laser Altimeter) or LRO DEM. Figure 6 presents the comparison between software generated images (right column) of the lunar and Mars surfaces and real images (left column). PANGU was used several times in literature, see Delaune et al. (2012) and Van Pham, Lacroix, and Devy (2012) for landmark matching, McCrum et al. (2010) for vision based rover navigation applications, Parkes et al. (2003) for a lidar based GNC and Dubois-Matra, Parkes, and Dunstan (2009) for an overview of the use of PANGU in ESA studies. One can see that even if it is possible to distinguish true and virtual images with the naked eye this kind of tools can provide a very handy way to validate the robustness of GNC solutions in different environmental conditions.

Secondly, if true images are available with a satisfactory resolution (and associated DEM) they can be used in simulations along with a camera model to render realistic descent images. Two main disadvantages are associated with this kind of simulations. Scalings are often required to modify artificially the altitude due to the fixed resolution of pixels. A landing simulation down to 10m with a fixed resolution of 0.5m/pixel for a tight field of view could lead to only a dozen of pixels in the view field yielding to very noisy, non-representative, visual measurements. The second pitfall of this approach is that illumination conditions could not be easily modified since only one or few images of a certain area are available. True-images based simulations were realized by Izzo and de Croon (2013) to assess performances of nonlinear model predictive control for lunar landing on LROC images. Mourikis et al. (2009), using Apollo, Galileo, MER and Mars Odyssey images, validated the VISINAV system presented in the paper. This was also

realized for relative terrain navigation performance validation on an asteroid (images from the NEAR Shoemaker's mission) by Li (2008). NASA's Clementine mission images were used by Singh and Lim (2008) for vision-based navigation simulations on the lunar surface. Finally Cheng and Ansar (2005) tested their crater recognition system from the Mars Odyssey probe images.

Eventually, the more advanced validation technique concerns testbed hardware validation to prove the performance of the system in a physical environment. Hardware-in-the-loop simulations were realized on the Testbed for Robotic Optical Navigation (TRON) developed by DLR (*Deutsches Zentrum für Luft- und Raumfahrt*: the German space center) to support the development of optical navigation technologies, and to qualify breadboards up to TRL 4 (Technology Readiness Level), and to qualify flight models to TRL 5-6 (Krüger and Theil, 2010). This facility can generate planetary approach images using an industrial robotic arm, scaled relief models and special lighting. Another test bench facility was developed by ESA and called VisiLab. It provides lunar-analogue planetary mock-up, a camera mounted on a robotic arm, an illumination system and a calibration framework (Voirin et al., 2013). Finally, outside tests on flying robots were also achieved in order to include flight disturbances. Visual navigation on aerial robot have been extensively studied in literature. The NASA's MORPHEUS project consisting of a planetary lander prototype is currently used to validate the Autonomous Landing Hazard Avoidance Technology (ALHAT) Project (Rutishauser, Epp, and Robertson, 2012). The ALHAT System will identify and avoid hazards to ensure a safe and accurate landing on a planetary surface under any lighting conditions. The Precision Landing GNC Test Facility (PLGTF) has been developed with the purpose to test, in a realistic environment, GNC techniques and technologies to be implemented on future Mars and Moon landers by ESA. It reproduces the dynamic of the powered descent phase of a planetary lander in order to perform precise landing (Guizzo et al., 2011).

### 1.3 Bio-inspired robotics

Among the entire robotics domain, biorobotics (also called bio-inspired robotics) represents a very promising approach. Biorobotics is the science of taking inspiration from nature to tackle some of the most advanced challenges in robotics. Biorobotics is used to model sensorimotor processing observed among animals to create tight bounds between perception and action. It brings new capabilities to robots and at the same time improves biological models. These models might then be validated through robotics testing in the same experimental conditions as the animals. Since millions of years,

nature had developed, enhanced and specialized innovative principles. Some of them provide ideas worth considering regarding GNC tasks. Biologists and neurophysiologists (studying the nervous system through electrophysiological recordings) tried to understand the underlying principles that allow plants and animals to realize such remarkable achievements. For example, one of the most famous biomimetic invention is Velcro® tape which mimics hooks of the burs. Various other examples of application of biomimetics are presented by Kumakura (2000). Inspiration from nature to develop new technologies has spread across many fields of research from nanotechnologies, robotics, artificial intelligence (AI), medical industry, and military. Biomimetics is the larger term gathering all the disparate disciplines dedicated to transferring functions from the natural world to artificial devices. Interesting review articles concerning biomimetics were published in the last decade. Lepora, Verschure, and Prescott (2013) presented a state-of-the-art of biomimetics based on a statistical survey of publications on biomimetics in engineering and related sciences with a very complete bibliography. Authors pointed out the fact that the total number of scientific papers focusing on this areas is growing at a very high pace, doubling every two to three years (see Fig. 7). An interesting

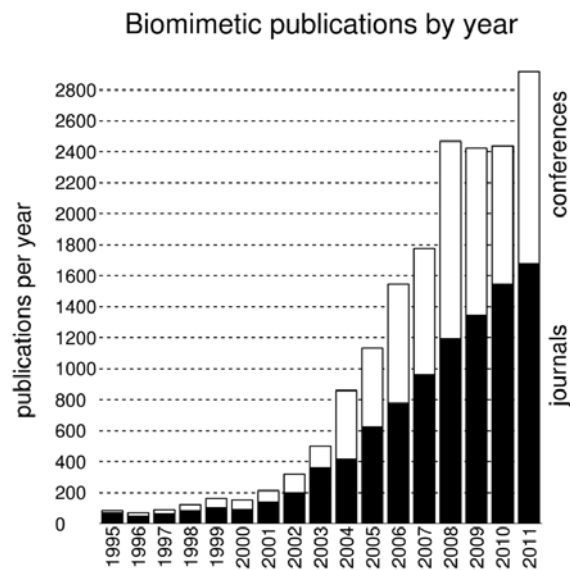


Figure 7 – Growth of biomimetic research papers over the last 16 years. The bar chart plots the number of papers published each year in biomimetics starting from 1995. The black bars indicate the proportion of journal papers and the white bars the proportion in books and conferences. Reprinted from Lepora, Verschure, and Prescott (2013).

handbook covering advances of biomimetics and bioinspiration in the medicine and engineering fields is presented in Jabbari et al. (2014). Recently, Ma et al. (2013) presented an insect-scaled flapping-wing robot (80-milligrams) was developed. This impressive robotic implementation was able to perform unconstrained stable hovering and basic controlled flight maneuvers.

In this section, we describe the visual motion sensors considered in this work. First

the optic flow is defined, and then the foundations of the bio-inspired principles are described. The visual flight system of the fly is described from two different perspectives. First the anatomical composition of the fly's eye is presented along with the others sensory systems present in such insects. The second part describes the visuo-motor reflexes observed in previous studies. Finally, several robotics implementations of these findings are presented. Franceschini (2014) presented a very nice and in-depth review presenting the work initiated by Franceschini regarding the design and construction of small insect-like robots that navigate and control their motion on the basis of optic flow. Three PhD students from Viollet & Ruffier's Biorobotics team recently defended their thesis on the use of optic flow in flying insects (Portelli, 2011), and application to robotics (Roubieu, 2013; Expert, 2013). Additional details could be found in the introduction parts of their manuscripts.

### 1.3.1 Definition of the optic flow visual cue

Optic flow in its simplest definition proposed more than sixty years ago by Gibson (1950) corresponds to the direction and magnitude of image motion due to movements of the visual system relative to a static environment (see Fig. 8). This two-dimensional vector field is often quite complex since it depends both on the self-motion and 3D structure of the environment.

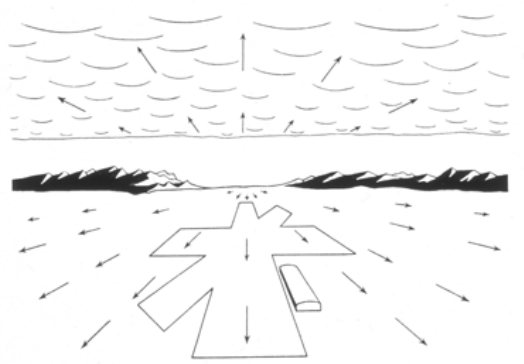


Figure 8 – Optic flow vector field generated on the retina of the pilot while landing. Arrows represent local optic flow vectors (magnitude and orientation). It is worth noting that clean sky does not generate optic flow due to the absence of contrasts edges, and that the pole of optic flow, namely the Focus of Expansion (FoE) is located in the direction of motion and is associated with a null optic flow. Reprinted from Gibson (1950).

Optic flow in a 3D environment is described as follow (Koenderink and Doorn, 1987):

$$\Omega(\Psi, \Theta) = -\frac{T - (T \cdot d(\Psi, \Theta) d(\Psi, \Theta))}{D(\Psi, \Theta)} - R \times d(\Psi, \Theta) \quad (1)$$

where  $\cdot$  denotes the scalar product and  $\times$  the cross product (see Fig. 9 for an illustration

of the notations).  $\Omega(\Psi, \Theta)$  correspond to the relative velocity of an object located at a distance  $D(\Psi, \Theta)$  in the direction  $d(\Psi, \Theta)$  while the observer is moving in translation along the vector  $T$  and in rotation along the vector  $R$ . The observed optic flow is always tangential to the unit sphere centered at the location of the visual sensor. From eq. (1), one can distinguish two different components in the optic flow definition: a translational optic flow  $\Omega_T$  and a rotational optic flow  $\Omega_R$ .  $\Omega_T$  depends on the vicinity to obstacles. The closer is the object in the gazing direction, the smaller is  $D(\Psi, \Theta)$ , the higher is  $\Omega_T$ . In contrast,  $\Omega_R$  depends only on the orientation of the gaze direction and on the self-motion of the agent. The optic flow patterns could be extremely difficult to analyze when a combination of rotation and translation are used. We present visual hemisphere and Mercator maps for a pure translational and a pure rotational motion on Fig. 10. It can be noted that:

- $\Omega_T$  is maximal for an elevation of  $0^\circ$  for a vertical motion (angle of  $90^\circ$  between the direction of motion and the gaze direction),
- $\Omega_R$  is maximal for an azimuth of  $\pm 90^\circ$  for a rotation around the horizontal axis (angle of  $90^\circ$  between the axis of rotation and the gaze direction),
- $\Omega_T$  and  $\Omega_R$  are both null in the direction of motion (and on the opposite direction). These points are called pole of optic flow or focus of expansion.
- Even with pure rotation and translation motions it can be impossible to distinguish self-motion if sensing only local optic flows, as it can be seen for an azimuth of  $90^\circ$ .

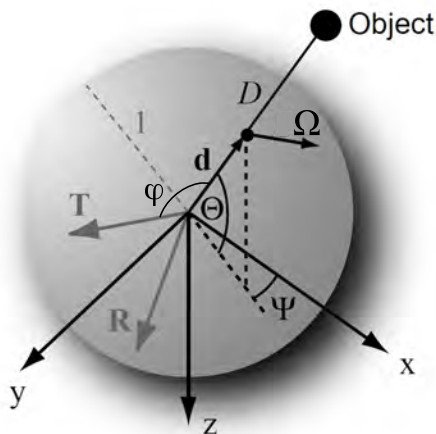


Figure 9 – Notations for optic flow definition. The sensor is located at the origin moving in translation  $T$  and rotation  $R$ . The relative angular velocity, the optic flow  $\Omega(\Psi, \Theta)$ , thus depends on this motion and on the position of an object at a distance  $D(\Psi, \Theta)$  in the direction  $d(\Psi, \Theta)$ .  $\Psi$  represents the azimuth and  $\Theta$  the elevation. Modified from Zufferey (2005).

To avoid indistinguishable optic flow patterns, flying insects seems to actively control their flight and head position to generate only translational optic flow as explained in section 1.3.4. From a robotic point of view, two different solutions were usually used in literature. The first one consist of gimbaled stabilized optic flow sensors to keep the gazing direction constant no matter the rotations and thus only sense translational optic flow (Ruffier and Franceschini, 2003; Kerhuel, Viollet, and Franceschini, 2010; Manecy, Viollet, and Marchand, 2012; Manecy et al., 2013; Expert, 2013). This intuitive solution is complex from a mechanical point of view since it requires bulky and elaborated devices for each sensor and IMU. The second one, called the derotation process, consist in measuring both the full optic flow  $\Omega = \Omega_T + \Omega_R$  and the attitude and then remove the rotational component from the optic flow measurement (Argyros, Tsakiris, and Groyer, 2004; Beyeler, Zufferey, and Floreano, 2009a; Zufferey, Beyeler, and Floreano, 2010; Hérissé et al., 2012). This last solution will be discussed further in the following chapters.

In the robotics literature, the optic flow in often considered in a 2D planar motion which allows simplification of the mathematical expression. In the case of a pure translational motion the optic flow can be expressed as follows (Whiteside and Samuel, 1970):

$$\Omega_T = \frac{V}{D} \sin(\varphi) \quad (2)$$

where  $V$  represent the velocity vector,  $D$  is the distance to the object in the viewing direction and  $\varphi$  is the angle between the velocity vector orientation and the gaze direction (see Fig. 9). As observed on the Mercator maps, it is interesting to note that for an angle of  $\varphi = k\pi$ ,  $k \in \mathbb{Z}$ ,  $\Omega_T$  is always equal to zero and is maximum for  $\varphi = (2k+1)\frac{\pi}{2}$ ,  $k \in \mathbb{Z}$ . For a pure rotational motion around the roll axis ( $\Omega_{roll}$ ) for example, the rotational optic flow in written as follows:

$$\Omega_R = \Omega_{roll} \sqrt{1 - \cos^2(\psi) \cos^2(\theta)} \quad (3)$$

In the following chapters of this thesis we consider a planar motion which further simplifies mathematical definition:

$$\omega = \frac{V}{D} \sin(\varphi) - q = \omega_T + \omega_R \quad (4)$$

where lower case  $\omega$  denotes the optic flow in planar motion and is thus a scalar (respectively capital letter  $\Omega$  denotes the optic flow in case of 6 degrees of freedom motion and is thus a vector).

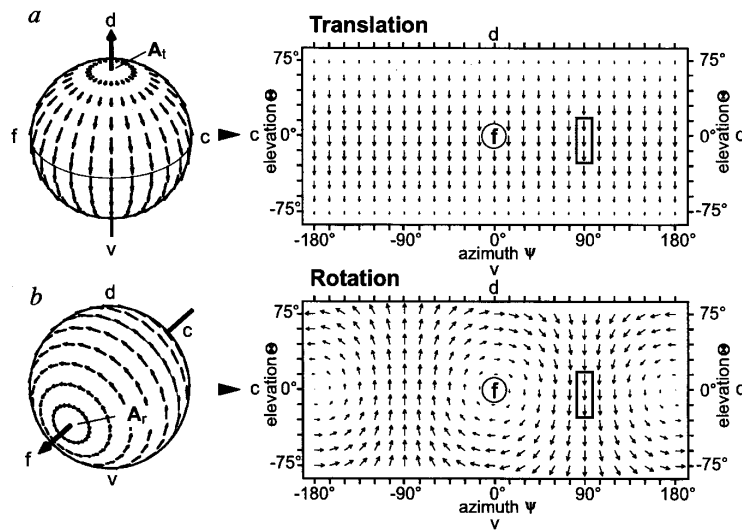


Figure 10 – Spherical hemispheres and Mercator maps of optic flow vector field for pure rotation and translation motion. Reprinted from Krapp and Hengstenberg (1996).

### 1.3.2 The compound eye of the flying insects

Animal kingdom makes extensive use of visual cues as feedback to navigate safely through their environment. Depending on the species and on the requirements for the visual system the number of pixels and thus the visual abilities can vary largely. For instance, with a very large number of pixels (see Fig. 11) human's eye allows us to distinguish objects in our view field thanks to the very high acuity of the fovea<sup>4</sup> (0.008°) and estimate accurately distances to obstacles thanks to our stereo vision. Among all living species, such high definition visual system is not always the rule.

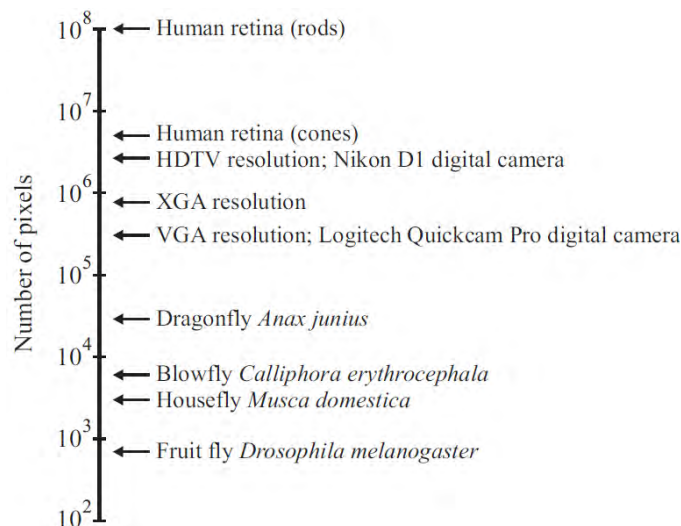


Figure 11 – Comparison of the number of pixels in insects' eye, humans' eye and commercial cameras. Reprinted from Harrison (2000).

Unlike us, flying insects are equipped with two compound eyes that allow a very

<sup>4</sup>Fovea is a part of the eye responsible for sharp central vision

wide field of view (FOV) but with a very low resolution (see Fig. 12). Indeed, insects' eyes can have fewer pixels than commercial cameras but they are still capable of navigation prowess with very limited processing resources. We will see that even with fewer pixels, very ingenious and elaborate mechanisms can be used to control autonomous flight in unknown complex environments.



Figure 12 – Portrait of bluebottle fly (*Calliphora vomitoria*) featuring two large compound eyes composed of several hundreds of facets. Picture from JJ Harrison licensed under © BY-SA.

The structure of the compound eye is based on a large number of repeating unit called ommatidia. Each ommatidia is composed of a facet (hexagonal lenses) which focuses the incoming light toward the photosensitive visual cells (Franceschini, 1975) of a part of the total scene. Each ommatidia optical axis are separated by an inter-ommatidial angle  $\Delta\varphi$  which defines the spatial acuity of the visual system (Land, 1997). The  $\Delta\varphi$ , and thus, the spatial acuity, varies over the eye showing a finest resolution in the frontal region. A smaller  $\Delta\varphi$  implies a higher resolution of the sensed environment and allows for a better detection of further located objects. On top of that spatial sampling, a low pass filtering is performed on the visual signals reaching the photosensitive cells due to the narrowness of the ommatidia. The diffraction of the light through the lens leads to a Gaussian angular sensitivity (Götz, 1964) which acts as a blurring effect. The tighter the ommatidia, the lower the cut-off frequency of the low pass filtering. This angular sensitivity is described by the width at half height called acceptance angle and noted  $\Delta\rho$  (see Fig. 13). The Gaussian angular sensitivity function  $A(\varphi)$  is described as follow:

$$A(\varphi) = e^{-K\left(\frac{\varphi}{\Delta\rho}\right)^2} \quad (5)$$

In 1997, Land showed that in diurnal insect the acceptance angle and the inter-ommatidial angles are roughly equal which allows for continuity in visual signals (low aliasing) and avoid oversampling the environment.

This low resolution of the insect eye can be seen as a necessary evil to allow such a

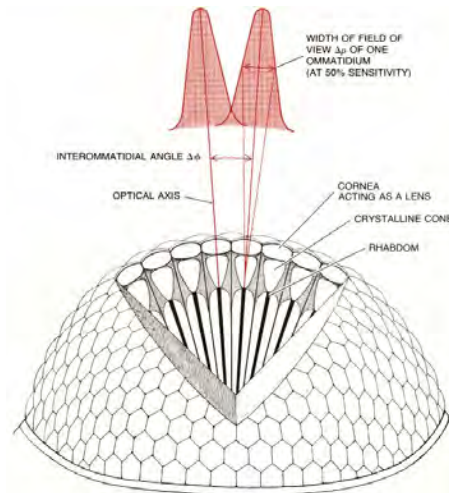


Figure 13 – Schematic of the compound insects' eye. The visual environment is spatially sampled into several elementary eyes called ommatidia oriented in different directions (optical axis). Ommatidia are separated by an inter-ommatidial angle  $\Delta\phi$ . Angular sensitivity of each viewing direction is characterized by a Gaussian shaped function defined by a width at half height called acceptance angle and noted  $\Delta\rho$ . Reprinted from Horridge (1977).

compactness of this quasi-panoramic visual system (small blind-area). Indeed, in order to provide the same resolution accessible with the human eye, the compound eye would need to be ridiculously large as depicted on Fig. 14.

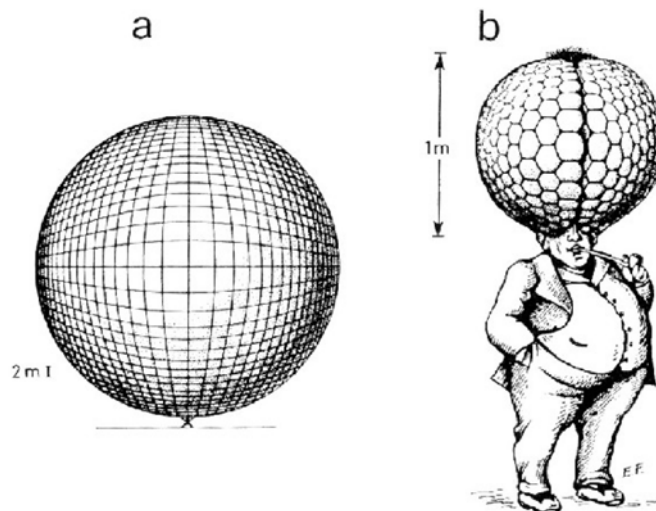


Figure 14 – Kuno Kirschfeld's illustration of the equivalent compound eye applied to human resolution. In order to obtain the same resolution than the human eye in every direction, the compound version would have to be extremely large (24m in diameter) in order to have ommatidias large enough to ensure that the diffraction limit is not reached. Since humans see very precisely only in the center of the retina, Kirschfeld took into account the mean resolution which gave a 1m in diameter compound eye. Reprinted from Land and Nilsson (2012) and original from Kirschfeld (1976).

Another key advantage associated with the insect eye is the temporal frequencies achievable up to 300Hz well beyond the Human 25 to 30Hz temporal resolution.

Once the visual signal went through the first step of the visual processing, it reaches

the retina composed of several photoreceptors located behind each facet. Figure 15 presents the spatial distribution of the eight photoreceptors inside a facet.

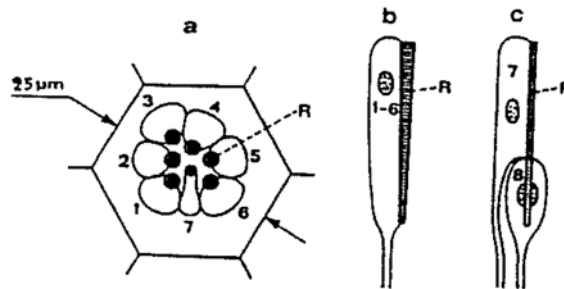


Figure 15 – *Spatial layout of the eight photoreceptors located behind each facet. The receptor number eight is placed under the number seven as shown on c. Reprinted from Franceschini (1983).*

After the visual signal is caught by the photoreceptors, it goes to the neuronal system composed of three successive ganglia called the lamina, the medulla and the lobula complex. A simplified schematic of the visual system of the fly is presented on Fig. 16.

**Lamina** The main objective of the lamina is to increase the signal to noise ratio (as usually performed at the beginning of a signal processing algorithm). This is done thanks to a high pass filtering and an automatic gain control which delivers only the transient signals at a roughly constant value (no matter the mean illuminance of the environment),

**Medulla** It seems that the local motion detection is performed in these quite complex and small structure which makes their study very complicated (Douglass and Strausfeld, 1996). Separation between ON (dark to light) and OFF (light to dark) contrasts pathways could also occurs in the medulla as observed by Franceschini, Riehle, and Nestour (1989) and recently showed by Strother, Nern, and Reiser (2014).

**Lobula** Finally, the lobula fuses all the local motion measurements provided by the medulla. The lobula is composed of 65 specialized wide-field motion sensitive neurons which are described below.

It has been observed in the lobula plate that the wide-field neurons called Lobula Plate Tangential Cell (LPTC) are sensitive to a preferred direction of motion (Hausen, 1982; Franceschini, 1985; Krapp and Hengstenberg, 1996). When stimulated in the preferred direction the rate of spikes increases and a depolarization of the membrane potential occurs (positive-going change in a cell's membrane potential, making it less negative). For the opposite direction of motion the neuron get inhibited (no more spikes and hyperpolarization of the membrane). Figure 18.A presents such experiments with

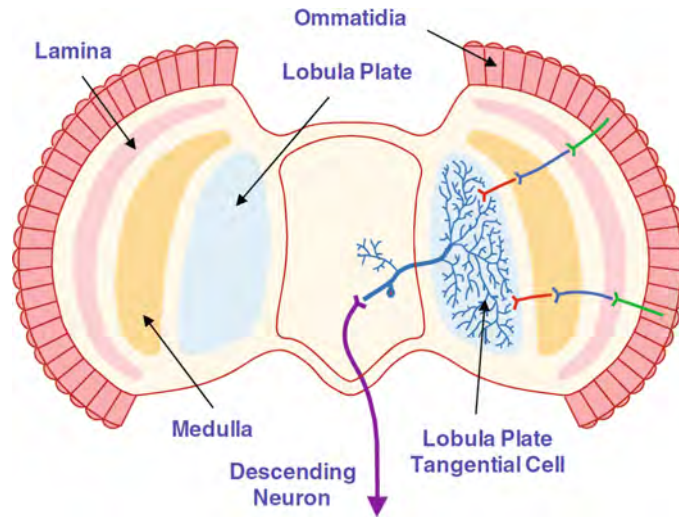


Figure 16 – Simplified schemata of the visual system of the fly. The visual signals go through three ganglia (or neuropils) called the lamina, the medulla and finally the lobula complex (lobula and lobula plate) before being sent to the thoracic ganglia which control its flight. Reprinted from Hyslop, Krapp, and Humbert (2010).

a HS neuron. Neurophysiological studies were performed: a microelectrode was placed in the fly's lobula plate to record electric activity of the different LPTCs. A microscope-telescope was used to stimulate selected receptors alternatively to create an apparent motion (Franceschini, Riehle, and Nestour, 1989). Thanks to this meticulous work, a classification of the LPTCs was realized by Hausen (1982) with two main categories: VS cells sensitive to vertical motion and 3 HS cells sensitive to horizontal motion in the body fixed reference frame. An example of the dendritic structures of VS<sub>1</sub> and Hx are presented on Fig. 17 along with the response field to visual stimuli. One can see that VS<sub>1</sub> is highly sensitive to downward motion in the frontal area and to horizontal motion in its dorsolateral region which is similar to rotational optic flow field along the pitch axis. Hx is very sensitive only to translational back to front motion.

Finally these very interesting studies also pointed out the fact that the insects' eye senses the optic flow in a limited range as it can be seen on Fig. 18.B. A visual stimulation triggers a pulse train whose frequency (pulse per seconds) depends on the time delay between the two successive stimuli (which can be seen as the time of flight of a contrast from one photoreceptor to its neighbor). It seems that for a time delay shorter than 10 ms or longer than 230 ms no neuronal stimulation appears. This time delay range can be expressed in terms of optic flow (taking into account an inter-ommatidial angle of  $\Delta\varphi = 3.6^\circ$ ) ranging from  $16^\circ/s$  to  $360^\circ/s$ .

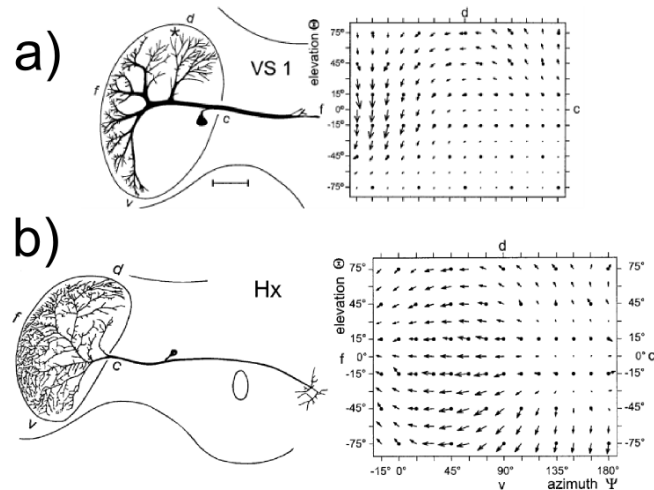


Figure 17 – Denritic structure of neurons  $VS_1$  and  $Hx$  along with response to visual stimuli on the entire view field.  $VS_1$  is sensitive to downward motion in the frontal area and to horizontal motion in its dorsolateral region which is similar to rotational optic flow field along the pitch axis.  $Hx$  is very sensitive only to translational back to front motion. Reprinted and modified from Krapp and Hengstenberg (1996).

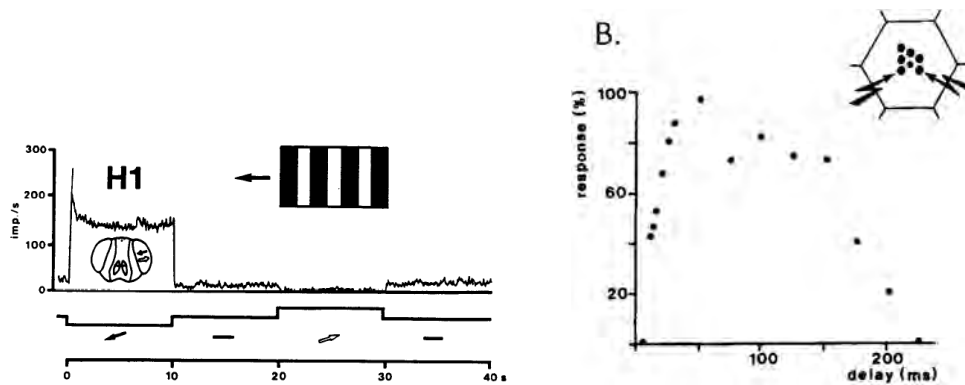


Figure 18 – A. Neuronal response of  $H_1$  neuron to a visual stimuli in the preferred direction and in the opposite one. One can see the hyperpolarization of the membrane for the opposite direction and the depolarization of the membrane for the preferred direction. B. Response to visual stimuli for different time delays between successive illuminations of adjacent photoreceptors. The time delay is proportional to the inverse of the angular velocity of the contrast (optic flow). Sub-figure A. reprinted from Riehle and Franceschini (1984) and B. from Franceschini (1985).

### 1.3.3 Other sensory systems observed in flying insects

We described in detail the visual system of the winged insects, but it has been shown that they are equipped with other kinds of sensory modalities: compass based on light polarization, color vision, antennae for taste and airspeed modalities, halteres as rate-gyros, ocelli for horizon detection, trichoid sensilla for wind measurements...

In this thesis, we endeavor to show that landing can be performed on the sole knowledge of the optic flow. Yet, in a first step, we also consider inertial measurements in the GNC scheme. That is why, except for inertial sensory modality, all sensory capabilities

observed in insects are not described here (see Taylor and Krapp (2007) for a detailed review of the sensory mechanisms).

As already explained, the inertial measurement unit is a critical component to stabilize a flying robot. In flies, halteres play that role. This limb comes from atrophied pair of wings that oscillates in antiphase at the same frequency as the functioning wings. Thanks to the Coriolis forces these halteres tend to bend while the insect is rotating which provides 3-axis angular rate measurements (Hengstenberg, 1988). Experiments showed that the inertial measurements are completed by vision for lower angular rates ( $< 50^\circ/s$ ). Further details on inertial sensory modalities in flying insect could be found in literature (Nalbach, 1993; Sane et al., 2007).

#### 1.3.4 Flying insect use visual relative motion for flight control

Following the presentation of the visual system of flying insects allowing the measurement of the optic flow, it is time to see how insects use this visual cue to control their flight and to navigate safely in complex unknown environments. Here we present ethological results obtained on winged insects.

When controlling the pose of a flying robot, we often consider two successive steps. The first one concerns attitude stabilization since attitude dynamics (rotations) have to be faster than position dynamics (translation). Indeed, once the robot is stabilized in attitude (able to hover despite external disturbances), position control might be achieved using only translations created with small attitude angles. This decoupling between rotational and translational dynamics copes with insects' sensory modalities (such as HS and VS cells) but also with reflexes-based behaviors. Insects do not only passively process the optic flow of the surrounding environment, they actively interact with it by means of specific mechanisms to avoid rotational optic flow in the measurements (Egelhaaf et al., 2012). Here we describe such mechanisms to segregate the rotational from the translational optic flow component through various strategies for the pitch, roll and yaw rotations.

##### **Roll pitch and yaw motion**

First of all, to counteract optic flow generated by roll rotations of the body during a lateral motion, the vestibulo-ocular reflex of the insect is used to keep the head (and hence the visual sensing system) horizontal. Hengstenberg (1988) showed that the head compensates for body motion around the roll axis on the basis of inertial measurements sensed by its halteres (no contra-rotations are observed in the absence of halteres). Figure 19 showed the experimental setup which provided such interesting results. On top

of that it was shown that the vision is also used somehow to enhance such compensatory mechanism (see sub-figure 19.II.d).

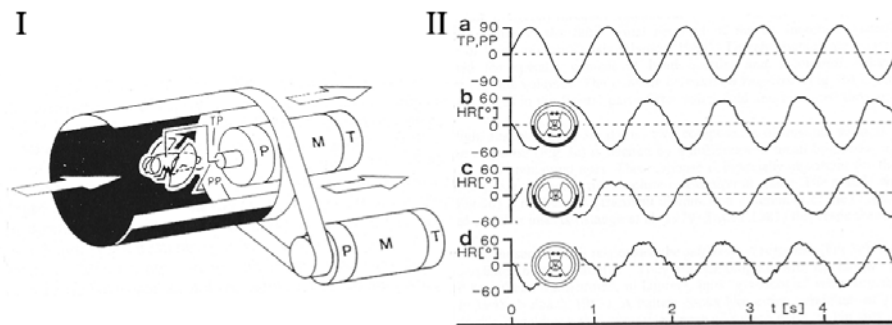


Figure 19 – I) The fly is rotated inside a drum covered with artificial patterns. II) a) The fly's body is rotated with a sinusoidal wave around the roll axis. b) Head roll compensation of body rotation with inertial and vision sensory capabilities enabled (antiphase rotation between body and roll). c) Head roll compensation when the drum is rotated and the body fixed. d) Same experiment as in b) but with only inertial sensory mechanism enabled (no visual contrasts). Reprinted from Hengstenberg (1988).

Regarding pitch motion, it was observed that thorax motion, required to control the orientation of the thrust, is compensated for by body and head saccades (Hateren and Schilstra, 1999).

Finally, concerning yaw compensation, two different mechanisms were observed in previous research. The first one deals with the need for large turns during flight. Unlike pitch and roll reflexes, during large horizontal turns the insect head cannot compensate for several tens of degrees of rotation. The head has to follow the change of flying direction. High pace body and head saccades around the yaw axis were observed (Collett and Land, 1975; Hateren and Schilstra, 1999). Since the visual system of flying insects is sensitive to a limited range of optic flow and due to the very fast velocity of the saccades (up to  $1400^\circ/s$ ); the optic flow sensed is not disturbed by the rotational optic flow generated by the saccades. The second mechanism developed to compensate for yaw motion is dedicated to maintaining a straight flight. In the presence of wind gust, yaw rotations could be created and the flight direction modified. The optomotor response counteracts this disturbance by generating an antagonistic torque to restore the lost course. Experiments performed by Reichardt (1969) showed that the flying insect placed in a circular drum displaying artificial contrasts will follow the rotation to cancel the horizontal optic flow.

### Velocity control

Ethological studies have shown evidence that flying insects adjust their flight speed to keep the lateral, ventral and dorsal optic flow constant. Srinivasan performed studies on the honeybee and showed that these insects reduce their flight speed in a tighter

corridor (Srinivasan et al., 1996). The tighter the corridor is, the higher the perceived optic flow for a constant forward velocity.

**Hypothesis** Forward speed control might result from a regulation of lateral optic flows in insects' visual flight control.

Since this major breakthrough, several studies have helped us to understand flying principles used in insects. Baird et al. (2006) validated these findings by moving corridor walls in the flying direction thus reducing the lateral optic flows and observed an increase in the flight speed. More recently, Portelli et al. (2011) studied which parts of the optical flow field insects use to control their speed using horizontally and vertically tapered corridors with trained honeybees.

### **Altitude control**

Similar studies have shown the importance of ventral optic flow in altitude control (Baron and Srinivasan, 2006; Baird et al., 2006; Portelli et al., 2010). Using moving floors, authors showed that altitude of the bees decreased when the floor was moving in the same direction as the flight (tending to decrease the perceived optic flow) probably to restore some kind of reference ventral optic flow (Portelli, Ruffier, and Franceschini, 2010). These observations account for the previously defined optic flow regulator hypothesis described by Ruffier (2004), Ruffier and Franceschini (2005), and Franceschini, Ruffier, and Serres (2007) where the height would also have been lowered and the flight speed kept constant.

**Hypothesis** In altitude control, winged insects seems to have a preferred optic flow value as observed since the 50s by Kennedy on mosquitoes and locust (Kennedy, 1940; Kennedy, 1951).

When it comes to animals, we have to keep in mind that conclusions drawn from experiments might not include all reflexes involved in the studied behavior. We thus distinguish observations from hypothesis inferred from these observations.

Straw, Lee, and Dickinson (2010) brought evidences that flies use three reflexes for altitude control (edge tracking, wide-field stabilization and expansion avoidance). Yet, Straw et al. hypotheses did not really explained the results obtained by Portelli et al. in 2010 and other studies by Srinivasan et al on honeybees.

### **Landing behaviors**

Optic flow regulation was shown to be at work in winged insects also during another important flight task: the landing. Srinivasan et al. (1996) performed experiments on honeybees and observed that bees seem to hold image velocity constant as the surface is approached, ensuring low flight speeds at touchdown (see Fig. 20).

**Hypothesis** Automatic smooth landing might result from the ventral optic flow regulation.

In the case of a pure translation, from eq. 1.3.1, the ventral optic flow could be expressed as follow:

$$\omega_x = \frac{V_x}{h} \quad (6)$$

where the viewing direction is oriented at  $90^\circ$  from the local horizontal. Maintaining  $\omega_x$  constant while landing ensures proportionality between  $V_x$  and  $h$ .

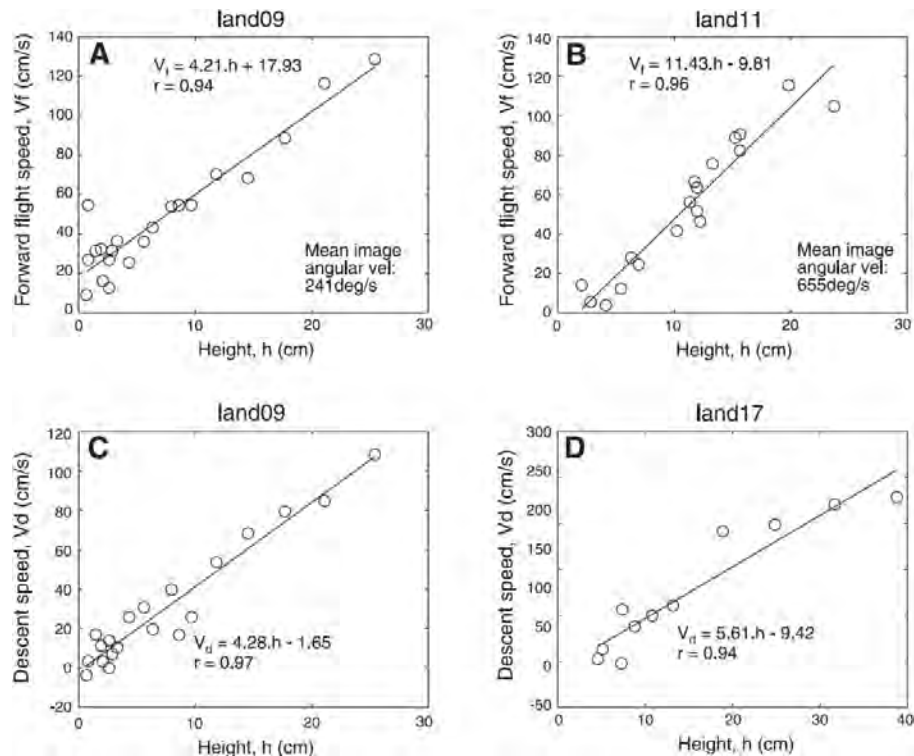


Figure 20 – Grazing landing in bees on a horizontal surface. Maintaining the ventral optic flow ensures that the horizontal velocity is kept proportional to the height as it can be seen on sub-figures A and B showing the variation of forward flight speed  $V_f$  with height ( $h$ ). It is interesting to notice that expansion optic flow  $\omega_z = V_z/h$  is probably used also since as observed on sub-figure C and D, the descent speed (noted  $V_d$ ) is also kept proportional to the height. Reprinted from Srinivasan (2011).

Franceschini, Ruffier, and Serres (2007) presented an optic-flow regulator that explain and validate several observations and assumptions that were made on insect flight control. The control scheme explains for instance how insects manage to fly, take off and land safely without any of the instruments used onboard aircraft to measure the ground height, ground speed, and descent speed. Authors made insisted on the parallel between biology and robotics trying to match any behavior observed in flying insects with robotics experimentation.

Since then, optic flow based altitude control, speed control and landing have been also observed among other insects such as drosophila (David, 1982), butterfly (Kuenen

and Baker, 1982), bees (Baird et al., 2006; Serres et al., 2008b; Portelli, Ruffier, and Franceschini, 2010; Portelli et al., 2011) and thus paved the way for the GNC strategy presented in this thesis.

### 1.3.5 Determining the optic flow as insects does: the “Time of travel scheme”

Various research teams have proposed different algorithms to compute the optic flow either based on pure computer vision processing or on dedicated sensors. In this thesis we do not describe all the algorithms developed to this end, more details could be found in these two review articles which present the optic flow estimation techniques (Barron, Fleet, and Beauchemin, 1994; Srinivasan, 1994). Here, we focus on a minimalistic approach which requires very little computational power. Our dedicated sensors measure only the local optic flow based on a very limited number of pixels which allows the calculation to be carried out on a conventional microcontroller.

#### 1.3.5.1 Presentation of the “Time of travel scheme”

As discussed on Fig. 18, the neuronal system of flying insects seems to respond to visual stimuli of adjacent photoreceptors by a pulse train which depends on the time delay between the successive stimuli. Following these observations, electrophysiological studies were performed on the H1 LPTC neurons of the lobula plate to understand the underlying signal processing algorithm that compute this time delay, or time of travel (Riehle and Franceschini, 1984; Franceschini, 1985; Franceschini, Riehle, and Nestour, 1989). From these observation, a first model measuring the optic flow was realized using analog component and was called Elementary Motion Detector (EMD) (Blanes, 1986). To avoid ambiguities with the Reichardt correlator described later, the EMD described by Blanes et al. is referred to as a Local Motion Sensors or LMS (Expert and Ruffier, 2012). The electrophysiological study are described in further details in section 1.3.2. The LMS processing using only two photoreceptors implemented a very elegant bio-inspired principle later called the “Time of travel scheme” as renamed later by Benson and Delbrück (1992) and Moeckel and Liu (2007). This principle compute the time elapsed  $\Delta t$  from the detection of a contrast edge by a photoreceptor and the detection by an adjacent photoreceptor offering an optical axis separated by angle  $\Delta\varphi$ . The local 1D optic flow is then deduced by:

$$\omega = \frac{\Delta\varphi}{\Delta t} \quad (7)$$

This optic flow actually represents the mean angular velocity of the contrast in the

field of view of the sensor over  $\Delta t$  seconds since the contrast edge does not have to keep a constant velocity during his course between the two optical axes. Figure 21 presents the initial implementation of this scheme from a signal processing perspective.

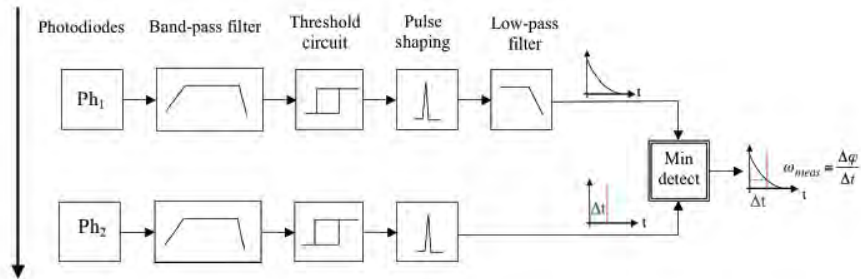


Figure 21 – Initial signal processing implementation of LMS. Reprinted from Franceschini (2009)

This processing contains several successive main steps (Blanes, 1986; Pichon, Blanes, and Franceschini, 1989):

1. Spatial sampling realized by the photoreceptor's optical axes separated by an angle  $\Delta\varphi$ ,
2. Low pass spatial filtering performed by the Gaussian angular sensitivity function of the defocused lens (correspond to a blurring effect), cut-off frequency defined by the acceptance angle  $\Delta\rho$ ,
3. Band pass filtering to remove the continuous component (accentuate the transient signals created by contrasts edges) and increase SNR (Signal to Noise Ratio) by filtering high frequency measurement noise.
4. Hysteresis thresholding improving robustness to the remaining noise which might trigger the  $\Delta t$  computation when no contrasts are detected.
5. Actual  $\Delta t$  computation: an impulsion is generated on the first channel and then low pass filtered to generated a exponentially decreasing signal. This exponentially decreasing function is multiplied by the second channel which generated an impulsion  $\Delta t$  seconds later. The output of the multiplication gave an analog image of the  $\Delta t$  and from eq. 1.3.5.1 of the optic flow.

Two major benefits of this approach have to be discussed. The first one lies in the fact that the response of the sensor is monotonically increasing for increasing values of optic flow. The second one is related to the insensitivity to spatial frequency and illumination conditions. These characteristics are opposed to the other well-known elementary motion detector called the "Reichardt correlator" or "Hassenstein-Reichardt (HR) detector" (Reichardt, 1957; Reichardt, 1969; Reichardt, 1987; Borst, 2000) (see also

Harrison and Koch (1999) for a VLSI (Very Large Scale Integration) implementation of the correlator).

This first implementation of the time of travel allowed computing the optic flow in a single direction (from Ph1 to Ph2). An enhancement to sense two opposite directions of motion was proposed by Blanes (1991) based on empirical findings. Two LMSs could be placed in opposite directions and the maximum value would give the corresponding optic flow (the output of the “wrong” direction is expected to be lower).

### 1.3.5.2 Evolution of the LMS

Following this major breakthrough, several hybrid analog-digital implementations of LMSs were realized in the following decades (see Ruffier et al. (2003) for a FPAA implementation, Aubépart and Franceschini (2007) for an FPGA version and finally Amic (2002), Ruffier et al. (2003), Pudas et al. (2007), and Serres et al. (2008b) for microcontrollers implementations).

More recently, Roubieu et al. (2011) proposed an improvement used in this thesis to enhanced robustness of the measured optic flow thanks to the fusion of 5 LMSs. Using a photoreceptor array containing 6 pixels the iC-Haus LSC retina associated to a novel fusion step based on the median operator, the precision of the measurement was improved (the standard deviation of the output was reduced and the refresh rate was increased). The iC-Haus LSC chip was fully characterized by Expert, Viollet, and Ruffier (2011).

Another version of the LMS was presented by Ruffier and Expert (2012) where an analog programmable gain was added in the processing algorithm to further increase the signal to noise ratio.

Finally an interpolation scheme was proposed by Expert, Roubieu, and Ruffier (2012) to run the algorithm at a lower sampling rate and then reduce the computational requirements.

### 1.3.5.3 Other optic flow sensors technologies

A large number of studies presented optic flow sensors based on VLSI technology which offers very tight integration and sensors dedicated to a specific task (Deutschmann, 1997; Moini, 2000; Moeckel and Liu, 2010; Xu, Humbert, and Abshire, 2011).

Mouse sensors is another suited device to compute the optic flow (Griffiths et al., 2006; Beyeler, Zufferey, and Floreano, 2009b; Chan, Mulla, and Stol, 2010). Those sensors are often associated with a laser light source, are easily implemented and are self-contained (the optic flow is directly accessible at the output). A recent study compared dynamic and static characteristics of a mouse sensor with a sensor based on 5 LMSs

(Expert, Viollet, and Ruffier, 2011) and despite a larger number of pixel (900 for the Avago ADNS-9500 against 6 for the iC-Haus) results showed that the mouse sensor was less accurate (higher standard deviation of the error). Recently a velocity sensor called PX4FLOW based on the fusion of optic flow (sensed by a mouse sensor) with attitude and range measurement was presented by Honegger et al. (2013).

Finally, an European project called CurvACE aimed at developing a compound curved optic flow sensor (Floreano et al., 2013). The functional prototype showed very promising results with its 630 pixels offering a very wide field of view of  $180 \times 60^\circ$  over a wide range of illumination conditions and weighting only 1.95g (See table 1 in Floreano et al. (2013) for a comparison of CurvACE characteristics with *Drosophila melanogaster* compound eye). Figure 22 presents the actual CurvACE compound eye prototype.

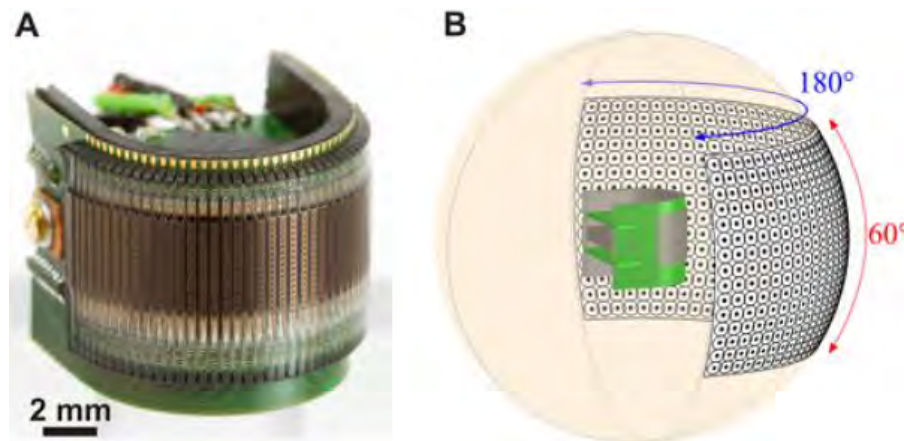


Figure 22 – A. Picture of the curved compound eye CurvACE. B. Illustration of the panoramic field of view. Reprinted from Floreano et al. (2013)

### 1.3.6 Developing robots inspired by flying insects' vision based control

Based on all the knowledge acquired on insects' vision which led to the design of the previously described LMSs, the Biorobotics team (ISM UMR AMU/CNRS) in Marseilles<sup>5</sup> went a step further onto the robotic implementation of such behaviors. The main idea of biorobotics is to create a virtuous circle from biology to robotics. Starting from observations made on nature, hypotheses are developed and formalized into sensori-motor algorithms. This algorithm is then experimentally tested on robots to either validate or disprove the previously made hypothesis. If the hypotheses are validated, then our knowledge of biology has thus increased, if they are invalidated, then we can make new assumptions and start over.

The “robot-mouche” was the first wheeled robot using optic flow to navigate au-

<sup>5</sup>www.biorobotics.eu

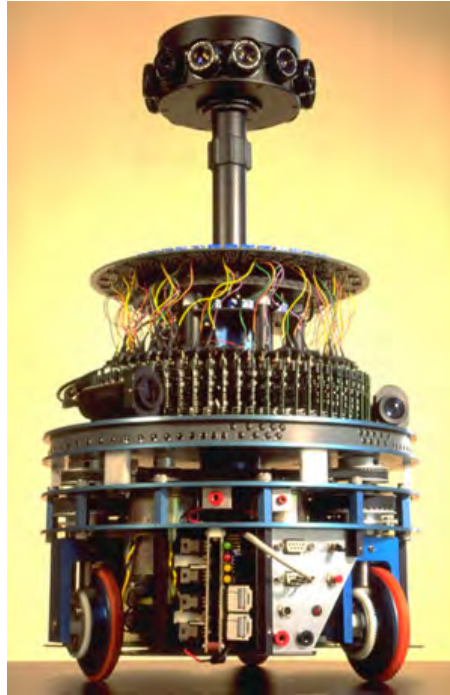


Figure 23 – The “Robot-mouche” was designed in the early 90’s by Franceschini, Pichon and Blanes (see Pichon (1991), Blanes (1991), and Franceschini, Pichon, and Blanes (1992) for more details on the design). It was able to navigate autonomously and safely in a cluttered environment thanks to a vision based system composed only 118 pixels. The robot was traveling in translation at a known forward speed of 50 cm/s and could avoid hazardous areas thanks to the optic flow measurements. Reprinted from Franceschini, Pichon, and Blanes (1992).

autonomously in unknown complex environment (Franceschini, Riehle, and Nestour, 1989). Thanks to a vision based system composed only 118 pixels, the 12 kg robot was traveling in translation at a known forward speed of 50 cm/s and could thus avoid hazardous areas thanks to the optic flow measurements (Pichon, Blanes, and Franceschini, 1989; Franceschini, Pichon, and Blanes, 1992). Indeed, for a constant forward velocity, vicinity from obstacle can be directly derived from the optic flow. This achievement triggered several other implementations of such optic flow based robots. Here we present a time-line of the studies which involved a robotic platform using optic flow for navigation purposes.

- Srinivasan et al. (1999) presented a wheeled robot equipped with a camera balancing lateral optic flows. The robot was able to stay centered in a corridor as it has been observed in honeybees (Srinivasan et al., 1996).
- On the robot called Robee, Santos-Victor et al. (1995) implemented the centering response enhanced with a behavior allowing one wall to be feature-less.
- Zwaan and Santos-Victor (1999) presented a robot with a panoramic visual sensor and a heading control system which was similar to the “robot-mouche”.

- A small low-power visual sensor based on the Reichardt correlator was designed by Harrison and Koch (1999). This computational efficient sensor was implemented on a wheeled robot endowed with a control system allowing to reproduce the optomotor behavior observed in insects.

Then aerial robotics was extensively studied since it provides very challenging dynamic systems.

- Obstacle avoidance and course stabilization behaviors were demonstrated by Iida (2001; 2003) on the robot Melissa a blimp-type robotic platform.
- Then, the robot FANIA presented by Netter and Francheschini (2002) was an aircraft tethered to a whirling-arm on which authors integrated 19 LMSs. It was able to do automatic terrain-following flights. Simulations of autonomous landings were successfully realized.
- The robot OCTAVE (Optic flow based Control sysTem for Aerial VEhicles) presented for the first time by Ruffier and Franceschini (2003), and developed during Ruffier's PhD thesis (Ruffier, 2004) was a 100 g rotorcraft performing ground avoidance (Ruffier and Franceschini, 2008), terrain following, automatic take off, automatic landing, responding appropriately to wind disturbances over a textured surface (Ruffier and Franceschini, 2005), and landing over a moving platform (Ruffier and Franceschini, 2014). Based on a single LMS looking downward and thus measuring the ventral optic flow a control loop was designed to act on the robot's altitude via its lift force created by the rotor (see picture on Fig. 24). The regulation of the ventral optic flow toward a constant reference value as observed by Kennedy more than sixty year earlier was validated on an airborne vehicle (Ruffier, 2004; Ruffier and Franceschini, 2005). Figure 25 presents the OCTAVE autopilot featuring a closed loop regulating the ventral optic flow around a constant reference value and an open loop control for the vehicle's pitch angle. Due to the small pitch angle experienced on this robot, the two degrees of freedom in translation were virtually decoupled where the pitch angle controlled the surge dynamics and the optic flow the vertical dynamics even though a single actuator controlled in closed loop was available. Recently, Ruffier and Franceschini (2014) presented new results on OCTAVE and suggested a second feedback loop based on the elevation angle of the target in the visual field to drive the rotorcraft's pitch, and hence its forward thrust which control its forward airspeed.



Figure 24 – The OCTAVE (Optic flow based Control system for Aerial VEHicles) robot is a 100g rotorcraft with 3 degrees of freedom (2 in position and 1 in attitude). Based on the optic flow regulation principle it is able to perform complex navigation tasks. Among these tasks we find taking-off, landing, wall following, and adjusting flight regime accordingly to wind disturbances. ©H. Raguet.

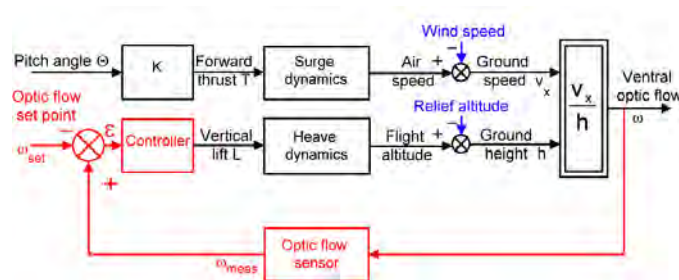


Figure 25 – Block diagram of the OCTAVE autopilot. The OCTAVE robot is composed of two actuators: a servomotor acting on the pitch angle which is controlled in open loop and the thrust of the rotor which is controlled via the optic flow feedback. The pitch angle is used to set a ground speed and the thrust to maintain an optic flow setpoint and thus a safe distance from the obstacles. Reprinted from Franceschini, Ruffier, and Serres (2007).

- A fixed wing aircraft flying indoors was used to validate a lateral obstacle avoidance strategy presented by Green, Oh, and Barrows (2004) featuring small 4.8 g optic flow sensors.
- Indoor Micro Aerial Vehicle (MAV) weighting only 30 g was flown by Zufferey and Floreano (2006) in a contrasted environment using an on-board I2A algorithm estimating the optic flow. I2A minimizes the error at each time step between the acquired image and the interpolated one based on a set of previous images (see Srinivasan (1994) for a description of the I2A algorithm). Zufferey et al. (2007) presented experiments on a 10 g MAV.
- Flight tests were presented in Griffiths et al. (2006; 2007) on a MAV performing obstacle and terrain avoidance using laser range finder along with optic-flow sensors with specific application to canyon navigation.

- The OptiPilot presented by Beyeler, Zufferey, and Floreano (2009a) was implemented on a 400 g outdoor fixed wing UAV sensing the optic flow. Optical mouse sensors were pointed at divergent viewing directions around the aircraft main axis. Recently, Zufferey, Beyeler, and Floreano (2010) showed how the previously defined OptiPilot can be coupled with a GPS in order to provide goal-directed, nap-of-the-Earth flight control in presence of obstacles. Long flights of 25 minutes each were performed at 10 m above ground in a circular path including two copses of trees requiring efficient collision avoidance action.
- Based on Fourier series decomposition of optic flow, Humbert et al. (2010) proposed a state estimation technique using an integration of a wide part of the field of view (technique called Wide Field Integration or WFI). This method can be compared to the LPTC neurons which fuse all the local optic flows computed in the medulla. Humbert and Hyslop (2010) implemented the WFI method on a wheeled robot traveling in an indoor corridor. The robot was able to center itself and control its speed. Then this technique has been successfully tested on-board a 6-DOF robot (Hyslop and Humbert, 2010) and on a quadrotor UAV (Conroy et al., 2009). Recently a visual-navigation approach combining bioinspired wide-field processing of optic flow information with control-theoretic tools for synthesis of closed loop systems was validated on a quadrotor UAV by Keshavan et al. (2014).
- In Herisse's PhD thesis (Hérissé, 2010), authors addressed the challenges of hovering flight, terrain following and regulation of automatic vertical landing on a moving platform using the expansion optic flow as feedback information on a quadrotor UAV (Hérissé et al., 2008; Hérisse et al., 2009; Hérisse et al., 2010; Hérisse et al., 2012). For the first time, nonlinear control design based on Lyapunov theory (Khalil and Grizzle, 2002) was used for optic flow based control. Regarding the design of the control laws based on a Lyapunov approach, Hérisse et al. (2012) started the design from a nonlinear PI control law and then designed a Lyapunov candidate function upon the control law. Another approach, as realized in this thesis, would be to design a Lyapunov candidate function and then choose an appropriate control law.
- Fusing optic flow with ground speed measurements, an 80 kg helicopter was flown at constant height above ground (Garratt and Chahl, 2008). The estimated height was used to act directly on the collective pitch control of the helicopter.
- Kendoul, Fantoni, and Nonamib (2009) proposed an autopilot based on an optic flow-based vision system for autonomous localization and scene mapping, and

a nonlinear control system for flight control and guidance. Experimental data validated the ability to perform autonomous flight using these vision and control algorithms. The nonlinear control system for flight control and target tracking were presented by Kendoul et al. (2009). A visual odometer which fuses optic flow and inertial measurements to perform pose estimation is also described. A nice paper concluded this work presenting the complete guidance and control scheme applied to the quadrotor UAV (Kendoul, Yu, and Nonami, 2010).

- Meanwhile OCTAVE regulates ventral optic flow with a LMS looking downward, Serres et al. (2008b) studied the centering behavior observed in flying insect by Kirchner and Srinivasan (1989). Kirchner and Srinivasan observed that honeybees tended to center themselves while flying in a corridor and they assumed that bees could balance right and left lateral optic flows. Serres et al. Serres et al. (2008b) showed that insects do not always center in tunnels but might follow only one wall that corresponds to the higher value of lateral optic flows. Serres et al. (2008a) proposed an autopilot implementing these observations along with the forward speed controlled to maintain the sum of lateral optic flows as previously suggested by Srinivasan et al. (1996)). This autopilot was called LORA III which stands for Lateral Optic flow Regulation Autopilot. This control scheme consisted in two intertwined feedback loops, each of which having its own OF setpoint and controlling either the surge or sway vehicle's translation dynamics.

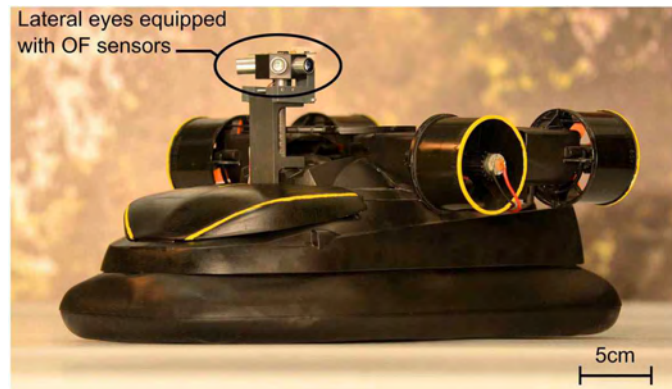


Figure 26 – Picture of the fully autonomous hovercraft equipped with 4 devices built on 5 LMSs oriented in different directions and a dual lateral optic flow regulator called LORA III (Lateral Optic flow Regulation Autopilot). It is worth noting that the hovercraft platform is fully actuated. Reprinted from Roubieu et al. (2012); Roubieu et al. (2014).

This autopilot was firstly validated in simulation on a miniature hovercraft and then implemented by Roubieu et al. (2012) and Roubieu et al. (2014) on a 800 g prototype (see Fig. 26). Figure 27 presents the control architecture of the autopilot implemented on the hovercraft and based on LORA III. The first loop (green loop) controlled the yaw angle thanks to a magnetic compass and a gyrometer in order

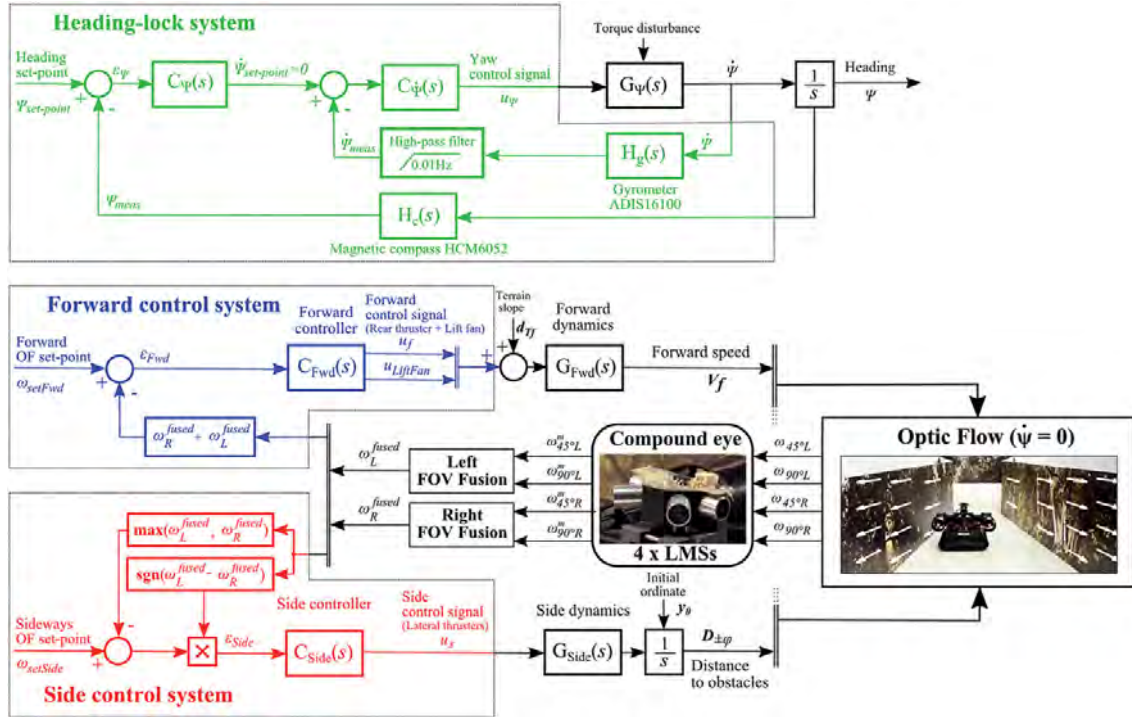


Figure 27 – Autopilot implemented on the 800 g hovercraft with three closed loops inspired from LORA III. This control scheme ensures heading lock, forward speed control and side control. Reprinted from Roubieu et al. (2014).

to keep the robot along the main direction of the corridor. The forward control system (blue loop) kept the sum of the optic flow measurement constant to ensure that the velocity was adapted to the wideness of the corridor (faster in a larger corridor and slower in a narrowed corridor). Finally, the side control system ensured safe distance from the wall by regulating the fused optic flow of higher value. In order to keep the clearance to the walls proportionnal to velocity, the intertwined two loops are required to work in parallel.

- Finally, the TwinCoax robot (see Fig. 30) is a 6 degrees of freedom micro aerial vehicle equipped with a single visual motion sensor looking downward. It flew indoors over a natural scene and was controlled manually using an IR remote control in order to assess the output of an optic flow sensor in an arena disturbed by a VICON system. Despite the complex, adverse lighting conditions, the optic flow measured on-board matched accurately the ground-truth optic flow generated by the free-flying helicopter’s trajectory. But the course (yaw and thrust level) of Twincoax was difficult to maintain constant. Because of these rotations and uncertainties, the feedback control loop did not have the correct effect on the altitude. The vibrations were also an important issue for the TwinCoax ventral optic flow sensor.



Figure 28 – The BeeRotor robot is an experimental platform composed of a tethered 80g tandem rotorcraft that mimics optic flow-based behaviors previously observed in flies and bees. This robot is able to perform autonomously ground and ceiling following while driving its forward speed but also automatic ceiling docking by simply regulating its dorsal or ventral optic flow. This proof-of-concept robot flew in a high-roofed tunnel depicting natural scenes and is autonomous in terms of its computational and signal processing power requirements. Reprinted from Expert and Ruffier (2012).

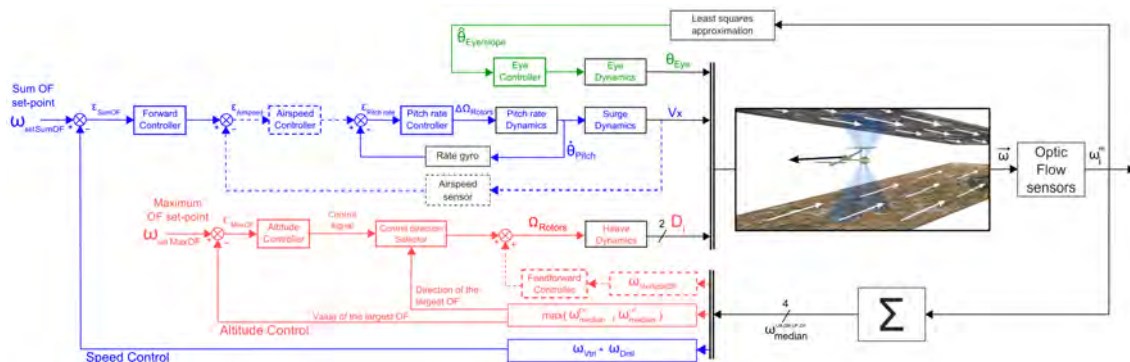


Figure 29 – GNC architecture of the BeeRotor autopilot controlling its eye orientation (green loop), its forward speed (blue loop) and its altitude (red loop) thanks to three feedback loops. Reprinted from Expert (2013).

- Following the OCTAVE autopilot outstanding results, a tandem rotorcraft called BeeRotor was developed during Expert's PhD (Expert, 2013) (see the picture on Fig. 28). This tethered robot of 80 g was equipped with a 13.5-g quasi-panoramic visual system consisting of 4 devices based on 5 LMSs and flew over natural scenes. The BeeRotor robot was designed to perform ground and ceiling following while also automatically driving its forward speed on the basis of the ventral or dorsal optic flow. In addition, the BeeRotor robot was able to realize automatic ceiling docking in high-roofed tunnel. Figure 29 presents the GNC architecture of the BeeRotor autopilot controlling its eye orientation (green loop), its forward speed (blue loop) and its altitude (red loop) thanks to three feedback loops. The eye is kept oriented parallel to the closest surface thanks to an optic flow based

least squares approximation. The altitude control loop acts on the vertical lift of the aircraft and therefore its altitude, the aircraft safely follows the closest surface at a distance depending on the setpoint and the forward speed of the robot. The forward speed control loop uses the optic flow measurements as well as pitch rate and optionally airspeed to act on the pitch angle of the robot. Thanks to the intertwined control loops, the BeeRotor robot always keeps a safe distance from both walls while adapting its forward speed to the size of the tunnel without any measurements of distance or ground speed thanks to this GNC scheme.



Figure 30 – The TwinCoAx micro aerial vehicle equipped with a single visual motion sensor looking downward which flew indoors over a natural scene. Reprinted from Ruffier and Expert (2012).

All these optic flow studies can be assimilated to IBVS (Image Based Visual Servoing) strategies since, the control laws do not require estimation of the state vector of the vehicle. The control is directly performed on a visual cue extracted from the images.

#### 1.4 Optic flow based lunar landing

As already discussed, optic flow regulation framework has been tested on various robotics applications. Several authors decided to test its potential contribution to space robotics via the challenge of lunar landing. Indeed, since several years, NASA and ESA are studying bio-inspired navigation for future planetary exploration missions (Thakoor et al., 2002; Chahl et al., 2003; Valette et al., 2010b; Medici et al., 2010). The aim of these two agencies is to test on Earth the potential application of such innovative principles to very critical systems such as landers or exploration robots.

We have seen that vision based TRN combined with PBVS or IBVS offer great perspectives to achieve safe landings. However, most of the drawbacks associated with classical computer vision solutions could possibly be tackled using biorobotics. Computational resources required to process images from a classical camera providing several

millions of pixels per seconds are greatly reduced on minimalistic optic flow sensors and thus output rate is increased. Figure 31 shows the point of view of Barrows and Neely (2000) comparing conventional machine vision with CCD imagers with so-called “hybrid sensor” (optic flow sensors based on 5 LMSs for instance). In hybrid sensors, processing could be distributed along the processing chain and the processing unit reduced to a single microcontroller or FPGA.

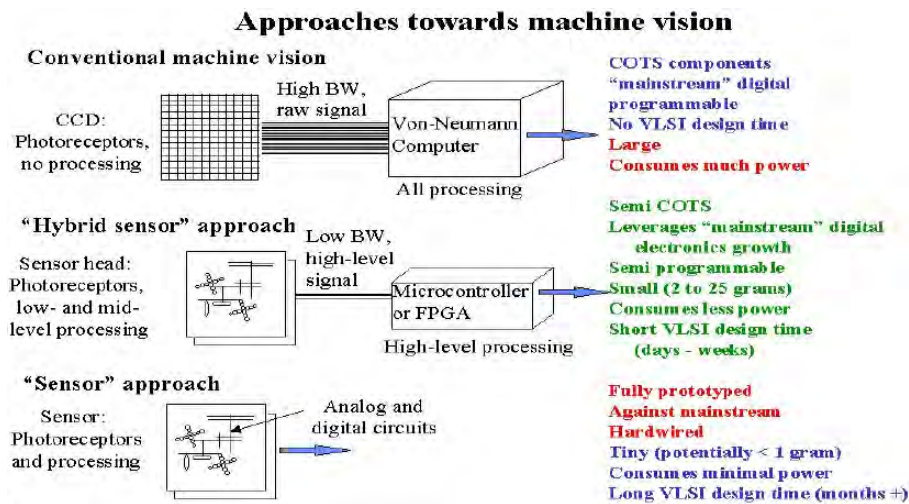


Figure 31 – Comparison of conventional computer vision sensors and hybrid sensors dedicated to a single processing task. Reprinted from Barrows and Neely (2000).

The Biorobotic team in Marseilles studied a solution to lunar landing based on optic flow regulation presented by Valette et al. (2010a). In this work, performed under ESA’s Ariadna contract (see Valette et al. (2010b) for the final report), authors proposed for the first time an optic flow-based strategy to perform soft landings using PANGU software with a single LMS (2 pixels) mounted on a gimbaled platform. Based on OCTAVE background, the OF perceived by the LMS was kept as close as possible to a constant setpoint using IMU measurements as well (acceleration and attitude). The control framework is presented on Fig. 32. Authors designed a linear quadratic regulator coupled to a nonlinear observer and realized several PANGU-based simulations to prove the feasibility of such bio-inspired strategy. In this first study, as in the OCTAVE autopilot, the pitch was controlled in open loop following either an exponentially or linearly decreasing law or staying at a constant value. This led to the conclusion that an attitude closed loop had to be implemented to enhance performances and robustness. Authors also established that such approach could be satisfying even with low sun elevation and temporary sensor blinding as it might occur at lunar South Pole.

Another ESA’s Ariadna study was presented by Medici et al. (2010) where authors considered various control laws on a fully actuated lander dynamic model. Authors investigated classical PID control, nonlinear predictive control, output feedback lineariza-

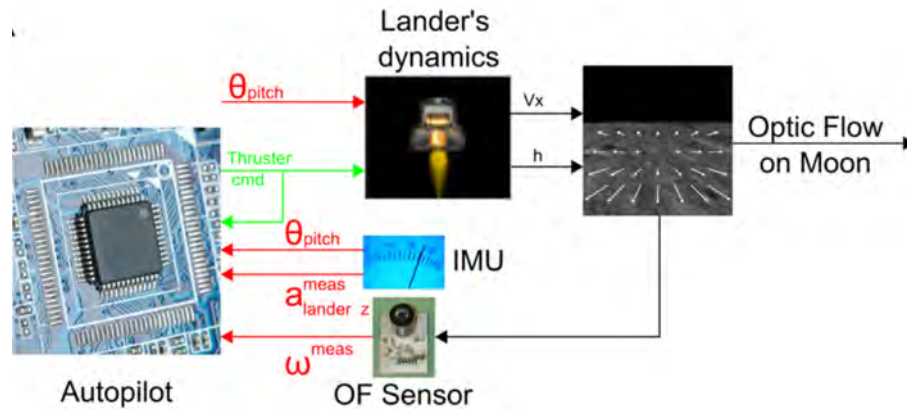


Figure 32 – Control framework for optic flow based lunar landing. Available measurement the pitch angle, the linear accelerations and the ventral optic flow obtained thanks to a gimbaled LMS. Reprinted from Valette et al. (2010b).

tion, sliding mode control for Mars landing considering a vertical landing scenario with constant optic flow. Then, using PID controllers, authors addressed the grazing lunar landing using firstly only one sensor and then two sensors oriented in different gaze directions. They also performed numerical simulations of neuromorphic analog VLSI technology for the computation of optic flow which prevent the need for a digital processor, such as a microcontroller or a FPGA (see sub-figure “Sensor” approach in fig. 31).

A crucial aspect that had not been discussed yet with optic flow framework concerns the optimality of the GNC solution with respect to fuel expenditure. One can assume that Darwinian evolution of flying insects brought an energy-efficient flight control system. Izzo, Weiss, and Seidl (2011) studied constant optic flow descent with respect to optimality from a theoretical point of view using Pontryagin’s maximum principle. Authors compared the results with unconstrained descents by performing simulations on Apollo-like scenario. They concluded that an optimal pitch law is required to lower the overall fuel consumption and that linear or exponential pitch laws may not be adequate.

Following this theoretical study of the optimal guidance under constant optic flow, ESA’s Advanced concept team researchers proposed an optic flow based landing strategy that makes use of both ventral optic flow and time-to-contact (TTC) (Izzo and de Croon, 2011). The TTC is a measure of the height divided by the vertical velocity and is known to play an important role in animal visual control systems (Lee et al., 1976). It can be noted that the TTC correspond to the opposite of the inverse of expansion optic flow ( $\omega_z = \frac{V_z}{h} = \frac{-1}{TTC}$  where  $V_z < 0$  when oriented toward the surface). In contrast with ventral optic flow regulation, integrating the TTC in the control scheme might then allow the GNC architecture to act on the vertical velocity to further reduce final velocities at the low gate. Using theoretical simulations (perfect knowledge of optic flow and TTC), Izzo and de Croon (2011) presented a linearly decreasing time-to-contact and

constant strategy which resulted in a soft landing with considerable mass expenditure as compared with the optimal case. Subsequently, an exponentially decreasing TTC has been studied which also lead to a soft landing and a significant improvement in fuel consumption.

de Croon and Izzo (2012) presented a state feedback solving an on-board optimal control problem (similar to a model predictive control approach) on a fully actuated lander model. Authors used ventral optic flow, TTC and acceleration measurement to estimate the entire state vector and feed the state feedback. It is interesting to notice that the optimal optic flow profiles obtained in the LROC based simulations presented in this paper, do not follow a constant optic flow reference. From simulation and GNC point of view a similar study was performed with PANGU which led to the same interesting results (de Croon, Izzo, and Schiavone, 2011). In this paper, authors used feature scale to estimate the TTC and ventral optic flow.

More recently Izzo and de Croon (2013) extended the solution proposed in the previously discussed study to a nonlinear model dynamics including pitch dynamics and performed successful landing simulation along with CPU performances analysis. Once again, one can notice that constant optic flow references may not be optimal with respect to energy consumption.

Regarding hardware implementation Janschek, Tchernykh, and Beck (2006) detailed the performances of a visual navigation system, based on a mono camera as vision sensor. The correlation based optical flow approach allows for ego-motion estimation and 3D map generation and matching using as input images, rough initial estimates and reference DEM. The 3D models were produced in real-time and the since optic flow was processed at a very high-speed thanks to a dedicated embedded optical correlator (see Fig 33 for the visual processing architecture providing the pose estimation). Simulations were performed on Mercury landing using the PANGU software.

From this state-of-the-art, one can see that the successive developments seem to indicate a certain path to follow in future studies. First of all, we should **keep increasing the number of optic flow sensors** to measure not only the ventral optic flow but also other signals to be able to act independently on the different dynamics of the lander. Secondly, the constant optic flow reference tracking as observed in winged insects may not be the optimal solution in terms of fuel consumption for lunar landing application. We should provide the guidance scheme with optimal **optic flow reference signals** instead. Finally, in all these studies, optic flow sensors or cameras were mounted on a gimbal system which is not an option when considering such minimalistic sensors: the gimbal system would be heavier than the sensor itself. From equation 1.3.1 one can see the optic flow before derotation depends only on velocity, proximity, attitude

and angular velocity information. As we have seen, flies use their compound eyes to possibly assess the rotational optic flow at low angular velocities to compensate for roll motion. Thus, **non-gimbaled optic flow sensors might help us to avoid the need for IMU devices.**

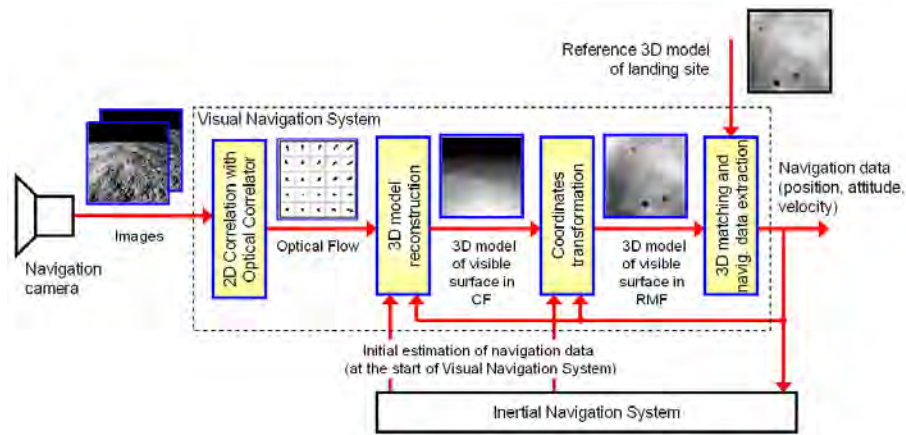


Figure 33 – Visual processing architecture providing the pose estimation from camera images, rough initial estimates and reference DEM. Reprinted from Janschek, Tchernykh, and Beck (2006).

## Objectives of the thesis

In this thesis, we present results obtained on visual motion sensors development and testing phases and a vision-based GNC framework for autonomous planetary landing applications.

The core challenges addressed here are:

1. Guidance, navigation and control without any need for pose measurements,
2. New algorithms of optic flow and attitude estimation,
3. Bio-inspired sensors development, characterization and outdoor testing.

The first part is devoted to the development of two versions of optic flow sensors based on 5 LMSs. The first one is able to measure accurately the OF in two opposite directions in the optic flow range  $[-350^\circ/s; -80^\circ/s] \cup [80^\circ/s; 350^\circ/s]$ . It is tested in the laboratory on natural scene and gave satisfying results. The second version of the sensor operates at low velocities such as those liable to occur during lunar landing  $[1.5^\circ/s; 25^\circ/s]$ . After developing these sensors, their performances are characterized both indoors and outdoors, and lastly, the low speed optic flow sensor is tested on-board an 80-kg helicopter flying in an outdoor environment.

The Guidance Navigation and Control (GNC) system is designed in the second part on the basis of several algorithms, using various tools such as optimal control, nonlinear

---

control design and observation theory. This is a particularly innovative approach, since it makes it possible to perform safe landing on the sole basis of OF measurements. The final constraints imposed by our industrial partners are met by mounting several non-gimbaled sensors oriented in different gaze directions on the lander's structure. Information about the lander's self-motion present in the OF measurements is extracted by navigation algorithms, which yield estimates of the ventral OF, expansion OF and pitch angle. It is also established that it is possible to bring the planetary lander gently to the ground by tracking a pre-computed optimal reference trajectory in terms of the lowest possible fuel consumption. Software-in-the-loop simulations are carried out in order to assess the potential of the proposed GNC approach by testing its performances. In these simulations, the sensor firmware was taken into account and virtual images of the lunar surface were used in order to improve the realism of the simulated landings.

Particular emphasis was placed on validation through realistic simulations and outdoor testing. The choice was made to give priority to validation in a sense that when theory was validated through simple simulations instead of improving further control laws or navigation algorithm, more realistic simulations were run involving simulated images on the lunar ground and the actual code implemented in the sensors.

Our approach aims at establishing proofs of concept for an optic flow based autonomous lunar landing using minimalistic sensors rather than developing advanced control laws or estimation filters or even optimal control frameworks.

## Thesis overview

Part 2. presents the two versions of optic flow sensors based on 5 LMSs that were developed and tested during this thesis. A sensor based on 5 LMSs sensing the optic flow in two opposite directions is presented in Chapter 2.1. The adaptation of 5 LMSs based sensor to low speed optic flow sensing is detailed along with the outdoor testing results in Chapter 2.2<sup>6</sup>. Part 3. details the design of a full GNC solution based on the outputs of optic flow sensors fixed to the lander's structure. Performances of the GNC strategy are assessed via numerical simulations including software-in-the-loop and computer generated images of the lunar surface. Chapter 3.2 pave the way for optic flow based GNC presenting the novel GNC algorithm. An improved version of the control design is presented in chapter 3.3. Chapter 3.4 concludes the GNC design with a navigation filter able to estimate high interest optic flow as well as pitch angle of the lander on the sole knowledge of optic flow measurements. Eventually, Chapter 4 offers a final discussion and concludes over the contributions of this work.

---

<sup>6</sup>5 neighboring LMSs based sensors are referred to as Visual Motion Sensors (VMS) in the articles

## **Part 2**

# **Development and characterization of bio-inspired optic flow sensors**



ARTICLE 1: A TWO-DIRECTIONAL  
1-GRAM VISUAL MOTION SENSOR  
INSPIRED BY THE FLY'S EYE

CONTENTS

---

ABSTRACT . . . . .	59
I INTRODUCTION . . . . .	59
II DESCRIPTION OF THE DEVICE . . . . .	60
III EXPERIMENT . . . . .	62
IV RESULTS . . . . .	63
V ESTIMATION OF THE DIRECTION AND MAGNITUDE OF THE VISUAL MOTION . .	63
VI CONCLUSION . . . . .	66
ACKNOWLEDGMENT . . . . .	68
REFERENCES . . . . .	68



---

## Article 1: A two-directional 1-gram visual motion sensor inspired by the fly's eye

Article published in 2013 in IEEE Sensors Journal, 13(3): pp. 1025-1035.

Authors: F.L. Roubieu, F. Expert, G. Sabiron and F. Ruffier

**I**N this chapter, we present the design and experimental validation of bio-inspired optic flow sensors. Based on previous versions of LMS, we present two innovative solutions to improve performances and enhance capability of these bio-inspired sensors.

Using a 6-pixel array, the fusion of 5 LMS (one LMS consists in a single pair of pixels) using the median operator is realized. In comparison with LMS, performances in terms of refresh rate and standard deviation of the error are greatly improved.

Then, we proposed a solution to compute optic flow without any need for knowledge of the direction of relative visual motion.

Indeed, during flight, the sign of the sensed optic flow might change due to different behaviors. This situation may arise if the direction of the velocity vector is changed or if rotational optic flow is greater than translational optic flow. For instance, flying UAVs create translational motion thanks to attitude maneuvers. The UAV tilts itself around the yaw, pitch or roll axis which generates a negative (or positive) rotational optic flow and this inclination creates a translational motion generating a positive (or negative) translational optic flow. Both positive and negative optic flows have thus to be determined as accurately as possible.

We propose a method based on the fusion of two optic flow measurements to determine the sign of the angular velocity of the scene. The optic flow processing based on the "time of travel" scheme is performed twice. The time delay of contrasting edges are computed in both ways between photodiodes  $n$  and  $n + 1$  and at the same time between photodiodes  $n + 1$  and  $n$ . Empirical findings have shown that angular speed of contrast detected in the correct direction of motion is greater than in the wrong direction which inspired the use of the maximum operator (Blanes, 1991).

Drastic constraints related to UAV applications are kept in mind since the proposed solution offers a very lightweight, low power consumption and low computational requirements device. The new sensor developed and characterized indoors on natural scene is able to measure accurately optic flow in the  $[-350 \text{ }^\circ/\text{s}; -80 \text{ }^\circ/\text{s}] \cup [80 \text{ }^\circ/\text{s}; 350 \text{ }^\circ/\text{s}]$  range.

It is worth noting that intended applications of this new sensor is not planetary landing applications since the optic flow range is greater than  $[1.5 \text{ }^\circ/\text{s}; 25 \text{ }^\circ/\text{s}]$ . Here

the emphasis is placed on the two new features: 5-LMS fusion and sign determination. In order to highlight the benefits of those enhancements, we worked on faster angular speed measurements which reduce the duration of experimental validations. The considered range of optic flow corresponds to Micro Aerial Vehicles (MAV) autonomous vision based navigation tasks.

Another aspect of this paper concerns experiments and characterizations performed to show the improvements brought by the fusion of 5 LMS outputs with the median operator.

We show that the 5-LMS fusion scheme associated with the search for the maximum of positive and negative optic flow give outstanding performances regarding the new optic flow sensor with limited weight (1 g), size and power consumption.

G. Sabiron's main joint contributions:

1. Optimization of the sensor firmware to be able to run 10 VMS on a single 16-bits microcontroller,
2. Design and tuning of the sliding window filtering step,
3. Realization of the main experiments presented on figures 4, 5, 7 and 8.

Author contributions:

F.L.R., F.E., F.R. designed research;

F.L.R., F.E., G.S. performed research;

F.L.R., F.E., G.S., F.R. contributed with technical and analytic tools;

F.L.R., F.E., G.S., F.R. analyzed data;

and F.L.R., F.E., G.S., F.R. wrote the paper.

# Two-Directional 1-g Visual Motion Sensor Inspired by the Fly's Eye

Frédéric L. Roubieu, *Student Member, IEEE*, Fabien Expert, *Student Member, IEEE*,  
Guillaume Sabiron, *Student Member, IEEE*, and Franck Ruffier, *Member, IEEE*

**Abstract**—Optic flow based autopilots for Micro-Aerial Vehicles (MAVs) need lightweight, low-power sensors to be able to fly safely through unknown environments. The new tiny 6-pixel visual motion sensor presented here meets these demanding requirements in term of its mass, size and power consumption. This 1-gram, low-power, fly-inspired sensor accurately gauges the visual motion using only this 6-pixel array with two different panoramas and illuminance conditions. The new visual motion sensor's output results from a smart combination of the information collected by several 2-pixel Local Motion Sensors (LMSs), on the basis of the “time of travel” scheme originally inspired by the common housefly's Elementary Motion Detector (EMD) neurons. The proposed sensory fusion method enables the new visual sensor to measure the visual angular speed and determine the main direction of the visual motion without any prior knowledge. Through computing the median value of the output from several LMSs, we also ended up with a more robust, more accurate and more frequently refreshed measurement of the 1-D angular speed.

**Index Terms**—Optic flow, Vision, Fly, Bio-inspiration, Neuro-morphic, Motion sensor.

## I. INTRODUCTION

**M**ICRO AERIAL VEHICLES (MAVs) constitute a class of Unmanned Aerial Vehicles (UAVs) which can be used for the remote observation of hazardous environments without any risk to human life. MAVs need to be equipped with onboard sensors and flight control devices in order to perform tasks such as those performed by optic flow (OF) based aerial robots: obstacle avoidance [1]–[7], terrain following and automatic landing [2], [8]–[12], tracking a moving target [13], [14] and controlling their forward speed [15]. MAVs endowed with these abilities would acquire greater autonomy, and at the same time, the ground operators' arduous task of piloting an almost constantly invisible aircraft would be greatly simplified.

Copyright© 2012 IEEE. Personal use of this material is permitted. However, permission to use this material for any other purposes must be obtained from the IEEE by sending a request to pubs-permissions@ieee.org.

An earlier version of this paper was presented at the 2011 IEEE SENSORS Conference and was published in its proceedings.

This research was supported partly by CNRS Institutes (Life Science; Information Science; Engineering Science and Technology), Aix-Marseille University, the French National Research Agency (ANR) (EVA project under ANR-ContInt grant number ANR608-CORD-007-04), and by European Commission via the CURVACE project. The CURVACE project acknowledges the financial support of the European Commission's Future and Emerging Programme for Research, under FET-Open grant number: 237940.

The authors are with Aix-Marseille University, CNRS, Institute of Movement Science, Biorobotics Dept. UMR7287, 13288, Marseille, France e-mail: {frederic.roubieu, fabien.expert, guillaume.sabiron, franck.ruffier}@univ-amu.fr.

G. Sabiron is also with the French Aerospace Lab (ONERA, Systems Control and Flight Dynamics -DCSD-), 31055 Toulouse, France.

Nature has taught us that flying insects, which came into existence several hundred million years ago, have developed particularly elegant solutions to the problem of navigating swiftly in unfamiliar and complex environments. Winged insects are able to enter and explore unknown environments without any sonar or laser range-finder: their visually guided performances depend mainly on OF sensing processes [10], [16]–[25]. The OF perceived by a moving agent (an animal, human or robot) is a vector field that gives the angular speed  $\omega$  (magnitude in  $^\circ/s$ ) at which any contrasting object in the environment is moving past the eyes [26]. The fly's eye has been shown to be sensitive to two-directional motion [27] and also to be driven by a minimum of two photoreceptors inside the same ommatidium [28], [29]. The fly's eye is therefore one of the most suitable animal model available for studies on motion detecting neurons. Based on studies on the fly's visual system previously conducted at our Laboratory, in which electrophysiological recordings were performed on single neurons while microstimuli were being applied to single photoreceptor cells in a single ommatidium of the compound eye [28], a 2-pixel Local Motion Sensor (LMS) was developed [30], based on the principle known today as the “time of travel” scheme [31].

Using such bio-inspired sensors, various simulated vision-based autopilots [31]–[34] based on OF sensing techniques were subsequently developed at our Laboratory, and a series of terrestrial [31], [35] and aerial robots [9], [14], [36], [37] were constructed. The “robotfly” (“Robot Mouche” in French) built by Franceschini's team in 1991 was a completely autonomous wheeled robot equipped with a compound eye consisting of 114 electronic LMSs implemented in analog technology using Surface Mounted Devices (SMDs) [35]. The “robotfly” was able to steer its way through an unknown field full of obstacles at a relatively high speed (up to 50  $cm/s$ ) [35]. The “robotfly” also implemented two-directional analog LMSs using a maximum operator to determine the direction of motion [35], [38]. However, the size and mass of these analog sensors were not compatible with the drastic constraints imposed on free flying MAVs in terms of their mass (they have to weigh less than 100  $g$ ), size (they must measure less than 15  $cm$ ) and power consumption.

Several teams therefore started to design new visual motion sensors by mixing analog and digital processing, which are lighter and easier to implement onboard MAVs than a camera-based system [39] or fully analog sensors. One possible approach consisted in developing visual motion sensors using analog and digital Very-Large-Scale Integration (VLSI) tech-

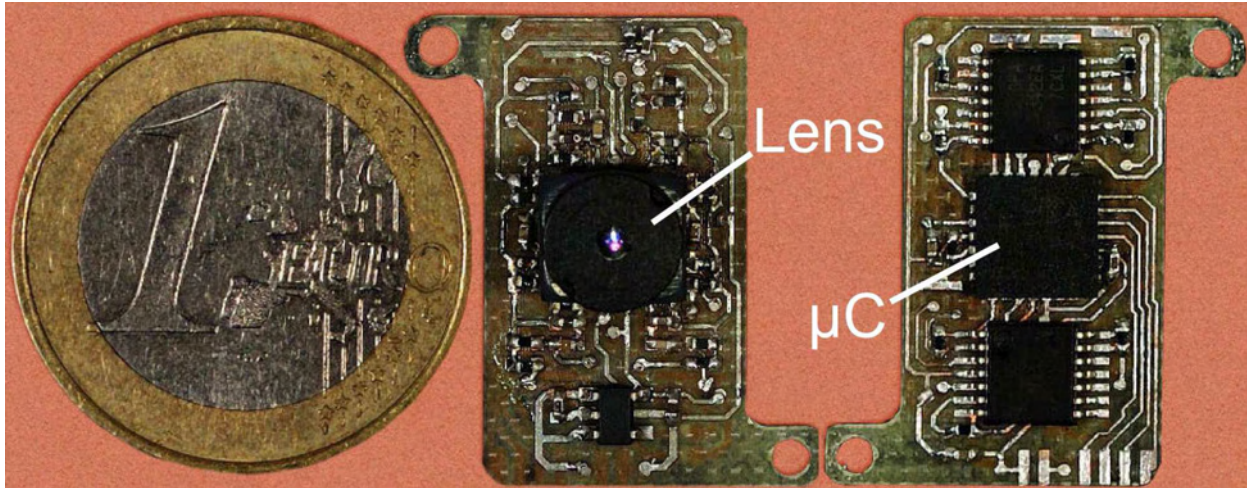


Fig. 1. Top view of the 1-gram microcontroller-based visual motion sensor (size:  $23.3 \times 12.3 \text{ mm}$ ) with its lens (focal length:  $2 \text{ mm}$ ) mounted on the one-dimensional 6-photosensor array, and bottom view of the PCB (thickness:  $0.4 \text{ mm}$ ) with its tiny low-power 16-bit  $\mu\text{C}$  (dsPIC from Microchip© Company).

nologies, such as those based on the Reichardt correlator [40]–[43], the Pulse-based velocity sensor [44] or Barrows’ design [45]. Only a few VLSI-based sensors have been implemented onboard MAVs so far (flight with limited degrees of freedom: [46], free-flight: [2], [45]).

Off-the-shelf mouse sensors were also recently characterized [47] and mounted onboard terrestrial [48], [49] and aerial robotic platforms [5], [50]. The performances of these systems have not been properly assessed so far in terms of their resolution, accuracy, invariance to illuminance and contrast, apart from two studies [51], [52].

At our Laboratory, several versions of 2-pixel motion sensors based on the “time of travel” scheme originally based on the fly’s eye [29] were developed using either a Field Programmable Gate Array (FPGA) [53] or a microcontroller ( $\mu\text{C}$ ) [54]–[60].

In the current study, we present a new tiny  $\mu\text{C}$ -based visual motion sensor weighing only 1 gram (Fig. 1), which receives visual inputs from a 6-pixel array integrated circuit. By combining several 2-pixel motion sensors, the performances of the visual motion sensor were highly improved. The first sensory fusion method of this sensor produces a combined output based on the median value of 5 LMS measurements in a single pre-determined direction of motion which drastically improved the accuracy and the refresh rate ( $f_{refresh}$ ) of the angular speed measurements [58]. An improved sensory fusion method determines an accurate estimation of the direction and the magnitude of the angular speed in the detected direction of motion. This whole processing was embedded into a  $\mu\text{C}$  which has sufficient computational resources for carrying out the requisite signal processing tasks efficiently, while its mass is compatible with the very low avionic payload allowed on MAVs.

The first sensory fusion method implemented in our tiny  $\mu\text{C}$ -based visual motion sensor is presented in the section II that gives a short description of the bio-inspired visual system and the principles underlying the 2-pixel “time of travel” scheme. Experiments performed on the visual motion sensor, which

was tested indoors, are described in Section III. The results of these experiments are presented in Section IV. Section V describes the results obtained thanks to an improved sensory fusion method able to perfectly determine the direction of motion without any prior knowledge and to give an accurate and robust assessment of the magnitude of the motion in term of angular speed.

## II. DESCRIPTION OF THE DEVICE

1) *Photoreceptor configuration*: The front end of the visual motion sensor designed and developed in this study was based on an off-the-shelf photosensor array (iC-LSC from iHaus Company, <http://www.ichaus.de>) consisting of 2 rows of 6 photodiodes. A fixed-gain current amplifier is integrated into each photodiode. In order to detect a large number of contrasting objects at low illuminance levels, the photosensors in each column were paired to increase the signal to noise ratio by increasing the sensitive surface two-fold from  $300 \mu\text{m} \times 800 \mu\text{m}$  to  $300 \mu\text{m} \times 1600 \mu\text{m}$ . This one-dimensional 6-pixel array was then mounted on a cheap, lightweight lens (Sparkfun SEN-00637) borrowed from a mobile telephone camera (Fig. 1). As in flies, each photosensor features a Gaussian Angular Sensitivity Function (ASF), [61] [Fig. 2(b)], which results in insects from the spatial convolution of the photoreceptor’s diameter with the point spread function of the facet lenslet [62], [63] and in our sensor, from the defocusing of the lenslet. The ASF of the “lens-photoreceptor” system was assessed by slowly rotating the visual motion sensor placed  $50 \text{ cm}$  in front of a point light source [Fig. 2(a)]. By defocusing the lens (i.e., by reducing the distance between the lens and the retina), we obtained a similar Gaussian sensitivity profile to that of the housefly. The full width at half height of the Gaussian curve (the acceptance angle)  $\Delta\rho$  determines the cut-off frequency of the low-pass spatial filtering process (Fig. 3), whereas the inter-receptor angle  $\Delta\varphi$  (i.e., the angle between two adjacent optical axes) determines the angular speed ( $\omega_i^m$ ) measurement range.

The defocusing process was adjusted to obtain an appropriate

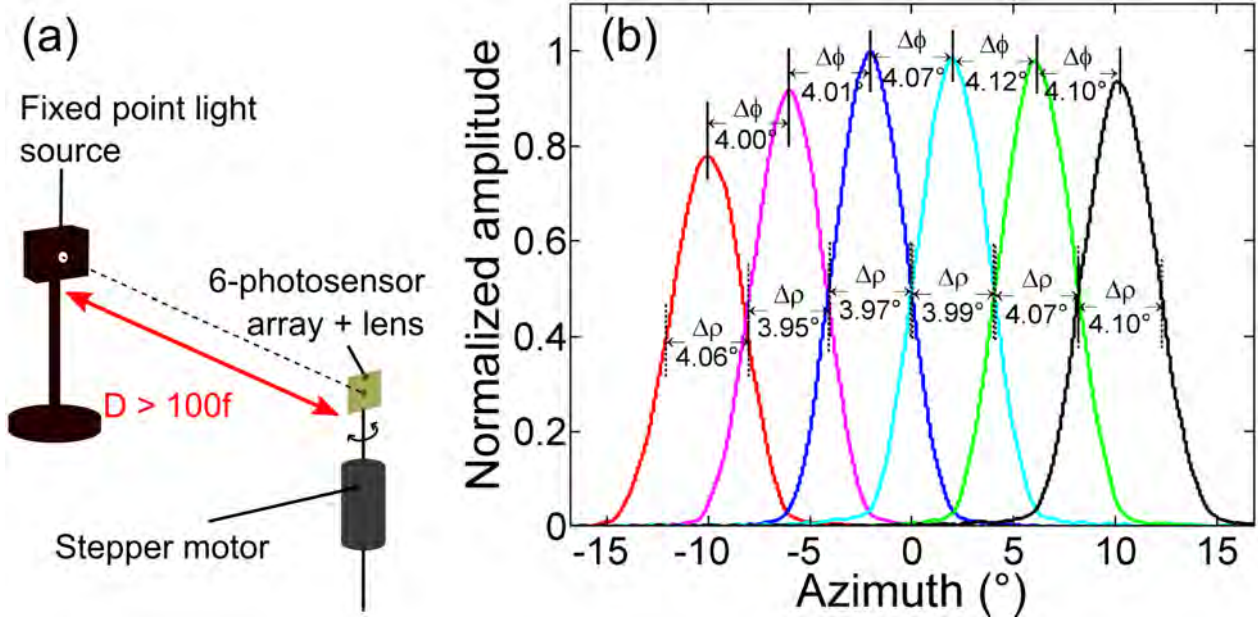


Fig. 2. (a) Scheme of the test bench used to determine the Gaussian ASFs of the 6-photosensor array obtained by slowly rotating the visual motion sensor mounted on the motor shaft of a stepper motor and placed at a distance  $D = 50 \text{ cm}$  in front of a fixed point light source. (b) Raw Gaussian ASFs of the photosensor array.

bell-shaped ASF projected onto the photosensor array, as occurs in some diurnal insects [66], where:

$$\Delta\varphi = \Delta\rho \quad (1)$$

The visual photoreceptor axes are separated by an inter-receptor angle  $\Delta\varphi = 4^{\circ}$  and each pixel features an acceptance angle  $\Delta\rho = 4^{\circ}$  [Fig. 2(b)]. The horizontal Field Of View (FOV) of the visual motion sensor is  $28.8^{\circ}$ .

2) *Local Motion Sensor (LMS)*: Each LMS assesses the angular speed  $\omega_i$  [i.e., a 1-D component of the OF, Fig. 3(a)] of any dark-to-light (ON) or light-to-dark (OFF) contrast in the same way as the fly’s motion-detecting neurons. This “perceived” angular speed  $\omega_i$  is transformed by the optical system into a delay  $\Delta t_i$  between 2 neighboring photosensor signals defined as follows:

$$\Delta t_i = \frac{\Delta\varphi}{\omega_i} \quad (2)$$

The functional “time of travel” scheme used here consists of 6 processing steps [30], [54], [65] measuring the delay  $\Delta t_i$ , thus giving the angular speed  $\omega_i^m$  (Fig. 3):

- Step 1: Low-pass spatial filtering is achieved by defocusing the lens, thus giving each pixel a Gaussian ASF.
- Step 2: Analog bandpass filtering: high-pass filtering ( $f_c = 20 \text{ Hz}$ ) enhances the contrast information and eliminates the DC component of the photoreceptor signals. This step is followed by a first-order low-pass filtering step, where  $f_c = 136 \text{ Hz}$ .
- Step 3: Digitizing and filtering: second-order fixed-point digital low-pass filtering ( $f_c = 30 \text{ Hz}$ ) reduces any high frequency noise introduced by the artificial indoor lighting ( $100 \text{ Hz}$ ).
- Step 4: Hysteresis thresholding is performed to distin-

guish between ‘ON’ and ‘OFF’ contrast transitions (i.e. dark-to-light and light-to-dark transitions, respectively) in each channel.

- Step 5: A time delay circuit is triggered by one channel and stopped by the neighboring channel. This circuit measures the time  $\Delta t_i$  elapsing between similar (‘ON’ or ‘OFF’) transitions occurring in two adjacent photoreceptors.
- Step 6: Computing the 1-D angular speed of a contrast in the visual field of the LMS, using a look-up table which converts the delay  $\Delta t_i$  into the measured angular speed  $\omega_i^m$ .

3) *Implementation and optimization*: Our visual motion sensor generates 5 simultaneous local measurements  $\omega_i^m$  of the 1-D angular speed of a moving natural panorama in a measurement range of more than one decade, ranging from  $25^{\circ}/s$  to  $350^{\circ}/s$ . The sensor output is the median value  $\omega_{median}^m$  of the 5 LMSs. The whole processing of the 5 LMSs and the computation of the median value were carried out on a dsPIC33FJ128GP802  $\mu C$  working at a sampling frequency of  $2 \text{ kHz}$  and running at 40 MIPS. This low-power 16-bit  $\mu C$  was a very good candidate in term of size footprint (28 pins QFN-S package, see Table I for dimension), power consumption and performances allowing it to carry out the whole processing using a 16-bit MAC unit (“Multiplier + ACcumulation”), 1 SPI and  $6 \times 12\text{-bit}$  ADCs (Analog to Digital Converters) while meeting with the constraints of MAVs [see Fig. 3(a)].

The  $\mu C$  embedded onboard the visual motion sensor (Fig. 1) is connected to an external Bluetooth module via a test-board. This radio link allows the operator to record all the data synchronously and to convey it to a computer for analysis. The program of the 16-bit  $\mu C$  was developed on

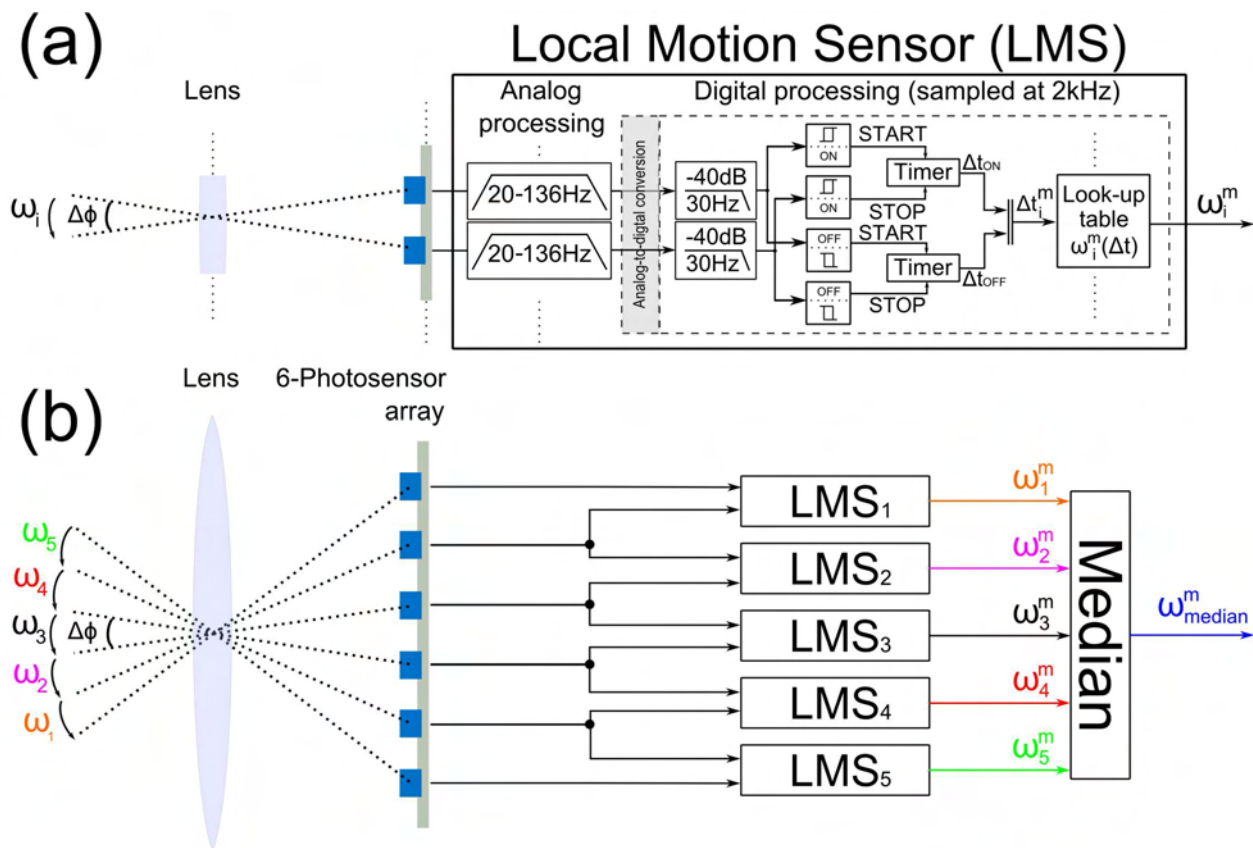


Fig. 3. General processing architecture of the visual motion sensor, including its 5 LMSs. (a) Processing architecture of one LMS. The visual signals delivered by neighboring photoreceptors are filtered both spatially and temporally by an analog bandpass filter with cut-off frequencies [20 Hz, 136 Hz] and a second order fixed-point digital low-pass filter with a cut-off frequency of 30 Hz. The filtered photoreceptor signals are then thresholded to determine the angular speed  $\omega_i^m$ , using the “time of travel” scheme previously developed at our Laboratory [30], [31], [64], [65]. The “time of travel”  $\Delta t_i$ , which is proportional to the inverse of  $\omega_i^m$ , elapsing between two filtered photoreceptor signals is measured by a timer:  $\Delta t_{ON}$  and  $\Delta t_{OFF}$  are measured by means of ON and OFF contrast distinguishing processes [29]. These delays  $\Delta t_i$  are used to generate the 1-D angular speed  $\omega_i^m$  in the visual field of the 1-D LMS. (b) The 5 LMS output signals are combined to generate a more robust and frequently refreshed 1-D median measured angular speed  $\omega_{median}^m$ . The overall processing was carried out on a tiny low-power 16-bit  $\mu C$  at a sampling rate of 2 kHz.

Matlab/Simulink© environment and compiled using a specific toolbox (available on <http://www.kerhuel.eu>) developed for dsPIC  $\mu C$ s.

In order to be able to perform all the processing with the limited computational power of a tiny  $\mu C$ , several optimizations in the sensory fusion method were required to reduce the computational load. The order of the digital low-pass filter embedded in the  $\mu C$  was reduced two-fold from the 4<sup>th</sup> [54] to 2<sup>nd</sup> order. This reduction was possible thanks to the on-chip pre-amplification unit of the LSC retina, which reduces the noise. One simple 16-bit free counter was used to measure the 10 delays  $\Delta t$  ( $\Delta t_{ON}$  and  $\Delta t_{OFF}$  of the 5 LMSs) required to estimate visual motion in the FOV of the 5 LMSs.

4) *Characteristics of the visual motion sensor:* The mass balance of our tiny device, including all the electronics, does not exceed 1 gram, which amounts to only 0.2 g per LMS (Table I). It is also a low-power visual motion sensor with a consumption of only 74 mA. The specifications of the visual motion sensor are summarized in Table II.

We recently showed that using the same fusion algorithm, the measurement range of a similar sensor can be tuned to lower angular speeds by adjusting the optical parameters as shown

in [67].

TABLE I  
MASS BALANCE OF THE VISUAL MOTION SENSOR

Parts	Mass (g)
PCB thickness 0.4 mm, 3 cm <sup>2</sup>	0.402
Lenslet Sparkfun SEN-00637	0.17
Lenslet-mount	0.11
LSC iC-Haus retina	0.13
$\mu C$ dsPIC 6 × 6	0.1
Electronic components	0.162
Estimated total mass =	1.074
Real mass =	0.98 g
Mass per 1-D LMS <	0.2 g

### III. EXPERIMENT

The visual motion sensor was tested indoors in natural light at a constant illuminance of approximately 1500 lux, corresponding to the sunny daylight coming from a window. The visual motion sensor was placed at an orthogonal distance

TABLE II  
 SPECIFICATIONS OF THE VISUAL MOTION SENSOR

Retina	LSC iC-Haus
Inter-receptor angle $\Delta\varphi$ ( $^\circ$ )	4
Acceptance angle $\Delta\rho$ ( $^\circ$ )	4
Photodiode size (m)	$300 \times 1600$
Pixel pitch (m)	420
Focal length of the lens (mm)	2
$F_{number}$ of the lens	2.8
Angular velocity range ( $^\circ/s$ )	[25; 350]
Resolution ( $^\circ/s$ ) [Min; Max]	$[7 \times 10^{-2}; 14.5]$
Sensitivity ( $^\circ/s/LSB$ )	$7.63 \times 10^{-4}$
Measured mass with optics (g)	0.98 g

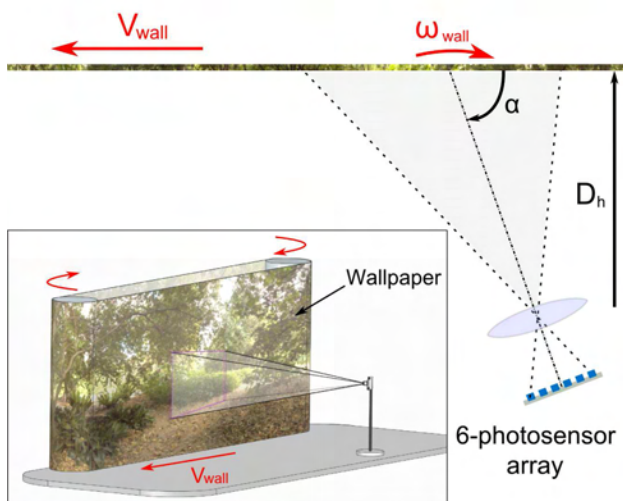


Fig. 4. Test bed used to assess the performances of the first sensory fusion method of the visual motion device based on a 6-pixel 1-D array. The visual motion sensor was placed at an orthogonal distance  $D_h$  from a piece of wallpaper (forming a printed belt), at an arbitrary angle  $\alpha$  between the direction of the wall motion ( $\vec{V}_{wall}$ ) and the main sensor axis. The printed belt depicting a natural colored panorama (inset) was stretched between two drums actuated thanks to a motor and a V-belt. The printed belt was made to move horizontally in a pre-determined preferred direction in front of the visual motion sensor at an angular speed  $\omega_{wall}$ .

$D_h$  from a printed belt of wallpaper showing a natural colored panorama. The printed band was stretched between 2 drums actuated thanks to a motor and a V-belt (see enclosed frame Fig. 4). The visual motion sensor was oriented at an arbitrary angle  $\alpha$  between the direction of the wall motion ( $\vec{V}_{wall}$ ) and the main sensor axis (Fig. 4). The panorama was therefore made to move horizontally with respect to the visual motion sensor at a ground-truth optic flow  $\omega_{wall}$ , as given by (3):

$$\omega_{wall} = \frac{V_{wall}}{D_h} \times \sin^2 \alpha \quad (3)$$

By imposing an arbitrary orientation angle  $\alpha$  to the visual motion sensor, we wanted to check if the measurements

obtained with each  $i^{th}$  LMS were in line with (4):

$$\omega_i^m = \frac{V_{wall}}{D_h} \times \sin^2(\alpha + (i-3) \times \Delta\varphi) \quad (4)$$

The dynamic indoor responses were assessed by the visual motion sensor at  $\alpha = 60^\circ$  and  $\alpha = 80^\circ$  with 2 different printed belts:

- The first belt was decorated with a natural colored panorama [Fig. 5(m)],
- The second one was lined with a colored indoor panorama featuring a laboratory [Fig. 5(n)].

The wallpaper was moved using a triangular speed law involving a series of velocity ramps with various slopes ranging from  $27^\circ/s$  to  $230^\circ/s$  with  $\alpha = 60^\circ$  and from  $28^\circ/s$  to  $312^\circ/s$  with  $\alpha = 80^\circ$ .

#### IV. RESULTS

The dynamic indoor responses of the visual motion sensor and the median output of the 5 LMSs were studied in terms of the refresh rate ( $f_{refresh}$ ) and the standard deviation error ( $Std_{error}$ ) computed as follows:

$$Std_{error} = std(\omega_i^m - \omega_{wall}) \quad (5)$$

The  $Std_{error}$  therefore corresponds to the dispersion of the data between the measured angular speed  $\omega_i^m$  and the ground-truth value  $\omega_{wall}$ . The main contributor is that of the 5 angular speed measurements  $\omega_i^m$  which is most frequently used to calculate the median angular speed  $\omega_{median}^m$ . The refresh rate ( $f_{refresh}$ ) was defined as the number of new motion measurements per second. A new motion measurement occurs when a contrast transition is detected by one pixel and then by the second pixel with any delay  $\Delta t$  in the angular speed measurement range [i.e. in the  $25^\circ/s$  to  $350^\circ/s$  range, see (2)].

As was to be expected in view of (4), the 5 LMS output measurements are different [Fig. 5(a), (d), (g) and (j)] because of the different orientations of the visual axes of the LMSs in the sensor's FOV. Figs. 5(c), (f), (i) and (l) show that the main contributors to the median value at the orientation angles  $\alpha = 60^\circ$  and  $\alpha = 80^\circ$  were the 3<sup>rd</sup> LMS and the 5<sup>th</sup> LMS, respectively. For both panoramas, the median value accurately followed the angular speed of the wall  $\omega_{wall}$ , giving a  $Std_{error}$  smaller than  $12^\circ/s$  in comparison with the value obtained with the main contributor, which was between  $19^\circ/s$  and  $24^\circ/s$ . In addition, the refresh rate of the median value was found to increase more than 4-fold ( $67 Hz$ ) in comparison with that observed in the case of the LMS main contributor ( $15.7 Hz$ ) [Figs. 5(b), (e), (h) and (k)].

#### V. ESTIMATION OF THE DIRECTION AND THE MAGNITUDE OF THE VISUAL MOTION

##### A. Device description

The improved sensory fusion method of the new visual motion sensor presented in this section is based on the front end described in section II-1, having the optical characteristics described in Table II in terms of the inter-receptor angle  $\Delta\varphi$  and the acceptance angle  $\Delta\rho$ . This visual motion sensor

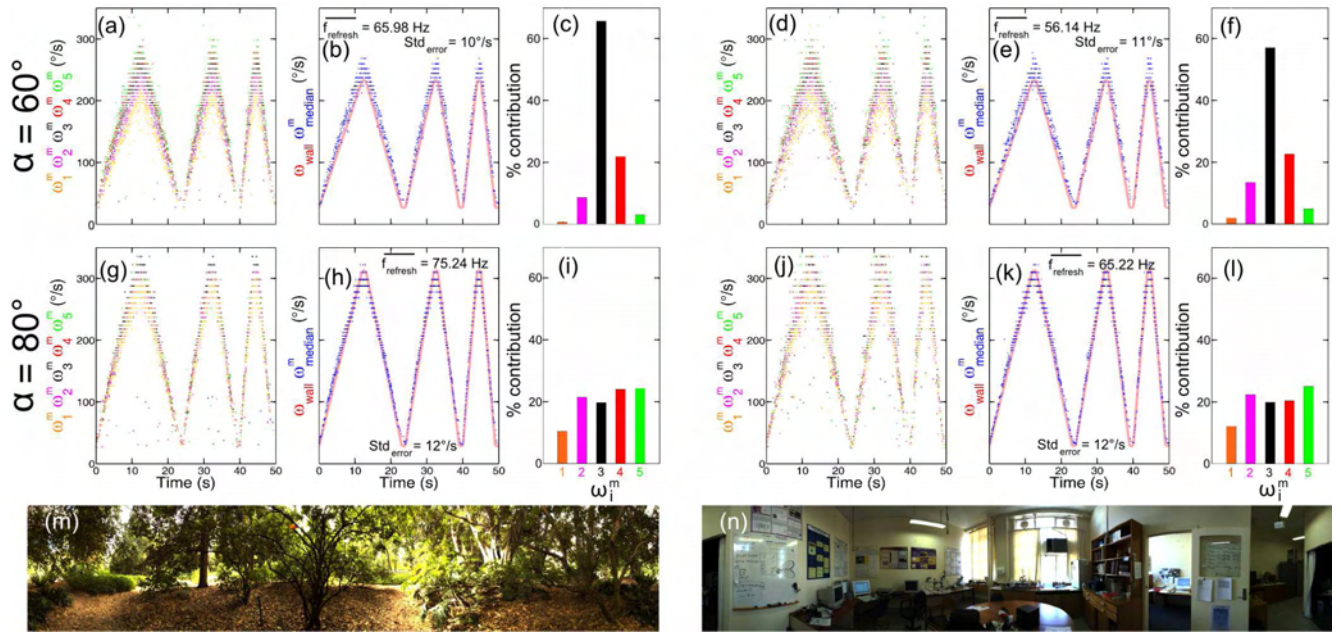


Fig. 5. Dynamic indoor responses of the visual motion sensor. The visual motion sensor was placed at an orthogonal distance  $D_h = 24 \text{ cm}$  from a moving printed belt lined with a colored natural panorama depicting either bushes and trees or a laboratory. The visual motion sensor was placed at 2 different orientation angles  $\alpha = 60^\circ$  and  $\alpha = 80^\circ$  between the direction of the wall motion ( $\vec{V}_{wall}$ ) and the main sensor axis to check that each LMS measures visual motion in its own visual field [see (4)]. The printed belt was moved using a triangular law giving a triangular pattern of angular speed variations involving a series of velocity ramps with different slopes ranging from  $27^\circ/s$  to  $230^\circ/s$  ( $\alpha = 60^\circ$ ) and from  $28^\circ/s$  to  $312^\circ/s$  ( $\alpha = 80^\circ$ ) [see (3)]. (a), (d), (g) and (j) Dynamic indoor responses of each LMS in the visual motion sensor placed at an orientation angle  $\alpha = 60^\circ$  [(a) and (d)] and  $\alpha = 80^\circ$  [(g) and (j)]. Note that each LMS output differed from the others because of the different orientations of the LMS visual axes in the sensor's FOV as expected according to (4). (b), (e), (h), and (k) Dynamic indoor responses in terms of median values in comparison with those predicted by the main contributor, along with the standard deviation error ( $Std_{error}$ ) and refresh rate ( $f_{refresh}$ ) characteristics. (c), (f), (i), and (l) Vertical bar graph showing which LMS in the visual motion sensor was the main contributor to the median value computed. (m) and (n) The natural colored panorama depicted on the printed belt (Fig. 4) used to assess the visual motion sensor's performances.

is able to estimate the direction and the magnitude of the visual motion  $\omega_{median}^{max}$  on the basis of 10 angular speed measurements: 5 LMSs are used to compute the median angular speed  $\omega_{median+/-}^m$  in each direction of motion (“+” or “-”) (Fig. 6). In order to determine the direction of the visual motion without any prior knowledge, empirical findings [38] have shown that, within a given angular speed range, the angular speed of the contrasts detected in the correct motion direction is usually greater than that measured in the opposite direction. Based on this finding, by simply choosing the maximum value of the median angular speeds in the two directions  $\omega_{median+}^m$  and  $\omega_{median-}^m$ , it is possible to determine the direction of the visual motion accurately in the  $[-350^\circ/s; -80^\circ/s] \cup [80^\circ/s; 350^\circ/s]$  range. The  $]-80^\circ/s; 80^\circ/s[$  range corresponds to an uncertainty range, where the direction and the magnitude of the angular speed cannot be assessed accurately. As soon as the sensor detects visual motion in the  $]-80^\circ/s; 80^\circ/s[$  range, the output signal  $\omega_{median}^{max}$  magnitude and direction are voluntarily set to “no value” without any error.

### B. Optimization of the motion direction estimates

To optimize the motion direction estimation, we decided to filter each median angular speed measurement ( $\omega_{median+}^m$  and  $\omega_{median-}^m$ ) using a rate-limiter that removes any value that is too different from the previous angular speed measurement

knowing the OF rate is bounded. A sliding window filters out any motion direction error by selecting the direction occurring more than 8 times among the last 16 detected motion directions. Thanks to this filtering process, the motion direction was perfectly determined (Fig. 6).

The improved sensory fusion method was optimized in order to increase the number of LMSs embedded into the same  $\mu C$  two-fold. The same filtered visual signals were recombined in order to compute an accurate visual angular speed and the direction of the visual motion while keeping the digital processing frequency at  $2 \text{ kHz}$ . The median computation step was optimized by computing the median value only whenever a new visual motion measurement occurred, i.e., whenever a new  $i^{th}$  LMS angular speed  $\omega_{i+/-}^m$  was measured: this algorithm optimization prevents the  $\mu C$  from being overloaded by computing the median value at all the time steps at which none of the LMS outputs are refreshed.

All these improvements have made the tiny  $\mu C$  capable of carrying out all the processing operations required to determine the median 1-D angular speed of a natural panorama  $\omega_{median}^{max}$  and to estimate the direction of motion with a mean computational load of only 53% (minimum: 43%; maximum: 82% -very short peaks-) at a sample frequency of  $2 \text{ kHz}$ .

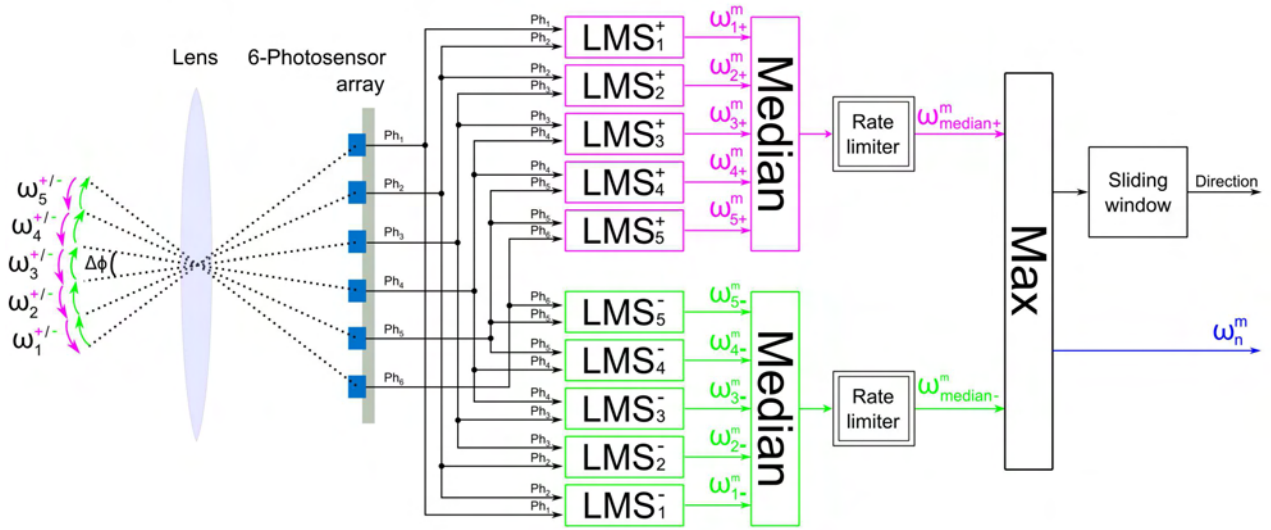


Fig. 6. General processing architecture of the improved sensory fusion method based on 10 LMSs. The visual signals delivered by the photoreceptors are filtered and thresholded by the LMSs to determine the angular speeds  $\omega_{i+/-}^m$  using the “time of travel” scheme in the two directions of motion [30], [31], [38], [65]. The visual motion is measured in the opposite direction by reversing the inputs to each LMS. A rate limiter function filters out any median angular speed measurement that changes too fast. The motion direction and magnitude  $\omega_n^m$  are estimated based on a simple algorithm, using the maximum median value of the angular speed  $\omega_{median+}^m$  and  $\omega_{median-}^m$  computed from the 5 LMSs in the 2 directions of motion. A sliding window removes any motion direction error by selecting the direction occurring more than 8 times among the last 16 detected motion directions. This improved sensory fusion method allows to measure the motion magnitude efficiently in the  $[-350^\circ/s; -80^\circ/s] \cup [80^\circ/s; 350^\circ/s]$  range and to determine the direction of motion without any prior knowledge.

### C. Experiment

The static and dynamic responses of the improved sensory fusion method of the visual motion sensor presented here were obtained under 2 lighting conditions. The background irradiance values were measured in  $W.cm^{-2}$  using a digital radiometer (ILT1700) which gives the irradiance in the direction of the radiometer’s sensor. The visual motion sensor was placed at an orthogonal distance  $D_h = 24\text{ cm}$  from a printed belt, oriented at an angle  $\alpha = 90^\circ$ . The printed belt was stretched between 2 drums actuated by a motor and a V-belt which could be made to rotate either clockwise or anticlockwise (see inset in Fig. 7). The panorama was therefore made to move horizontally in two directions with respect to the visual motion sensor at an angular speed  $\omega_{wall}$  according to (3). The static responses of the visual motion sensor were assessed by applying a series of  $30^\circ/s$  fifteen-second steps to the moving wall at a rotational speed  $\omega_{wall}$  in the  $[-315^\circ/s; -105^\circ/s] \cup [105^\circ/s; 315^\circ/s]$  range in the two opposite directions. These experiments were conducted with an irradiance of  $5 \times 10^{-3} W.cm^{-2}$ .

The dynamic characteristics of the visual motion sensor were assessed at two different illuminance values: at  $2.5 \times 10^{-2} W.cm^{-2}$ , which corresponds to strong sunlight coming from a windows and  $5 \times 10^{-3} W.cm^{-2}$ , which corresponds to strong indoor lighting. We applied a 60-second stimulus to the moving wall, involving a series of velocity ramps with different slopes in the  $[-300^\circ/s; 300^\circ/s]$  range. The belt was covered with a natural colored panorama showing bushes and trees [Fig. 8(g)] or with a colored indoor panorama featuring a laboratory [Fig. 8(h)].

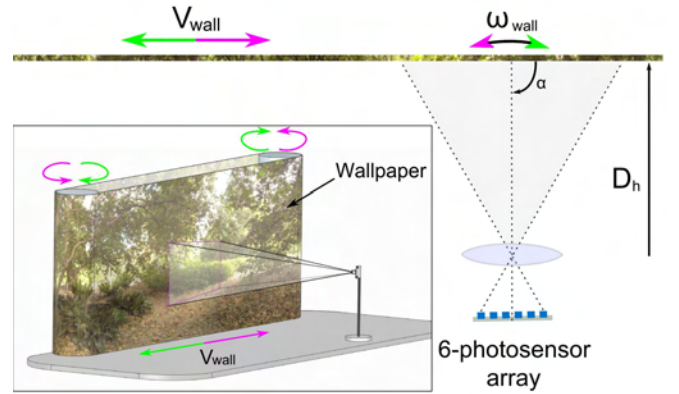


Fig. 7. Test bed used to assess the performances of the visual motion device including the 10 LMSs and the motion direction detection unit. The visual motion sensor was placed at an orthogonal distance  $D_h = 24\text{ cm}$  from a printed belt. In this case, the angle  $\alpha$  between the direction of the wall motion ( $\vec{V}_{wall}$ ) and the main sensor axis was  $\alpha = 90^\circ$ . The belt printed with a natural colored panorama depicting either bushes and trees or a laboratory, was stretched between two drums actuated by a motor and a V-belt: the belt could be made in this case to rotate either clockwise or anticlockwise. The panorama was therefore made to move horizontally in either direction.

### D. Results

To assess the static characteristics of the visual motion sensor, we studied the mean standard deviation of the data, which was computed as follows:

$$\overline{Std} = \overline{std(\omega_{median}^{max})} \quad (6)$$

The best linear approximation was computed to determine the accuracy of our visual motion sensor. This criterion was

calculated on the basis of (7):

$$\omega_{median}^{max} = a \times \omega_{wall} \quad (7)$$

where  $\omega_{median}^{max}$  is the output signal of the visual motion sensor and  $\omega_{wall}$  is the angular speed of the moving wall as seen by the visual motion sensor. The regression coefficient  $a$  of (7) was used to compute the linearity error given by (8):

$$Linearity\ Error(\%) = |(a - 1)| \times 100 \quad (8)$$

The dynamic responses of the median output  $\omega_{median}^{max}$  of the tiny visual motion sensor were assessed in comparison with the perceived angular speed  $\omega_{wall}$  in terms of the refresh rate and the  $Std_{error}$  defined in (5).

1) *Static characteristics*: Figs. 8(a) and (b) show the static characteristics of the visual motion sensor tested indoors in front of a moving wall at an irradiance value of  $5 \times 10^{-3} W.cm^{-2}$ . As shown in Figs. 8(a) and (b), the visual motion sensor responded accurately with a really low *LinearityError* rate [see (8)] of less than 1% and an excellent dispersion of less than  $7^\circ/s$ . In the measurement range of  $[-350^\circ/s; -80^\circ/s] \cup [80^\circ/s; 350^\circ/s]$ , the visual motion sensor estimated the direction of motion perfectly without making a single direction error.

2) *Dynamic characteristics*: Figs. 8(c) and (d) show the dynamic responses of the visual motion sensor at an irradiance of  $2.5 \times 10^{-2} W.cm^{-2}$ . The median value closely obeyed the triangular law imposed on the angular speed of the wall  $\omega_{wall}$ , giving a low  $Std_{error}$  of only  $7.4^\circ/s$  and  $6.23^\circ/s$  with the outdoor and indoor panoramas, respectively. At a lower irradiance of  $5 \times 10^{-3} W.cm^{-2}$ , the median value  $\omega_{median}^{max}$  again closely obeyed the triangular law imposed on the angular speed of the moving wall  $\omega_{wall}$ , with a  $Std_{error}$  of  $9.2^\circ/s$  in the case of the bushes and trees panorama and  $5.44^\circ/s$  in that of the laboratory panorama. Despite the difference in the irradiance, the  $Std_{error}$  was always of a similar order of magnitude. In any case, the visual motion sensor gave a highly refreshed output. As was to be expected from [57], the  $f_{refresh}$  increased with the irradiance, amounting to  $50.6 Hz$  at an irradiance of  $5 \times 10^{-3} W.cm^{-2}$  and  $74.5 Hz$  at a higher value of  $2.5 \times 10^{-2} W.cm^{-2}$  when the outdoor panorama was displayed on the printed belt [Fig. 8(c) and (e)]. Similar results were obtained with the indoor panorama:  $f_{refresh}$  of  $39.7 Hz$  at  $5 \times 10^{-3} W.cm^{-2}$  and  $62.1 Hz$  at  $2.5 \times 10^{-2} W.cm^{-2}$  [Fig. 8(d) and (f)]. The motion direction was estimated perfectly by the sensor without making a single error.

In view of these performances, this novel tiny visual motion sensor can be said to provide a remarkably promising tool for performing robotic tasks such as obstacle avoidance and terrain following in forward flight, while meeting the requirements in very low avionic payload, since the total mass balance of the two-directional visual motion sensor does not exceed 1 g.

## VI. CONCLUSION

In this study, two different sensory fusion methods of a 1-gram insect-inspired visual motion sensor were evaluated indoors under two different lighting conditions. The dynamic and static responses of this novel fly-inspired visual motion

sensor were used to assess the performances of these very lightweight, low-power sensors, which can be mounted on-board tomorrow's MAVs for obstacle avoidance and speed control purposes.

The first sensory fusion method of our 1-gram  $\mu C$ -based visual motion sensor, consisting of a 5-LMS array, gave 5 simultaneous angular speed measurements and a single combined output in the  $[25^\circ/s; 350^\circ/s]$  range, in a single preferred direction of visual motion. The results obtained in the study (Fig. 5) show how the accuracy and the robustness of the angular speed measurement have been improved thanks to our simple method of data combination based on the median operator. This method improves the  $Std_{error}$  more than 1.7-fold from  $19^\circ/s$  in the case of the main contributor to the median value to  $11^\circ/s$  in the case of the median angular speed  $\omega_{median}^m$ . The refresh rate of the visual motion sensor was found to have increased at least 4-fold ( $67 Hz$ ) in comparison with that of the main contributor ( $15.7 Hz$ ).

The excellent performances obtained with the first sensory fusion method of this 1-gram fly-inspired visual motion sensor led us to design an improved sensory fusion method incorporated into our visual sensor based on the same electronics. These improvements allowed to determine the direction and magnitude  $\omega_{median}^{max}$  of visual motion without any prior knowledge by recombining the filtered visual signals and processing the "time of travel" in the two opposite directions. This improved sensory fusion method of the 1-gram  $\mu C$ -based visual motion sensor designed and built at our Laboratory is based on a 10 LMS-array which can measure the direction and the magnitude of motion in the  $[-350^\circ/s; -80^\circ/s] \cup [80^\circ/s; 350^\circ/s]$  range, thanks to the maximum operator value computed between the median angular speed in the two directions of motion ( $\omega_{median+}^m$  and  $\omega_{median-}^m$ ). The dynamic and static characteristics of this novel sensor (Fig. 8) were used to assess its performances. It consistently measured the 1-D angular speed accurately with an excellent  $LinearityError < 1\%$ . The impressive results obtained indoors were robust since the  $Std_{error}$  was of the same order of magnitude (less than  $10^\circ/s$ ) under two different irradiance conditions, whether the printed belt simulating an unknown environment depicted a natural landscape or a laboratory. Due to the size of the setup we used, the performances have been assessed only indoors. Nevertheless, we have shown recently in [57] that a very similar visual motion sensor based on the same retina could robustly and accurately measure the OF indoors and outdoors in a 1.5-decade illuminance range with strong transient variations.

This stand-alone sensor weighs less than 1 g. The outstanding performances of this tiny  $\mu C$ -based visual motion sensor show that it constitutes a good trade-off between the need for reliable motion sensors and the limited power and avionic payload available on MAVs. This 1g two-directional visual motion sensor yields at its output an accurate and highly refreshed angular speed measurement in the range of  $[-350^\circ/s; -80^\circ/s] \cup [80^\circ/s; 350^\circ/s]$  perfectly adapted to any MAV flying forward and performing robotic tasks such as obstacle avoidance, terrain following, take-off, landing and speed-control purposes in forward flights even possibly for

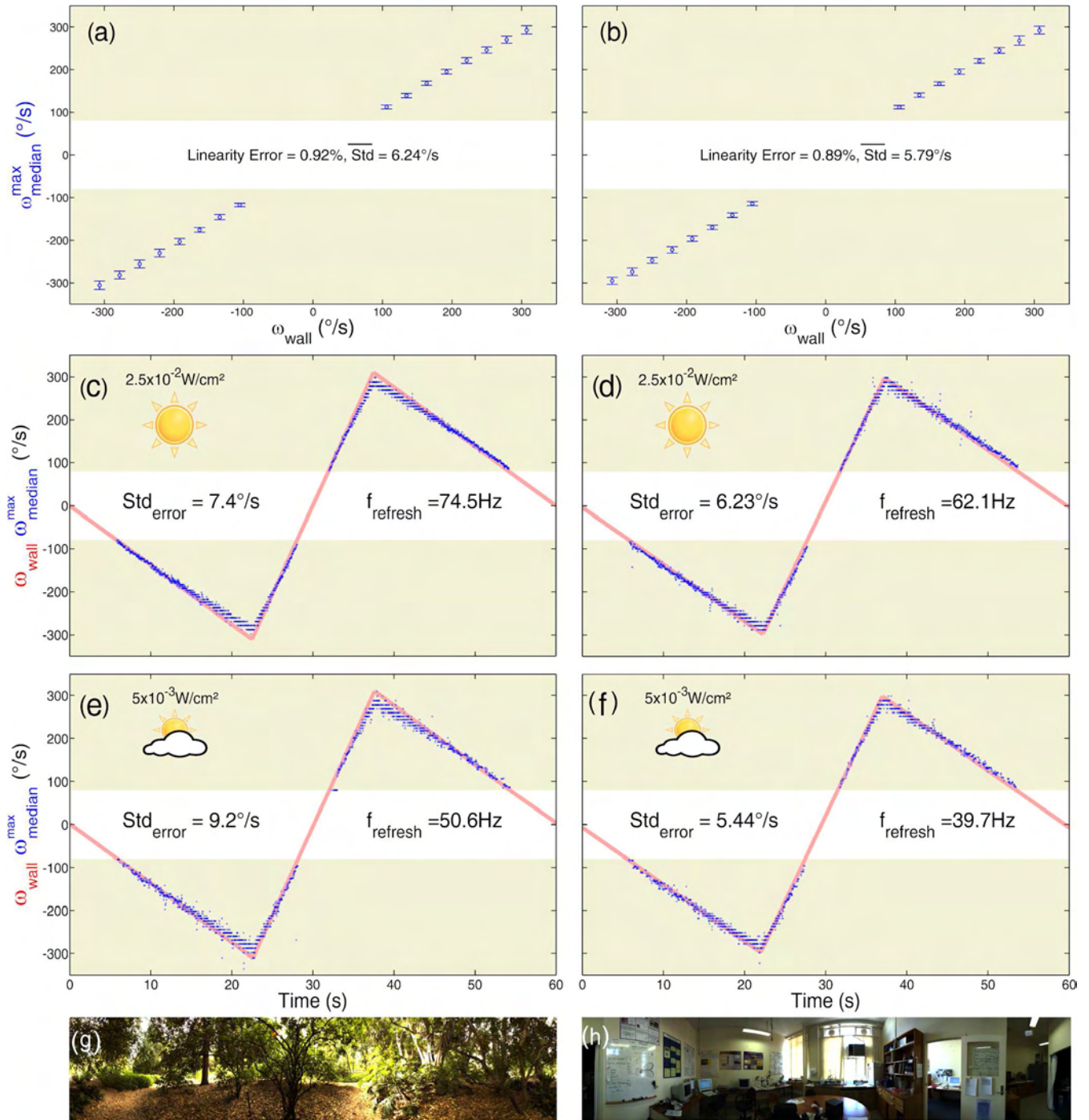


Fig. 8. Dynamic and static indoor responses of the visual motion sensor placed at an orthogonal distance  $D_h = 24 \text{ cm}$  from the moving wall at an angle  $\alpha = 90^\circ$ . The static indoor characteristics of the visual motion sensor were assessed by applying  $30^\circ/\text{s}$  steps (lasting 15s) to the printed belt in the  $[-315^\circ/\text{s}; -105^\circ/\text{s}] \cup [105^\circ/\text{s}; 315^\circ/\text{s}]$  range. The mean visual motion recorded at each angular speed  $\omega_{wall}$  is plotted in the figure with its standard deviation. The best linear approximation obtained in each experiment was computed, and the departure from linearity is given as a percentage. The dynamic responses of the visual motion sensor were assessed at two different irradiances values of  $5 \times 10^{-3} \text{ W.cm}^{-2}$  and  $2.5 \times 10^{-2} \text{ W.cm}^{-2}$  with the two printed panoramas. The printed belt was moved using a triangular law giving a triangular pattern of angular speed variation involving a series of velocity ramps ranging from  $-300^\circ/\text{s}$  to  $300^\circ/\text{s}$ . A fusion algorithm based on the maximum median value of the two opposite directions was used to determine the magnitude  $\omega_{median}^{max}$  and the direction of the angular speed. (a) and (b) Static indoor characteristics of the visual motion sensor. With both panoramas, the visual motion sensor yielded accurate median angular speed measurements with only a small *LinearityError* of less than 1% and an excellent *Std* of less than  $7^\circ/\text{s}$ . (c)-(f) Dynamic indoor responses of the median angular speed  $\omega_{median}^{max}$  of the visual motion sensor, along with the standard deviation error (*Stderror*) and refresh-rate (*frefresh*) data. With the printed belt depicting bushes and trees [Fig. 8(c) and (e)], the results showed a small dispersion of less than  $10^\circ/\text{s}$  and the refresh rate increased from  $50.6 \text{ Hz}$  to  $74.5 \text{ Hz}$  with the irradiance. With the printed belt depicting a laboratory, the results show that the dispersion was less than  $7^\circ/\text{s}$ , and the refresh rate again increased with the irradiance from  $39.7 \text{ Hz}$  to  $62.1 \text{ Hz}$ . (g) and (h) The natural colored panorama depicted on the printed belt (Fig. 7) used to assess the visual motion sensor's performances.

lunar landers [68].

In future works an other optimization of the “time of travel”, called the interpolation-based “time of travel” scheme [60] can be used to implement a larger number of 2-pixel LMS into a single dsPIC  $\mu C$  and therefore process the OF from a much larger 2D retina.

#### ACKNOWLEDGMENT

We thank the anonymous referees. We are grateful to S. Viollet and N. Franceschini for their fruitful comments and suggestions during this study. We thank J. Blanc for correcting the English manuscript and R. Brinkworth and D. O’Carroll (Adelaide Uni., Australia) for kindly making their High Dynamic Range panoramic images available to us. We are most grateful to J. Diperi, D. Dray and Y. Luparini for their involvement in the mechanical design of the test bed and to M. Boyron and B. Fuschlock for their involvement in the overall electronic design of the test board and the visual motion sensor.

#### REFERENCES

- [1] F. Iida, “Goal-directed navigation of an autonomous flying robot using biologically inspired cheap vision,” in *Proceedings of the 32nd International Symposium on Robotics (ISR)*, vol. 21, Seoul, South Korea, April 2001, pp. 1404–1409.
- [2] W. Green, P. Oh, and G. Barrows, “Flying insect inspired vision for autonomous aerial robot maneuvers in near-earth environments,” in *IEEE International Conference on Robotics and Automation (ICRA)*, vol. 3, New-Orleans, USA, April 2004, pp. 2347–2352.
- [3] J. C. Zufferey and D. Floreano, “Fly-inspired visual steering of ultralight indoor aircraft,” *IEEE Transactions on Robotics*, vol. 22(1), pp. 137–146, 2006.
- [4] F. Ruffier and N. Franceschini, “Aerial robot piloted in steep relief by optic flow sensors,” in *Proceedings of the IEEE/RSJ International Conference on Intelligent Robots and Systems (IROS)*, Nice, France, September 2008, pp. 1266–1273.
- [5] A. Beyeler, J.-C. Zufferey, and D. Floreano, “optiPilot: control of take-off and landing using optic flow,” in *European Micro Aerial Vehicle Conference (EMAV)*, vol. 27, Delft, Netherlands, September 2009, pp. 201–219.
- [6] J. Humbert, J. K. Conroy, C. Neely, and G. Barrows, “Widefield integration methods for visuomotor control,” in *Flying insects and robots*, D. Floreano, J. C. Zufferey, M. Srinivasan, and C. Ellington, Eds. Berlin: Springer Berlin Heidelberg, 2009, pp. 63–71.
- [7] G. de Croon, E. de Weerd, C. de Wagter, B. Remes, and R. Ruijsink, “The appearance variation cue for obstacle avoidance,” *IEEE Transactions on Robotics*, vol. 28(2), pp. 529–534, 2012.
- [8] F. Ruffier and N. Franceschini, “Octave, a bioinspired visuo-motor control system for the guidance of micro-air vehicles,” in *SPIE Conference on Bioengineered and Bioinspired Systems*, A. Rodriguez-Vazquez, D. Abbott, and R. Carmona, Eds., vol. 5119, Maspalomas, Spain, May 2003, pp. 1–12.
- [9] —, “Optic flow regulation: the key to aircraft automatic guidance,” *Robotics and Autonomous Systems*, vol. 50(4), pp. 177–194, 2005.
- [10] N. Franceschini, F. Ruffier, and J. Serres, “A bio-inspired flying robot sheds light on insect piloting abilities,” *Current Biology*, vol. 17(4), pp. 329–335, 2007.
- [11] J. Zufferey, A. Beyeler, and D. Floreano, “Autonomous flight at low altitude using light sensors and little computational power,” *International Journal of Micro Air Vehicles*, vol. 2(2), pp. 107–117, 2010.
- [12] B. Herisse, T. Hamel, R. Mahony, and F.-X. Russotto, “Landing a VTOL Unmanned Aerial Vehicle on a moving platform using optical flow,” *IEEE Transactions on Robotics*, vol. 28(1), pp. 77–89, 2012.
- [13] F. Kendoul, I. Fantoni, and K. Nonami, “Optic flow-based vision system for autonomous 3D localization and control of small aerial vehicles,” *Robotics and Autonomous Systems*, vol. 57(6-7), pp. 591–602, 2009.
- [14] L. Kerhuel, S. Viollet, and N. Franceschini, “Steering by gazing: an efficient biomimetic control strategy for visually guided micro aerial vehicles,” *IEEE Transactions on Robotics*, vol. 26(2), pp. 307–319, 2010.
- [15] F. L. Roubieu, J. Serres, N. Franceschini, F. Ruffier, and S. Viollet, “A fully-autonomous hovercraft inspired by bees; wall-following and speed control in straight and tapered corridors,” in *IEEE International Conference on Robotics and Biomimetics (ROBIO)*, Guangzhou, China, December 2012 (in press).
- [16] T. Collett, “Some operating rules for the optomotor system of a hoverfly during voluntary flight,” *Journal of Comparative Physiology A: Neuroethology, Sensory, Neural, and Behavioral Physiology*, vol. 138(3), pp. 271–282, 1980.
- [17] H. Wagner, “Flow-field variables trigger landing in flies,” *Nature*, vol. 297(5862), pp. 147–148, 1982.
- [18] M. Srinivasan, S. Zhang, M. Lehrner, and T. Collett, “Honeybee navigation en route to the goal: visual flight control and odometry,” *Journal of Experimental Biology*, vol. 199(1), pp. 237–244, 1996.
- [19] L. F. Tammero and M. H. Dickinson, “The influence of visual landscape on the free flight behavior of the fruit fly *Drosophila melanogaster*,” *Journal of Experimental Biology*, vol. 205(3), pp. 327–343, 2002.
- [20] E. Baird, M. Srinivasan, S. Zhang, R. Lamont, and A. Cowling, “Visual control of flight speed and height in the honeybee,” in *From Animals to Animals 9*, S. Nolfi, G. Baldassarre, R. Calabretta, J. Hallam, D. Marocco, J.-A. Meyer, O. Miglino, and D. Parisi, Eds. Springer Berlin / Heidelberg, 2006, vol. 4095, pp. 40–51.
- [21] J. Serres, G. Masson, F. Ruffier, and N. Franceschini, “A bee in the corridor: centering and wall-following,” *Naturwissenschaften*, vol. 95(12), pp. 1181–1187, 2008.
- [22] E. Baird, T. Kornfeldt, and M. Dacke, “Minimum viewing angle for visually guided ground speed control in bumblebees,” *The Journal of Experimental Biology*, vol. 213, pp. 1625–1632, 2010.
- [23] A. Straw, S. Lee, and M. Dickinson, “Visual control of altitude in flying *Drosophila*,” *Current Biology*, vol. 20(17), pp. 1550–1556, 2010.
- [24] G. Portelli, F. L. Roubieu, F. Ruffier, and N. Franceschini, “Honeybees’ speed depends on dorsal as well as lateral, ventral and frontal optic flows,” *PLoS ONE*, vol. 6(5), p. e19486, 2011.
- [25] M. Srinivasan, “Honeybees as a model for the study of visually guided flight, navigation, and biologically inspired robotics,” *Physiological Reviews*, vol. 91(2), pp. 413–460, 2011.
- [26] J. Gibson, *The perception of the visual world*. New York: Houghton Mifflin, 1950.
- [27] K. Hausen, “The lobula-complex of the fly: structure, function and significance in visual behaviour,” in *Photoreception and Vision in Invertebrates*, M. Ali, Ed. New York: Plenum, 1984, pp. 523–559.
- [28] N. Franceschini, “Early processing of colour and motion in a mosaic visual system,” *Neuroscience Research (Suppl. 2)*, pp. 17–49, 1985.
- [29] N. Franceschini, A. Riehle, and A. Le Nestour, “Directionally selective motion detection by insect neurons,” in *Facets of vision*, D. Stavanga and R. Hardie, Eds. Berlin: Springer-Verlag, 1989, pp. 360–390.
- [30] C. Blanes, “Appareil visuel élémentaire pour la navigation à vue d’un robot mobile autonome (Adviser: N. Franceschini),” Master’s thesis, 1986.
- [31] J. Pichon, C. Blanes, and N. Franceschini, “Visual guidance of a mobile robot equipped with a network of self-motion sensors,” in *Proceedings of SPIE: Mobile Robots IV*, W. J. Wolfe and W. H. C. Editors, Eds., vol. 1195. Bellingham, USA: Society of Photo-optical Instrumentation Engineers, 1989, pp. 44–53.
- [32] N. Martin and N. Franceschini, “Obstacle avoidance and speed control in a mobile vehicle equipped with a compound eye,” in *Proceedings of the Intelligent Vehicles Symposium (IV)*, Paris, France, October 1994, pp. 381–386.
- [33] J. Serres, D. Dray, F. Ruffier, and N. Franceschini, “A vision-based autopilot for a miniature air vehicle: joint speed control and lateral obstacle avoidance,” *Autonomous Robot*, vol. 25(1), pp. 103–122, 2008.
- [34] G. Portelli, J. Serres, F. Ruffier, and N. Franceschini, “Modelling honeybee visual guidance in a 3D environment,” *Journal of Physiology-Paris*, vol. 104(1-2), pp. 27–39, 2010.
- [35] N. Franceschini, J. M. Pichon, and C. Blanes, “From insect vision to robot vision,” *Philosophical Transactions of the Royal Society B: Biological Sciences*, vol. 337, pp. 283–294, 1992.
- [36] T. Netter and N. Franceschini, “A robotic aircraft that follows terrain using a neuromorphic eye,” in *IEEE/RSJ International Conference on Intelligent Robots and Systems (IROS)*, Lausanne, Switzerland, September 2002, pp. 129–134.
- [37] F. Expert and F. Ruffier, “Controlling docking, altitude and speed in a circular high-roofed tunnel thanks to the optic flow,” in *IEEE/RSJ International Conference on Intelligent Robots and Systems (IROS)*, Vilamoura, Portugal, October 2012 (in press).

- [38] C. Blanes, "Guidage visuel d'un robot mobile autonome d'inspiration bionique (Adviser: N. Franceschini)," Ph.D. dissertation, INP Grenoble, 1991.
- [39] J. Plett, A. Bahl, M. Buss, K. Khlenz, and A. Borst, "Bio-inspired visual ego-rotation sensor for MAVs," *Biological cybernetics*, vol. 106(1), pp. 51–63, 2012.
- [40] R. Harrison and C. Koch, "A robust analog VLSI motion sensor based on the visual system of the fly," *Autonomous Robots*, vol. 7(3), pp. 211–224, 1999.
- [41] S. Liu and A. Usseglio-Viretta, "Fly-like visuomotor responses of a robot using a VLSI motion-sensitive chips," *Biological Cybernetics*, vol. 85(6), pp. 449–457, 2001.
- [42] R. Brinkworth, P. Shoemaker, and D. O'Carroll, "Characterization of a neuromorphic motion detection chip based on insect visual system," in *5th International Conference on Intelligent Sensors, Sensor Networks and Information Processing (ISSNIP)*, Melbourne, Australia, December 2009, pp. 289–294.
- [43] P. Xu, J. Humbert, and P. Abshire, "Analog VLSI implementation of wide-field integration methods," *Journal of Intelligent & Robotic Systems*, vol. 64(3), pp. 465–487, 2011.
- [44] J. Krammer and C. Koch, "Pulse-based analog VLSI velocity sensors," *IEEE Transactions on Circuits and Systems II: Analog and Digital Signal Processing*, vol. 44(2), pp. 86–101, 1997.
- [45] G. Barrows and C. Neely, "Mixed-mode VLSI optic flow sensors for in-flight control of a Micro Air Vehicle," in *SPIE : Critical technologies for the future of computing*, vol. 4109, 2000, pp. 52–63.
- [46] P.-E. Duhamel, N. Perez-Arancibia, G. Barrows, and R. Wood, "Altitude feedback control of a flapping-wing microrobot using an on-board biologically inspired optical flow sensor," in *IEEE International Conference on Robotics and Automation (ICRA)*, Minnesota, USA, May 2012, pp. 4228–4235.
- [47] R. Chan, A. Mulla, and K. Stol, "Characterisation of low-cost optical flow sensors," in *Proceedings of the IEEE of the Australasian Conference on Robotics and Automation (ACRA)*, Brisbane, Australia, December 2010, pp. 1–8.
- [48] J. D. Jackson, D. W. Callahan, and J. Marstrander, "A rationale for the use of optical mice chips for economic and accurate vehicle tracking," in *Proceedings IEEE International Conference on Automation Science and Engineering CASE*, Scottsdale, USA, September 2007, pp. 939–944.
- [49] H. Dahmen, A. Millers, and H. A. Mallot, "Insect inspired odometry by optic flow recorded with optical mouse chips," in *Flying insects and robots*, D. Floreano, J. C. Zufferey, M. V. Srinivasan, and C. Ellington, Eds. Berlin: Springer, 2009, pp. 115–126.
- [50] S. Griffiths, J. Saunders, A. Curtis, B. Barber, T. McLain, and R. Beard, "Maximizing miniature aerial vehicles," *IEEE Robotics & Automation Magazine*, vol. 13, pp. 34–43, 2006.
- [51] A. Beyeler, J. C. Zufferey, and D. Floreano, "Vision-based control of near-obstacle flight," *Autonomous Robots*, vol. 27(3), pp. 201–219, 2009.
- [52] F. Expert, S. Viollet, and F. Ruffier, "A mouse sensor and a 2-pixel motion sensor exposed to continuous illuminance changes," in *IEEE Sensors 2011 Conference*, Limerick, Ireland, October 2011, pp. 974–977.
- [53] F. Aubépart and N. Franceschini, "Bio-inspired optic flow sensors based on FPGA: Application to Micro-Air Vehicles," *Microprocessors and Microsystems*, vol. 31, pp. 408–419, 2007.
- [54] F. Ruffier, S. Viollet, S. Amic, and N. Franceschini, "Bio-inspired optical flow circuits for the visual guidance of micro-air vehicles," in *IEEE International Symposium on Circuits and Systems (ISCAS)*, vol. 3, Bangkok, Thailand, May 2003, pp. 846–849.
- [55] M. Pudas, S. Viollet, F. Ruffier, A. Kruusing, S. Amic, S. Leppävuori, and N. Franceschini, "A miniature bio-inspired optic flow sensor based on low temperature co-fired ceramics (ltcc) technology," *Sensors and Actuators A: Physical*, vol. 133(1), pp. 88–95, 2007.
- [56] S. Viollet, F. Ruffier, T. Ray, M. Menouni, F. Aubépart, L. Kerhuel, and N. Franceschini, "Characteristics of three miniature bio-inspired optic flow sensors in natural environments," in *Fourth International Conference on Sensor Technologies and Applications (SENSORCOMM)*, Venice, Italy, July 2010, pp. 51–55.
- [57] F. Expert, S. Viollet, and F. Ruffier, "Outdoor field performances of insect-based visual motion sensors," *Journal of Field Robotics*, vol. 28(4), pp. 974–977, October 2011.
- [58] F. L. Roubieu, F. Expert, M. Boyron, B.-J. Fuschlock, S. Viollet, and F. Ruffier, "A novel 1-gram insect based device measuring visual motion along 5 optical directions," in *IEEE Sensors Conference*, Limerick, Ireland, October 2011, pp. 687–690.
- [59] F. Ruffier and F. Expert, "Visual motion sensing onboard a 50-g helicopter flying freely under complex vicon-lighting conditions," in *IEEE International Conference on Complex Medical Engineering (CME)*, Kobe, Japan, July 2012, pp. 634–639.
- [60] F. Expert, F. Roubieu, and F. Ruffier, "Interpolation based "time of travel" scheme in a visual motion sensor using a small 2d retina," in *IEEE Sensors Conference*, Taipei, Taiwan, October 2012, pp. 2231–2234.
- [61] K. Götz, "Optomotorische untersuchung des visuellen systems einiger augenmutanten der fruchtfliege drosophila," *Biological Cybernetics*, vol. 2(2), pp. 77–92, 1964.
- [62] N. Franceschini and K. Kirschfeld, "In vivo optical study of photoreceptor elements in the compound eye of drosophila," *Biological Cybernetics*, vol. 8(1), pp. 1–13, 1971.
- [63] D. G. Stavanga, "Angular and spectral sensitivity of fly photoreceptor. I. integrated facet lens and rhabdomere optics," *Journal of Comparative Physiology A: Neuroethology, Sensory, Neural, and Behavioral Physiology*, vol. 189(1), pp. 1–17, 2003.
- [64] J.-M. Pichon, "Guidage visuel d'un robot mobile autonome d'inspiration bionique," Tech. Rep., 1991.
- [65] N. Franceschini, F. Ruffier, J. Serres, and S. Viollet, *Aerial vehicles*. Vienna: In-Tech, 2009, ch. 35 : Optic flow based visual guidance: from flying insects to miniature aerial vehicles, pp. 747–770.
- [66] M. F. Land, "Visual acuity in insects," *Annual Review of Entomology*, vol. 42(1), pp. 147–177, 1997.
- [67] G. Sabiron, P. Chavent, T. Raharijaona, P. Fabiani, and F. Ruffier, "Low-speed optic-flow sensor onboard an unmanned helicopter flying outside over fields," in *IEEE International Conference on Robotics and Automation (ICRA)*, 2013 (submitted).
- [68] F. Valette, F. Ruffier, S. Viollet, and T. Seidl, "Biomimetic optic flow sensing applied to a lunar landing scenario," in *Proceedings of IEEE International Conference on Robotics and Automation (ICRA)*, Anchorage, USA, May 2010, pp. 2253–2260.



ARTICLE 2: LOW-SPEED OPTIC-FLOW  
SENSOR ONBOARD AN UNMANNED  
HELICOPTER FLYING OUTSIDE OVER  
FIELDS

CONTENTS

---

ABSTRACT . . . . .	75
I INTRODUCTION . . . . .	75
II DEFINITION OF THE GROUND-TRUTH OPTIC FLOW . . . . .	76
III PRESENTATION OF THE LOW-SPEED VISUAL MOTION SENSOR . . . . .	76
IV EXPERIMENTAL RESULTS . . . . .	78
V CONCLUSION . . . . .	81
VI ACKNOWLEDGMENT . . . . .	81
REFERENCES . . . . .	81



## Article 2: Low-speed optic-flow sensor onboard an unmanned helicopter flying outside over fields

Article published in 2013 in IEEE International Conference on Robotics and Automation (ICRA), pp. 1734-1741, Karlsruhe, Germany, 6-10 May 2013.

Authors: G. Sabiron, P. Chavent, T. Raharijaona, P. Fabiani and F. Ruffier

**I**N this paper, we broach the topic of the electronic design and outdoor testing of a visual motion sensor measuring 1-D optic flow in a range representative of a lunar landing scenario. In the previous chapter, we showed the strong potential of such bio-inspired devices which were able to compute accurately the optic flow in two opposite directions.

The following step is to show that the optic flow range might be switched to the intended application by adapting the optics, the electronics and the algorithm. This sensor has to satisfy usual constraints in terms of size, weight and power consumption in order to be embedded as a backup solution on-board a lunar lander.

The main difficulty to overcome lies in the fact that for low velocities, fewer contrasts appear in the line of sight of the sensor which means fewer information. This decreased amount of information implies that the measurements have to be very precise and the optics have to allow higher frequency contrast to be measured. The Gaussian angular sensitivity function of the photoreceptor acts as a low pass spatial filter and adds a blurring effect on the images. To measure low optic flows, this blur has to be reduced (lower cut-off frequency for the spatial low pass filter). As explained in introduction, blurring effect of the Gaussian ASF is determined by  $\Delta\rho$ , the acceptance angle. In this paper, we present the commercial off-the-shelf (COTS) components and the tuning realized to tighten the acceptance angle and finally obtain a low-speed optic flow sensor.

Based on the fusion of 5 pairs of photodiodes (as presented in the previous chapter), a robust time of travel scheme is implemented on a 2.8g sensor featuring a 16-bits microcontroller measuring the angular velocity of the images sweeping backward in the view field in the range  $1.5^\circ/s$  to  $25^\circ/s$ . We present the analog and digital processing embedded along with outdoor ground testing campaign.

Finally, the paper culminates with the experimental results of open loop testing on-board a 80kg unmanned helicopter giving satisfying results in the entire range. In order to provide enabling technologies for future space missions a particular focus has to be placed on raising the TRL. This is done here by performing test in real life conditions on a 6 degrees of freedom system as close as possible to a lunar lander platform.

Author contributions:

G.S., P.F., F.R. designed research;

G.S. performed research;

G.S., F.R., P.C contributed with technical and analytic tools;

G.S., F.R. analyzed data;

and G.S., T.R., F.R. wrote the paper.

# Low-speed optic-flow sensor onboard an unmanned helicopter flying outside over fields\*

Guillaume Sabiron<sup>1,2</sup>, Paul Chavent<sup>2</sup>, Thibaut Raharijaona<sup>1</sup>, Patrick Fabiani<sup>2</sup> and Franck Ruffier<sup>1</sup>

**Abstract**—The 6-pixel low-speed Visual Motion Sensor (VMS) inspired by insects’ visual systems presented here performs local 1-D angular speed measurements ranging from  $1.5^\circ/s$  to  $25^\circ/s$  and weighs only  $2.8g$ . The entire optic flow processing system, including the spatial and temporal filtering stages, has been updated with respect to the original design. This new lightweight sensor was tested under free-flying outdoor conditions over various fields onboard a  $80kg$  unmanned helicopter called ReSSAC. The visual disturbances encountered included helicopter vibrations, uncontrolled illuminance, trees, roads, and houses. The optic flow measurements obtained were finely analyzed online and also offline, using the sensors of various kinds mounted onboard ReSSAC. The results show that the optic flow measured despite the complex disturbances encountered closely matched the approximate ground-truth optic flow.

## I. INTRODUCTION

Finding means of sensing the optic flow onboard unmanned aerial and terrestrial vehicles has been a key research topic during the last few decades. The term “optic flow” is used to denote the angular velocity (in  $^\circ/s$ ) of the images sweeping backward across the visual field. Several flight control systems based on optic flow cues have been constructed so far for performing hazardous tasks such as hovering and landing on a moving platform [1], avoiding obstacles [2]–[4], following terrain [5] and tracking a moving target [6]. Insects are able to navigate safely in complex, unfamiliar environments thanks to the built-in abilities they have developed and improved during several hundred millions of years. Based on the findings obtained at our Laboratory on the fly’s visual system [7], several versions of the 2-pixel Local Motion Sensor (LMS) [8]–[12] were developed, using an algorithm introduced by [13], [14], which was later called the “time of travel scheme” (see [15], [16]). Several vision-based systems have been previously designed to measure the optic flow onboard UAVs (Unmanned Aerial Vehicles) [17]–[19] and in particular in the  $1.5 - 25^\circ/s$  range [3], [6], [20]. Most of these visual systems were quite demanding in terms of their computational requirements and/or their

weight or were not very well characterized, except for the optical mouse sensors [21], with which a standard error of approximately  $\pm 5^\circ/s$  around  $25^\circ/s$  was obtained in a  $\pm 280^\circ/s$  overall range. However, very few studies have been published so far to our knowledge in which visual motion sensors have been implemented and tested outdoors onboard an unmanned aircraft subject to vibrations, where the illuminance cannot be easily controlled (see [2] in the case of linear 1-D motion sensors and see [3], [5], [21], [22] in that of 2-D optic flow sensors). It therefore seemed to be worth testing the reliability of the present 1-D optic flow-based visual sensor onboard a free-flying helicopter in terms of its resolution, accuracy, sensitivity and invariance to contrast in real outdoor environments. The output signals produced by this tiny 6-pixel visual motion sensor dedicated to gauging low visual angular speeds was tested onboard the ONERA’s unmanned helicopter called ReSSAC (ReSSAC stands in French for *Recherche et Sauvetage par Système Autonome Coopérant*) travelling over an uninhabited village, where the dynamics and vibrations involved were assessed using real data acquired (see Fig. 1). In Section 2, the basic

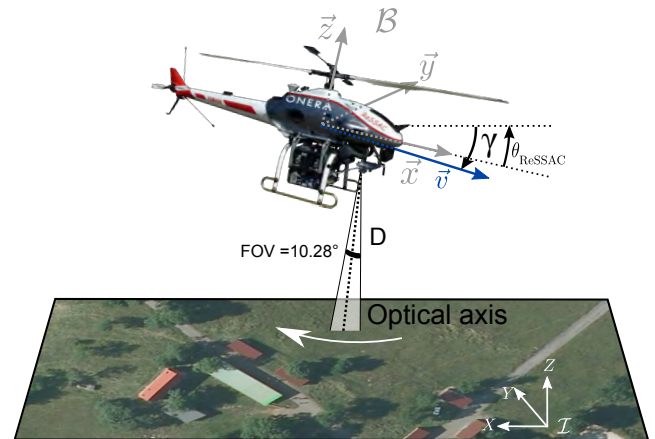


Fig. 1. 1-D optic flow generated by ReSSAC flying at the velocity  $\vec{v}$  with the pitch angle  $\theta_{ReSSAC}$ .  $D$  is the actual distance from the sensor to the ground and  $\gamma$ , the flight path angle, is defined as the angle between the local horizontal plane and the velocity vector’s orientation. Aerial view of the flight environment obtained on [geoportail.fr](http://geoportail.fr)

\* This research was supported by the French Aerospace Lab (ONERA, Systems Control and Flight Dynamics department), CNRS Institutes (Life Science; Information Science; Engineering Science and Technology), Aix-Marseille University, Astrium Satellites and ESA under NPI contract.

<sup>1</sup> G. Sabiron, T. Raharijaona and F. Ruffier are with Aix-Marseille University, CNRS, Institute of Movement Science, Biorobotics Dept., UMR7287, 13288, Marseille, France {Thibaut.Raharijaona, Franck.Ruffier}@univ-amu.fr.

<sup>2</sup> G. Sabiron, P. Chavent and P. Fabiani are with the French Aerospace Lab (ONERA, Systems Control and Flight Dynamics -DCSD-), 31055 Toulouse, France {Guillaume.Sabiron, Paul.Chavent, Patrick.Fabiani}@onera.fr

equations of the optic flow are defined. Section 3 gives a brief description of the 6-pixel 1-D visual motion device and outlines the processing algorithm as well as the optical and electrical assembly involved. The results of the outdoor experiments performed in basic forward flight condition are presented and analyzed in Section 4.

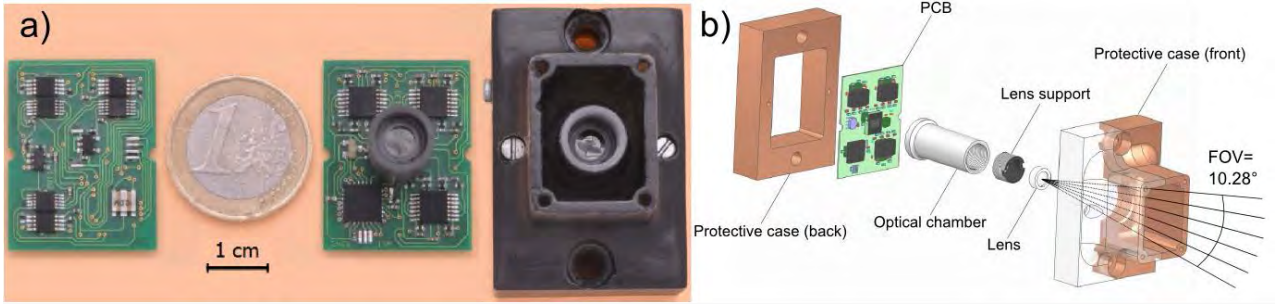


Fig. 2. (a) Top and bottom view of the electronic board (size:  $33 \times 40\text{mm}$ ) of a low-speed visual motion sensor with its lens mounted on the LSC photosensor array. The custom-made protective case is presented on the right. (b) Exploded view of the complete assembly, including the custom-made protective case (front and back), the electronic board, and the optical assembly (lens, lens support, optical chamber).

## II. DEFINITION OF THE GROUND-TRUTH OPTIC FLOW

The ground-truth optic flow  $\omega_{\text{grd-trh}}$  can be described as the sum of the two distinct components defined by [23], i.e. the translational and rotational optic flow:

$$\omega_{\text{grd-trh}} = \omega_T + \omega_R \quad (1)$$

The translational optic flow depends on the linear velocity  $v$  expressed in the inertial frame  $\mathcal{I}$  associated with the vector basis  $(\vec{X}, \vec{Y}, \vec{Z})$ , the distance from the ground  $D$  and the elevation angle  $\Phi$  (i.e., the angle between the gaze direction and the heading direction).

$$\omega_T = \frac{v}{D} \cdot \sin(\Phi) \quad (2)$$

Since the roll and pitch angles are small during the whole flight,  $D$  can be approximated as  $D \approx \frac{h}{\cos(\varphi) \cdot \cos(\theta)}$ , where  $\varphi$  denotes the roll angle,  $\theta$  denotes the pitch angle and  $h$  denotes the local ground height. The rotational optic flow depends only on the angular speed  $\Omega_j$  expressed in  $\mathcal{B}$  associated with the vector basis  $(\vec{x}, \vec{y}, \vec{z})$ , where  $j$  denotes the axis of rotation, and on the elevation angle  $\lambda$  between the gaze direction and the axis of rotation which is always  $\frac{\pi}{2}$  in the 2D case (see [24] for a graphical illustration).

$$\omega_R = \Omega_j \sin(\lambda) \quad (3)$$

In our case,  $\Phi = \theta + \gamma + \frac{\pi}{2}$  (with the sensor oriented downward,  $\gamma < 0$ ,  $\theta > 0$ ),  $\lambda = \frac{\pi}{2}$  and  $\Omega_j = \Omega_2$ , where  $\Omega_2$  is the pitch angular velocity defined in  $\mathcal{B}$ , the approximate ground-truth optic flow is therefore computed as follows:

$$\omega_{\text{grd-trh}} = \left( \frac{v}{h} \cdot \cos(\theta) \cdot \cos(\varphi) \cdot \sin\left(\theta + \gamma + \frac{\pi}{2}\right) \right) + \Omega_2 \quad (4)$$

where  $\gamma$  denotes the angle between the orientation of the velocity vector  $\vec{v}$  and the local horizontal plane. We computed the ground-truth optic flow as precisely as possible. But, since the data are coming from cartographic data previously recorded and from different sensors with different accuracy as well as different noise sources,  $\omega_{\text{grd-trh}}$  is the approximate ground-truth optic flow. Fig. 1 shows the Inertial  $\mathcal{I}$  and Body-fixed  $\mathcal{B}$  frames and the main variables defining the optic flow. During the experiments described below, the approximate ground-truth optic flow  $\omega_{\text{grd-trh}}$  was computed

using data from the inertial measurement unit (IMU), the global positioning system (GPS) and the data grabbed by a LIDAR (Light Detection And Ranging) during previous flights over the same fields.

## III. PRESENTATION OF THE LOW-SPEED VISUAL MOTION SENSOR

The new low-speed visual motion sensor consists mainly of a low-cost plastic lens placed in front of an off-the-shelf photosensor array. The photosensor used in this study, which is called the LSC, was purchased from iC-Haus: it features six photodiodes, each having a large sensitive area of  $300 \times 1600\mu\text{m}$  and an integrated preamplifier. The LSC conveys the visual signals received to a hybrid analog/digital processing algorithm, where the optic flow value  $\omega_{\text{meas}}$  is computed. The cheap, lightweight lens used here was a CAX183 from Thorlabs (focal length  $18.33\text{mm}$ , f-number 4.07). A custom-made protective case was added in order to protect the low-weight sensor and the optical assembly from unfavorable weather conditions (see Fig. 2.a for pictures and Fig. 2.b for an exploded view). The new visual motion sensor and its custom-made protective case weighed  $29.4\text{g}$ . Many of the parameters of the original visual motion detecting scheme presented in [13], [14] have been updated, especially in terms of the optical angles and the cut-off frequency of the temporal filters. The six optical axes formed by the photodiodes are separated by an interreceptor angle  $\Delta\varphi$ . By defocusing the lens (i.e., by adjusting the distance between the lens and the photosensors), we obtained Gaussian angular sensitivity functions for each photoreceptor with a correlation coefficient greater than 99% ( $R_{LSC}^2 > 0.990$  see Fig. 3), in line with what occurs in the common fly's eye [25]. These features were assessed by slowly rotating the lens in front of a point light source placed at a distance of  $85\text{cm}$ . The local 1-D angular speed  $\omega_{\text{meas}}$  measured by the sensor was defined as the ratio between the interreceptor angle  $\Delta\varphi$  and the time elapsing  $\Delta t$  between the moments when two adjacent photodiode signals reach the threshold (i.e., the time of travel of a contrast from the optical axis of one photodiode to the optical axis of the following one).

$$\omega_{\text{meas}} = \frac{\Delta\varphi}{\Delta t} \quad (5)$$

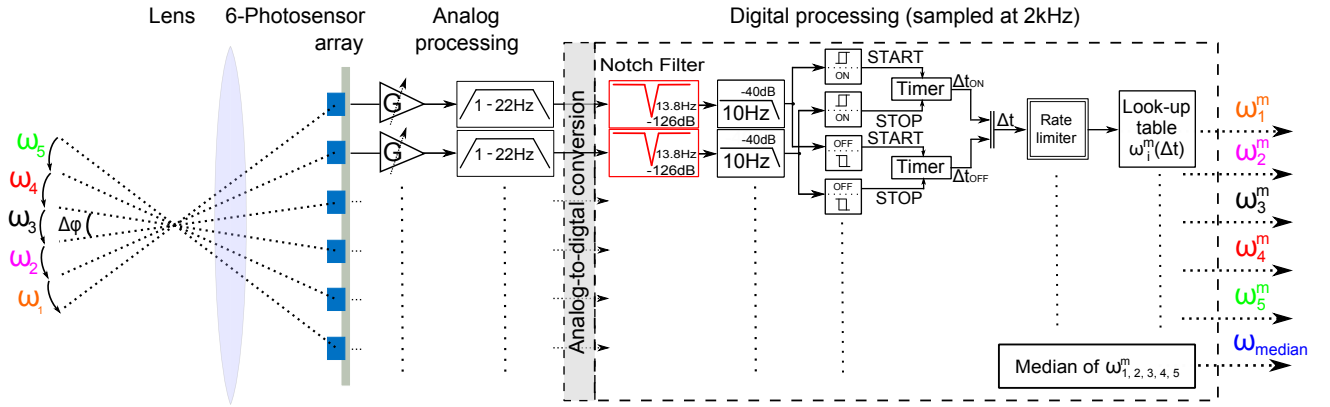


Fig. 4. General processing architecture of the low-speed visual motion sensor. First of all, the defocused lens carries out the spatial sampling and spatial low-pass filtering steps. The six photodiode signals are amplified by a programmable gain in order to increase the signal to noise ratio, before being filtered by an analog bandpass filter ( $1 - 22Hz$ ). The digital stage begins with a second order fixed-point notch filter centered on the main rotor frequency of ReSSAC,  $13.8Hz$ . It is followed by a second order fixed-point low pass filter with a cut-off frequency set at  $10Hz$ . A hysteresis thresholding process is associated with the computation of the time  $\Delta t$  elapsing between two adjacent signals (with either ON or OFF contrasts). Lastly, after an outlier filtering step, the output signal of the 1-D visual motion sensor is obtained from a precomputed look-up table and the median value is calculated.

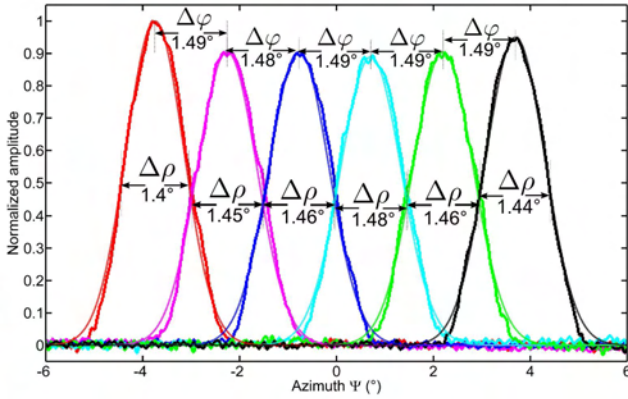


Fig. 3. Gaussian angular sensitivity functions of the LSC photosensor array with a CAX183 plastic aspherical lens, raw data (thick curves) and approximate Gaussian-shaped fit (thin curves). By adjusting the distance between the lens and the LSC photosensor, we obtained a correlation coefficient almost equal to 1 ( $R_{LSC}^2 > 0.990$ ), and a  $\Delta\varphi$  value approximately equal to  $\Delta\rho$ .

In [11], the measurement range of the sensor covered a large range of high speeds from  $50^\circ/s$  to  $300^\circ/s$ , whereas the present study focused on low velocities giving a range of  $1.5^\circ/s$  to  $25^\circ/s$ , which is more than tenfold slower. In order to stay in the same range of  $\Delta t$ , whose accuracy of measurement depends on the microcontroller's sampling frequency, we therefore had to narrow  $\Delta\varphi$ .  $\Delta\varphi$  corresponds to the angle separating two adjacent photodiodes optical axis: it depends on the focal lens, on the pitch (distance between the center of two adjacent photodiodes) and also on the distance from the photodiode plane to the focal point which is the easiest setting to adjust.

The large 18.33mm focal length increases the defocalizing effects of the lens, giving a suitably small mean interreceptor angle of  $\overline{\Delta\varphi} = 1.488^\circ$ . The second advantage of the defocusing process is that it adds a blurring effect giving

Gaussian-shaped angular sensitivity functions and change  $\Delta\rho$ . As found to occur in some diurnal insects [26],

$$\Delta\varphi = \Delta\rho \quad (6)$$

Achieving a tight  $\Delta\rho$  made it possible for the sensor to respond to higher spatial frequency contrasts. The acceptance angle, defined by  $\Delta\rho$ , acts like an optical low pass spatial filter.

We eventually reached  $1.4 \geq \Delta\varphi \approx \Delta\rho < 1.5^\circ$ , corresponding to a field of view in the direction of the visual motion sensor of  $10.28^\circ$  ( $\sum_{i=1}^5 \Delta\varphi_i + \frac{\Delta\varphi_1}{2} + \frac{\Delta\varphi_5}{2}$ ). Table I gives the optical characteristics of the sensor. The general processing

Focal length of the lens CAX183 [mm]	18.33
$f_{number}$ of the lens [#]	4.07
Angular velocity range [ $^\circ/s$ ]	[1.5; 25]
Field of view of a single photodiode [ $^\circ$ ]	$2.90 \times 15.44$
Sensitivity [ $^\circ/s/LSB$ ]	$4.58 \text{ e-}5$
Mean interreceptor angle $\overline{\Delta\varphi}$ [ $^\circ$ ]	1.488
Mean acceptance angle $\overline{\Delta\rho}$ [ $^\circ$ ]	1.448
Photodiode size [ $\mu m$ ]	$300 \times 1,600$
Pixel pitch [ $\mu m$ ]	420
Resolution [ $^\circ/s$ ] [min; max]	[0.01; 0.21]
Mass of the visual motion sensor in a stand-alone version [g]	2.8

TABLE I

CHARACTERISTICS OF THE NEW LOW-SPEED VISUAL MOTION SENSOR

algorithm consists of two parts: an analog processing part converts the six visual signals into electrical signals with a high signal to noise ratio, and the digital processing part then simultaneously computes five optic flow values plus the median value (see Fig. 4). The analog processing begins with a programmable gain connected to the microcontroller via a SPI communication bus [12]. A pass-band filter then differentiates the visual signal and acts as an anti-aliasing filter.

The digital processing algorithm starts with a second order

fixed-point notch filter centered on the ReSSAC's main rotor frequency. The center frequency of the filter is  $f_0 = 13.8Hz$  with a Q-factor  $Q = 6.9$  at a sampling frequency  $f_s = 500Hz$ . Its transfer function, which has been defined in [27], is as follows:

$$H_{notch}(z) = b \frac{1 - 2 \cos(\omega_0) z^{-1} + z^{-2}}{1 - 2b \cos(\omega_0) z^{-1} + (2b - 1)z^{-2}} \quad (7)$$

with

$$b = \frac{1}{1 + \frac{\sqrt{1-G_B^2}}{G_B} \tan(\frac{\Delta\omega}{2})}$$

where  $\Delta\omega$  is the full width at a level  $G_B^2$  and  $\omega_0$  is the center frequency. We chose  $\omega_0 = 2 \cdot \pi \frac{f_s}{f_0}$ ,  $\Delta\omega = 2 \cdot \pi \frac{\Delta f}{f_s}$  with  $\Delta f = 2Hz$  and  $G_B^2 = -3dB$ . As the visual angular speed  $\omega_{meas}$  is quite low, the temporal frequency  $f_t$  of the visual signal (which consists of contrasts) is also quite low, as expressed by the following equation [28]:

$$f_t = \omega_{meas} \cdot f_{spatial}$$

where  $f_{spatial}$  is the spatial frequency (in *cycles/°*) associated with the contrasting pattern. Therefore, a second order fixed-point low pass filter was used to enhance the signal to noise ratio by removing the noise remaining at frequencies of more than  $10Hz$ .

The algorithm called the "Time of travel scheme" implemented here consists mainly of a hysteresis thresholding process with separate ON and OFF pathways [13], [14], [29]–[31] followed by the  $\Delta t$  computation, the result of which is fed into a corresponding table. Lastly, the five simultaneously computed optic flows  $\omega_i^m$  are combined by the median operator in order to increase the robustness and the refresh rate of the output [31].

The microcontroller used for this purpose is a dsPIC33FJ128GP802 working at a sampling frequency of  $2kHz$ , except for the digital filters, which are sampled at a rate of  $500Hz$ . Special efforts were made to optimize the algorithm, and a computational load of only 17% was eventually obtained.

#### IV. EXPERIMENTAL RESULTS

##### A. Dynamic visual motion characteristics on the ground

The characteristics of the present visual motion sensor (VMS) were assessed by performing optic flow measurements under controlled motion conditions (orientation and velocity) outdoors on the ground. Pure rotational motion was applied to the sensor with angular speed variations ranging from  $1^\circ/s$  to  $20^\circ/s$  using a previously described outdoor ground-based set-up [11]. The triangular response pattern obtained corresponds closely to the reference angular speed (see Fig. 5). It can therefore be said that this tiny 6-pixels sensor is able to accurately compute the 1-D visual angular speed within its operating range. The refresh rate is defined as the ratio between the total number of new measurements of each  $\omega_i$  occurring within the acceptable range [ $1.5^\circ/s$  -  $25^\circ/s$ ] and the time elapsing. The median value is delivered at  $2 kHz$  (output data rate) even if the measure is not

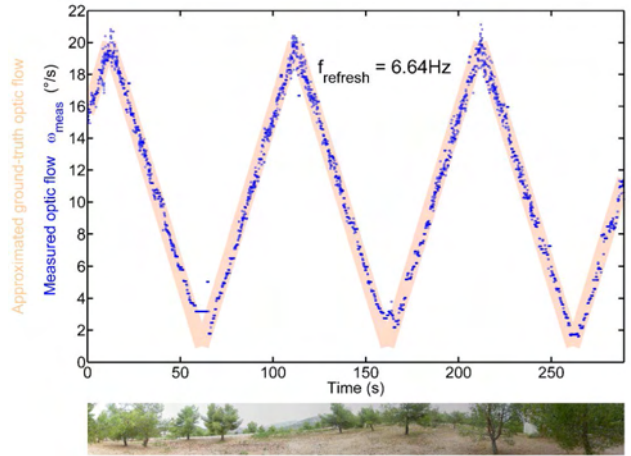


Fig. 5. Dynamic outdoor response of the low-speed VMS (blue), as compared with the ground-truth optic flow (red). The visual motion sensor was rotated by means of a conveyor belt driven by a stepping motor (103H5208-0440 from Sanyo-Denki) [11]. Rotations from  $1^\circ/s$  to  $20^\circ/s$  were applied to the sensor, which is designed to operate in the  $1.5^\circ/s$  to  $25^\circ/s$  range. The optic flow measured closely matched the reference signal, with a refresh rate of  $6.64Hz$ . Since no synchronization signal was available, the ground-truth optic flow has been roughly synchronized here.



Fig. 6. The ONERA ReSSAC Unmanned Autonomous Helicopter before takeoff, featuring the on-board low-speed VMS mounted at the front end looking downward

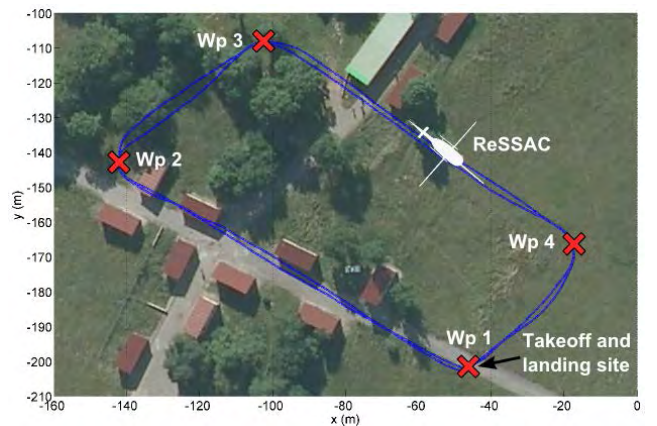


Fig. 7. Top view of the trajectory taken by ReSSAC, as defined by 4 GPS waypoints. The UAV flew over a complex textured environment containing houses, trees, roads and a sloping field. The UAV was controlled manually during the takeoff and landing phases (these parts of the trajectory are not shown on the figure). Aerial view obtained on geoportail.fr.

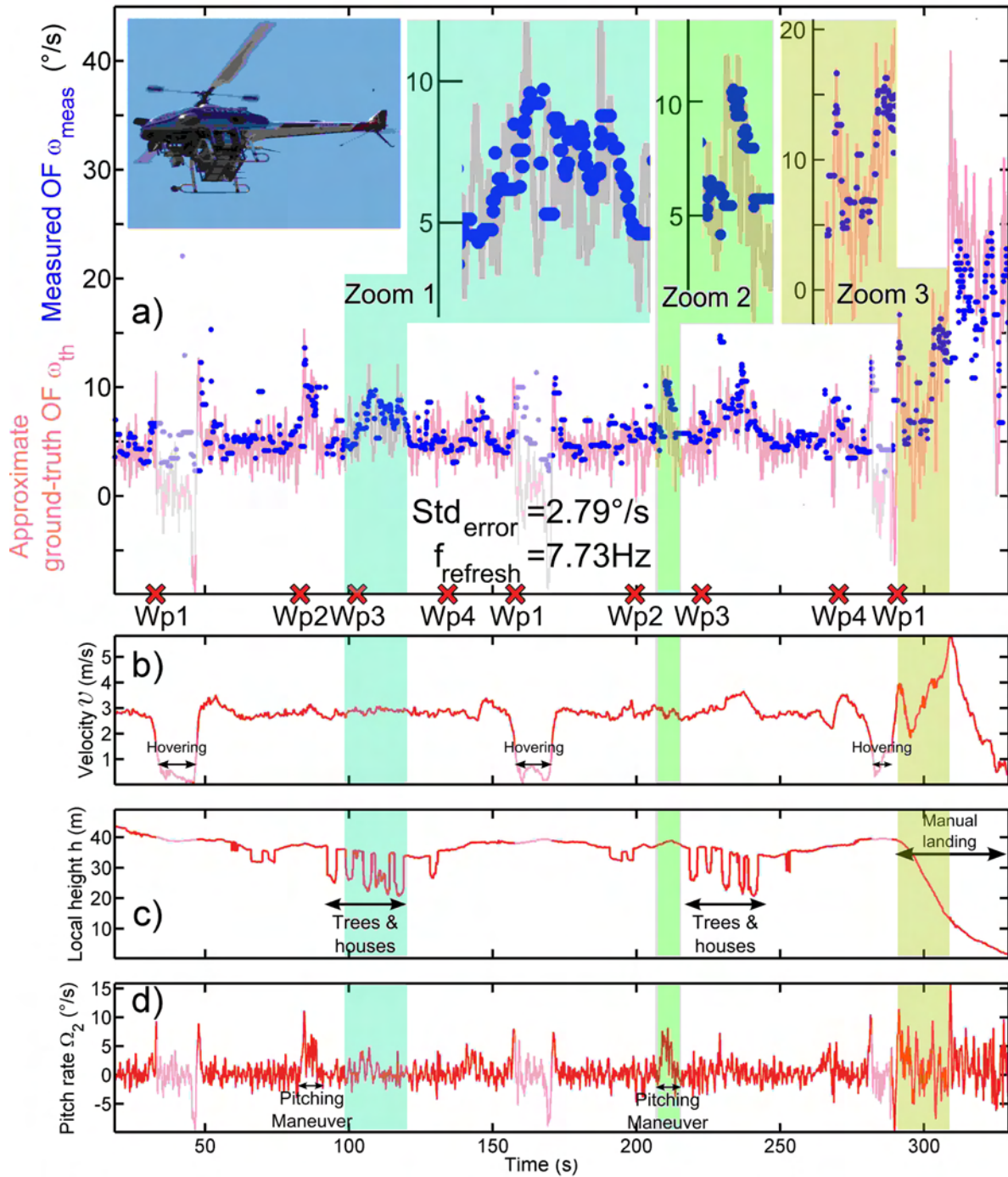


Fig. 8. Low-speed visual motion sensor and flight data sensed on-board the ReSSAC UAV. (a) Ground-truth optic flow (see (4)) (red) and measured optic flow  $\omega_{meas} = \Delta\varphi/\Delta t$  (blue dots). Despite the strong variations mainly due to vibrations, the low-speed visual motion sensor's output closely matched the ground-truth optic flow, giving a standard deviation of  $2.79^\circ/s$  and a refresh rate of  $7.73Hz$ . The first area highlighted (Zoom 1) shows the effects of strong variations in the local height due to the successive trees and houses: the low-speed VMS sensed these height variations. After reaching Wp2 in the second lap (inside the second area highlighted), one can see a strong pitch angular speed peak, which is again directly reflected in the low-speed VMS measurement signal (Zoom 2). Lastly, during the manual landing phase (Zoom 3), as the forward speed increased and the local height decreased, both the ground-truth and sensed optic flows increased sharply and the measurements were still accurate (the standard deviation was not computed during the landing phase or while hovering because the ground-truth optic flow was not entirely in the sensor's measurement range). (b) Norm of the velocity vector during the trajectory. (c) Local ground height measured by combining GPS data (OEM4 G2 from NovAtel) and previously mapped LIDAR data (Sick LDMRS 400001). The nominal height was around 40 m. But due to the variable relief, the local height often changed suddenly by 15 meters. (d) Pitch rate of ReSSAC as measured by the IMU.

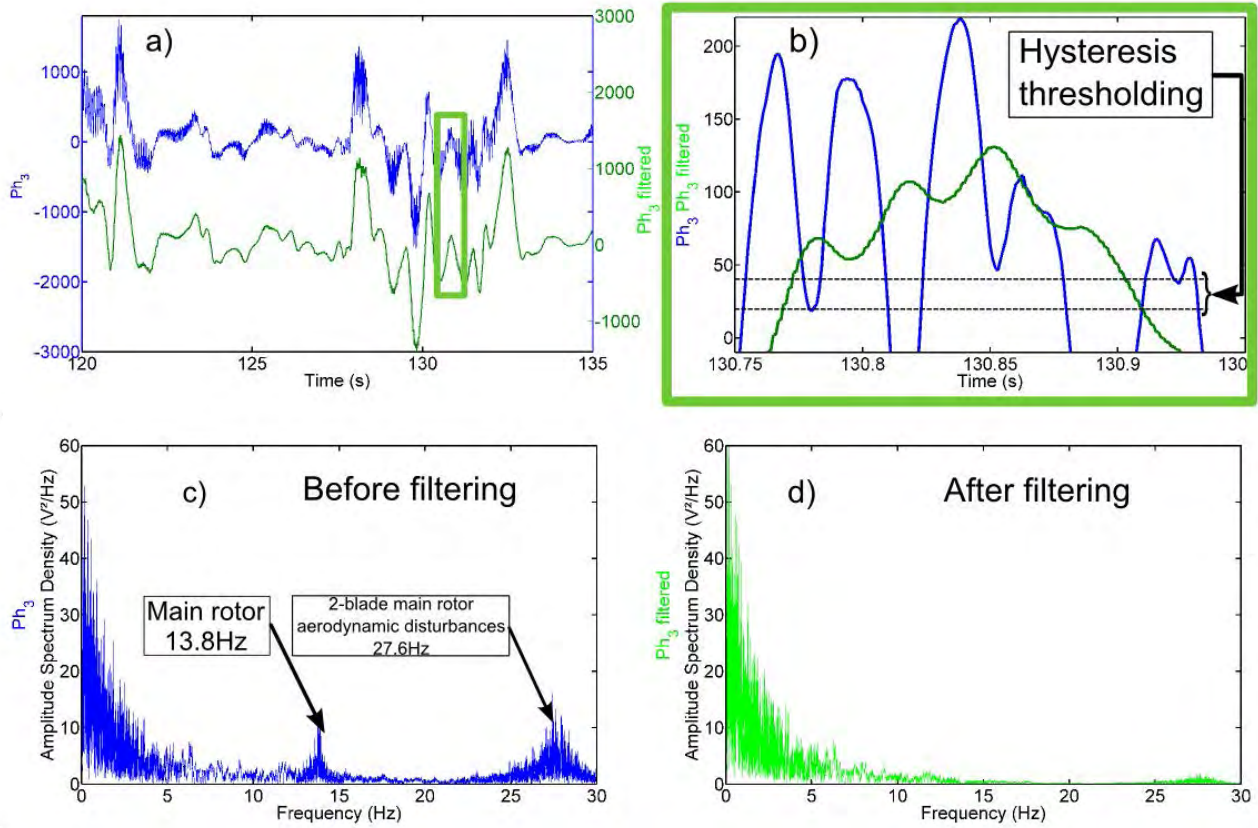


Fig. 9. Visual signal before and after the digital fixed point filtering step (notch and low pass filter): (a) Large view of the signals before (blue) and after (green) the filtering. (b) Zoom on the signals. Without any filtering, the visual motion sensor would have detected contrasts whenever, the signal was greater than 40 and then decreased to less than 20 (because of the hysteresis thresholding). One can see that the filtered signal detected only one contrast during this phase. (c) Power spectrum of the 3rd photosensor sampled at 1kHz before (blue) and after the filtering (green). The rotor's main rotational speed was 828 rpm (i.e. 13.8Hz): this disturbance was filtered out by adding a second-order notch filter.

refreshed, that is why the refresh rate metric is needed to evaluate the performance of the sensor. The mean refresh rate achieved during the dynamic performances evaluation was  $f_{refresh} = 6.64Hz$ : this value depends on the richness of the visual environment, as well as on the actual angular speed.

### B. Free-flying helicopter's trajectories

The low-speed VMS performances were studied on a free-flying UAV during forward flight over fields. The ONERA's ReSSAC unmanned helicopter was used to test the sensor's dynamic responses. The characteristics of ReSSAC (Yamaha Rmax) in terms of the mass balance have been described in [32]. Its mass, its flight envelope and the vibration dynamics due to the main rotor's rotational speed presented us with quite a challenging ground-truth optic flow profile. The low-speed visual motion sensor was embedded at the front end of ReSSAC pointing directly downward with a clear field of view (see Fig. 6). The sensor was connected to the embedded PC (pip22 from MPL) via a serial port. VMS, IMU and GPS data were logged locally onto the embedded PC with a system clock timestamp for subsequent processing purposes. A WiFi network was used to set and adapt the programmable

gain and the threshold value during the experiments, via a graphical user interface displaying raw visual signals and optic flow signals on the ground station. The trajectory to be taken was set offline in the form of a parallelogram-like shape defined by four GPS waypoints called Wp1 to Wp4 (see Fig. 7). The experiment was carried out over an uninhabited village providing a very rich and complex visual environment consisting of various components:

- From Wp1 to Wp2: roads and buildings,
- From Wp2 to Wp3: trees,
- From Wp3 to Wp4: trees, road, a sloping green field,
- From Wp4 to Wp1: road, a green field.

Data logging started at the beginning of the scenario and ended after landing. During the automatic phase, ReSSAC's flight envelope was tightened to ensure the helicopter's safety, whereas in the manual mode, the human pilot was able to reach greater speeds at lower heights. According to (4), increasing the velocity while decreasing the altitude will increase the ground-truth optic flow  $\omega_{grd-trh}$ . The flight was performed in South-western France in mid-July around 5pm on a bright sunny day: the mean illuminance was approximately  $10000lx$ .

### C. Free-flying results

Fig. 8 shows an accurate response of the low-speed visual motion sensor mounted onboard the unmanned ReSSAC helicopter. Despite the complex ground-truth optic flow, the visual motion sensor responded appropriately to the visual stimuli. The standard deviation of the error between the approximate ground-truth optic flow  $\omega_{grd-trh}$  and the measured optic flow  $\omega_{meas}$  was less than  $2.8^\circ/s$ , which is quite low. The standard deviation was computed only during automatic flight phases. Measurements performed during hovering flight phases (i.e.  $\omega_{grd-trh}$  outside the measurement range) were rejected offline (white blurred zones). The refresh rate  $f_{refresh}$  was greater than  $7.7Hz$ , which is even slightly higher than in the dynamic measurements performed during a rotating motion on ground-based set-up (see Fig. 5). Fig. 8.b, 8.c, 8.d giving the velocity norm, the local ground height and the pitch angular speed, show how well the sensor responded to its visual environment. Three areas of particular interest (highlighted areas in Fig. 8) emerge from these results:

Zoom 1: ReSSAC helicopter flying over houses and trees, giving several sudden changes in the local height (nominal height during flight: 35-40m). Once again, the low-speed VMS accurately sensed these height variations and yielded similar values to the approximate ground-truth value.

Zoom 2: ReSSAC helicopter pitched forward after Wp2 (see Fig. 8.d), which produced a series of high angular speed variations around  $5^\circ/s$ . These variations in the visual motions are directly reflected in the low-speed VMS measurement output signal, which closely matched the approximate ground-truth optic flow pattern. This rotational optic flow occurs on the right hand side of (4) and corresponds to  $\Omega_2$ .

Zoom 3: ReSSAC helicopter was piloted manually during the landing phase, which significantly increased the speed and decreased the height. Both the approximate ground-truth and sensed optic flows reflect this sharp increase. The results obtained during this phase are interesting because they show the performances of the visual sensor over its whole measurement range.

The robust and accurate performances observed during this experiment show that the low-speed visual motion sensor is highly suitable for use in many high-scaled robotic applications. A close look at the raw (blue) and filtered (green) photodiode signals (see Fig. 9.a-d) shows the value of the filtering stage, which reduces the noise induced by the helicopter's main rotor. One can see the high spectrum density occurring around  $13.8Hz$  and  $27.6Hz$  on the raw signal (blue) and the low spectrum density on the filtered one (green) (see Fig. 9.c and 9.d). The whole body of the rotorcraft was vibrating continuously around its equilibrium point at the higher angular speeds, resulting in fairly strong oscillations in the unfiltered visual signals. The noise due to

rotor-vortex interactions in the main 2-blade rotor (see [33] for further details about helicopters' aerodynamic disturbances) was even stronger than the main rotor's fundamental frequency, and it is therefore proposed to add another dedicated notch filter centered on  $27.6Hz$  in future studies.

## V. CONCLUSION

A 6-pixel visual motion sensor dedicated to low visual angular speeds was developed and successfully tested outdoors onboard a free flying unmanned helicopter under real-life dynamic and vibratory conditions as a means of measuring local 1-D angular speeds ranging from  $1.5^\circ/s$  to  $25^\circ/s$ . The results obtained here show that the 6-pixel visual motion sensor is able to accurately sense low visual angular speeds, giving quite frequently refreshed measurements even at high heights over an unknown complex outdoor environment. Among the large range of potential applications to which this 6-pixel sensor lends itself, landing on extra-planetary bodies immediately comes to mind. Soft lunar landing involves a similar optic flow range to that studied here [34]–[36], with demanding final conditions in terms of the longitudinal and vertical velocities, which makes this new visual motion sensor a good candidate for applications of this kind, given the promising results obtained here. In conclusion, this lightweight, low cost, low power and minimalist visual motion sensor also seems to be well suited for equipping UAV helicopter autopilots designed to perform hazardous tasks such as outdoor landing/takeoff and obstacle avoidance.

## VI. ACKNOWLEDGMENTS

We are most grateful to S. Viollet, L. Burlion, E. Kervendal, E. Bornschlegl, F. Roubieu and F. Expert for their fruitful suggestions and comments during this study. We thank H. de Plinval, A. Amiez and V. Fuertes for the successful flight of ReSSAC, T. Rakotomamonjy and A. Piquereau for their expertise in helicopter dynamics, M. Boyron for his assistance with the electrical design, J. Diperi for his involvement in the mechanical design and J. Blanc for improving the English manuscript.

## REFERENCES

- [1] B. Hérisse, T. Hamel, R. Mahony, and F.-X. Russotto, "Landing a VTOL unmanned aerial vehicle on a moving platform using optical flow," *IEEE Transactions on Robotics*, vol. 28, no. 1, pp. 77–89, February 2012.
- [2] G. Barrows and C. Neely, "Mixed-mode VLSI optic flow sensors for in-flight control of a Micro Air Vehicle," in *in SPIE : Critical technologies for the future of computing*, vol. 4109, San Diego, CA, USA, Aug 2000, pp. 52–63.
- [3] S. Griffiths, J. Saunders, A. Curtis, B. Barber, T. McLain, and R. Beard, "Maximizing miniature aerial vehicles," *IEEE Robotics & Automation Magazine*, vol. 13, pp. 34–43, 2006.
- [4] A. Beyeler, J. Zufferey, and D. Floreano, "OptiPilot: control of take-off and landing using optic flow," in *European Micro Aerial Vehicle Conference (EMAV)*, vol. 27, Delft, Netherlands, September 2009.
- [5] M. Garratt and J. Chahl, "Vision-based terrain following for an unmanned rotorcraft," *Journal of Field Robotics*, vol. 25, pp. 284–301, 2008.
- [6] F. Kendoul, K. Nonami, I. Fantoni, and R. Lozano, "An adaptive vision-based autopilot for mini flying machines guidance, navigation and control," *Autonomous Robots*, vol. 27, pp. 165–188, 2009.

- [7] N. Franceschini, A. Riehle, and A. Nestour, *Facets of vision*. Springer, 1989, ch. Directionally selective motion detection by insect neurons, pp. 360–390.
- [8] N. Franceschini, J. Pichon, and C. Blanes, “From insect vision to robot vision,” *Philosophical Transactions of the Royal Society of London*, vol. 337, pp. 283–294, 1992.
- [9] F. Ruffier and N. Franceschini, “Visually guided micro-aerial vehicle: automatic take off, terrain following, landing and wind reaction,” in *IEEE International Conference on Robotics and Automation (ICRA)*, vol. 3, April 2004, pp. 2339 – 2346.
- [10] N. Franceschini, F. Ruffier, and J. Serres, “A bio-inspired flying robot sheds light on insect piloting abilities,” *Current Biology*, vol. 17, pp. 329–335, 2007.
- [11] F. Expert, S. Viollet, and F. Ruffier, “Outdoor field performances of insect-based visual motion sensors,” *Journal of Field Robotics*, vol. 28, pp. 529–541, 2011.
- [12] F. Ruffier and F. Expert, “Visual motion sensing onboard a 50-g helicopter flying freely under complex VICON-lighting conditions,” in *International Conference on Complex Medical Engineering*, Kobe, Japan, July 2012, pp. 634–639.
- [13] C. Blanes, “Appareil visuel élémentaire pour la navigation à vue d’un robot miobile autonome,” (Advisor: N. Franceschini), Neurosciences, Univ. Aix-Marseille II, 1986.
- [14] J.-M. Pichon, C. Blanes, and N. Franceschini, “Visual guidance of a mobile robot equipped with a network of self-motion sensors,” in *SPIE Conf. on Mobile Robots IV*, W. Wolfe and W. Chun, Eds., vol. 1195, Bellingham, U.S.A., 1989, pp. 44–53.
- [15] R. Benson and T. Delbrück, *Direction selective silicon retina that uses null inhibition*, D. S. Touretzky, Ed. San Mateo, CA: Morgan Kaufman, 1992.
- [16] R. Moeckel and S.-C. Liu, “Motion detection circuits for a time-to-travel algorithm,” in *IEEE International Symposium on Circuits and Systems (ISCAS)*, may 2007, pp. 3079–3082.
- [17] W. Green, P. Oh, and G. Barrows, “Flying insect inspired vision for autonomous aerial robot maneuvers in near-earth environments,” in *International Conference on Robotics and Automation (ICRA)*, vol. 3, april-1 may 2004, pp. 2347–2352 Vol.3.
- [18] S. Hrabar, G. Sukhatme, P. Corke, K. Usher, and J. Roberts, “Combined optic-flow and stereo-based navigation of urban canyons for a uav,” in *International Conference on Intelligent Robots and Systems (IROS)*, aug. 2005, pp. 3309–3316.
- [19] J. Conroy, G. Gremillion, B. Ranganathan, and J. Humbert, “Implementation of wide-field integration of optic flow for autonomous quadrotor navigation,” *Autonomous Robots*, vol. 27, pp. 189–198, 2009.
- [20] Y. Watanabe, P. Fabiani, and G. Le Besnerais, “Simultaneous visual target tracking and navigation in a gps-denied environment,” in *International Conference on Advanced Robotics (ICAR)*, june 2009, pp. 1–6.
- [21] A. Beyeler, J. C. Zufferey, and D. Floreano, “Vision-based control of near-obstacle flight,” *Autonomous robots*, vol. 27, pp. 201–219, 2009.
- [22] F. Kendoul, I. Fantoni, and K. Nonamib, “Optic flow-based vision system for autonomous 3d localization and control of small aerial vehicles,” *Robotics and Autonomous Systems*, vol. 57, pp. 591–602, 2009.
- [23] J. Koenderink and A. Doorn, “Facts on optic flow,” *Biological Cybernetics*, vol. 56, pp. 247–254, 1987.
- [24] F. Ruffier, “Pilote automatique biomimétique. Système générique inspiré du contrôle visuomoteur des insectes pour: le suivi de terrain, la réaction au vent et l’atterrissage automatiques d’un micro-aéronef,” Ph.D. dissertation, Institut National Polytechnique de Grenoble, 2004.
- [25] K. Götz, “Optomotorische untersuchung des visuellen systems einiger augenmutanten der fruchtfliege drosophila,” *Biological Cybernetics*, vol. 2, pp. 77–92, 1964.
- [26] M. F. Land, “Visual acuity in insects,” *Annual Review of Entomology*, vol. 42, pp. 147–177, 1997.
- [27] S. J. Orfanidis, *Introduction to signal processing*, P.-H. Inc, Ed. Prentice-Hall, Inc. Upper Saddle River, NJ, USA, 1995.
- [28] A. Landolt and A. Mitros, “Visual sensor with resolution enhancement by mechanical vibrations,” *Autonomous Robots*, vol. 11 (3), pp. 233–239, 2001.
- [29] F. Ruffier, S. Viollet, S. Amic, and N. Franceschini, “Bio-inspired optical flow circuits for the visual guidance of micro air vehicles,” in *IEEE International Symposium on Circuits and Systems (ISCAS)*, vol. 3, Bangkok, Thailand, 2003, pp. 846–849.
- [30] F. Ruffier and N. Franceschini, “Optic flow regulation: the key to aircraft automatic guidance,” *Robotics and Autonomous Systems*, vol. 50, pp. 177–194, 2005.
- [31] F. Roubieu, F. Expert, M. Boyron, B. Fuschlock, S. Viollet, and F. Ruffier, “A novel 1-gram insect based device measuring visual motion along 5 optical directions,” in *IEEE Sensors conference*, Limerick, Ireland, 2011, pp. 687–690.
- [32] Y. Watanabe, C. Lesire, A. Piquereau, P. Fabiani, M. Sanfourche, and G. Le Besnerais, “The ONERA ReSSAC unmanned autonomous helicopter: Visual air-to-ground target tracking in an urban environment,” in *American Helicopter Society 66th Annual Forum*, Phoenix, AZ, USA, 2010.
- [33] A. Bramwell, G. Done, and D. Balmford, *Helicopter Dynamics*, 2nd ed. London: AIAA, Butterworth-Heinemann, 1986.
- [34] D. C. Cheatham, F. V. Bennett, and T. M. Branch, “Apollo lunar module landing strategy,” in *Proceedings of the Apollo Lunar Landing Mission Symposium*, 1966.
- [35] F. Valette, F. Ruffier, S. Viollet, and T. Seidl, “Biomimetic optic flow sensing applied to a lunar landing scenario,” in *International Conference on Robotics and Automation (ICRA)*, 2010, pp. 2253–2260.
- [36] D. Izzo, N. Weiss, and T. Seidl, “Constant-optic-flow lunar landing: Optimality and guidance,” *Journal of Guidance, Control, and Dynamics*, vol. 34, pp. 1383–1395, 2011.

## CONCLUSION

In this part, we addressed the design and validation of two versions of optic flow sensors based on the “Time of Travel” scheme. In line with previous work on LMS, we enhanced the capabilities of such sensors in two different ways:

1. Firstly, in Roubieu et al. (2013), thanks to two sensory fusion methods, we proposed a 1-gram optic flow sensor composed of only 6 pixels able to detect the optic flow in two opposite directions.
  - i The first fusion consist in using the median value of the outputs of 5 LMSs giving simultaneously an angular speed measurement in the  $[25^\circ/s; 350^\circ/s;]$  range. The median operator allows to improve robustness to outliers and measurement noise but also increase the refresh rate of the output. Indeed, the standard deviation of the error was improved more than 1.7-fold and the refresh rate more than 4-fold.
  - ii The second improvement comes from the ability to measure the optic flow in two opposite directions. Based on Blanes (1991), we implemented 10 LMSs on a single 16-bit microcontroller, 5 measuring optic flow in one direction, and 5 in the opposite direction, the maximum value of the two medians gave the correct signed optic flow. Experiments performed indoors showed the robustness and accuracy of the solution since the device made no errors on the sign determination.
2. Secondly, in Sabiron et al. (2013), the challenge of low speed optic flow measurements based only on 6 pixels was addressed. We presented the optic and electronic design along with the tests results obtained during a flight campaign on a rotorcraft. Thanks to a higher spatial filtering cut-off frequency than on other optic flow sensors developed in our laboratory, we managed to measure with a high accuracy and a high output refresh rate very low values of optic flow representative of the approach phase of a lunar landing. The sensor measured optic flow in the range  $[1.5^\circ/s; 25^\circ/s;]$ . Experiments performed onboard of a free flying helicopter

showed the precision of the measurement with respect to the ground truth optic flow despite the strong disturbances generated by the rotors, the complex flight dynamics and a uneven ground.

We showed that LMSs device can be upgraded and thus provide a very good candidate for various kinds of application ranging from micro aerial vehicles, planetary landing thanks to their very light weight (only a few grams), small size and low energy requirements.

The next step would be to test in real life conditions performances of such minimalistic device in a closed loop onboard an unmanned airborne vehicle featuring six degrees of freedom.

## **Part 3**

# **Guidance Navigation and Control based on minimalistic optic flow sensors**



## INTRODUCTION

**H**ERE we address the core challenge of the development of a full GNC strategy based firstly on optic flow and IMU measurements and secondly only on optic flow to achieve soft lunar landing.

Based on earlier findings regarding biorobotics discussed in introduction, we adapted the bio-inspired framework of optic flow regulation to this challenging aerospace application.

In (Hérissé et al., 2012), authors astutely point out the fact that:

*[...] the flight regime of insects is highly damped due to their high drag to mass ratios. The control strategies that have been observed in the various biological studies do not necessarily generalize to high-inertia, low-drag aerial vehicles.*

which is even more true on another planet without atmosphere. Previous studies have shown that optic flow regulation could be successfully applied for UAVs on earth which have a relatively high drag to mass ratio compared to a lunar lander. However, studies performed by Izzo, de Croon and their colleagues showed that from an energy consumption perspective, constant optic flow was not the best suited strategy. Furthermore, winged insects actively compensate for rotational motion in order to sense only translational optic flow. This strategy is not possible with miniature sensors since a gimbal system could be heavier than the sensor itself. In our targeted application, we had to design and adapt each block of the GNC architecture to cope with this challenge and, at the same time, fulfill the demanding embedded system-related requirements which are focused on cheaper, lighter, less energy-consuming devices.

The ultimate goal is to extract all necessary information from the optic flow to be able to control all the lander's degrees of freedom which consists in the attitude (limited to the pitch dynamics in the case of the considered planar scenario) and the

translational states (position and velocity).

Due to the nature of the optic flow cue, relative navigation is worth considering since the optic flow contains information about relative attitude, relative velocity (which is absolute in the case of a static environment) and vicinity to obstacles. The underlying principle behind optic flow based regulation is that if we know how fast images have to sweep during a nominal landing it is thus possible to compute the required braking and torque forces to cope with the expected angular velocity of the images of the surrounding environment no matter the surface topology.

A particular attention was placed on enhancing realism of simulation. In part 2, we demonstrated the feasibility of developing sensors dedicated to sense the optic flow in a range representative of lunar landing scenario. Unfortunately, the full GNC architecture could not be validated experimentally due to the low availability of the test platforms and the time-consuming aspect of in-flight experiments. The choice was made to propose extended simulations using the actual sensor code and the entire image processing through the use of the PANGU software. On the one hand it allows realistic software in the loop simulations, which further pushes the validation of our solution. On the other hand, for closed-loop simulations, it requires hours of processing on a powerful computer, which prevents from the use of repeated random sampling methods such as Monte-Carlo methods (Metropolis and Ulam, 1949) often used to analyze performances and robustness to initial conditions and uncertainties in space applications.

We could have chosen to perform only theoretical simulations (use of additive modeled noise on the visual feedback), which might have led us to improved GNC architecture. The choice was made to focus on realistic simulations to prove the feasibility of such bio-inspired concept instead of enhancing control laws, navigation filters or guidance strategies.

In the next chapter we lay the foundations for optic flow based planetary landing in terms of GNC architecture.

- The first paper introduces a full guidance navigation and control framework with a focus on the fuel consumption aspect. The guidance produces offline an optimal trajectory. Thanks to the nonlinear control laws fed with the estimates of  $\omega_x$  and  $\omega_z$  this optimal trajectory is tracked. The navigation filters carries out the data

---

fusion of 20 VMS outputs after derotation. The landing scenario is then validated on PANGU.

- The second paper presents an improved control scheme ensuring asymptotical convergence of optical flows toward their reference signals. Design and theoretical stability analysis are provided along with validation through simulations.
- The last paper tackles the issue of the dependency on the IMU suite. From the mathematical expression of the optic flow, it can be noted that both pose and attitude information are available in this visual cue. Using only few visual motion sensors attached to the lander's structure, we developed a linear parameter varying (LPV) observer able to accurately estimate ventral optic flow, expansion optic flow and local pitch angle. A simulation was run using PANGU based optic flow flow measurements to validate performances of the designed solution.

## Main assumptions

Key assumptions adopted during this thesis are the following:

- Since we only consider the approach phase of landing (initial height below 1800m), several physical phenomenons might be neglected
  - Moon's rotation velocity is considered null with respect to the lander,
  - Moon's radius of curvature is considered infinite,
  - Moon's gravitational acceleration is considered constant such that  $g_{Moon} = 1.63m/s^2$ ,
- The terrain is considered flat. Hills, craters and boulders are not taken into account in the control design equations. These irregularities act as external disturbances in the PANGU based simulations.
- Sun's elevation during landing simulations is sufficient enough to illuminate the landing scene,
- Control allocation<sup>1</sup> of the on-off type thrusters is not dealt with (Krøvel, 2005; Singhose et al., 2006; Johansen and Fossen, 2013). The delivered control signal is a continuous signal expressed in terms of thrust taking values in the entire reachable range.
- Lander's mass is considered measured (or estimated) accurately along the descent,

---

<sup>1</sup>Control allocation deals with the problem of distributing a given control demand among the available set of actuators.

- A planar test case is considered (lateral motion is marginal compared to longitudinal motion),
- The environment is stationary, so that only self-motion of the lander generates optic flow.

# ARTICLE 3: SUB-OPTIMAL LUNAR LANDING GNC USING NON-GIMBALED BIO-INSPIRED OPTIC FLOW SENSORS

## CONTENTS

---

ABSTRACT . . . . .	97
I INTRODUCTION . . . . .	97
II SCENARIO DEFINITION AND ITS FULL GNC SOLUTION . . . . .	99
III LUNAR LANDER DYNAMIC MODEL AND OPTIC FLOW EQUATIONS . . . . .	100
IV SIMULATED VISUAL ENVIRONMENT: PANGU SOFTWARE AND OF SENSOR MODEL . . . . .	101
V OPTIMAL FUEL-EFFICIENT OF REFERENCE TRAJECTORY DESIGN . . . . .	102
VI CONTROL LAW DESIGN . . . . .	104
VII NON-GIMBALED OF SENSOR SET-UP . . . . .	106
VIII COMPLETE GNC SIMULATION USING PANGU . . . . .	110
IX CONCLUSION . . . . .	110
ACKNOWLEDGMENT . . . . .	113
REFERENCES . . . . .	113



## Article 3: Sub-optimal Lunar Landing GNC using Non-gimbaled Bio-inspired Optic Flow Sensors

Article submitted in 2013 in IEEE Transactions on Aerospace and Electronic Systems (in revision)

Authors: G. Sabiron, T. Raharijaona, L. Burlion, E. Kervendal, E. Bornschlegl and F. Ruffier

As we have seen in introduction, various strategies exist regarding GNC for EDL applications with their own pros and cons. Here we focus on vision based GNC avoiding the usual step of state estimation as it can be found in PBVS approaches. In view of the interesting results obtained on robotics platforms using bio-inspired sensorimotor behaviors and devices, we propose a framework for a full GNC solution based on optic flow and attitude sensing. The objective is to adapt each block of the GNC architecture to make the optic flow and the attitude, the only necessary measurements.

In order to do that we need to express the reference trajectory in terms of optic flow, to design control laws relying only on available measurements and to propose a new algorithm to estimate high interest optic flow values.

Regarding implementation aspects, two different ways to achieve our goals arises. The first option to sense the ventral and expansion optic flow would be to use gimbal mounted vision sensors as usually proposed with literature.

Indeed as we explained in introduction, many authors have worked on the decoupling existing in flying insects between their body motion and their visual sensing apparatus, that is to say their head. All of the observed mechanisms seem to indicate that the vision system of the flying insects is predominantly used for measuring translational optic flow which contains information of velocity and vicinity with obstacles meanwhile rotational optic flow indicates information already measured with inertial measurement devices.

Recent robotics studies have developed ingenious implementations and algorithms to make this decoupled vision system possible and enhance UAVs capabilities (Ruffier and Franceschini, 2003; Ruffier and Franceschini, 2005; Kerhuel, Viollet, and Franceschini, 2010; Manecy, Viollet, and Marchand, 2012; Manecy et al., 2013; Expert, 2013).

We took the opposing view of these approaches using visual motion sensors fixed to the lander's structure. The fact that the lander's angular rate is reasonably small during the descent compared to the translational optic flow component makes it easier to extract interesting parameters. As mentioned in introduction, it has been observed

that for low angular rates insects use their vision system to counteract the rotational optic flow generated by roll rotations. For all those reasons we chose the second solution to sense the ventral and expansion optic flows. We decided to give advantage to another specific feature of the compound insect eyes namely the large field of view. Sampling the surrounding environment with visual motion sensors fixed to the structure oriented toward different directions gives richer information and allows estimation of ventral and expansion optic flow.

In other words, we developed technological building blocks regarding:

### Guidance

Compute a fuel efficient trajectory from the high gate to the low gate and express it in terms of pitch angle, ventral and expansion optic flow. Using nonlinear programming, an optimal control problem is defined and solved. The optimal control sequences are run on a nonlinear model of the lander in open loop to extract the corresponding optimal states and most importantly the optimal optic flow and pitch profiles. During the landing, these optimal profiles are embedded in the GNC computer to feed the control laws.

### Navigation

Develop a navigation filter to get ventral and expansion optic flow from  $N$  non gimbaled optic flow sensors outputs oriented in various viewing directions known by design. The  $N$  measurements are derotated and then fused using a linear least square compression which estimates  $\omega_x$  and  $\omega_z$ .

### Control

Design attitude inner loop and optic flow outer loop relying only the available measurements ensuring low residual velocities at the low gate. The attitude control system uses IMU measurements to track the pitch optimal reference trajectory thanks to classical PID control with a feedforward action. In parallel to that inner loop, the optic flow nonlinear control is made up of a nonlinear dynamic inversion, feedforward terms, and output feedback. Global asymptotical stability is ensured by a Lyapunov based analysis of the closed loop. Depending on initial conditions we showed that either  $(\omega_x \ \omega_z)^T \rightarrow (\omega_x^* \ \omega_z^*)^T$  or  $(V_x \ V_z)^T \rightarrow (V_x^* \ V_z^*)^T$ .

This paper introduces a new framework for a GNC architecture mainly based on optic flow visual cues applied to planetary landing. Firstly, we describe the optimal control problem to compute offline a reference trajectory efficient in terms of fuel consumption using non linear programming. Then the nonlinear control laws based on the Lyapunov theory are presented and validated through realistic simulations. Finally the non-gimbaled problem is addressed and a solution based on a linear least squares

formulation is proposed. These three critical blocks forming the GNC architecture are then validated via an image-simulated based complete simulation.

The results presented in this paper paved the way for future optic flow based autonomous landing related work.

*Author contributions:*

G.S., T.R., L.B., E.K., E.B., F.R. designed research;

G.S. performed research;

G.S., T.R., L.B., F.R. contributed with technical and analytic tools;

G.S., F.R. analyzed data;

and G.S., T.R., L.B., F.R. wrote the paper.



# Sub-optimal Lunar Landing GNC using Non-gimbaled Bio-inspired Optic Flow Sensors

Guillaume Sabiron, Thibaut Raharijaona, Laurent Burlion, Erwan Kervendal, Eric Bornschlegl, and Franck Ruffier,

**Abstract**—Autonomous planetary landing is a critical phase in every exploratory space mission. Autopilots have to be safe, reliable, energy-saving, and as light as possible. The 2-D Guidance Navigation and Control (GNC) strategy presented here makes use of biologically inspired landing processes. Based solely on the relative visual motion known as the Optic Flow (OF) assessed with minimalistic 6-pixel 1-D OF sensors and Inertial Measurement Unit measurements, an optimal reference trajectory in terms of the mass was defined for the approach phase. Linear and nonlinear control laws were then implemented in order to track the optimal trajectory. To deal with the demanding weight constraints, a new method of OF estimation was applied, based on a non-gimbaled OF sensor configuration and a linear least squares algorithm. The promising results obtained with Software-In-the-Loop simulations showed that the present full GNC solution combined with our OF bio-inspired sensors is compatible with soft, fuel-efficient lunar spacecraft landing and might also be used as a backup solution in case of conventional sensor failure.

## LIST OF ABBREVIATIONS

GNC:	Guidance Navigation and Control
HG:	High Gate
LG:	Low Gate
LMS:	Local Motion Sensor
LROC:	Lunar Reconnaissance Orbiter Camera
MPC:	Model Predictive Control
OF:	Optic Flow
PANGU:	Planet and Asteroid Natural scene Generation Utility
SIL:	Software-In-the-Loop
TTC:	Time-To-Contact
VLSI:	Very Large Scale Integration
VMS:	Visual Motion Sensor

## I. INTRODUCTION

The latest vision-based systems are of great interest for Guidance Navigation and Control (GNC) applications and are therefore being widely used in space exploration missions, especially during the entry, descent and landing phases. Several recent studies have focused on visual methods for estimating the position and velocity of spacecraft such as planetary landers [5], [11], [22], [28] or performing hazard

G. Sabiron, T. Raharijaona and F. Ruffier are with Aix-Marseille University, CNRS, ISM UMR7287, Biorobotics Department, 13288, Marseille cedex 09, France (e-mail: Thibaut.Raharijaona@univ-amu.fr; Franck.Ruffier@univ-amu.fr).

G. Sabiron and L. Burlion are with the French Aerospace Lab (ONERA, Systems Control and Flight Dynamics -DCSD-), Toulouse 31055, France (e-mail: Guillaume.Sabiron@onera.fr; Laurent.Burlion@onera.fr).

E. Kervendal is with Airbus Defence and Space, Toulouse, France (e-mail: Erwan.Kervendal@astrium.eads.net).

E. Bornschlegl is with the European Space Agency (ESTEC), 2200 AG Noordwijk, The Netherlands (e-mail: Eric.Bornschlegl@esa.int).

avoidance [39]. Most of these methods involve the use of cameras and other classical remote sensors such as RADAR (Radio Detection And Ranging) or LIDAR (Light Detection And Ranging) devices [29]. To deal with potential failure of the main sensors, the latest small spacecraft often feature redundant conventional sensors that are heavy, bulky and highly energy-consuming. In the case of backup solution, our strategy presented here, featuring lightweight sensors do away with redundant heavy equipment of this kind.

The need for miniature GNC devices entails challenging constraints in terms of weight, size, cost, and power consumption. Developing advanced miniature GNC sensors is an important challenge for the years to come: these requirements could possibly be met, for instance, by combining the advantages of visual sensors, LIDAR, and RADAR in a small, lightweight, low-cost GNC sensor. In parallel with the time-consuming size-reduction efforts involved in reaching these goals, it is necessary to develop an efficient, reliable sensor fusion algorithm to compensate for the losses incurred by the miniaturization. Another alternative might be to apply an innovative robotic approach to lunar landing problems: miniature biologically-inspired sensors could be developed, for example, based on the visual cues used by tiny airborne creatures such as insects to control their flight.

Based on their previous neurophysiological studies on the fly's eye, Franceschini et al. [13] developed a simple principle, which was subsequently called the "Time of Travel principle" (see Fig. 4). This algorithm can be used to calculate the angular velocity of the images sweeping backward across the view field in one direction forming the 1-D Optic Flow (OF), which is detected by a small device known as a 2-pixel Local Motion Sensor (LMS) (see [9], [12], [33] for several implementations). Nature has shown the great potential of the rich visual OF information used by flying insects [13], [31], [38] to perform hazardous robotic tasks in complex, unknown environments. OF processing methods could be used in control systems in several ways:

- First as a means of estimating the usual states of the system in combination with other more classical sensors such as Inertial Measurement Units (IMUs), sonars, GPS, and/or accelerometers [14].
- Secondly, OF data can be used directly in a control loop without any need for information about the velocity, acceleration, altitude or even about the characteristics of the terrain, and hence without any bulky, power-consuming sensors. Many OF based robotic control systems have been developed which are able to perform take-

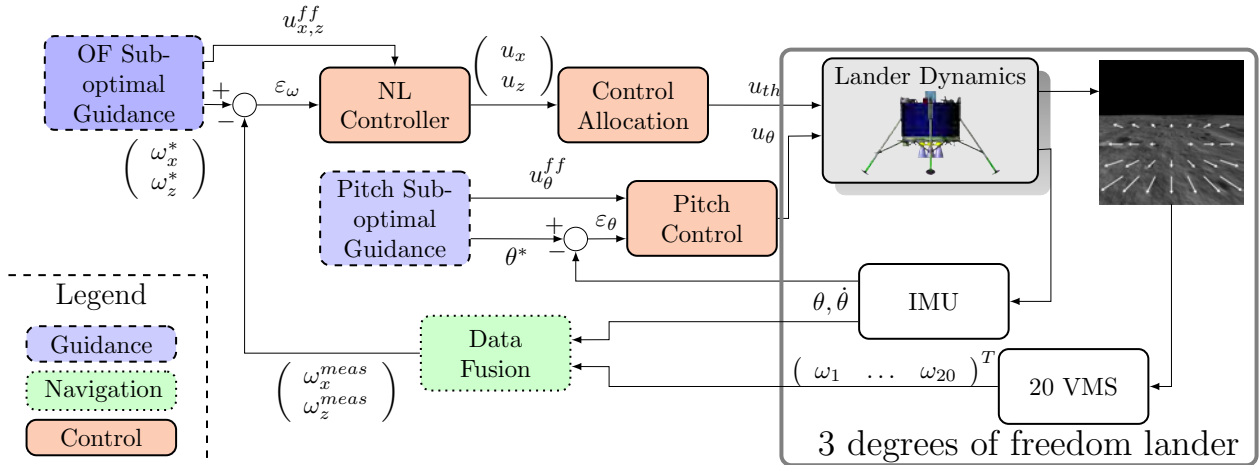


Fig. 1. Sketch of the full GNC solution presented in this paper. In the non-gimbaled sensor configuration presented here, twenty 6-pixel VMSs feed the data fusion block along with an IMU. The data fusion block based on a linear least squares algorithm feeds the nonlinear controller with the high interest OF values estimated. The control allocation block transforms the control signal into a braking force defining the magnitude of the thrust vector. The inner attitude control loop delivers the torque control signal  $u_\theta$  assessed via a linear output feedback controller and the sub-optimal guidance strategy defining the orientation of the thrust vector. The reference signals  $\omega_x^*(t)$ ,  $\omega_z^*(t)$  and  $\theta^*(t)$  are precomputed using nonlinear programming methods.

off, terrain-following and landing safely and efficiently by mimicking insects' behavior [16], [33], avoiding frontal obstacles [2], [3], [15], [34], tracking a moving target [25] as well as hovering and landing on a moving platform [17],

- and the OF has been used to extract relative-state information for navigation purposes in the Wide Field Integration methods presented by [6], [18], [37].

Several spacecraft landing studies have been recently performed by using direct means of regulating the downward OF (measured in the local vertical direction) and the Time To Contact (TTC, an index to the ground height, i.e., the local altitude, divided by the vertical velocity) to achieve soft landing. In [40], the authors presented the first simulations involving neuromorphic principles to process the 1-D OF and make a successful autonomous lunar landing. The autopilot used only the OF and the acceleration to regulate the spacecraft's flight without any need for velocity and height estimates or measurements. In two other studies [27], [40], the final velocities, pitch, and power consumption were too large to be compatible with the soft and fuel-efficient landing requirements: nevertheless, the autopilot's performances were assessed by running simulations on PANGU software (Planet and Asteroid Natural scene Generation Utility) developed for ESA by the University of Dundee (see [8], [30] for further information). PANGU is a tool which can be used to simulate visual environments on planetary surfaces. In 2011, Izzo et al. [19], [21] calculated optimal trajectories in terms of the duration of the landing phase and the fuel consumption by performing numerical simulations: the authors compared the fuel consumption penalty involved in various ventral OF and TTC-based flight paths imposed in open loop. Lastly, in [7], [20], optimal control and image processing were combined in a nonlinear Model Predictive Control (MPC) coupled to a state estimation scheme based on a sensor fusion process; with this

MPC control strategy, the optimal control sequences had to be computed online at each time step.

In all these previous studies [7], [19]–[21], [27], [40], the OF sensors were assumed to be always pointing vertically downward, which required the use of additional gimbal actuated systems that are too bulky for small planetary landers. Here, sub-optimal soft lunar landing performances were achieved using bio-inspired principles and devices without any state estimation methods, bulky classical sensor suites (such as RADAR, LIDAR, cameras, etc.), and especially, without any gimbal systems.

Step by step, the full GNC solution featuring several OF sensors fixed to the lander's structure, two control loops acting in parallel to make the spacecraft follow a pre-calculated optimal mass-efficient OF-based trajectory and requiring few online computational resources was developed. The reference OF profiles were neither constant nor did they take the form of classical functions: they were computed to avoid unnecessary fuel expenditure thanks to the use of optimal control tools. The reference trajectory computed (including the OF profiles) is optimal in terms of the fuel consumption during the nominal descent trajectory. The guidance scheme is said to be sub-optimal since it provides the control laws with the offline-computed trajectory, which might not be completely optimal during the actual descent due to the occurrence of tracking errors. A linear least squares algorithm was used here to estimate high interest OF values using several sensors oriented in different directions fixed to the structure. A dedicated method of determining the appropriate number of OF sensors was applied. To the best of our knowledge, no previous studies have addressed the problem of non-gimbaled OF sensors in the planetary landing context. Special efforts were made here with the simulations in order to develop a Matlab/Simulink simulator which was as realistic as possible. The OF sensor model used in the present Software-In-the-Loop (SIL) sim-

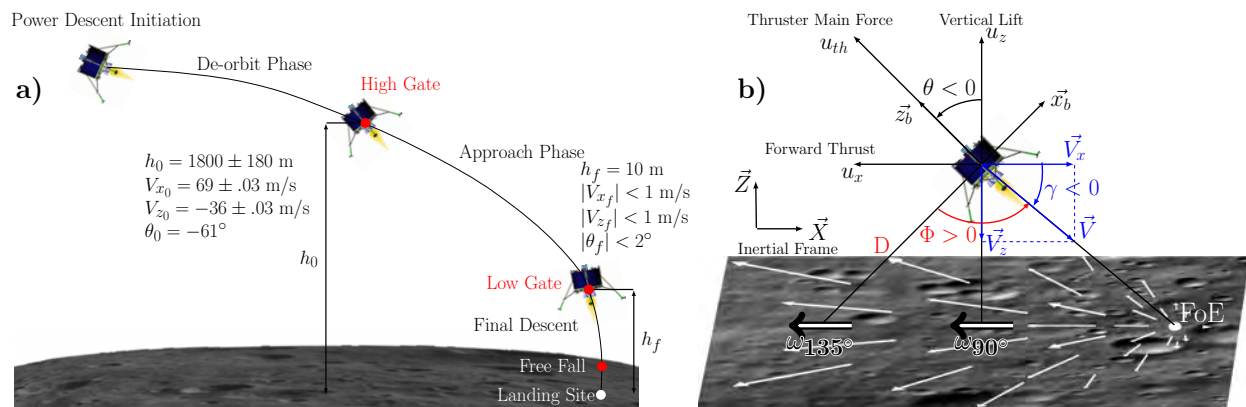


Fig. 2. Reference trajectory for lunar landing and notations (Lander sketch: by courtesy of Airbus Defence and Space (previously named ASTRIUM EADS)). a) The landing phase addressed in this study is defined as that between High Gate (HG) and Low Gate (LG) and called the approach phase. The objectives of the lander are to reach LG (at a height of 10 m) at both vertical and horizontal velocities of less than 1 m/s (in absolute values) and a pitch angle in the  $\pm 2^\circ$  range. Modified from [23]. b) Diagram of the lander in a planar motion, showing the inertial reference frame ( $\vec{X}$ ,  $\vec{Z}$ ), the velocity vector  $\vec{V}$ , the mean thruster force  $u_{th}$ , and its projections in the Local Vertical (collinear to  $\vec{Z}$  axis) Local Horizontal (collinear to  $\vec{X}$  axis) (LVLH) reference frame. Two specific optic flows are depicted on the lunar surface  $\omega_{90^\circ}$  and  $\omega_{135^\circ}$ . It can be noted that the point in the direction of motion of the lander is called the focus of expansion (FoE) and has an OF equal to zero. Adapted from [35].

ulations with the PANGU environment benefited from recent advances in 6-pixel Visual Motion Sensors (VMS) [32], which are self-contained devices. These VMSs involving analog and digital filtering stages as well as a contrast thresholding step were previously installed onboard a real large scale Unmanned Aerial Vehicle [36].

In Section II, the method used to design the full GNC solution and the landing scenario is presented. In Sections III and IV, the high-interest OF measurement variables, nonlinear dynamic model and vision-based SIL simulations are defined. In Section V, we describe how sub-optimal guidance laws were computed by performing nonlinear programming. Section VI describes the nonlinear controller based on Lyapunov theory developed for the OF feedback loop and the linear controller developed for the pitch feedback loop. In Section VII, we discuss the challenge involved in using non-gimbaled sensors and present a method based on a least squares algorithm. The full-GNC results were obtained by performing SIL simulations to calculate the fuel consumption and the final velocities (see Section VIII). Lastly, Section IX describes some paths for future research and ends with some final comments.

## II. SCENARIO DEFINITION AND ITS FULL GNC SOLUTION

In this paper, we present the full GNC solution for Lunar landing step by step (see Fig. 1) by:

- describing the dynamic model for the lander,
- defining the sub-optimal guidance laws with respect to the lander's fuel-consumption in terms of the OF and the pitch trajectories,
- developing a nonlinear controller based on Lyapunov theory,
- suggesting a control allocation scheme,
- fusing the 20 local OF measurements into relevant OF measurements for trajectory tracking,
- simulating the full GNC solution using a lunar environment simulated with PANGU software.

The lunar landing trajectory was divided into the following four phases (see Fig. 2.a):

- 1) De-orbit Phase,
- 2) Approach Phase,
- 3) Final Descent,
- 4) Free Fall.

The approach phase from High Gate (HG) ( $1800 \text{ m} \pm 10\%$  Above Ground Level -AGL-) to Low Gate (LG) (10 m AGL) defines the autonomous lunar landing problem. HG corresponds to the height at which the landing site can be detected by the spacecraft's visual system. LG corresponds to the height at which visual contact with the landing site is no longer possible due to the lunar dust raised by the thrusters. When reaching the LG, another GNC strategy is expected to take control of the final descent. Initial parameters are the horizontal velocity ( $V_{x_0} = 69 \pm .03 \text{ m/s}$ ), vertical velocity ( $V_{z_0} = -36 \pm .03 \text{ m/s}$ ), pitch angle ( $\theta_0 = -61^\circ$ ), ground height ( $h_0 = 1800 \pm 180 \text{ m}$ ), and lander's mass ( $m_{ldro} = 762 \pm 11 \text{ kg}$ ) (see Fig. 2.a).

This reference trajectory is therefore very similar to that involved in the Apollo test case scenario often used in the literature [4]. The solution targeted involves the following demanding final constraints at LG ( $h_f = 10 \text{ m}$ ):

- $|V_{x_f}| \leq 1 \text{ m/s}$ ,
- $|V_{z_f}| \leq 1 \text{ m/s}$ ,
- $|\theta_f| < 2^\circ$ .

The objectives are thus defined in terms of the velocity and the attitude. The position on the x-axis is not dealt with here since we are aiming at soft landing without any requirements about the final downrange. With the present approach, the propellant consumption will be decreased as far as possible by the autonomous lunar landing strategy. The main difficulty to be overcome is that the entire state vector is not given by the measurements. For instance, the velocities and positions are neither measured nor estimated: only the angular rates,

attitude, mass, and OF are measured and thus available for use as inputs to the controllers. To achieve soft lunar landing, the autopilot must be able to reduce the magnitude of its velocity vector and control the orientation of the velocity vector, which is called the flight path angle and denoted  $\gamma$  (see Fig. 2.b). This was achieved by jointly adjusting the lander's two available control signals: its pitch and its main thrust.

In this study, the approach phase is first defined by determining an optimal fuel-saving trajectory by computing the control sequence that requires the least fuel to reach the LG and complies with the demanding final constraints. The second step corresponds to following this trajectory during the actual landing phase, using IMU measurements, OF measurements, and linear/nonlinear controllers.

If sensor failure occurs, the backup solution presented here might suffice to control the GNC computer. However, sensor failure might not happen at the high gate. In order to initialize the GNC architecture, the last known value of the states (height, velocity, and attitude) could be used to switch to the corresponding part of the reference trajectory.

### III. LUNAR LANDER DYNAMIC MODEL AND OPTIC FLOW EQUATIONS

The autopilot consists here of an OF-based control system operating in the vertical plane  $(\vec{X}, \vec{Z})$ , which controls the spacecraft's main thruster force and pitch angle. To stabilize the lander, it is necessary to cope with nonlinearities and the inherent instability of the system. Since the lunar atmosphere is very thin, no friction or wind forces are applied to the lander. In the present model, the heave and surge dynamics are coupled via the lander's pitch (see Fig. 2.b). To incorporate the physical constraints into the model in line with the ESA/Airbus Defence and Space preliminary studies, the following assumptions are adopted:

- (H1)  $\left\{ \begin{array}{l} \text{The braking thrusters can produce only positive forces and the} \\ \text{thrust is limited to 3820 N, which means } 0 \leq u_{th} \leq 3820 \text{ N.} \end{array} \right.$
- (H2)  $\left\{ \begin{array}{l} \text{The attitude thrusters can produce forces up to} \\ \text{44 N, which means } -44 \leq u_{\theta} \leq 44 \text{ N.} \end{array} \right.$

In line with the ESA/Airbus Defence and Space preliminary studies, few other values related to thrusters performances, lander's characteristics and physical constants are defined in table I.

TABLE I  
CONSTANT PARAMETERS BASED ON ESA/AIRBUS DEFENCE AND SPACE STUDIES

Specific impulse (s)	Gravitational acc. ( $m/s^2$ )	Initial mass (kg)
$I_{sp_{th}} = 325$	$g_{Earth} = 9.81$	$m_{ldr}(t_0) = 762$
$I_{sp_{\theta}} = 287$	$g_{Moon} = 1.63$	

The specific impulse  $I_{sp}$ , an efficiency parameter defined by the ratio between the thrust and the mass flow rate times the Earth's gravitational acceleration constant ( $I_{sp_{th}} = u_{th}/(\dot{m}_{ldr} \cdot g_{Earth})$ ) is denoted  $I_{sp_{th}}$  in the case of the braking thrusters and  $I_{sp_{\theta}}$  in that of the attitude thrusters. The lunar acceleration due to the gravity is taken to be constant due to the low initial altitude

In line with previous authors' assumptions, the lunar ground is taken to be flat (with an infinite radius of curvature) [24]. The dynamic motion of the lander can be described in the time domain by the following dynamic system in the inertial frame  $\mathcal{I}$  associated with the vector basis  $(\vec{X}, \vec{Z})$ :

$$\begin{cases} a_{ldr_z}(t) = \frac{\cos(\theta(t))}{m_{ldr}(t)} u_{th}(t) - g_{Moon} \\ a_{ldr_x}(t) = \frac{\sin(\theta(t))}{m_{ldr}(t)} u_{th}(t) \end{cases} \quad (1)$$

where  $u_{th}$  corresponds to the control force applied to the lander,  $a_{ldr_{x,z}}$  are the lander's accelerations in the lunar inertial reference frame,  $m_{ldr}$  stands for the lander's mass,  $\theta$  is the pitch angle,  $t$  denotes the time, and  $g_{Moon}$  denotes the lunar acceleration due to the gravity. The pitch dynamics of the system are modeled as follows:

$$\frac{I}{R} \frac{d^2\theta}{dt^2} = u_{\theta}(t) \quad (2)$$

where  $u_{\theta}$  is the input signal controlling the spacecraft's pitch and  $\theta$  is assessed independently via an IMU,  $I$  is the moment of inertia, and  $R$  is the eccentricity of the attitude thrusters with respect to the center of mass. The lander's mass depends directly on the fuel consumption, as given by the following relation:

$$\dot{m}_{ldr}(t) = \frac{-u_{th}(t)}{I_{sp_{th}} \cdot g_{Earth}} + \frac{-|u_{\theta}(t)|}{I_{sp_{\theta}} \cdot g_{Earth}} \quad (3)$$

This means that:

$$m_{ldr}(t) = m_{ldr}(t_0) - \frac{1}{g_{Earth}} \int_{t_0}^t \left( \frac{u_{th}(\epsilon)}{I_{sp_{th}}} + \frac{|u_{\theta}(\epsilon)|}{I_{sp_{\theta}}} \right) d\epsilon \quad (4)$$

Since the initial mass is known and the lander's mass depends linearly on the integral of the lander's thruster control signal, the mass can be computed and assessed at any time during the descent.

Once the dynamic model of the spacecraft has been defined, one needs to state the OF equations to find what information can be deduced from this visual cue. The general OF  $\omega(\Phi)$  can be described as the sum of the two distinct components defined by [26], e.g. the translational and rotational OF in the vertical plane as follows:

$$\omega(\Phi) = \omega_T + \omega_R \quad (5)$$

The translational OF  $\omega_T$  depends on the linear velocity  $V$  expressed in the inertial frame, the distance from the ground  $D$  in the gaze direction and the elevation angle  $\Phi$  (i.e. the angle between the gaze direction and the heading direction).

$$\omega_T = \frac{V}{D} \sin(\Phi) \quad (6)$$

See Fig. 2.b for geometric notations. The rotational OF  $\omega_R$  depends only on the angular velocity  $\Omega_j$  expressed in the body's fixed frame  $\mathcal{B}$  associated with the vector basis  $(\vec{x}_b, \vec{z}_b)$ , where  $j$  denotes the axis of rotation, and on the elevation angle,  $\lambda$ , between the gaze direction and the axis of rotation.

$$\omega_R = \Omega_j \sin(\lambda) \quad (7)$$

On the vertical plane,  $\lambda = \frac{-\pi}{2}$  and  $\Omega_j = \dot{\theta}$  and hence,  $\omega_R = -\dot{\theta}$ . Lastly, on the 2-D plane, the ground-truth OF can be monitored as follows:

$$\omega_{grd-trh} = \frac{V}{D} \sin(\Phi) - \dot{\theta} \quad (8)$$

For the sake of clarity, the specific local translational optic flow  $\omega_T(\Phi)$  will be written as follows:

- $\omega_{90^\circ}$  in the case of the downward OF, i.e. in the nadir direction ( $90^\circ$  between the gaze direction and the local horizontal)
- and,  $\omega_{135^\circ}$  in that of the OF oriented at  $135^\circ$  from the local horizontal.

An illustration of  $\omega_{90^\circ}$  and  $\omega_{135^\circ}$  is presented in Fig. 2.b. From the previous equation, from the point of view of hazardous obstacle avoidance, it can be seen that whenever an obstacle appears in the OF sensor's line of sight, the distance  $D$  to the obstacle will be decreased or increased depending on whether it is a boulder or a crater: it will cause the autopilot to react by decelerating or accelerating accordingly so as to ensure the lander's soft descent regardless of the topology of the terrain. The rotational OF  $\omega_R$  is subtracted from the general OF  $\omega(\Phi)$  (see (5)), using the lander's mechanical rotation sensed by the IMU in order to benefit from the useful properties of the translational OF  $\omega_T$ : this operation is known as the derotation process [1].

Taking equation (6), under the assumption that the ground is practically flat (i.e.  $D = h / \cos(\frac{\pi}{2} - \Phi + \gamma)$ , where  $\gamma$  denotes the flight path angle (the orientation of the velocity vector with respect to the local horizontal as described in Fig. 2.b) and  $\Phi - \gamma$  denotes the angle between the gaze direction and the local horizontal:

$$\omega_{90^\circ} = \frac{V_x}{h} \quad (9)$$

with  $V = V_x / \cos(\gamma)$  and  $h$  the ground height.

For  $\Phi - \gamma = 135^\circ$ :

$$\omega_{135^\circ} = \frac{V}{2h} (\cos(\gamma) - \sin(\gamma)) = \frac{\omega_{90^\circ}}{2} (1 - \tan(\gamma)) \quad (10)$$

where  $\tan(\gamma) = \frac{V_z}{V_x}$ .

Lastly, the relevant values of OF, i.e., the ventral OF  $\omega_x$  and the expansion OF  $\omega_z$  used in the present regulators are then expressed directly in terms of  $\omega_{90^\circ}$  and  $\omega_{135^\circ}$ :

$$\omega_x = \frac{V_x}{h} = \omega_{90^\circ} \quad (11)$$

$$\omega_z = \frac{V_z}{h} = \omega_{90^\circ} - 2\omega_{135^\circ} \quad (12)$$

#### IV. SIMULATED VISUAL ENVIRONMENT: PANGU SOFTWARE AND OF SENSOR MODEL

To enhance the realism of the simulation, PANGU software was used to generate images of the lunar surface, taking the position of the system, the elevation of the sun and the camera's properties into account. The simulated lunar surface was irregular and sometimes included craters up to 40 m deep. The images generated by PANGU contained 256 gray-scale levels and had a resolution of  $256 \times 256$  pixels.

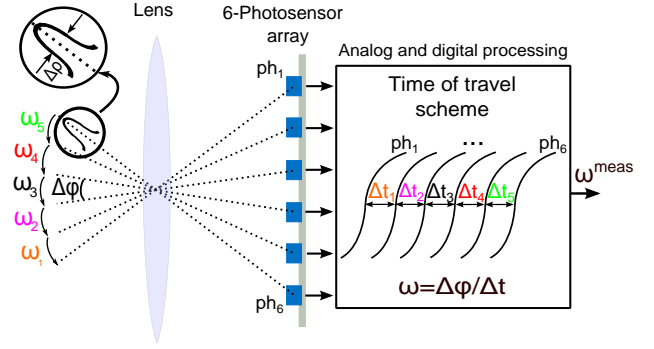


Fig. 4. Simplified processing algorithm of the VMS. Adapted from [32].

Each OF sensor included six photoreceptors: the visual axes of each pair of photoreceptors were separated by the inter-receptor angle  $\Delta\varphi = 0.1^\circ$ . The angular sensitivity of each photoreceptor obeyed a 2-D Gaussian function mimicking the angular sensitivity of the fly's photoreceptor with the acceptance angle (the angular width at half height)  $\Delta\rho = \Delta\varphi = 0.1^\circ$ . A simplified model of the processing algorithm of the VMS is presented in Fig. 4. Five OF are computed for each pair of photodiodes but only the median value is delivered as an output at 2kHz (a full description of the algorithm can be found in [36]). As soon as a contrast is detected, the time of travel algorithm calculates the time  $\Delta t$  elapsing between its detection by two adjacent photodiodes. The OF is directly computed using this equation  $\omega = \Delta\varphi / \Delta t$ . These small inter-receptor and acceptance angle values make it possible to compute very low velocities. Since we have such a narrow field of view, even high spatial frequency contrasts will be detected by the photodiodes, which is very helpful at low OF levels, where fewer contrasts occur in the sensor's line of sight.

In the simulated VMS model, the photoreceptors' output is simulated at each simulated time step (1 ms) by convolving the PANGU-generated lunar surface image with the 2-D Gaussian filter. The simulated 6-pixel VMSs then assess the OF. The Matlab/Simulink model of the 6-pixel VMS is exactly the same as that embedded in the real OF thus providing SIL<sup>1</sup>.

To validate the simulated sensor model in a realistic visual environment, we implemented, simulated and analyzed the above improvements on Lunar Reconnaissance Orbiter Camera (LROC) images<sup>2</sup>. We also compared the sensor output obtained in a LROC simulation with the results obtained outdoors with a real-life implementation of the low speed 6-pixel VMS, upon applying the same angular speed pattern.

As shown in Fig. 3, the characteristics of the sensor model were found to be very similar to those of the real-life implementation of the 6-pixel VMS. The OF measured closely matched the reference signal, with a refresh rate of 6.64Hz in the case of the real measurements and 6.93Hz in that of the simulated VMS to which LROC images were applied. Since the visual environment differed between the simulation (lunar ground) and the real-life experiment (scrubland on a sunny

<sup>1</sup>Toolbox used for rapid prototyping available at <http://www.kerhuel.eu>

<sup>2</sup>Images available at <http://lroc.sese.asu.edu>

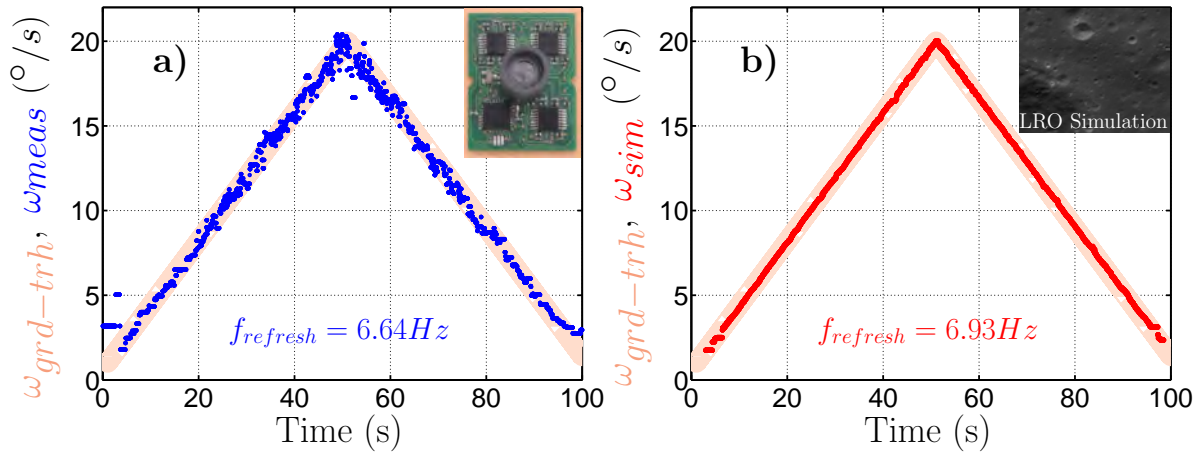


Fig. 3. Comparison between the real dynamic response of the low speed 6-pixel VMS (a - Modified from [36]) and the output of the simulated VMS on a LROC image (b). Rotations from  $1^\circ/s$  to  $20^\circ/s$  were applied to the sensor, which was designed to operate in the  $1.5^\circ/s$  to  $25^\circ/s$  range.

day), the simulated results were expected to be more satisfactory. It is worth noting that the simulated sensor responded appropriately to a LROC image by following precisely the OF reference signal called  $\omega_{grd-trh}$  without any outliers. Likewise, the results obtained in the outdoor experiments with an actual 6-pixel VMS were also accurate. The OF sensor code therefore proved to be fairly reliable when working with PANGU.

Although interesting results were obtained with LROC images, the fixed resolution of 0.24 m/px decreased the realism of the simulation at low altitudes. We therefore decided to use PANGU instead, which gives images with a variable resolution depending on the lander's height and attitude. PANGU yielded images with a resolution of  $256 \times 256$  px, regardless of the lander's position and attitude, which is nearer to reality. The main drawback of simulations involving the use of PANGU is the duration of the landing simulation. The approach phase lasts around 50 seconds, which means making 50000 TCP-IP requests to PANGU from Matlab/Simulink plus the remaining calculations required by the closed-loop system. A simulation involving two 6-pixel VMSs took 4.5 hours on an Intel® Core i7-2600 @ 3.40GHz and another one with twenty 6-pixel VMSs took more than 26 hours. This explains why the results of only two of these time-consuming closed-loop simulations are presented in this paper.

#### V. OFFLINE COMPUTATION OF THE OPTIMAL FUEL-EFFICIENT OF REFERENCE TRAJECTORY

We need to find an OF-based trajectory to be followed during landing. A valid strategy previously studied in literature was that obtained by keeping the OF constant around the value defined by the final constraints. For instance, the first possibility would be to set the reference value at  $\omega_{x_{ref}} = \frac{V_{x_f}}{h_f} = 0.1 \text{ rad/s}$  in order to reach 10m at a velocity equal to or lower than 1m/s. However, at the beginning of the trajectory, the OF is lower than this reference value during a few seconds ( $\frac{V_{x_0}}{h_0} \approx 0.04 < 0.1 \text{ rad/s}$  with  $V_{x_0} = 69 \text{ m/s}$  and  $h_0 = 1800 \text{ m}$ ). This would cause the lander to accelerate

horizontally and/or vertically in order to reach the reference value: it would instantaneously decrease its height and thus increase the OF. However, there is no need to reach 0.1rad/s so quickly or to wait without applying any actuation until the OF increases spontaneously, because the main goal here is to gradually brake the system efficiently while meeting the final constraints in terms of the overall fuel consumption.

Based on these findings, we decided to compute and analyze the optimal trajectory in order to obtain OF reference signals corresponding to the least fuel-consuming trajectory. The mass optimization problem was defined here along with the associated constraints, and its solution was computed in terms of the trajectory and the OF profiles.

In order to meet the low computational requirements, the optimal problem was solved offline only once: the OF and pitch profiles were determined and implemented in the form of constant vectors in the lander.

First of all, the optimal control sequence  $u^* = (u_{th}^*, u_\theta^*)$  was computed, taking  $u_{th}^*$  to denote the braking thrust and  $u_\theta^*$  to denote the pitch torque (the upper script \* indicates the optimality in terms of the mass, i.e., the fuel consumption). In this paper, optimality refers to the outputs of the optimization problem ( $u_{th}^*, u_\theta^*$ ) and the associated reference trajectory ( $V_x^*, V_z^*, h^*, \theta^*$ ).

Looking for the least fuel-consuming trajectory is equivalent to finding the control sequence  $u^*$  that minimizes the use of the control signal (see (3)).

The optimization problem can then be expressed as follows:

Solve

$$\min_{u_{th}(t), u_\theta(t)} \int_{t_0}^{t_f} (u_{th}(t) + |u_\theta(t)|) dt \quad (13)$$

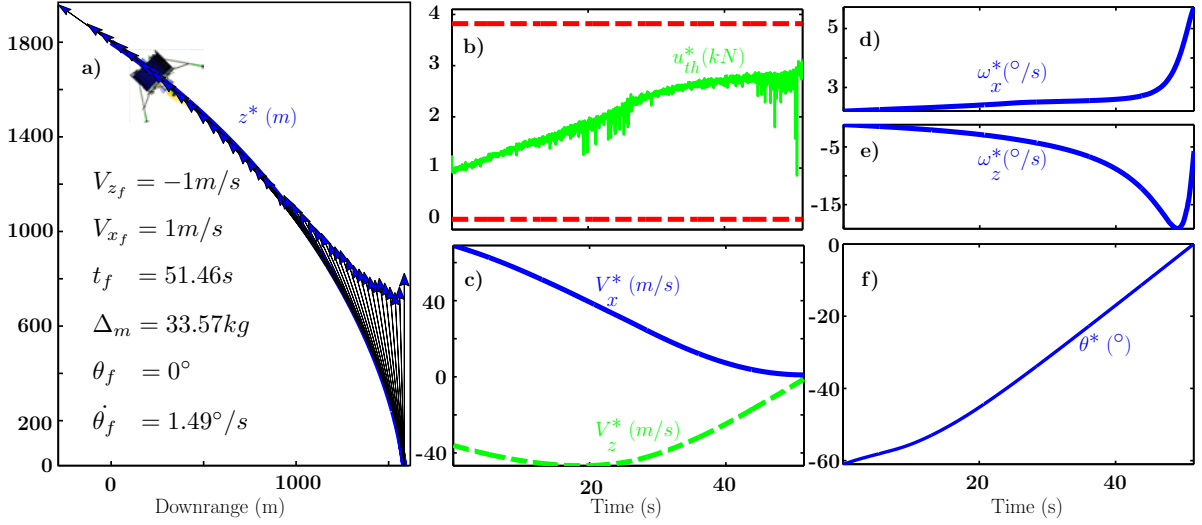


Fig. 5. Open loop trajectory under the optimal control sequences  $u_{th}^*$  and  $u_\theta^*$ . a) Height  $h^*$  versus downrange  $x^*$ , orientation and normalized magnitude of the optimal control  $u_{th}^*$ . b) Optimal control sequence  $u_{th}^* = \sqrt{u_{x^*}^2 + u_{z^*}^2}$ . The saturation imposed on the control signals  $u_{th}^*$  was chosen so that  $0 \text{ N} \leq u_{th}^* \leq 3438 \text{ N}$ . c) Velocities  $V_x^*$ ,  $V_z^*$ . d-e) Optimal reference OF profile versus time. f) Pitch reference trajectory  $\theta^*$  obtained under the optimal control sequence  $u_\theta^*$ .

subject to

$$\begin{pmatrix} \dot{V}_z \\ \dot{V}_x \\ \dot{z} \\ \dot{x} \\ \dot{\theta} \\ \dot{m} \end{pmatrix} = \begin{pmatrix} \frac{\cos(\theta)}{m} u_{th} - g_{Moon} \\ \frac{\sin(\theta)}{m} u_{th} \\ V_z \\ V_x \\ \frac{I}{R} u_\theta \\ \frac{-u_{th}}{I_{sp_{th}} \cdot g_{Earth}} + \frac{-|u_\theta|}{I_{sp_\theta} \cdot g_{Earth}} \end{pmatrix} \quad (14)$$

$$\begin{cases} V_z(t_0) = -36 \text{ m/s}, & |V_{z_f}| < 1 \text{ m/s} \\ V_x(t_0) = 69 \text{ m/s}, & |V_{x_f}| < 1 \text{ m/s} \\ h(t_0) = 1800 \text{ m}, & h_f = 10 \text{ m} \\ \theta(t_0) = -61^\circ, & |\theta_f| < 2^\circ \end{cases} \quad (15)$$

$$\begin{cases} 0 < u_{th} < 3438 \text{ N} \\ -44 < u_\theta < 44 \text{ N} & \forall t \in [t_0, t_f] \\ (-V_z, V_x, h, x) > 0 \\ |\dot{\theta}| < 1.5^\circ/\text{s} \end{cases} \quad (16)$$

This offline optimal control problem was implemented using Matlab optimization software on the nonlinear system under constraints to bring the system from HG to LG. To solve this continuous time optimization problem, many freely available Matlab toolboxes using various methods can be used. The solution provided by ICLOCS (Imperial College London Optimal Control Software, [10]) based on the IPOPT solver suited our needs for the numerical implementation of a nonlinear optimization procedure in the case of the continuous system subjected to boundary and state constraints using the interior point method. The simulation of the open loop optimal control was therefore run on the nonlinear system to assess the optimal OF and pitch profiles ( $\omega_x^*$ ,  $\omega_z^*$ ,  $\theta^*$ ).

Equation (14) describes the dynamic lander model, (15) the initial and final conditions and (16) the actuator and system

constraints along the trajectory. For safety reasons, a 10% clearance from the thrusters' physical saturation is added when pre-computing the optimal trajectory. This supplementary constraint gives the lander greater maneuverability around the pre-computed trajectory in closed loop. It is worth noting that a terminal constraint could be added if required to the downrange  $x$  to make pinpoint landing possible, but this might greatly increase the fuel consumption.

Since it may occur that  $\dot{\theta} = -\omega_R > \omega_T$  and thus  $\omega_{measured} < 0$ , we had to use a two-directional version of the 6-pixel VMS adapted for use in the following measurement range:  $\omega_{measured} \in [-20^\circ/\text{s}; -0.1^\circ/\text{s}] \cup [0.1^\circ/\text{s}; 20^\circ/\text{s}]$  (see Sec. IV)

The fuel consumed decreases the lander's mass by  $\Delta m$ , which is defined as the difference between the initial and final mass of the lander  $\Delta m = m_{ldr_0} - m_{ldr}(t_f)$  where  $m_{ldr_0} = 762 \text{ kg}$  and

$$m_{ldr}(t_f) = m_{ldr}(t_0) - \frac{1}{g_{Earth}} \int_{t_0}^{t_f} \left( \frac{u_{th}(\epsilon)}{I_{sp_{th}}} + \frac{|u_\theta(\epsilon)|}{I_{sp_\theta}} \right) d\epsilon \quad (17)$$

To ensure that the sum  $\omega_{grd-trh} = \omega_T + \omega_R$  does not cancel itself out (i.e.  $\omega_T = -\omega_R$ ), the pitch rate ( $\omega_R = \dot{\theta}$ ) was constrained as follows:  $|\dot{\theta}| = |\omega_R| < 1.5^\circ/\text{s}$ .

Under all these conditions, the optimal control sequences ( $u_{th}^*$ ,  $u_\theta^*$ ) were processed: the optimal solution was obtained with  $t_f = 51.46 \text{ s}$  and a decrease in the mass of  $\Delta m < 33.6 \text{ kg}$  (amounting to 4.4% of the initial mass).

The trajectory computed under these constraints can be said to be optimal in the case of a more highly constrained problem than the system fully allows (due to the addition of constraints on  $\dot{\theta}$  and the 10% margin on the thrust to account for the sensors' and actuators' operating ranges). In any case, both of these additional constraints (the pitch rate and the 10% margin added to the thrust) result in a very similar fuel expenditure

to that obtained without them (amounting to a difference of only 0.21%).

Controlling the nonlinear system using the precomputed sequences  $(u_{th}^*, u_\theta^*)$  gives an idea of the optimal trajectory taken by the lander to reach the final conditions targeted. Figure 5 gives an overview of the evolution of the states and outputs during the landing phase when the nonlinear system is subjected to the optimal open-loop control sequences  $(u_{th}^*, u_\theta^*)$ . Figure 5.a gives the trajectory of the lander in the plane and shows the evolution of the orientation and the normalized magnitude of the optimal control signal  $u_{th}^*$ . Figure 5.b presents the optimal control sequence  $u_{th}^* = \sqrt{u_x^{*2} + u_z^{*2}}$ . It can be seen from this figure that the control signal  $u_{th}^*$  delivered never reaches either the upper or the lower saturation, and that the variations are quite smooth during the entire trajectory. Figure 5.c shows the evolution of the vertical and horizontal velocities (in the LVLH frame), which meet the terminal constraints at  $t_f$ . The nonlinear control strategy described below in Sec. VI is used to perform the tracking of the optimal OF profiles presented in Fig. 5.d-e

It is worth mentioning that in the optimal control problem, the HG conditions are taken to be constant values. These nominal values are not necessarily reached when this GNC solution is switched on. As described in II, the initial height, velocity and mass can vary at HG. We decided to compute only one optimal trajectory from the initial HG conditions to the expected final conditions and let the nonlinear controller cancel any tracking errors which occur. An improvement to the guidance scheme could be made by solving the optimal control problem several times at various initial altitudes covering the admissible range. A bank of reference trajectories could be embedded into the GNC computer, and a selection algorithm would eventually choose the best suitable candidate trajectory at the actual HG on the basis of the available measurements. This enhanced guidance scheme would still be sub-optimal since the trajectories would be computed offline, but the initial errors with respect to the actual position and reference position would be greatly reduced.

As can be expected, neither the optimal OF profiles nor the ventral OF  $\omega_x^*$  nor the expansion OF  $\omega_z^*$ , are constant during the entire descent phase. The OF profiles end up as follows:

- $\omega_z$  decreases slowly down to  $19.16^\circ/s$  before increasing sharply toward  $\omega_{zf} = -5.7^\circ/s$ ,
- $\omega_x$  increases linearly during the first half of the descent up to  $2.5^\circ/s$  and then exponentially up to  $\omega_{xf} = 5.7^\circ/s$ .

The inner loop dynamics (i.e., the pitch evolution) are presented in Fig. 5.f under the optimal pitch control signal  $u_\theta^*$ : the pitch starts at  $-61^\circ$  and ends up at  $0^\circ$ , as was to be expected.

The final velocities are such that  $V_{xf} = -V_{yf} = 1m/s$ . In the final velocity ranges specified in 15, the solution is optimal in terms of the fuel expenditure (the task is less demanding in terms of braking). If tracking errors occur during the actual landing, this might prevent final objectives from being met. Another way of setting the constraints on the system's states would be to require that  $V_{xf} = -V_{yf} = 0m/s$ , thus increasing the error margin allowed at LG in the final velocities.

At this point, optimal, fuel-efficient, OF reference signals as well as pitch reference signal were computed along with

the control sequences  $(u_{th}^*, u_\theta^*)$  using nonlinear programming methods.

## VI. CONTROL LAW DESIGN

### A. Optic-flow nonlinear control

Once the optimal OF reference trajectory had been defined, we had to design the control laws required to close the loop based on the OF measurements obtained during the descent. Nonlinear controllers were therefore designed for this purpose, including a feedforward term based on the given optimal control sequences and output feedback with  $\omega_x$  and  $\omega_z$  measurements. Since both the height and the velocity show considerable variations during the approach phase, it was decided not to linearize the system around an equilibrium point, which would have differed from the actual dynamics most of the time. No state estimation methods, but only the visual OF cues  $\begin{bmatrix} \omega_x \\ \omega_z \end{bmatrix} = \begin{bmatrix} V_x/h \\ V_z/h \end{bmatrix}$  and the inertial measurements were therefore used to perform soft lunar landing. We can now write:

$$\begin{cases} a_{ldr_z}(t) = \dot{V}_z = \frac{u_z(t)}{m_{ldr}(t)} - g_{Moon} \\ a_{ldr_x}(t) = \dot{V}_x = \frac{u_x(t)}{m_{ldr}(t)} \end{cases} \quad (18)$$

along with the two virtual control inputs  $u_x(t) = u_{th}(t) \sin(\theta(t))$  and  $u_z(t) = u_{th}(t) \cos(\theta(t))$ .

Let the candidate Lyapunov function  $\mathcal{L}_1$  be defined by:

$$\mathcal{L}_1 = \frac{1}{2} (h\omega_x - h^*\omega_x^*)^2 \quad (19)$$

where  $h^*$  and  $\omega_x^*$  correspond to the height and the ventral OF impinging on the lander during the landing scenario with the optimal control sequences  $(u_{th}^*, u_\theta^*)$  computed offline (see Sect.V).  $\mathcal{L}_1$  is always positive ( $\mathcal{L}_1 \geq 0$ ). Its time derivative can then be expressed as follows:

$$\dot{\mathcal{L}}_1 = (V_x - V_x^*) (\dot{V}_x - \dot{V}_x^*) \quad (20)$$

where  $\dot{V}_x = a_{ldr_x} = \frac{u_x(t)}{m_{ldr}(t)}$ .

In the case of a control signal such that:

$$u_x = m_{ldr} (\dot{V}_x^* - k_x(t) (\omega_x - \omega_x^*)) \quad (21)$$

where  $k_x(t)$  is a strictly positive time varying gain (described below the proof), we obtain:

$$\dot{\mathcal{L}}_1 = (V_x - V_x^*) \left( -k_x(t) \left( \frac{V_x}{h} - \frac{V_x^*}{h^*} \right) \right) \quad (22)$$

This yields:

$$\dot{\mathcal{L}}_1 = (V_x - V_x^*) \left( \frac{-k_x(t)}{h} \left( V_x - V_x^* + \frac{\delta h V_x^*}{h^*} \right) \right) \quad (23)$$

where  $\delta h = h^* - h$ . Lastly:

$$\dot{\mathcal{L}}_1 = -\frac{k_x(t)\sqrt{2}}{h} \left[ \sqrt{2}\mathcal{L}_1 + \delta h\omega_x^* \text{sign}(V_x - V_x^*) \sqrt{\mathcal{L}_1} \right] \quad (24)$$

where  $\text{sign}(X) = \begin{cases} 1 & X \geq 0 \\ -1 & X < 0 \end{cases}$ .

Since the reference scenario adopted in this paper focuses on the approach phase from HG (1800m) to LG (10m), the height is always positive  $\forall t \geq 0$ .

Therefore, even with  $(k_x(t), h) \geq 0$ , a sign study had to be conducted in order to determine the evolution of  $\dot{\mathcal{L}}_1$ . Several possible cases could occur:

- 1)  $\text{sign}(\delta h) = \text{sign}(V_x - V_x^*)$

It can be seen here that  $\dot{\mathcal{L}}_1$  is strictly negative. This means that with  $\mathcal{L}_1 = \frac{1}{2}(h\omega_x - h^*\omega_x^*)^2 = \frac{1}{2}(V_x - V_x^*)^2 \geq 0$  and  $\dot{\mathcal{L}}_1 < 0$ ,  $V_x$  tends asymptotically toward  $V_x^*$ .

- 2)  $\text{sign}(\delta h) \neq \text{sign}(V_x - V_x^*)$

Therefore,

$$\dot{\mathcal{L}}_1 = -\frac{k_x(t)\sqrt{2}}{h} \left[ \sqrt{2}\mathcal{L}_1 - |\delta h|\omega_x^*\sqrt{\mathcal{L}_1} \right] \quad (25)$$

The sign of  $\sqrt{2}\mathcal{L}_1 - |\delta h|\omega_x^*\sqrt{\mathcal{L}_1}$  then has to be studied:

- a)  $\sqrt{2}\mathcal{L}_1 - |\delta h|\omega_x^*\sqrt{\mathcal{L}_1} > 0$ , which means:

$$\mathcal{L}_1(t) > \left( \frac{\omega_x^*(t)|\delta h(t)|}{\sqrt{2}} \right)^2 \quad (26)$$

Hence, as long as  $\mathcal{L}_1$  is greater than the curve described by  $\left( \frac{\omega_x^*(t)|\delta h(t)|}{\sqrt{2}} \right)^2$ ,  $\dot{\mathcal{L}}_1$  will be strictly negative.

- b)  $\sqrt{2}\mathcal{L}_1 - |\delta h|\omega_x^*\sqrt{\mathcal{L}_1} < 0$ , which means:

$$\mathcal{L}_1(t) < \left( \frac{\omega_x^*(t)|\delta h(t)|}{\sqrt{2}} \right)^2 \quad (27)$$

Therefore, as long as  $\mathcal{L}_1$  is smaller than the curve described by  $\left( \frac{\omega_x^*(t)|\delta h(t)|}{\sqrt{2}} \right)^2$ ,  $\dot{\mathcal{L}}_1$  will be strictly positive.

Up to this point, we have proved that  $\mathcal{L}_1$  converge toward  $\left( \frac{\omega_x^*(t)|\delta h(t)|}{\sqrt{2}} \right)^2$ . Let us now have a look at the system's behavior when we have equality. The latter case will now be studied to explain what the aforementioned convergence means from the physical point of view.

- c)  $\sqrt{2}\mathcal{L}_1 - |\delta h|\omega_x^*\sqrt{\mathcal{L}_1} = 0$ , which means:

$$\mathcal{L}_1(t) = \left( \frac{\omega_x^*(t)|\delta h(t)|}{\sqrt{2}} \right)^2 \quad (28)$$

Since  $\mathcal{L}_1 = \frac{1}{2}(h\omega_x - h^*\omega_x^*)^2$ , as long as  $\mathcal{L}_1$  is located on the curve described by  $\left( \frac{\omega_x^*(t)|\delta h(t)|}{\sqrt{2}} \right)^2$  ((28) is verified), we have:

$$|h\omega_x - h^*\omega_x^*| = \omega_x^*|\delta h| \quad (29)$$

Lastly, a trivial sign study has to be conducted on (29). The first case would be  $\text{sign}(\delta h) = \text{sign}(h\omega_x - h^*\omega_x^*) = \text{sign}(V_x - V_x^*)$ , which is not in keeping with the hypothesis stated above ( $\text{sign}(\delta h) \neq \text{sign}(V_x - V_x^*)$ ).

The only possible solution is then  $\text{sign}(\delta h) \neq \text{sign}(h\omega_x - h^*\omega_x^*)$  which yields:

$$h\omega_x - h^*\omega_x^* = -\omega_x^*\delta h = \omega_x^*h - \omega_x^*h^* \quad (30)$$

with  $\delta h = h^* - h$ , we obtain

$$h\omega_x - h^*\omega_x^* = \omega_x^*h - \omega_x^*h^*$$

Finally, when (28) is satisfied, this means that  $\omega_x = \omega_x^*$ .

Although the signs of  $\delta h$  and  $(V_x - V_x^*)$  are unknown and depend on the initial conditions, it was observed in practice that these signs remain unchanged throughout the descent. As can be seen from Fig. 6, at all values of  $\delta h_0 \in [-180; 180]$ ,  $\mathcal{L}_1(t)$  increases when it is smaller than the curve described by  $\left( \frac{|\delta h|\omega_x^*}{\sqrt{2}} \right)^2$  and decreases when it is greater, which means that  $\omega_x$  tends toward  $\omega_x^*$ . This theoretical sign study showed that:

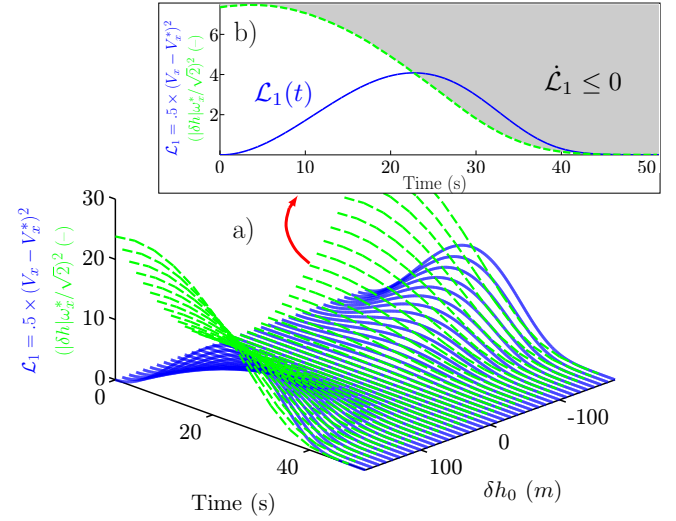


Fig. 6. a) Evolution of the Lyapunov function  $\mathcal{L}_1 = \frac{1}{2}(h\omega_x - h^*\omega_x^*)^2$  (solid blue) for  $h_0 = h_0^* \pm 10\%$  and  $V_{x0} = V_{x0}^* + 0.03$  b) Evolution of the Lyapunov function  $\mathcal{L}_1$  (solid blue) versus time with  $h_0 = h_0^* - 100$  and  $V_{x0} = V_{x0}^* + 0.03$

- the control law  $u_x$  ensures that  $V_x$  tends asymptotically toward  $V_x^*$  when there exists a time  $t^* > 0$  such that  $t \geq t^*$   $\text{sign}(\delta h) = \text{sign}(V_x - V_x^*)$ ,
- the control law  $u_x$  ensures that  $\omega_x$  tends asymptotically toward  $\omega_x^*$  when there exists a time  $t^* > 0$  such that  $t \geq t^*$   $\text{sign}(\delta h) \neq \text{sign}(V_x - V_x^*)$ .

In addition, although the convergence of  $V_x$  cannot be ensured in all cases, one can see that the Lyapunov function tends in practice toward 0 (i.e.,  $V_x$  tends toward  $V_x^*$ ) with all initial heights as from 1800 m  $\pm 10\%$ . The insert in Fig. 6 gives a typical example, where  $h_0 = h_0^* - 100$  and  $V_{x0} = V_{x0}^* + 0.03$ .

To deal with the vertical dynamics, we apply the same Lyapunov based approach, taking the control signal to be:

$$u_z = m_{ldr} \left( g_{Moon} + \dot{V}_z^* - k_z(t)(\omega_z - \omega_z^*) \right) \quad (31)$$

Which yields the same sign results and conclusions with:

$$\dot{\mathcal{L}}_2 = -\frac{k_z(t)\sqrt{2}}{h} \left[ \sqrt{2}\mathcal{L}_2 + \delta h\omega_z^*\text{sign}(V_z - V_z^*)\sqrt{\mathcal{L}_2} \right] \quad (32)$$

where  $k_z(t)$  is a strictly positive time varying gain (described below the proof). Based on a similar sign study, it can be proved that when  $\text{sign}(\delta h) = \text{sign}(V_z - V_z^*)$ , the control

law  $u_z$  ensures that  $V_z$  tends asymptotically toward  $V_z^*$  and when  $\text{sign}(\delta h) \neq \text{sign}(V_z - V_z^*)$ , the control law  $u_z$  ensures that  $\omega_z$  tends asymptotically toward  $\omega_z^*$ . It can be noted that a feedforward term was included in both  $u_x$  and  $u_z$  (see (21),(31)). The pre-determined optimal horizontal and vertical acceleration trajectories ( $\dot{V}_x^*$  and  $\dot{V}_z^*$ , respectively) are therefore used in this control scheme.

In order to account for the physical saturation of the delivered control signal  $u_{th} = \sqrt{u_x^2 + u_z^2}$ , the gains  $k_x(t)$  and  $k_z(t)$  are expressed as the product of a nominal part (positive constants) and a time varying part  $0 < \lambda \leq 1$  preventing saturation so that:

$$\begin{pmatrix} k_x(t) \\ k_z(t) \end{pmatrix} = \lambda \begin{pmatrix} k_x \\ k_z \end{pmatrix} \quad (33)$$

We now have to find an analytical solution for  $\lambda$ .

$$u_{th} = m_{ldr} \sqrt{\left(\dot{V}_x^* - \lambda k_x \varepsilon_{\omega_x}\right)^2 + \left(g_{Moon} + \dot{V}_z^* - \lambda k_z \varepsilon_{\omega_z}\right)^2}$$

In cases where  $u_{th} \leq u_{max}$  (where  $u_{max} = 3820$  N),  $\lambda$  is adopted so that  $\lambda = 1$  (no saturation is required).

In the saturated case ( $u_{th} > u_{max}$ ), the actually delivered control signal is set to  $u_{th} = u_{max}$  and we have to prove that a value of  $\lambda$  exists such that the stability proof holds (there exists a  $0 < \lambda \leq 1$  such that a positive gain  $k_x(t)$  exists).

We know that when  $\lambda = 1$ , we have  $u_{th} > u_{max}$  (the saturated case). In addition, when  $\lambda = 0$ , we have  $u_{th} = u_{th}^*$  (with no feedback) and we know that  $u_{th} = u_{th}^* < u_{max}$  (a 10% margin on the control signal is added in the optimal control problem so that the optimal control sequence does not reach saturation). Since the expression for  $u_{th}(\lambda)$  is a continuous function in  $\lambda \in ]0; 1[$ , there exists a  $\lambda \in ]0; 1[$  such that:

$$m_{ldr} \sqrt{\left(\dot{V}_x^* - \lambda k_x \varepsilon_{\omega_x}\right)^2 + \left(g_{Moon} + \dot{V}_z^* - \lambda k_z \varepsilon_{\omega_z}\right)^2} = u_{max} \quad (34)$$

Lastly, it can be concluded that  $\forall t \geq 0$  there exists a  $0 < \lambda \leq 1$  such that the control signal can be saturated ( $u_{th} = u_{max}$ ) if necessary.

It is worth noting that all the optimal signals appearing in the control laws (marked with a \*) could be replaced by any pre-computed reference signals, which do not have to be the optimal ones.

### B. Pitch control law

The inner control loop is based on a sub-optimal guidance scheme feeding a proportional derivative controller with a feedforward action.

Since the pitch dynamics were defined as a double integrator (2), the control law was designed as follows:

$$u_{\theta}(t) = u_{\theta}^{ff}(t) + K_p \varepsilon_{\theta}(t) + K_d \frac{d}{dt} \varepsilon_{\theta}(t) \quad (35)$$

where  $u_{\theta}^{ff}(t)$  corresponds to the optimal control sequence  $u_{\theta}^*(t)$  computed in Sec. V and  $\varepsilon_{\theta}(t) = \theta_{meas}(t) - \theta_*(t)$ .

Another possible approach would have consisted in defining the reference pitch trajectory based on the control signals  $u_x$  and  $u_z$  such that  $\theta_{ref}(t) = \arctan\left(\frac{u_x}{u_z}\right)$ . However, the results obtained using this strategy showed that  $\theta_{ref}(t) = \arctan\left(\frac{u_x}{u_z}\right)$  were liable to give a very noisy, non-smooth reference signal (e.g. when  $u_z \rightarrow 0$ ). In addition, since the closed-loop system closely matches the optimal OF trajectory, which was defined in keeping with a optimal pitch trajectory,  $\theta^*(t)$  was used as the attitude control loop reference signal. In conclusion, this virtual decoupling between the two loops prevents noise from being transmitted from the 6-pixel VMS to the pitch controller while providing a consistent reference pitch trajectory.

Gains  $K_p$  and  $K_d$  were defined using classical pole placement methods on a double integrator system, thus giving the closed-loop faster dynamics than the outer loop (OF control).

### C. Simulation results

The results of the closed-loop simulation performed with PANGU using 2 gimbaled OF sensors show that the GNC strategy implemented with software-in-the-loop constitutes an efficient means of performing soft landing, since the final constraints in terms of the velocity and the attitude are almost met ( $V_{x_f}$  is slightly higher than 1 m/s). In this study, the attitude measurements were taken to be perfect throughout the whole simulated descent phase. Well-known drawbacks of IMU devices such as drift and measurement noise extensively studied in the literature are beyond the scope of this paper. Figure 7 shows the landing scenario simulated in closed loop using the sub-optimal guidance strategy, the two decoupled feedback loops in a SIL simulation using PANGU and 2 gimbaled 6-pixel VMSs taking simplified actuator dynamics (as first order systems) and thrust saturation into account.

From Fig. 7.a, Fig. 7.d and Fig. 7.e, the present sub-optimal guidance and control scheme makes it possible to obtain a trajectory ( $V_x(t)$ ,  $V_z(t)$ ,  $x(t)$ ,  $h(t)$ ,  $\theta(t)$ ) which is similar to the optimal trajectory computed using non-linear programming methods. In Fig. 7.b, it can be seen that the OF follows the reference signals. Figure 7.c shows the control input ( $u_{th}$ ), which is very similar to the optimal control sequences presented in Fig. 5.b).

The black dots in this figure indicate the sensor initiation phase. Two seconds before reaching HG, the sensors are switched on. In simulations, the lander is in open loop up to  $h = 1800$ m. In real landings, however, another GNC strategy would have to be used prior to High Gate.

Up to this point, we have taken the two 6-pixel VMSs to be gimbaled and therefore to be able to directly measure  $\omega_x = \frac{V_x}{h}$  and  $\omega_z = \frac{V_z}{h}$  (see (11) and (12)).

In the following section, a linear least squares regression is performed to estimate  $\omega_x$  and  $\omega_z$  using 20 OF sensors fixed to the lander's structure, thus doing away with the need to use any gimbaled system.

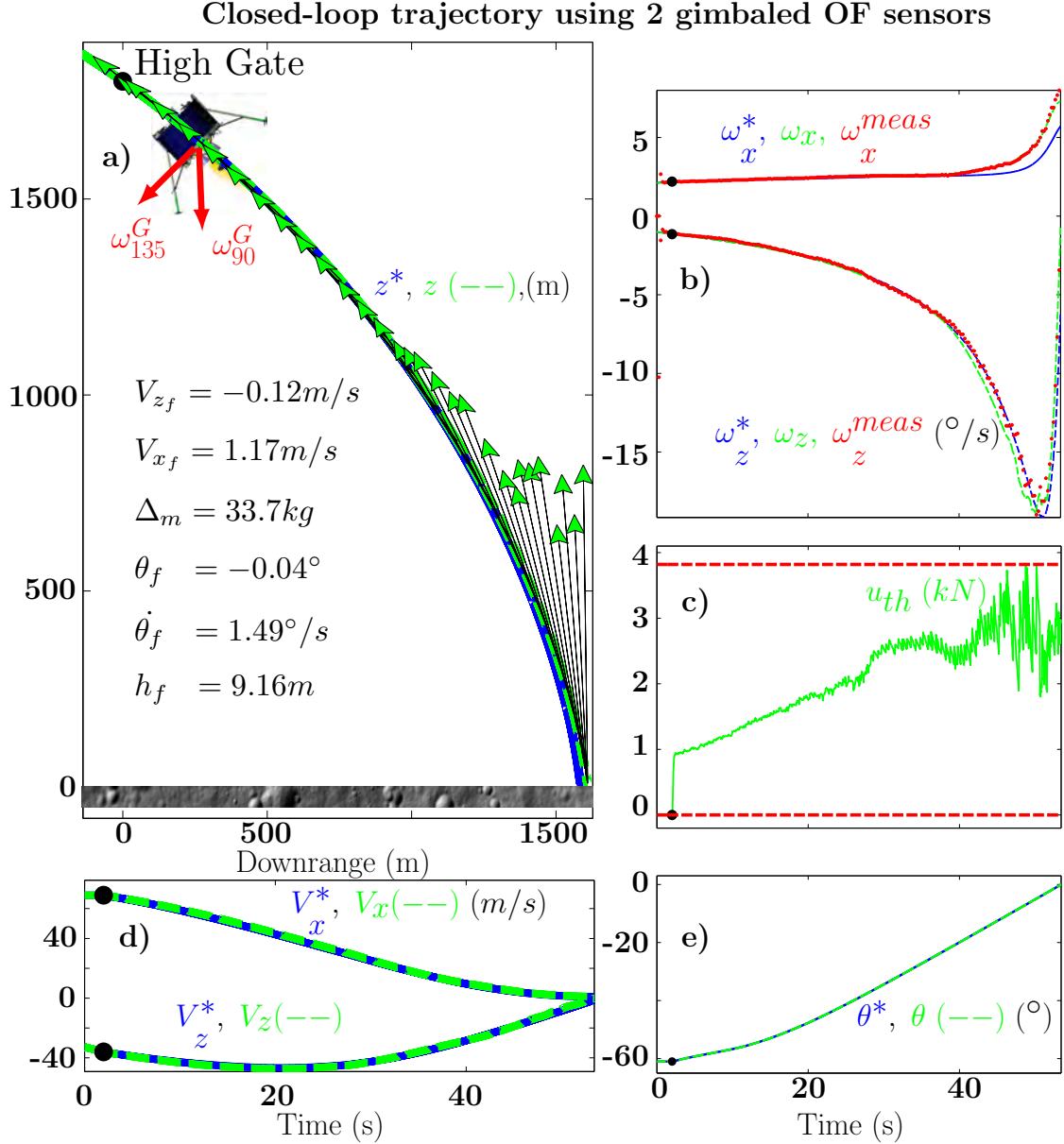


Fig. 7. Closed-loop response from HG to LG in a SIL simulation performed on PANGU using 2 gimbaled OF sensors. a) Height  $h$  versus downrange  $x$  (green dashed), optimal trajectory  $h^*(x)$  (solid blue line), orientation and normalized magnitude of the control input  $u_{th}$ . b) Optimal reference OF profiles (dashed black lines), ground-truth OF (solid red lines) and measured OF (dotted blue lines). c) Control sequence  $u_{th} = \sqrt{u_x^2 + u_z^2}$ . Saturation of the control signal  $u_{th}$  is such that  $0 \text{ N} \leq u_{th} \leq 3820 \text{ N}$ . d) Velocities  $V_x$ ,  $V_z$  (dashed lines) and optimal references (solid lines). e) Optimal pitch reference trajectory (solid line) and actual pitch (dashed line). Black dots indicate the times at which the lander reaches HG.

## VII. NON-GIMBALED OF SENSOR SET-UP

### A. Problem formulation

Since the goal pursued here consists in ensuring soft lunar landing and the solution therefore needs to be cost- and weight-saving, it was not proposed to embed a gimbal system onboard the lander. In the presence of sensors fixed to the lander's structure, the OF measurements depend on the pitch angle, which directly affects the distance to the ground in the gaze direction  $D$ , as illustrated in Fig. 8.

The control strategy based on the OF regulators described in section VI involved the use of only a few specific OF values,

which were of particular interest due to their mathematical expressions:  $\omega_x$  and  $\omega_z$ , as defined in (11)-(12).  $\omega_x$  and  $\omega_z$  can easily be obtained from  $\omega_{90^\circ}$  and  $\omega_{135^\circ}$  when they are available, but this is rarely the case. An estimation algorithm is therefore required to approximate the values of  $\omega_x$  and  $\omega_z$  from the OF measurements available at each time step. The main idea here is to increase the number of VMSs on the lander so as to be able to estimate these useful values. To express  $\omega_x$  and  $\omega_z$  based on just a few measurements, we implemented and simulated a method involving the use of a linear least squares algorithm using multiple sensors' outputs.

The general expression for the translational OF after the

derotation process (i.e.  $\omega_\Phi = \omega_T = \omega_{measured} - \omega_R$ ) is defined as follows:

$$\omega_\Phi = \frac{V}{D} \sin(\Phi) \quad (36)$$

with  $\Phi = \alpha + \theta + \gamma$ , where  $\alpha > 0$  is the fixed angle between the orientation of the OF sensor and the vector  $\vec{x}_b$  and  $(\theta; \gamma) < 0$ .

Figures 8.a-c and Fig. 8.e show the actual low-speed VMS electronic board (Fig. 8.b gives the front view, and Fig. 8.c gives the rear view) and custom-made packaging (Front view in Fig. 8.a, top view in Fig. 8.e), Fig. 8.d gives the notations, reference frames and illustrates the previous statement  $\Phi = \alpha + \theta + \gamma$  about an enhanced OF sensor configuration. Figures 8.f-g show the lander equipped with 20 VMSs installed  $5^\circ$  apart.

We now have to find the equation that describes the evolution of the OF at a given ground height  $h$  and velocity  $V$ , depending on the gaze direction (defined by  $\alpha$  and  $\theta$ ). Assuming the presence of a flat terrain, the distance to the ground in the gaze direction can be expressed as follows:

$$D = \frac{h}{\cos(\alpha - \frac{\pi}{2} + \theta)} = \frac{h}{\sin(\alpha + \theta)} \quad (37)$$

Finally, we obtain:

$$\omega_{\alpha+\theta}(t) = \frac{V(t)}{h(t)} \sin(\alpha + \theta(t)) \sin(\alpha + \theta(t) + \gamma(t)) \quad (38)$$

where  $\alpha$  and  $\theta$  are initially given and measured parameters, respectively.

Equation (38) describes the evolution of the OF in the case of a sensor oriented at the angle  $\alpha$ . It is worth noting that this is a nonlinear time varying expression.

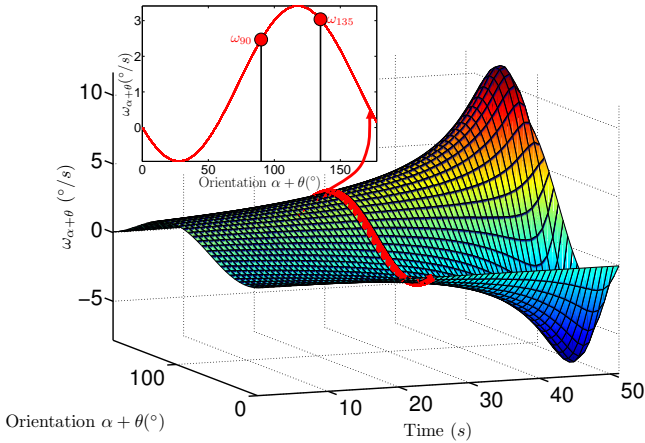


Fig. 9. a) Evolution of  $\omega_{\alpha+\theta}(t)$  with time in the case of the optimal reference descent trajectory presented in Fig. 5. b) OF characteristics depending on the gaze direction at  $t = 25.72$  s (i.e. for  $V_x = 29.25$  m/s,  $V_z = -44.52$  m/s and  $h = 675.12$  m). Values of particular interest  $\omega_{90^\circ}$  and  $\omega_{135^\circ}$  are given in red.

Figure 9 gives the evolution of the OF  $\omega_{\alpha+\theta}(t)$  with time during the optimal reference descent trajectory presented in Fig. 5 with  $\theta(t_i) = 0$  and  $\alpha \in [0; \pi]$  (the boundary values correspond to an infinite ground). The insert in the Fig. 9 shows the values of particular interest  $\omega_{90^\circ}$  and  $\omega_{135^\circ}$  at time  $t_i$ . It is worth noting that from one time step to the next, the

number of ground-oriented OF sensors is liable to vary, which affects the magnitude and hence the difficulty of the problem.

Assuming the presence of a flat ground, the OF sensor fixed at the angle  $\alpha$  will no longer be ground-oriented when the following inequality is not satisfied:

$$-\alpha \leq \theta \leq -\alpha + \pi \quad (39)$$

It is necessary to identify all the OF sensors that do not satisfy the ground orientation condition (39). Figure 10 gives an overview of the evolution of the orientation of each OF sensor depending on the pitch angle. Only the OF sensors oriented between  $0^\circ$  and  $180^\circ$  (between the two dash-dotted black lines in Fig. 10) will provide useful OF measurements, since they are oriented toward the ground. Under real-life conditions, these boundaries have to be tightened due to the fact that the lunar radius is not infinite. The OF at the Focus of Expansion (FoE) is always null, and in the immediate neighborhood, it is approximately null: there is therefore no point in having any OF sensors oriented in this direction. The red dashed line in Fig. 10 gives the orientation of the FoE defined by  $\tan^{-1}\left(\frac{V_z}{V_x}\right)$ .

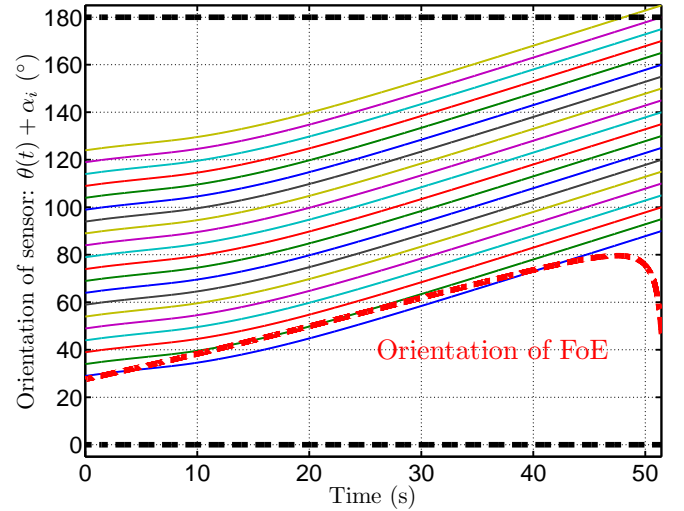


Fig. 10. Evolution of the OF sensor's orientation  $\theta(t) + \alpha_i$  during a reference descent trajectory in a set-up including 20 OF sensors oriented every  $5^\circ$ .

It is worth noting that in this configuration, at least 19 out of the 20 sensors are pointing in an appropriate direction at any time, i.e., in a ground-oriented direction which is far enough from the FoE.

Equation (39) is checked in the case of each OF sensor by applying a ground-oriented sensor selection algorithm at each time step.

During the PANGU simulations, OF sensors were sky-oriented even when the condition described in (39) was met, because of the size of the Digital Elevation Model, which is limited to  $2^n \times 2^n$  m (N is usually set at 12 or 13 depending on the sensor configuration). Without knowing either the height or the absolute position on the Digital Elevation Model, geometric criteria cannot be used to determine which OF sensors are pointing out of the map. Whenever a 6-pixel OF sensor is sky-oriented, its photodiodes' raw visual signals decrease

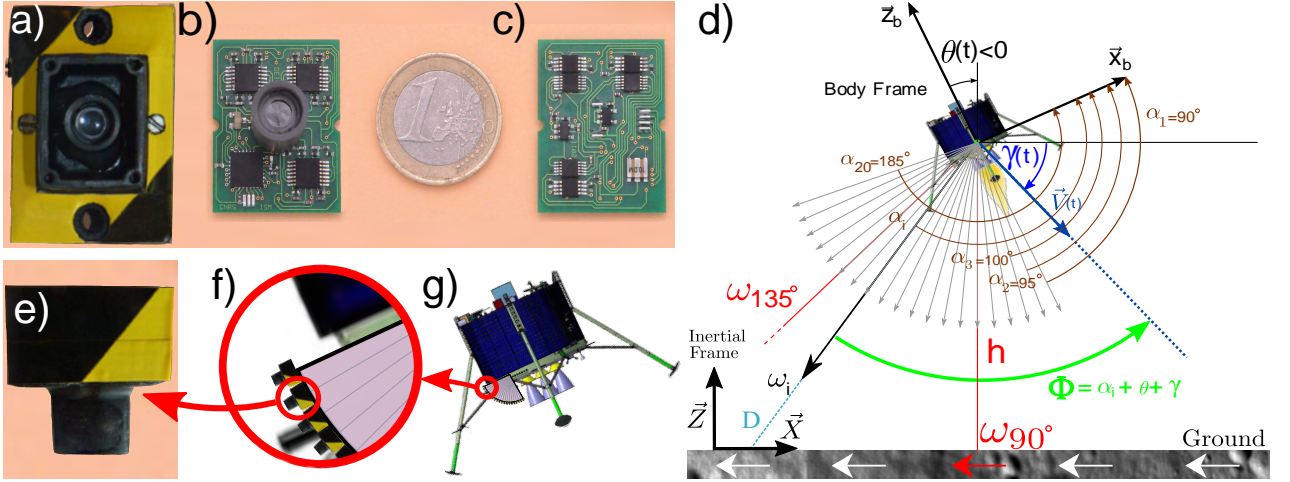


Fig. 8. a) Front view of the custom-made protective case of the VMS. b)-c) Front and back view of the low-speed 6-pixel VMS. From [36]. d) Lander with 20 embedded VMSs with a non-null pitch angle:  $\omega_i = \frac{V}{D} \sin(\alpha_i + \theta + \gamma)$ ,  $(\theta; \gamma) < 0$ . e) Top view of the VMS. f) Zoom on the proposed implementation of the VMSs fixed to the lander's structure (1 sensor every  $5^\circ$  from  $90^\circ$  to  $185^\circ$ ). g) Overall view of the lander equipped with 20 embedded VMSs approaching the lunar ground.

to approximately zero (PANGU generates stars, which trigger a residual visual signal): this OF sensor is then rejected as long as  $\sum_{i=1}^6 ph_i < threshold$ , where  $ph_i$  denotes the  $i^{th}$  photodiode signal ( $threshold$  is set experimentally at a higher value than the sum of six photodiodes oriented toward a sky full of stars).

### B. Least squares estimation

It was then proposed to estimate both  $\omega_x$  and  $\omega_z$  based on a limited number of OF measurements giving results which were at least as accurate as those which would have been obtained with a gimbaled mounted sensor subjected to the same measurement dispersion. Instead of estimating  $(\omega_{90^\circ}, \omega_{135^\circ})$  to compute  $\hat{\omega}_x$  and  $\hat{\omega}_z$ , an expression for the OF measurement can be obtained for every  $\alpha_i$  in terms of  $\omega_x = \frac{V_x(t)}{h(t)}$  and  $\omega_z = \frac{V_z(t)}{h(t)}$ .

$$\omega_{\alpha_i + \theta(t)} = \frac{1}{2} \begin{bmatrix} 1 - \cos(2(\alpha_i + \theta(t))) & \sin(2(\alpha_i + \theta(t))) \end{bmatrix} \begin{bmatrix} \frac{V_x(t)}{h(t)} \\ \frac{V_z(t)}{h(t)} \end{bmatrix} \quad (40)$$

It is therefore theoretically possible to deduce  $\omega_x$  and  $\omega_z$  based on only two measurements as long as the matrix is invertible:

$$\begin{bmatrix} \omega_x \\ \omega_z \end{bmatrix} = \frac{1}{2} \begin{bmatrix} 1 - \cos(2(\alpha_1 + \theta)) & \sin(2(\alpha_1 + \theta)) \\ 1 - \cos(2(\alpha_2 + \theta)) & \sin(2(\alpha_2 + \theta)) \end{bmatrix}^{-1} \begin{bmatrix} \omega_{\alpha_1 + \theta} \\ \omega_{\alpha_2 + \theta} \end{bmatrix} \quad (41)$$

By increasing the number of measurements, the estimated output can be improved and null determinant issues can be avoided. However, since the matrix will no longer be a square matrix, the Moore-Penrose pseudoinverse defined as  $A^+ = (A^T A)^{-1} A^T$  can be used to obtain an estimation of  $\begin{bmatrix} V_x(t)/h(t) & V_z(t)/h(t) \end{bmatrix}^T$ .

$$\begin{bmatrix} \hat{\omega}_x^{LS}(t) \\ \hat{\omega}_z^{LS}(t) \end{bmatrix} = \frac{1}{2} A^+ \begin{bmatrix} \omega_{\alpha_1 + \theta(t)} \\ \vdots \\ \omega_{\alpha_N + \theta(t)} \end{bmatrix} \quad (42)$$

where

$$A = \begin{bmatrix} 1 - \cos(2(\alpha_1 + \theta(t))) & \sin(2(\alpha_1 + \theta(t))) \\ \vdots & \vdots \\ 1 - \cos(2(\alpha_N + \theta(t))) & \sin(2(\alpha_N + \theta(t))) \end{bmatrix} \quad (43)$$

and the upper script  $LS$  denotes the output of the linear least squares algorithm. It is worth noting that the expressions described in (11) and (12) correspond to a specific case of the least squares formulation, where two gimbaled sensors are oriented toward  $90^\circ$  and  $135^\circ$  from the local horizontal.

### C. Results

A study of the standard deviation of the error was conducted in order to determine the number of OF sensors to be used in the least squares algorithm. This basically amounts to making a trade-off between the accuracy required in the estimation and the complexity and weight of the embedded sensors and the algorithm. Figure 11.a shows the standard deviation of the error for all possible implementations from 2 sensors to 50. The noise added to the measurements consists of pseudo-random values based on the standard uniform distribution in the interval  $[-3^\circ/s, 3^\circ/s]$ .

To make the number of sensors selected at least as accurate as that obtained with the gimbaled solution, the standard deviation error of the  $\hat{\omega}_x^{LS}$ ,  $\hat{\omega}_z^{LS}$  estimated using  $N$  non-gimbaled OF sensors was compared with the result obtained using a direct method of estimation based on 2 gimbaled sensors  $\omega_{90^\circ}^G$  and  $\omega_{135^\circ}^G$  (see (11)-(12)), where the upper script  $G$  denotes the output of a gimbaled sensor. As a design criterion for setting the number of OF sensors, the standard deviation of the error in the least squares estimation had to be of the same order of magnitude as the value obtained in the case of gimbaled sensors.

The results of the simulation showed that the use of the linear least squares algorithm to estimate  $\hat{\omega}_x^{LS}$  and  $\hat{\omega}_z^{LS}$  in a setup including 20 OF sensors separated by a fixed angle

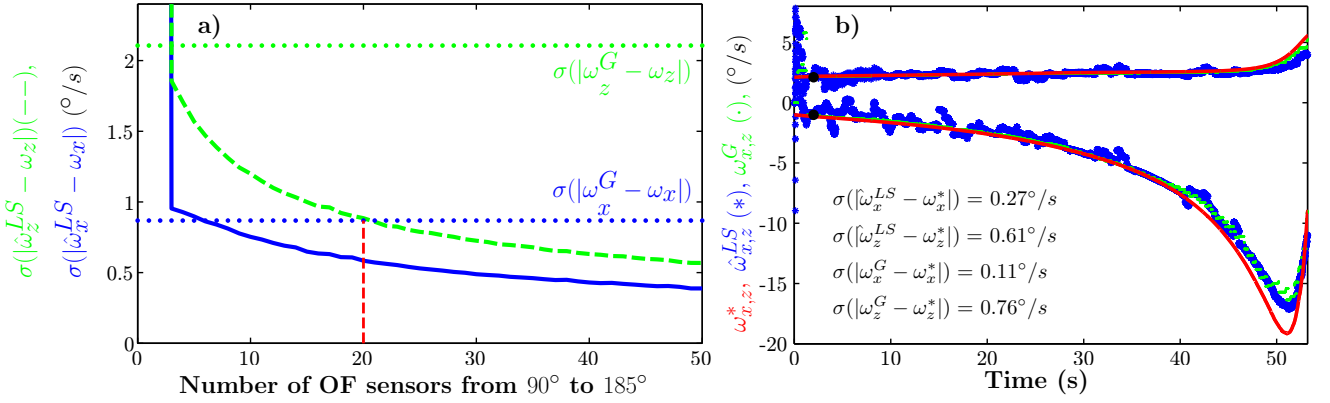


Fig. 11. a) Standard deviation of the error between  $\omega_x$  and  $\hat{\omega}_x^{LS}$  (blue) ( $\omega_z$  and  $\hat{\omega}_z^{LS}$  (green)) versus the number of OF sensors equally spaced between  $90^\circ$  and  $185^\circ$  during an optimal reference descent trajectory. The dashed horizontal line gives the standard deviation of the error of the estimates obtained using 2 gimbaled OF sensors:  $\omega_x^G = \omega_{90^\circ}^G$  and  $\omega_z^G = \omega_{90^\circ}^G - 2\omega_{135^\circ}^G$  where  $\omega_{i^\circ}^G$  denotes the measurement obtained with an OF sensor oriented downward at  $i^\circ$  from the local horizontal. A total number of 20 sensors (placed  $5^\circ$  apart) therefore constitutes an acceptable compromise between the accuracy requirements and the complexity of the implementation. b) Validation of the least squares algorithm with a 20 OF sensor configuration. Comparison between the true values of  $\omega_x$ , and  $\omega_z$  during a descent trajectory (red) and the estimated values  $\hat{\omega}_x^{LS}$  and  $\hat{\omega}_z^{LS}$  (blue) and the values that would have been measured with a sensor mounted on a gimbal system subjected to the same noise level(s)  $\omega_x^G$  and  $\omega_z^G$  (green). Black dots indicate the times at which the lander reaches HG.

is a suitable procedure. The angle between each of the sensors was set experimentally at  $5^\circ$ , from  $\alpha_{min} = 90^\circ$  up to  $\alpha_{max} = 185^\circ$ . With this configuration, it can be seen from Fig. 11.a that  $\sigma(|\hat{\omega}_x^{LS} - \omega_x|) = 0.47^\circ/s$  is below  $\sigma(|\omega_x^G - \omega_x|) = 0.87^\circ/s$  and  $\sigma(|\hat{\omega}_z^{LS} - \omega_z|) = 0.89^\circ/s$  is way below  $\sigma(|\omega_z^G - \omega_z|) = 2.11^\circ/s$  and very near  $\sigma(|\hat{\omega}_x^G - \omega_x|) = 0.87^\circ/s$  ( $0.02^\circ/s$  higher), which means that 20 OF sensors is a number giving an appropriate trade-off when the non-gimbaled method is used to estimate  $\omega_x$  and  $\omega_z$ . This procedure was then tested using PANGU: this simulation was run in open loop on the optimal scenario in order to test the validity of the navigation solution. The results obtained with the least squares algorithm using 20 non-gimbaled OF sensors on PANGU and the results of the estimation based on 2 gimbaled OF sensors are given in Figure 11.b.

It can be seen from Fig. 11.b as expected, that the standard deviation of the error with  $\hat{\omega}_x$  was reasonably similar to the value obtained with the gimbaled measurements ( $\sigma(|\hat{\omega}_x^{LS} - \omega_x|) = 0.27^\circ/s$  versus  $\sigma(|\omega_x^G - \omega_x|) = 0.11^\circ/s$ ) and that the standard deviation of the error with  $\hat{\omega}_z^{LS}$  was even better than in the case of gimbaled measurements ( $\sigma(|\hat{\omega}_z^{LS} - \omega_z|) = 0.61^\circ/s$  versus  $\sigma(|\omega_z^G - \omega_z|) = 0.76^\circ/s$ ). Differences with the results of the theoretical study presented in Fig. 11.a are due to the fact that the actual VMS noise (occurring with the simulated VMS on PANGU generated images) differed from the pseudo-random values based on the standard uniform distribution. It can be noted that  $\sigma(|\hat{\omega}_z^{LS} - \omega_z|)$  is slightly higher than  $\sigma(|\omega_x^G - \omega_x|)$ . These results again confirm that the estimation of  $\omega_x$  and  $\omega_z$  via a least squares algorithm and 20 non-gimbaled 6-pixels VMS is sufficiently accurate in comparison with that obtained with the 2 gimbaled OF sensor method.

A well-known drawback of the least squares method of estimation is its sensitivity to noise. Even with noisy measurements, however, the linear least squares algorithm is accurate enough in the present context. Other estimation techniques

could be used in this framework. One possibility which comes to mind is to use an improved least squares regression method using weighting matrices, iterative methods or nonlinear least squares, but this method failed to improve the estimates obtained in the preliminary investigations (not shown).

#### VIII. COMPLETE GNC SIMULATION USING PANGU

Lastly, the full GNC strategy presented in this paper was simulated using PANGU. The main features on which this strategy is based are:

- sub-optimal OF and pitch guidance with respect to the fuel consumption,
- two decoupled control loops for performing OF and pitch reference tracking
- and the non-gimbaled OF fusion algorithm for estimating  $\omega_x$  and  $\omega_z$  using 20 OF sensors in SIL simulations.

In the simulation 20 OF sensors are fixed to the lander's structure every  $5^\circ$  at an angle of  $\alpha \in [90^\circ; 185^\circ]$ .

Table II gives the results of the SIL simulation performed in closed-loop with PANGU using 2 gimbaled versus 20 non-gimbaled OF sensors and shows the relative errors in the fuel consumption, vertical velocity braking and horizontal velocity braking:

*Relative error computation*

$$\varepsilon_{\Delta m} = \frac{\Delta m - \Delta m^*}{\Delta m^*}, \quad \varepsilon_{V(x,z)} = \frac{(V_{(x,z)_0} - V_{(x,z)_f})(V_{(x,z)_0}^* - V_{(x,z)_f}^*)}{V_{(x,z)_0}^* - V_{(x,z)_f}^*}$$

This simulation shows that the closed-loop control strategy almost meets the demanding final constraints despite the decoupling of the two control loops, the control input transformation ( $u_{th} = \sqrt{u_x^2 + u_z^2}$ ) and the input control saturation.

In addition, simulations performed with 2 gimbaled (Fig. 7) and 20 non-gimbaled (Fig. 12) OF sensors yielded practically the same results at LG, which confirms the validity of our new navigation strategy based on OF sensors fixed to the structure. Figure 12 gives the results obtained on PANGU using the linear least squares algorithm. Figure 12.a gives the

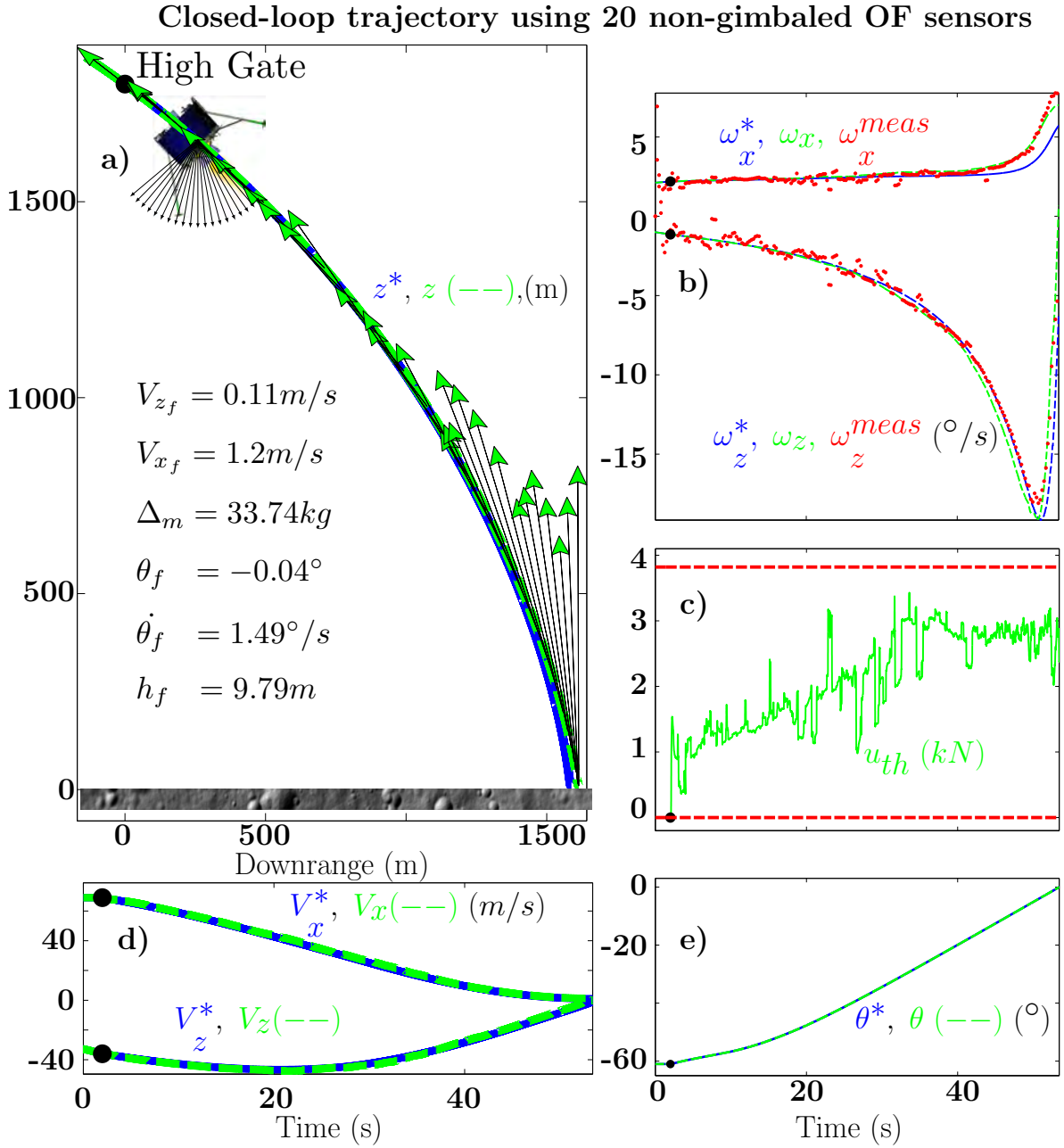


Fig. 12. Closed-loop response from HG to LG obtained in a SIL simulation on PANGU using 20 non-gimbaled OF sensors. a) Height  $h$  versus downrange  $x$ , orientation and normalized magnitude of the control input  $u_{th}$ . b) Measured OF (red dotted lines), ground-truth OF (dashed green lines) and optimal reference OF profile (blue solid lines). c) Control sequence  $u_{th} = \sqrt{u_x^2 + u_z^2}$ . Saturation of the control signals  $u_{th}$  was such that  $0 \text{ N} \leq u_{th} \leq 3820 \text{ N}$ . d) Velocities  $V_x$ ,  $V_z$ . e) Pitch reference trajectory (solid line) and actual pitch signal. Black dots indicate the times at which the lander reaches HG.

trajectory taken and the final conditions obtained at LG. It can be seen that the vertical velocity (Fig. 12.e along with the horizontal velocity) and the pitch angle (Fig. 12.f) met the final constraints. The horizontal velocity was still slightly higher than necessary:  $V_{x_f} = 1.2 \text{ m/s}$ , which amounts to a 0.3% error in the expected braking (from 69m/s at HG to 1m/s at LG). In terms of the fuel consumption, 33.74kg of propellant was consumed, which amounts to only 0.51% more than in the optimal open-loop control case. The input signals in Fig. 12.d are quite far from the upper saturation point (except

during the last few seconds); and the output of the linear least squares algorithm run using the 20 bidirectional low speed OF sensors as shown in Fig. 12.b-c is quite smooth. In conclusion, the present results show that our sub-optimal GNC approach based on the use of non-gimbaled bio-inspired OF sensors meets the demanding final constraints at LG without any need for linear velocity or altitude data.

TABLE II

COMPARISON BETWEEN FINAL CONDITIONS IN THE OPTIMAL OPEN LOOP CONTROL AND SUB-OPTIMAL CLOSED-LOOP SIMULATIONS WITH PANGU (RELATIVE ERRORS IN THE FUEL CONSUMPTION AND VELOCITIES WITH RESPECT TO THE OPTIMAL TRAJECTORY ARE PRESENTED).

	Optimal computed trajectory in terms of the fuel consumption ( $u_x^*$ , $u_z^*$ )	Closed-loop response with 2 gimbaled OF sensors oriented at angles of 90° and 135°	Closed-loop response with non-gimbaled 20 OF sensors oriented every 5°
$h_f$ (m)	10	9.16	9.79
$x_f$ (m)	1585	1610	1614
$\Delta m$ (kg)	33.57	33.7 (0.39%)	33.74 (0.51%)
$V_{x_f}$ (m/s)	1	1.17 (-0.25%)	1.2 (-0.29%)
$V_{z_f}$ (m/s)	-1	-0.12 (2.51%)	0.11 (3.17%)
$\theta_f$ (°)	0	-0.04	-0.04
$\dot{\theta}_f$ (°/s)	1.49	1.49	1.49

## IX. CONCLUSION

The novel GNC solution to the complex challenge of autonomous lunar landing presented here was achieved using only an IMU and insect inspired visual motion sensors. This solution involving the use of lightweight sensors might also be used as a backup GNC solution in the case of main sensors failure.

This study shows that optimal OF and pitch trajectories in terms of the fuel consumption can be obtained from the optimal control sequence computed using nonlinear programming methods in the lander's dynamic model. The optimal profiles can be fed as reference signals to the two decoupled loops driving the translational/expansional OF ( $\omega_x$  and  $\omega_z$ ) and the attitude (i.e. the pitch angle). In this new approach to the problem of OF based landing, which has been widely studied in the literature, the entire OF and pitch profiles are determined in order to follow the optimal trajectory during the descent instead of taking an arbitrary constant reference OF value or one dictated by the objectives.

The next step will consist in increasing the complexity of the model used to deal with the optimal control problem, using a 3-D set-up (a 6 degree of freedom (DOF) configuration). Adopting planar motion for planetary landing in the case of a planet with atmosphere such as Mars would be a strong assumption. Since the wind gusts on Mars might induce strong lateral translation and rotation movements, the 6-DOF setup is mandatory even at this stage in the design process. There exist no external phenomena on the moon liable to create very strong motion on the roll, yaw and  $e_y$  axes. Thrusters' manufacturing flaws and misalignments could result in small movements (on the roll, yaw and  $e_y$  axes) that might be taken care of by an attitude control designed to keep the roll and yaw angles (and/or angular rates) at a zero reference value throughout the descent. Null yaw and roll angles (and angular rates) keep the y-motion down to zero, which means that the planar case would correspond to a full 6-DOF configuration.

However, as it is, our application could be sensitive to small angular roll and yaw motions. The time of travel scheme assesses the OF by computing the difference between the times at which two adjacent photodiodes detect a contrast, assuming that the contrast is moving in a straight line. In the case of lateral motion, contrasts are no longer moving in straight lines, which could add some bias to the measurements. If we go one step further, we could imagine hazard avoidance strategies that could be performed during the approach phase.

Avoidance maneuvers might require creating strong lateral motion to move from one landing site to another. It is therefore mandatory to provide the GNC solution with 6-DOF abilities in the following design steps. Using sensors of this kind, this could be achieved by increasing the number of pixels and adopting matrix-shaped photoreceptors.

In order to further improve the robustness of this control strategy to initial uncertainties, a set of optimal reference trajectories could be calculated offline and the most suitable one could be chosen as soon as the lander reaches High Gate, since the uncertainty about the initial OF is mainly due to uncertainty about the initial height. As previously discussed, the guidance scheme could be improved by adding a final constraint on the downrange. In addition to the bank of reference trajectories, this should make it possible to achieve roughly the same level of accuracy as that observed in the present case: landing within  $\pm 30\text{m}$  of the optimal landing site, which would correspond to making the GNC strategy capable of dealing with pinpoint landing.

Even with an elementary control scheme based on a nonlinear controller, the performances obtained here were similar to the optimal OF reference values and hence to the optimal landing profile. The closed-loop fuel consumption showed that the objectives in terms of the fuel costs and the velocities are almost met (the horizontal velocity is 0.2m/s higher than the objective at LG). It is now planned to further improve the control design in terms of the control allocation and the controllers themselves to prevent the occurrence of decoupling between the OF and the pitch feedback loop. Here we have provided theoretical proof of the asymptotic convergence of the OF and that of the velocities with the reference values in the nonlinear system.

The second major improvement made in this study was the use of a non-gimbaled sensor setup. Instead of using a bulky gyro-stabilized system, which is not feasible with these lightweight sensors, we introduced a new method of fusion using 20 sensors ingeniously oriented in fixed directions to extract the same information as that which can be obtained with a heavy gimbaled sensor system. These sensors are used to accurately determine the translational and expansional OF ( $\omega_x$  and  $\omega_z$ ). The results obtained show that thanks to the use of a suitable number of sensors, the values of ( $\hat{\omega}_x^{LS}$ ,  $\hat{\omega}_z^{LS}$ ) estimated have similar standard deviations of the error as those ( $\omega_x^G$ ,  $\omega_z^G$ ) obtained using two gimbaled OF sensors measuring ( $\omega_{90^\circ}$ ,  $\omega_{135^\circ}$ ) subjected to the same noise levels. This strategy

basically amounts to making a trade-off between the accuracy of the estimation and the complexity of the physical implementation (and the weight of the system). We have focused here on the methodological aspects of the solution, and this numerical application was based on a compromise between the computational cost and the estimation accuracy, which can be adapted to the application in question. The mathematical formulation of the problem is presented above and the solution obtained was implemented for the first time to our knowledge with such minimalistic sensors.

One of the main advantages of this distributed OF sensor configuration is that if one VMS failure occurs, the solution will keep on functioning, giving slightly lower performances but without jeopardizing the success of the entire landing, contrary to what occurs with classical solutions based on a single main sensor.

The next step will be to develop a theoretical approach for determining the optimal orientation, spacing and number of sensors required to ensure accurate estimates. Thanks to the light weight of our bio-inspired sensors, which weigh only about 2.8g despite the relatively large number of OF devices used, the present solution is still much lighter than the traditional sensor suite used to meet this GNC challenge.

This approach should therefore constitute a promising candidate for future lunar exploration missions. Every constitutive block of the GNC solution was found to be efficient in a SIL simulation involving the actual VMS code and the use of simulated images of the lunar ground generated by PANGU software.

In conclusion, the results presented here provide a promising answer to the challenge of designing means of handling the autonomous approach phase in terms of the guidance, navigation, and control of a lunar lander using the 6-pixel insect-inspired sensors mounted onboard, which were validated here using simulated images of the lunar ground.

#### ACKNOWLEDGEMENTS

We thank the editor and the two anonymous reviewers for their constructive comments, which helped us to greatly improve the manuscript. We are most grateful to P. Mouyon, S. Viollet and G. Jonniaux for their fruitful suggestions and comments during this study. We thank J. Blanc for improving the English manuscript. This research work was co-funded by CNRS Institutes (Life Science; Information Science; Engineering Science and Technology), the Aix-Marseille University, the European Space Agency, ONERA - the French Aerospace Lab - , Airbus Defence and Space (previously named ASTRIUM EADS), and ESA (European Space Agency) under the Networking/Partnering Initiative program (NPI) for advanced technologies for space.

#### REFERENCES

[1] A.A. Argyros, D.P. Tsakiris, and C. Groyer. Biomimetic centering behavior [mobile robots with panoramic sensors]. *Robotics Automation Magazine*, 11(4):21 – 30, 68, Dec. 2004.

[2] G.L. Barrows and C. Neely. Mixed-mode VLSI optic flow sensors for in-flight control of a Micro Air Vehicle. In *SPIE : Critical technologies for the future of computing*, volume 4109, pages 52–63, San Diego, CA, USA, Aug. 2000.

[3] A. Beyeler, J.C. Zufferey, and D. Floreano. OptiPilot: control of take-off and landing using optic flow. In *European Micro Aerial Vehicle Conference (EMAV)*, volume 27, Delft, Netherlands, Sept. 2009.

[4] D.C. Cheatham, F.V. Bennett, and T.M. Branch. Apollo lunar module landing strategy. In *Proceedings of the Apollo Lunar Landing Mission Symposium*, 1966.

[5] Y. Cheng and A. Ansar. Landmark based position estimation for pinpoint landing on mars. In *IEEE International Conference on Robotics and Automation (ICRA)*, pages 1573 – 1578, Apr. 2005.

[6] J. Conroy, G. Gremillion, B. Ranganathan, and J. Humbert. Implementation of wide-field integration of optic flow for autonomous quadrotor navigation. *Autonomous Robots*, 27:189–198, 2009.

[7] G. de Croon and D. Izzo. Real-time landing based on optimality principles and vision. In *23rd International Symposium on Space Flight Dynamics (ISSFD)*, 2012.

[8] O. Dubois-Matra, S. Parkes, and M. Dunstam. Testing and validation of planetary vision-based navigation systems with PANGU. In *21st International Symposium on Space Flight Dynamics (ISSFD)*, Toulouse, France, 2009.

[9] F. Expert, S. Viollet, and F. Ruffier. Outdoor field performances of insect-based visual motion sensors. *Journal of Field Robotics*, 28:529–541, 2011.

[10] P. Falugi, E. Kerrigan, and E. Van Wyk. *Imperial College London Optimal Control Software User Guide (ICLOCS)*. Department of Electrical Engineering, Imperial College London, London, UK, 2010.

[11] G. Flandin, B. Polle, B. Frapard, P. Vidal, C. Philippe, and T. Voirin. Vision based navigation for planetary exploration. In *32nd Annual AAS Rocky Mountain Guidance and Control Conference*, 2009.

[12] N. Franceschini, J.M. Pichon, and C. Blanes. From insect vision to robot vision. *Philosophical Transactions of the Royal Society of London*, 337:283–294, 1992.

[13] N. Franceschini, A. Riehle, and A.L. Nestour. *Facets of vision*, chapter 17: Directionally selective motion detection by insect neurons, pages 360–390. Springer, 1989.

[14] M.A. Garratt and J.S. Chahl. Vision-based terrain following for an unmanned rotorcraft. *Journal of Field Robotics*, 25:284–301, 2008.

[15] S. Griffiths, J. Saunders, A. Curtis, B. Barber, T. McLain, and R. Beard. Maximizing miniature aerial vehicles. *IEEE Robotics & Automation Magazine*, 13:34–43, 2006.

[16] B. Hérisse, T. Hamel, R. Mahony, and F. Russotto. A terrain-following control approach for a vtol unmanned aerial vehicle using average optical flow. *Autonomous Robots*, 29(3-4):381–399, 2010.

[17] B. Hérisse, T. Hamel, R. Mahony, and F.-X. Russotto. Landing a VTOL unmanned aerial vehicle on a moving platform using optical flow. *IEEE Transactions on Robotics*, 28(1):77 –89, Feb. 2012.

[18] A.M. Hyslop and J.S. Humbert. Autonomous navigation in three-dimensional urban environments using wide-field integration of optic flow. *Journal of guidance, control, and dynamics*, 33(1):147–159, 2010.

[19] D. Izzo and G. de Croon. Landing with time-to-contact and ventral optic flow estimates. *Journal of Guidance, Control, and Dynamics*, 35(4):1362–1367, 2011.

[20] D. Izzo and G. de Croon. Nonlinear model predictive control applied to vision-based spacecraft landing. In *Proceedings of the EuroGNC 2013, 2nd CEAS Specialist Conference on Guidance, Navigation & Control, Delft University of Technology*, pages 91–107, Delft, The Netherlands, Apr. 10-12 2013.

[21] D. Izzo, N. Weiss, and T. Seidl. Constant-optic-flow lunar landing: Optimality and guidance. *Journal of Guidance, Control, and Dynamics*, 34:1383–1395, 2011.

[22] K. Janschek, V. Tchernykh, and M. Beck. Performance analysis for visual planetary landing navigation using optical flow and DEM matching. In *AIAA Guidance, Navigation, and Control Conference and Exhibit*, 2006.

[23] T. Jean-Marius and S.E. Strandmoe. Integrated vision and navigation for a planetary lander. Technical report, AEROSPATIAL, Espace et Défense, Les Mureaux-France. ESA, ESTEC, 1998.

[24] T. Jean-Marius and S. Trinh. Integrated vision and navigation for planetary exploration - final report. Technical Report RM-TN-00-18-AS/M, Aérospatiale Espace & Défense, 1999.

[25] F. Kendoul, K. Nonami, I. Fantoni, and R. Lozano. An adaptive vision-based autopilot for mini flying machines guidance, navigation and control. *Autonomous Robots*, 27:165–188, 2009.

[26] J.J. Koenderink and A.J. Doorn. Facts on optic flow. *Biological Cybernetics*, 56:247–254, 1987.

[27] V. Medici, G. Orchard, S. Ammann, G. Indiveri, and S.N. Fry. Neuromorphic computation of optic flow data bio-inspired landing using biomorphic vision sensors. Technical report, ESA, 2010.

- [28] A.I. Mourikis, N. Trawny, S.I. Roumeliotis, A.E. Johnson, A. Ansar, and L. Matthies. Vision-aided inertial navigation for spacecraft entry, descent, and landing. *IEEE Transactions on Robotics*, 25(2):264–280, Apr. 2009.
- [29] S. Parkes, M. Dunstan, D. Matthews, I. Martin, and V. Silva. LIDAR-based GNC for planetary landing: Simulation with PANGU. In R.A. Harris, editor, *Data Systems in Aerospace (DASIA)*, page 18.1, Prague, Czech Republic, Jun. 2003.
- [30] S. Parkes, I. Martin, and M. Dunstan. Planet surface simulation with PANGU. In *8th International Conference on Space Operations (2004)*, pages 1–10, Montréal, Canada, 2004.
- [31] W. Reichardt. Movement perception in insects. *Processing of optical data by organisms and machines, International School of Physics "Enrico Fermi": Course XLIII, 1968, Academic Press*, pages 465–493, 1969.
- [32] F.L. Roubieu, F. Expert, G. Sabiron, and F. Ruffier. Two-directional 1-g visual motion sensor inspired by the fly's eye. *Sensors Journal, IEEE*, 13(3):1025–1035, 2013.
- [33] F. Ruffier and N. Franceschini. Optic flow regulation: the key to aircraft automatic guidance. *Robotics and Autonomous Systems*, 50:177–194, 2005.
- [34] F. Ruffier and N. Franceschini. Aerial robot piloted in steep relief by optic flow sensors. In *IEEE/RSJ International Conference on Intelligent Robots and Systems (IROS)*, pages 1266–1273. IEEE, 2008.
- [35] G. Sabiron, P. Chavent, L. Burlion, E. Kervendal, E. Bornsclegl, P. Fabiani, T. Raharijaona, and F. Ruffier. Toward an autonomous lunar landing based in low-speed optic flow sensors. In *Proceedings of the EuroGNC 2013, 2nd CEAS Specialist Conference on Guidance, Navigation & Control, Delft University of Technology*, pages 993–1011, Delft, The Netherlands, Apr. 10-12 2013.
- [36] G. Sabiron, P. Chavent, T. Raharijaona, P. Fabiani, and F. Ruffier. Low-speed optic-flow sensor onboard an unmanned helicopter flying outside over fields. In *IEEE International Conference on Robotics and Automation (ICRA)*, 2013.
- [37] M.A. Shoemaker and Hokamoto S. Comparison of integrated and nonintegrated wide-field optic flow for vehicle navigation. *Journal of Guidance, Control, and Dynamics*, 36:3:710–720, 2013.
- [38] M.V. Srinivasan. Honeybees as a model for the study of visually guided flight, navigation, and biologically inspired robotics. *Physiological Reviews*, 91(2):413–460, 2011.
- [39] S. Strandmoe, T. Jean-Marius, and S. Trinh. Toward a vision based autonomous planetary lander. In *AIAA Guidance, Navigation, and Control Conference and Exhibit*, Portland, OR, AIAA-99-4154, 1999.
- [40] F. Valette, F. Ruffier, S. Viollet, and T. Seidl. Biomimetic optic flow sensing applied to a lunar landing scenario. In *International Conference on Robotics and Automation (ICRA)*, pages 2253–2260, 2010.

## Software in the loop simulation: the PANGU<sup>1</sup> software

In the previous study, validations of the GNC scheme were performed on the so-called software in the loop simulations.

As discussed in introduction, following the design step of GNC comes a crucial simulation procedure which aims at validating theoretical aspects on the most representative configuration available. Several approaches might be considered.

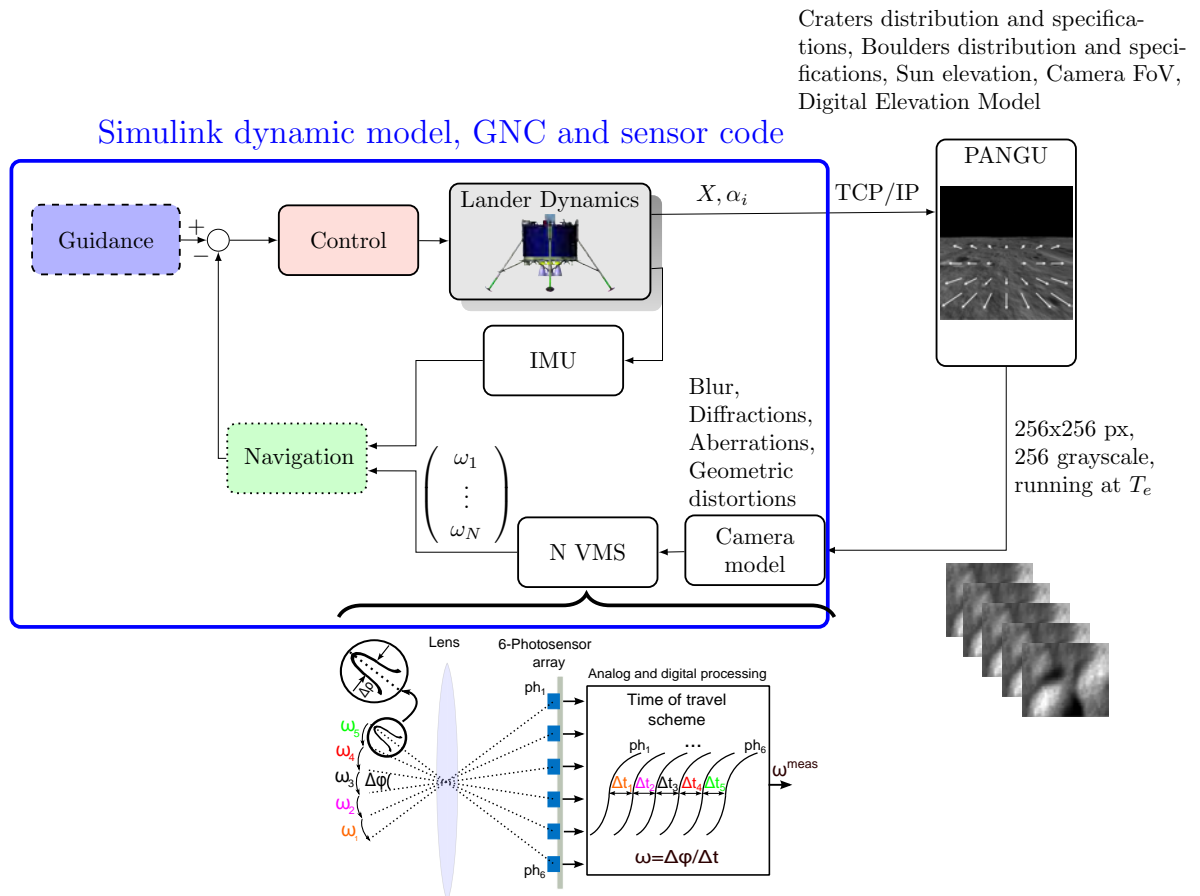


Figure 3.2.1 – Description of the software in the loop simulator. The Simulink file features the model dynamics, the GNC algorithm, the sensor actual code and a camera model. The communication between Simulink and PANGU is a TCP/IP connection used by the model to provide its position and orientation relative to the map and also used by PANGU to send the generated images back to the simulator. Images sent at 1 kHz are then processed to extract the optic flow based on the time of travel scheme.

1. The first one could be to validate the GNC on a nonlinear model of the lander using Matlab/Simulink to assess the dynamics of the system in closed loop. Knowing the entire state vector, one could extract the theoretical optic flow measurements based on analytical expression of the latest. Sometimes, a noise modeling

<sup>1</sup><https://www.star-dundee.com/products/pangu-planet-and-asteroid-natural-scene-generation-utility>

step is required to obtain sensors characteristics in the loop (delays, measurement noise, quantization of the output, ...). However, such noise models might bring other modeling uncertainties or errors.

2. Another, more advanced, solution consists in software in the loop simulations. When the sensor processing algorithm is available as well as representative data, one could add into the loop this more realistic way to produce measurements. For instance, PANGU plays the role of the representative data. It takes as input the absolute position and orientation of a vehicle and associated sensors, a digital map of the environment and camera parameters at a chosen sample time. Then PANGU provides to Matlab via TCP/IP connection the generated image which is then pre-processed by a camera model (adding blur, diffraction, aberrations, and geometric distortions). Finally, comes the sensor processing algorithm:

- Selection of the area of the image seen by each photoreceptors (50x50 pixels),
- Convolution to the Gaussian spatial angular sensitivity of the photoreceptor (to obtain a scalar which represent the illumination of the area),
- $\Delta t$  and  $\omega_{\alpha+\theta}$  computation using the code described in Chapter 2.2,

Figure 3.2.1 presents the full SIL simulation framework. One can see that the Simulink model contains the entire processing related to the vehicle's motion as well as the sensor code and finally a camera model.

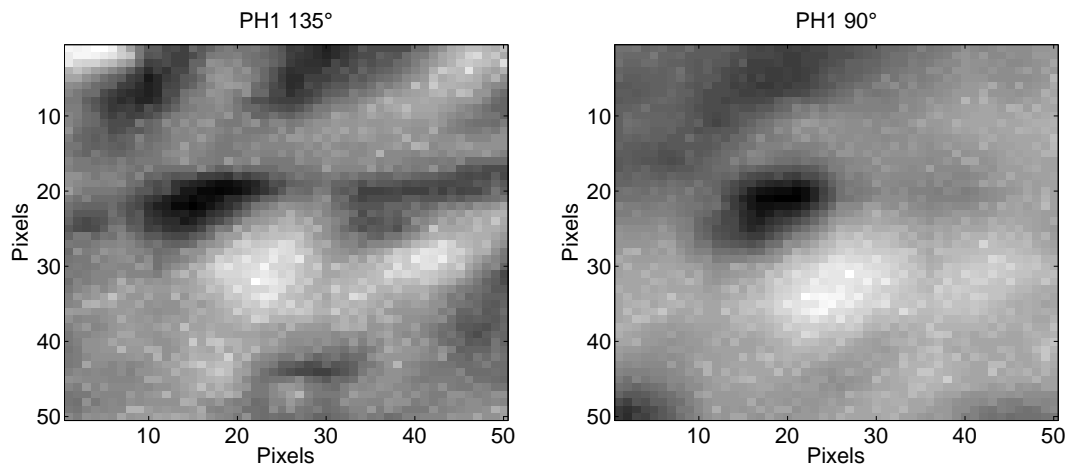


Figure 3.2.2 – 50x50 pixels images sent at 1 kHz by PANGU after the camera model processing step and before the convolution to the Gaussian angular sensitivity function of the photoreceptors.

Figure 3.2.2 presents the 50x50 pixels images right before the convolution to the Gaussian angular sensitivity function of the photoreceptors. One can see the images

seen by the photodiode 1 of the sensors looking at  $90^\circ$  and  $135^\circ$  from the local horizontal.

For all heights, PANGU provides  $256 \times 256$  pixels images. Then, the regions corresponding the field of view of each photoreceptors are extracted from this large image. These regions have a fixed resolution of  $50 \times 50$  pixels at all heights. This PANGU feature is quite interesting as compared with the use of real images such as LRO data. Indeed with LRO images, as soon as the height is greatly reduce, the resolution of the region captured by the photodiode drops to only few pixels which is not representative of the physical reality. Indeed, experimentally, when the height is decreased, the wealth of contrasts is not decreased since smaller contrasts become visible to the sensor which have been shown by Ruderman and Bialek (1994). Any natural image power density spectrum is composed of various frequencies which allows to detect contrasts regardless of the scale of the image and therefore of the distance between the system and the surrounding environment.



# ARTICLE 4: OF-BASED NONLINEAR CONTROL AND SUB-OPTIMAL GUIDANCE FOR LUNAR LANDING

## CONTENTS

---

ABSTRACT . . . . .	123
I INTRODUCTION . . . . .	123
II LUNAR LANDER DYNAMIC MODELING AND OPTIC FLOW EQUATIONS . . . . .	123
III SUB-OPTIMAL GUIDANCE STRATEGY . . . . .	124
IV LYAPUNOV-BASED NONLINEAR CONTROL DESIGN . . . . .	125
V SIMULATION RESULTS . . . . .	127
VI CONCLUSION . . . . .	128
ACKNOWLEDGMENT . . . . .	129
REFERENCES . . . . .	129



## Article 4: OF-based Nonlinear control and Sub-Optimal Guidance for lunar landing

Article submitted in IEEE International Conference on Robotics and Biomimetics (ROBIO) 2014, (In press)

Authors: G. Sabiron, L. Burlion, T. Raharijaona and F. Ruffier

In the previous chapter, we presented a full GNC solution for lunar landing based on visual motion sensors and proved the feasibility of such new approach through extensive simulations. Interesting results were obtained with an elementary control scheme featuring decoupled attitude and optic flow loops. However, this decoupling might become an issue in presence of uncertainties on the initial states. It is possible that a time discrepancy arises between the lander's attitude reference tracking and optic flow reference tracking if initial conditions are far away from nominal initial conditions. When a thrust  $u_{th}$  is delivered by the optic flow control laws, the pitch is assumed to be following closely the sub-optimal reference pitch signal. Both optic flow and attitude control loop track their respective pre-computed reference signal without any interactions between each other. Furthermore, we proved that the designed control laws ensured either the convergence of velocities or the convergence of optic flows toward their reference signals depending on a states-dependent condition.

- The control laws  $u_x$  (and respectively  $u_z$ ) ensures that  $V_x$  (and respectively  $V_z$ ) tends asymptotically toward  $V_x^*$  (and respectively toward  $V_z^*$ ) when there exists a time  $t^* > 0$  such that  $t \geq t^* \text{sign}(h^* - h) = \text{sign}(V_x - V_x^*)$  (and respectively  $\text{sign}(h^* - h) = \text{sign}(V_z - V_z^*)$ ),
- the control law  $u_x$  (and respectively  $u_z$ ) ensures that  $\omega_x$  (and respectively  $\omega_z$ ) tends asymptotically toward  $\omega_x^*$  (and respectively  $\omega_z^*$ ) when there exists a time  $t^* > 0$  such that  $t \geq t^* \text{sign}(h^* - h) \neq \text{sign}(V_x - V_x^*)$  (and respectively  $\text{sign}(h^* - h) \neq \text{sign}(V_z - V_z^*)$ ).

Even if it was not an issue in practice during the simulations performed, from a theoretical point of view it could lead to the instability if the convergence kept changing between optic flows and velocities.

We decided to improve the non linear control laws such a single type of convergence is possible (i.e.  $\omega_{x,z}$  toward  $\omega_{x,z}^*$ ). Based on a Lyapunov approach, we derived a new non linear optic flow controller ensuring global asymptotical stability and convergence

of ventral and expansion optic flow. We kept the idea of IBVS strategies, avoiding the unnecessary step of the classical state estimation and giving advantage to direct optic flow regulation. The nonlinear control laws are based on a sliding mode architecture in order to ensure robustness and optic flow convergence properties when no velocities or height are measured. The innovation lies in the fact that using an integration of  $\omega_z$ , bounds on the altitude can be obtained.

On top of that, we used the outputs of the optic flow controllers ( $u_x$  and  $u_z$ ) to compute the pitch reference signal to guarantee that the actual pitch is set in accordance with the expected thrust vector orientation. Using this new method robustness to initial uncertainties is improved as compared to the previous version of the decoupled control loops. Both loop are nested and no longer act separately to follow two separate pre-computed trajectories. We also propose theoretical simulations to validate the guidance and control strategy on a landing scenario with bias on the initial altitude.

Author contributions:

G.S. L.B., F.R. designed research;

G.S. performed research;

G.S., L.B. contributed with technical and analytic tools;

G.S. analyzed data;

and G.S. L.B., T.R., F.R. wrote the paper.

# Optic Flow-Based Nonlinear Control and Sub-optimal Guidance for Lunar Landing

Guillaume Sabiron<sup>1,2</sup>, Laurent Burlion<sup>2</sup>, Thibaut Raharijaona<sup>1</sup>, and Franck Ruffier<sup>1</sup>

**Abstract**—A sub-optimal guidance and nonlinear control scheme based on Optic Flow (OF) cues ensuring soft lunar landing using two minimalistic bio-inspired visual motion sensors is presented here. Unlike most previous approaches, which rely on state estimation techniques and multiple sensor fusion methods, the guidance and control strategy presented here is based on the sole knowledge of a minimum sensor suite (including OF sensors and an IMU). Two different tasks are addressed in this paper: the first one focuses on the computation of an optimal trajectory and the associated control sequences, and the second one focuses on the design and theoretical stability analysis of the closed loop using only OF and IMU measurements as feedback information. Simulations performed on a lunar landing scenario confirm the excellent performances and the robustness to initial uncertainties of the present guidance and control strategy.

## I. INTRODUCTION

During the last few decades, increasing attention has been paid to autonomous planetary landing, especially small lander applications requiring few resources for use in situations where mass, size and low-consumption embedded devices are of crucial importance. Applications of this kind always require a Guidance Navigation and Control (GNC) algorithm and finely tuned sensors which are able to bring the lander gently onto the ground. Minimalistic vision based systems equipped with lightweight bio-inspired sensors providing rich sensory feedback are particularly suitable for this purpose. Many authors have used vision based systems for various applications such as terrain relative navigation (see [1]), automatic landing, 3-D environment mapping and hazard avoidance. However, in most of these recent developments, a high computational cost is associated with the image processing algorithm extracting visual cues from the onboard cameras' output.

Bio-inspired devices have provided interesting solutions based on the Optic Flow (OF) cues which convey information about the relative velocity and the proximity of obstacles. The OF has been used in several studies to perform hazardous tasks such as taking off, terrain-following, and landing safely and efficiently by mimicking insects' behavior (see

[2], [3]), avoiding frontal obstacles (see [4]–[7]), tracking a moving target (see [8]) and hovering and landing on a moving platform (see [9]). We previously tested a miniature 2.8 g 6-pixel OF sensor implemented on a 80 kg helicopter by flying it outdoors over various fields, with promising results [10].

OF based lunar landing has been addressed in several studies using either a nonlinear observer coupled to a Linear Quadratic (LQ) controller to track a constant OF reference in [11] or Proportional Integral Derivative (PID) type controllers to track a constant OF reference in [12], and more recently, using a Model Predictive Control approach in [13]. After presenting theoretical results on OF based optimal control in [14], previous authors adopted an OF reference signal based on the expansion OF (an index to the vertical velocity divided by the height) which was no longer constant, but decreased constantly or exponentially (see [15]).

In the present study, trajectory tracking was performed using a precomputed fuel-optimal trajectory assessed via nonlinear programming methods in order to avoid the unnecessary fuel expenditure liable to occur when following constant bio-inspired OF reference signals. In the control laws adopted, a rigorous Lyapunov approach was used to ensure the global stability and convergence of the closed loop including two nonlinear controllers based on translational and expansional OF measurements.

This paper is structured as follows. In section II, the dynamic model for the lander and the mathematical definition of the OF are presented. Section III describes the scenario studied and discusses the sub-optimal guidance scheme. Section IV presents the control strategy used for OF tracking purposes. Section V gives the results of the numerical simulations performed. Lastly, section VI contains some concluding comments and outlines our forthcoming projects.

## II. LUNAR LANDER DYNAMIC MODELING AND OPTIC FLOW EQUATIONS

In this section, the dynamic model for the system presented in Fig. 2 and the mathematical background to OF studies are described. The autopilot presented here consists of an OF-based control system operating in the vertical plane ( $\vec{e}_x, \vec{e}_z$ ) (2-D position plus 1-D attitude), which controls the spacecraft's main thruster force and pitch angle. To stabilize the lander, it is necessary to cope with nonlinearities and the inherent instability of the system. Since the lunar atmosphere is very thin, no friction or wind forces are applied here to the

\* This research work is co-funded by CNRS Institutes (Life Science; Information Science; Engineering Science and Technology), the Aix-Marseille University, European Space Agency, ONERA the French Aerospace Lab and Astrium Satellites under ESA's Networking/Partnering Initiative program (NPI) for advanced technologies for space.

<sup>1</sup> G. Sabiron, T. Raharijaona and F. Ruffier are with Aix-Marseille Université, CNRS, ISM UMR 7287, 13288 Marseille Cedex 09, France {Thibaut.Raharijaona, Franck.Ruffier}@univ-amu.fr.

<sup>2</sup>G. Sabiron, and L. Burlion are with the French Aerospace Lab (ONERA, Systems Control and Flight Dynamics -DCSD-), 31055 Toulouse, France {Guillaume.Sabiron, Laurent.Burlion}@onera.fr

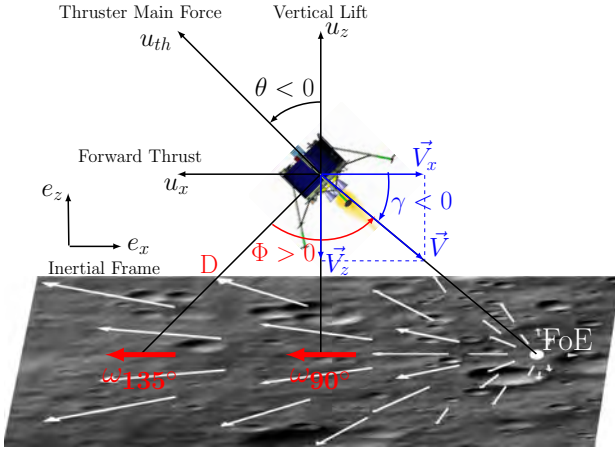


Fig. 1. Diagram of the lander, showing the inertial reference frame ( $e_x, e_z$ ), the velocity vector  $\vec{V}$ , the Focus of Expansion (FoE), and the mean thruster force  $u_{th}$  and its projections in the Local Vertical Local Horizontal (LVLH) reference frame.  $\omega_{90}$  and  $\omega_{135}$  are presented in red on the lunar ground. Adapted from [16].

lander. In line with previous studies, the lunar ground is taken to be flat (with an infinite radius of curvature) (see [17]). The lander's dynamic motion of the lander can be described in the time domain by the following dynamic system in the inertial frame ( $\mathcal{I}$  associated with the vector basis ( $e_x, e_z$ )):

$$\begin{cases} \dot{V}_x(t) = \frac{\sin(\theta(t))}{m_{ldr}(t)} u_{th}(t) & (1a) \\ \dot{x} = V_x & (1b) \\ \dot{V}_z(t) = \frac{\cos(\theta(t))}{m_{ldr}(t)} u_{th}(t) - g_{Moon} & (1c) \\ \dot{z} = V_z & (1d) \\ \ddot{\theta}(t) = \frac{R}{I} u_\theta(t) & (1e) \\ \dot{m}_{ldr}(t) = \frac{-u_{th}(t)}{I_{sp_{th}} \cdot g_{Earth}} + \frac{-|u_\theta(t)|}{I_{sp_\theta} \cdot g_{Earth}} & (1f) \end{cases}$$

where  $0 \leq u_{th} \leq 3820 \text{ N}$  corresponds to the control force applied to the lander and  $-44 \leq u_\theta \leq 44 \text{ N}$  is the control input signal driving the spacecraft's pitch.  $V_{x,z}$  are the lander's velocities in the lunar inertial reference frame,  $m_{ldr}$  stands for the lander's mass,  $\theta$  is the pitch angle,  $t$  denotes the time, and  $g_{Moon}$  denotes the lunar acceleration due to the gravity ( $g_{Moon} = 1.63 \text{ m/s}^2$ ,  $g_{Moon}$  is taken to be constant due to the low initial altitude).  $I$  is the lander's moment of inertia, and  $R$  is the eccentricity of the attitude thrusters from the center of mass.  $I_{sp}$  is the specific impulse:  $I_{sp_{th}} = 325\text{s}$  in the case of the braking thrusters,  $I_{sp_\theta} = 287\text{s}$  in that of the attitude thrusters and  $g_{Earth} = 9.81 \text{ m/s}^2$  is the Earth's gravity. Numerical values are taken from ESA/ASTRIUM studies or in accordance with literature. In the vertical plane, the OF  $\omega(\Phi)$  was defined by [18] as follows:

$$\omega(\Phi) = \frac{V}{D} \sin(\Phi) - \dot{\theta} \quad (2)$$

where the term  $\frac{V}{D} \sin(\Phi)$ , which is called the translational OF, depends on the linear velocity  $V$  expressed in the inertial frame, the distance from the ground  $D$  in the gaze direction and the elevation angle  $\Phi$  (i.e. the angle between the gaze direction and the heading direction). In order to use the useful properties of the translational OF, the angular velocity  $\dot{\theta}$  corresponding to the rotational OF is subtracted from the measured OF  $\omega_{meas}$ , using IMU measurements: this operation is known as the derotation process (see [19]). For the sake of clarity, the two specific local translational OFs used in this study will be written as follows:

- $\omega_{90^\circ}$  stands for the downward translational OF, i.e. in the nadir direction ( $90^\circ$  between the gaze direction and the local horizontal) after the derotation, and
- $\omega_{135^\circ}$  stands for the translational OF oriented at an angle of  $135^\circ$  with respect to the local horizontal after the derotation.

**In this study, the sensors available were an IMU and two OF sensors oriented at angles of  $90^\circ$  and  $135^\circ$  with respect to the local horizontal in a fixed position whatever the lander's attitude thanks to a gimbal system.**

From (2), under the assumption that the ground is practically flat (i.e.  $D = h / \cos(\frac{\pi}{2} - \Phi + \gamma)$ , where  $\gamma$  denotes the flight path angle (the orientation of the velocity vector with respect to the local horizontal),  $h$  is the ground height, and  $\Phi - \gamma$  is the angle between the gaze direction and the local horizontal:

$$\omega_{90^\circ} = \frac{V_x}{h} \quad (3)$$

$$\omega_{135^\circ} = \frac{V}{2h} (\cos(\gamma) - \sin(\gamma)) = \frac{\omega_{90^\circ}}{2} (1 - \tan(\gamma)) \quad (4)$$

where  $\tan(\gamma) = \frac{V_z}{V_x}$ . The highly informative OF values, that is to say, those of the ventral OF  $\omega_x$  and the expansion OF  $\omega_z$  used in the newly developed regulators are then expressed directly in terms of  $\omega_{90^\circ}$  and  $\omega_{135^\circ}$ :

$$\omega_x = \frac{V_x}{h} = \omega_{90^\circ} \quad (5)$$

$$\omega_z = \frac{V_z}{h} = \omega_{90^\circ} - 2\omega_{135^\circ} \quad (6)$$

### III. SUB-OPTIMAL GUIDANCE STRATEGY

Here it is proposed to study autonomous landing during the approach phase extending from the High Gate (HG) -1800m AGL- to the Low Gate (LG) -10m AGL. The mass optimization problem was defined here along with the constraints involved, and its solution was computed in terms of the trajectory and the OF profiles. In order to meet the low computational requirements, the optimal problem was solved offline only once: the OF and pitch profiles were determined and implemented in the form of constant vectors in the lander. Therefore, the guidance strategy is said to be sub-optimal since the offline computed optimal trajectory correspond to the nominal initial conditions which may not be met at the HG.

First of all, the optimal control sequence  $u^* = (u_{th}^*, u_\theta^*)$  was computed, taking  $u_{th}^*$  to denote the braking thrust and  $u_\theta^*$  to denote the pitch torque (the upper script

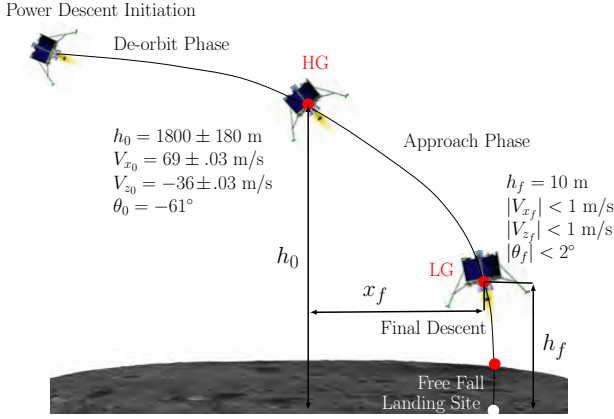


Fig. 2. The lander's objectives are to reach LG (10 m high) with both vertical and horizontal velocities of less than 1 m/s in absolute values and a pitch angle in the  $\pm 2^\circ$  range. Adapted from [16].

\* indicates the optimality in terms of the mass, i.e., the fuel consumption). In this paper, optimality refers to the outputs of the optimization problem ( $u_{th}^*$ ,  $u_\theta^*$ ) and the associated reference trajectory ( $\dot{V}_x^*$ ,  $\dot{V}_z^*$ ,  $V_x^*$ ,  $V_z^*$ ,  $h^*$ ,  $\theta^*$ ). Looking for the least fuel-consuming trajectory is equivalent to finding the control sequence  $u^*$  that minimizes the use of the control signal (see (1f)). The optimization problem can then be expressed as follows:

Solve

$$\min_{u_{th}(t), u_\theta(t)} \int_{t_0}^{t_f} (u_{th}(t) + |u_\theta(t)|) dt \quad (7)$$

Subject to

Equations (1a)-(1f)

$$\begin{cases} V_z(t_0) = -36 \text{ m/s}, & |V_{z_f}| < 1 \text{ m/s} \\ V_x(t_0) = 69 \text{ m/s}, & |V_{x_f}| < 1 \text{ m/s} \\ h(t_0) = 1800 \text{ m}, & h_f = 10 \text{ m} \\ \theta(t_0) = -61^\circ, & |\theta_f| < 2^\circ \end{cases} \quad (8)$$

$$\begin{cases} 0 < u_{th} < 3438 \text{ N} \\ -44 < u_{pitch} < 44 \text{ N} & \forall t \in [t_0, t_f] \\ (-V_z, V_x, h, x) > 0 \\ |\dot{\theta}| < 1.5^\circ/\text{s} \end{cases} \quad (9)$$

This offline sub-optimal guidance strategy was implemented using Matlab optimization software on the nonlinear system under constraints to bring the system from HG to LG. To solve this continuous time optimization problem, many freely available Matlab toolboxes based on various methods can be used. The solution provided by ICLOCS (Imperial College London Optimal Control Software, [20]) based on the IPOPT solver suited our needs for the numerical implementation of a nonlinear optimization problem in the case of the continuous system subjected to boundary and state constraints using the interior point method. The simulation of the open loop under optimal control was therefore run on the nonlinear system to assess the optimal OF and pitch profiles ( $\omega_x^*$ ,  $\omega_z^*$ ,  $\theta^*$ ).

Equation (1a)-(1f) describes the dynamic lander, (8) gives the initial and final conditions and (9) gives the actuator and system constraints imposed along the trajectory. For safety reasons, a 10% margin was added to the thrusters' physical saturation in order to give the lander greater maneuverability around the predefined trajectory at any point. It is worth noting that a terminal constraint could easily be added if required to the downrange  $x$  to make pinpoint landing possible, but this might greatly increase the fuel consumption. Since the case may arise where  $\dot{\theta} = -\omega_R > \omega_T$  and thus  $\omega_{measured} < 0$ , we had to use a bi-directional version of the 6-pixel VMS adapted for use in the following measurement range:  $\omega_{measured} \in [-20^\circ/\text{s}; -0, 1^\circ/\text{s}] \cup [0, 1^\circ/\text{s}; 20^\circ/\text{s}]$ . The fuel expenditure decreases the lander's mass by  $\Delta m$ , which is defined as the difference between the initial and final mass of the lander  $\Delta m = m_{ldr_0} - m_{ldr}(t_f)$  where  $m_{ldr_0} = 762 \text{ kg}$  and

$$m_{ldr}(t_f) = m_{ldr}(t_0) - \frac{1}{g_{Earth}} \int_{t_0}^{t_f} \left( \frac{u_{th}(\epsilon)}{I_{sp_{th}}} + \frac{|u_\theta(\epsilon)|}{I_{sp_\theta}} \right) d\epsilon \quad (10)$$

In order to make sure that the sum  $\omega_{grd-trh} = \omega_T + \omega_R$  does not cancel itself out (i.e.  $\omega_T = -\omega_R$ ), the pitch rate ( $\omega_R = \dot{\theta}$ ) was constrained as follows:  $|\dot{\theta}| = |\omega_R| < 1.5^\circ/\text{s}$ . Under all these conditions, the optimal control sequences ( $u_{th}^*$ ,  $u_\theta^*$ ) were processed: the optimal solution was obtained with  $t_f = 51.46\text{s}$  and a mass change of  $\Delta m < 33.6 \text{ kg}$  (amounting to 4.4% of the initial mass). The trajectory modeled under these constraints can be said to be optimal in the case of a more highly constrained problem. Additional constraints were imposed on  $\dot{\theta}$  and the 10% margin on the thrust to account for the sensors' and actuators' operating ranges, resulting in a more highly constrained problem than the system can actually deal with. In any case, both of these constraints (the saturated pitch rate and the 10% margin added to the thrust) resulted in very similar fuel expenditure predictions to that obtained without these additional constraints (amounting to a difference of only 0.21%).

#### IV. LYAPUNOV-BASED NONLINEAR CONTROL DESIGN

In this section, a control design ensuring soft lunar landing based on the knowledge of the OF and IMU measurements is presented. The control problem to be solved here focuses on the tracking of translational and expansional OF reference signals. In particular, two control signals are computed, one for the horizontal thrust  $u_x$  and one for the vertical thrust  $u_z$ . Both  $u_x$  and  $u_z$  are then fused into a jointly delivered control signal  $u_{th} = \sqrt{u_x^2 + u_z^2}$ .

##### A. Height boundedness

Here we look for a time varying bound on the height  $h$  From:

$$\omega_z = \frac{V_z}{h} = \frac{d}{dt} \ln(h) \quad (11)$$

we have

$$\int_{t_0}^t \omega_z(s) ds = \ln \left( \frac{h(t)}{h(t_0)} \right) \quad (12)$$

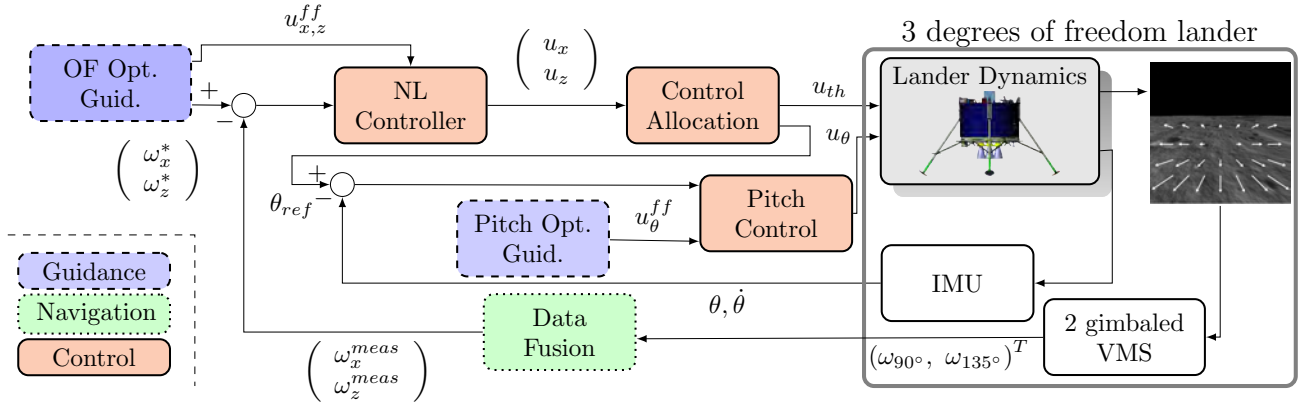


Fig. 3. Sketch of the full GNC solution. The dynamic model for the lander with  $2 \times 6$ -pixels VMS feeding the data fusion block along with an IMU. The data fusion block estimates high interest OF values, which are conveyed to the nonlinear controller. The control allocation block transforms the control signal into a braking force defining the magnitude of the thrust vector and a reference pitch angle. The inner attitude control loop delivers the torque control signal  $u_\theta$  assessed via the linear output feedback controller and a sub-optimal guidance strategy defining the feedforward term (corresponding to  $u_x^{ff} = \dot{V}_x^*$  and  $u_z^{ff} = \dot{V}_z^*$  in the control law equations). Adapted from [16].

which gives

$$h(t) = h(t_0) e^{\int_{t_0}^t \omega_z(s) ds} \quad (13)$$

where  $\omega_z(t) < 0$  and  $h(t) > 0$ . Since it can be deduced from the initial conditions that  $h(t_0) \in [1620, 1980]$ , from (13) it is thus possible to compute time-varying bounds on the height such that  $\forall t \geq t_0$   $h(t) \in [h_{min}(t), h_{max}(t)]$  where:

$$\begin{cases} h_{min}(t) = 1620 e^{\int_{t_0}^t \omega_z(s) ds} \\ h_{max}(t) = 1980 e^{\int_{t_0}^t \omega_z(s) ds} \end{cases} \quad (14)$$

which means that at each time step, an upper and a lower bound on  $h(t)$  depending on the uncertainty at HG are known.

**Remark** If the measurement  $\omega_z^{meas}(s)$  is corrupted with noise i.e.  $\omega_z^{meas}(s) - d \leq \omega_z(s) < \omega_z^{meas}(s) + d < 0$  where  $d \geq 0$  then

$$\begin{cases} h_{min}(t) = 1620 e^{\int_{t_0}^t \omega_z^{meas}(s) - d ds} \\ h_{max}(t) = 1980 e^{\int_{t_0}^t \omega_z^{meas}(s) + d ds} \end{cases}$$

### B. Z dynamics

The nonlinear control design is achieved using the following Lyapunov function candidate  $\mathcal{L}_1$  so that (see [21]):

$$\mathcal{L}_1 = \frac{1}{2} S_z^2 \quad (15)$$

where  $S_z$  is defined such as  $S_z = \omega_z - \omega_z^*$ . Its corresponding time derivative might therefore be expressed as follows:

$$\dot{\mathcal{L}}_1 = S_z \left[ \frac{\dot{V}_z}{h} - \frac{\dot{V}_z^*}{h^*} - \omega_z^2 + \omega_z^{*2} \right] \quad (16)$$

$$\dot{\mathcal{L}}_1 = S_z \left[ \frac{\dot{V}_z - \dot{V}_z^*}{h} + \dot{V}_z^* \left( \frac{1}{h} - \frac{1}{h^*} \right) - S_z^2 - 2\omega_z^* S_z \right] \quad (17)$$

Two possible cases then arise, depending on the sign of  $S_z$ . A sign study of  $S_z$  gives:

- When  $S_z > 0$

$$\dot{\mathcal{L}}_1 < S_z \left[ \frac{\dot{V}_z - \dot{V}_z^*}{h} + \dot{V}_z^* \left( \frac{1}{h} - \frac{1}{h^*} \right) - 2\omega_z^* S_z \right] \quad (18)$$

where  $h > 0$  in the reference scenario under consideration, using bounds on  $h(t)$  such that:

$$\frac{1}{h_{max}(t)} - \frac{1}{h^*(t)} \leq \left( \frac{1}{h(t)} - \frac{1}{h^*(t)} \right) \leq \frac{1}{h_{min}(t)} - \frac{1}{h^*(t)} \quad (19)$$

This gives

$$\dot{\mathcal{L}}_1 \leq S_z \left( \frac{\dot{V}_z - \dot{V}_z^*}{h} \right) + |S_z| |\dot{V}_z^*| h_{bound} + |2\omega_z^*| S_z^2 \quad (20)$$

where

$$h_{bound} = \max \left( \left| \frac{1}{h_{max}(t)} - \frac{1}{h^*} \right|, \left| \frac{1}{h_{min}(t)} - \frac{1}{h^*} \right| \right) \quad (21)$$

We now need to find a control signal satisfying  $\dot{\mathcal{L}}_1 < 0$ . The virtual control signal  $u_z$  features in the dynamic model for the lander in the form of  $\dot{V}_z = \frac{u_z}{m} - g_{Moon}$ , where  $u_z = \cos(\theta) u_{th}$ . We take:

$$u_z(t) = m \left( \dot{V}_z^* - k_a(t) S_z - k_b(t) \text{sgn}(S_z) + g_{Moon} \right) \quad (22)$$

$$\text{where } \text{sgn}(X) = \begin{cases} 1 & X \geq 0 \\ -1 & X < 0 \end{cases}$$

We obtain

$$\dot{\mathcal{L}}_1 \leq S_z^2 \left( \frac{-k_a(t)}{h} + |2\omega_z^*| \right) + |S_z| \left( \frac{-k_b(t)}{h} + |\dot{V}_z^*| h_{bound} \right) \quad (23)$$

Lastly, we take the gains  $k_a(t)$  and  $k_b(t) \forall t \geq 0$ :

$$k_a(t) > h_{max}(t) |2\omega_z^*(t)| \quad (24)$$

$$k_b(t) > h_{max}(t) |\dot{V}_z^*(t)| h_{bound} \quad (25)$$

so that  $\dot{\mathcal{L}}_1 < 0$ .

- When  $S_z < 0$

From equation (17), one can obtain

$$\dot{\mathcal{L}}_1 \leq S_z \left( \frac{\dot{V}_z - \dot{V}_z^*}{h} \right) + |S_z| |\dot{V}_z^*| h_{bound} + |2\omega_z^*| S_z^2 - S_z^3 \quad (26)$$

We now need to find a control signal satisfying  $\dot{\mathcal{L}}_1 < 0$   
We take:

$$u_z(t) = m \left( \dot{V}_z^* - k_a(t) S_z - k_b(t) \text{sgn}(S_z) - k_c(t) S_z^2 + g_{Moon} \right) \quad (27)$$

Hence

$$\dot{\mathcal{L}}_1 \leq S_z \left( \frac{-k_a(t) S_z - k_b(t) \text{sgn}(S_z) - k_c(t) S_z^2}{h} \right) + |S_z| |\dot{V}_z^*| h_{bound} + |2\omega_z^*| S_z^2 - S_z^3 \quad (28)$$

$$\begin{aligned} \dot{\mathcal{L}}_1 \leq & S_z^2 \left( \frac{-k_a(t)}{h} + |2\omega_z^*| \right) \\ & + |S_z| \left( \frac{-k_b(t)}{h} + |\dot{V}_z^*| h_{bound} \right) \\ & - S_z^3 \left( 1 + \frac{k_c(t)}{h} \right) \end{aligned} \quad (29)$$

where we choose the gain  $k_c(t) \forall t \geq 0$  so that:

$$k_c(t) < -h_{max}(t) \quad (30)$$

and  $k_a(t)$ ,  $k_b(t)$  such as (29-29) are ensured.

Therefore  $\dot{\mathcal{L}}_1 < 0$ , which means that  $\mathcal{L}_1$  tends asymptotically toward 0 (since  $\mathcal{L}_1 > 0$ ), and lastly, (15) ensures that  $\omega_z \rightarrow \omega_z^*$  asymptotically.

Let us now combine all the expressions for the control signal, with (22-27) to obtain the unified control signal equation:

$$u_z(t) = m \left( \dot{V}_z^* - k_a(t) S_z - k_b(t) \text{sgn}(S_z) - \left( \frac{1 - \text{sgn}(S_z)}{2} \right) k_c(t) S_z^2 + g_{Moon} \right) \quad (31)$$

### C. X dynamics

A similar Lyapunov function based approach is used on the X dynamics:

Let us define  $S_x$  as  $S_x = \omega_x - \omega_x^*$ :

$$\mathcal{L}_2 = \frac{1}{2} S_x^2 \quad (32)$$

$$\dot{\mathcal{L}}_2 = S_x \left[ \frac{\dot{V}_x}{h} - \frac{\dot{V}_x^*}{h^*} - \omega_x \omega_z + \omega_x^* \omega_z^* \right] \quad (33)$$

One can say that:

$$\dot{\mathcal{L}}_2 < S_x \left[ \frac{\dot{V}_x - \dot{V}_x^*}{h} + \dot{V}_x^* \left( \frac{1}{h} - \frac{1}{h^*} \right) + \omega_x \omega_z + \omega_x^* \omega_z^* \right] \quad (34)$$

with  $h > 0$  in the reference scenario adopted:

$$\frac{1}{h_{max}(t)} - \frac{1}{h^*} \leq \left( \frac{1}{h} - \frac{1}{h^*} \right) \leq \frac{1}{h_{min}(t)} - \frac{1}{h^*} \quad (35)$$

This gives:

$$\dot{\mathcal{L}}_2 \leq S_x \left( \frac{\dot{V}_x - \dot{V}_x^*}{h} \right) + \left[ |\dot{V}_x^*| h_{bound} + |\omega_x \omega_z + \omega_x^* \omega_z^*| \right] |S_x| \quad (36)$$

where  $h_{bound}$  as defined in (21).

We need to find a control signal that ensure  $\dot{\mathcal{L}}_2 < 0$ . The virtual control signal  $u_x$  features in the dynamic model for the lander in the form of  $\dot{V}_x = \frac{u_x}{m}$ , where  $u_x = \sin(\theta) u_{th}$ . We choose:

$$u_x(t) = m \left( \dot{V}_x^* - k_a(t) \text{sgn}(S_x) - k_b S_x \right) \quad (37)$$

where  $\forall t \geq 0$

$$k_a(t) > h_{max}(t) \left[ |\dot{V}_x^*| h_{bound} + |\omega_x \omega_z + \omega_x^* \omega_z^*| \right] \quad (38)$$

thus with  $\dot{\mathcal{L}}_2 < -k_b S_x$ , we choose a relatively small  $k_b > 0$  to prevent any chattering of  $S$  at values around zero.

Finally,  $\dot{\mathcal{L}}_2 < 0$ , which means that  $\mathcal{L}_2$  tends asymptotically toward 0 (since  $\mathcal{L}_2 > 0$ ), and lastly, (32) ensures that  $\omega_x \rightarrow \omega_x^*$  asymptotically.

### D. Pitch control law

To control the attitude, a proportional derivative controller drives the spacecraft's pitch (via the inner loop), which gives faster dynamics in the inner loop than on an outer loop:

$$u_\theta(t) = u_\theta^{ff}(t) + K_p \varepsilon_\theta(t) + K_d \frac{d}{dt} \varepsilon_\theta(t) \quad (39)$$

where  $u_\theta^{ff}(t)$  corresponds to the optimal control sequence  $u_\theta^*(t)$  computed with the mass-optimal trajectory and  $\varepsilon_\theta(t) = \theta_{meas}(t) - \theta_{ref}(t)$ . The reference signal  $\theta_{ref}$  is based on the two virtual control signals  $u_x$  and  $u_z$ , so that:

$$\theta_{ref} = \arctan \left( \frac{u_x}{u_z + \varepsilon} \right) \quad (40)$$

where  $\varepsilon$  is taken to be very small to avoid having to divide by zero.

## V. SIMULATION RESULTS

Once the optimal trajectory has been defined, the OF and pitch profiles ( $\omega_x^*$ ,  $\omega_z^*$ ,  $\theta^*$ ) as well as the optimal feedforward control signals  $\dot{V}_x^*$  and  $\dot{V}_z^*$  (see (27,37)) are available for implementation along with the control laws defined in (27), (37) and (39). Simulations were run on a Matlab/Simulink simulator taking the lander's dynamics, actuator dynamics (which were taken to be first order systems) and the saturation into account. Random noise was also added to the OF sensor model. In order to assess the robustness of the model to initial uncertainties, an initial height condition ( $h(t_0)$ ) was taken to be in the  $1800 \pm \delta_h$  range, where  $\delta_h = 180$  m. The result of simulations in which  $h(t_0)$  increased by 20 m after each run are presented in Fig. 4. As can be seen from this figure, which presents the trajectory in the 2-D plane and the final velocities, pitch angle and fuel consumption, our new G&C almost meets the tight specifications imposed. The final vertical velocity is slightly higher than the objective. The final pitch angle was in the  $\pm 2^\circ$  range, the horizontal velocity was below 1 m/s, whereas the final vertical velocity was only 0.68 m/s above the objective (corresponding to a decrease in the speed of  $100 \frac{V_{z_f} - V_z(t_0)}{V_z^*(t_f) - V_z(t_0)} = 98\%$  of the tight requirements)

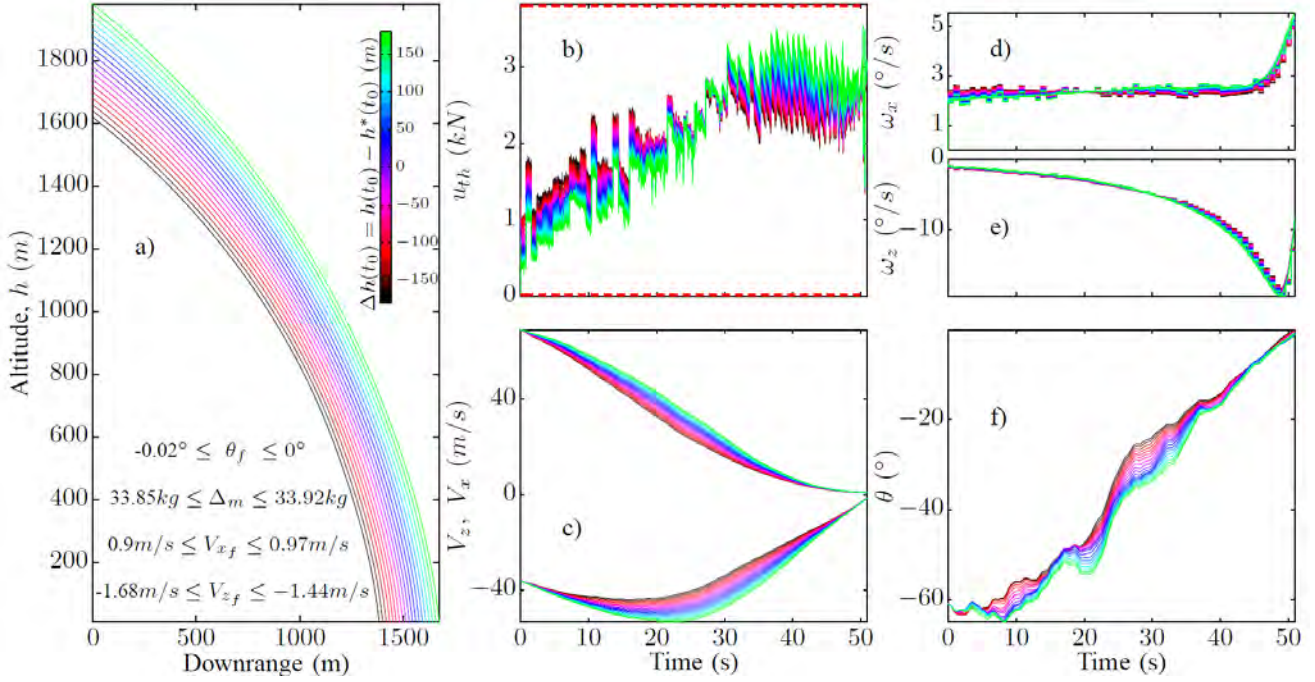


Fig. 4. Closed loop behavior from HG to LG in simulations with  $h(t_0) \in [h_{min}(t_0), h_{max}(t_0)]$ . a) Height  $h$  versus downrange  $x$ . b) Control sequence  $u_{th} = \sqrt{u_x^2 + u_z^2}$ . Saturation of the control signal  $u_{th}$  is defined in such a way that  $0 \text{ N} \leq u_{th} \leq 3820 \text{ N}$ . c) Velocities  $V_x, V_z$ . d) Measured OF and optimal reference OF profile (black dashed lines). e) Pitch trajectories corresponding to various initial heights.

in the worst simulated case. The fuel consumption was  $\Delta m \leq 34.22 \text{ kg}$ , although we observed that  $\Delta m^* = 33.6 \text{ kg}$ , which means that even when the initial height was far above the pre-computed optimal trajectory, the fuel consumption approached the optimal value very closely (it was only 1.2% higher) although the final constraints were almost met. It is worth noting that the control signal  $u_{th}(t)$  presented in Fig. 4.b never reached the upper or lower saturation levels depicted in dashed red lines. The evolution of the velocities, which tended toward 1 m/s in absolute values, is presented in Fig. 4.c, whereas Fig. 4.d-e shows the evolution of the optic flow measured superimposed on the optimal reference signals. Noise was modeled based on previous results obtained on the real sensor, which showed the occurrence of a refresh rate of approximately 7 Hz and a standard deviation of the error of  $0.4^\circ/\text{s}$ . Lastly, Fig. 4.f presents the pitch evolution starting at  $\theta(t_0) = -61^\circ$  and moving toward  $-2^\circ \geq \theta_f \geq 2^\circ$  in the case of all the initial heights. In conclusion, the G&C strategy presented in this study can be said to be suitable for handling the approach phase during lunar landing, even in the presence of large initial uncertainties as far as the height is concerned.

## VI. CONCLUSION

This paper presents a nonlinear soft lunar landing controller, in which optical flow measurements are used along with the IMU data. The originality of our approach lies in the fact that neither the linear velocity nor the distance from the target need to be determined. The present approach involves an image based visual control algorithm which

requires only  $2 \times 6$  pixels and inertial data for performing the derotation of the flow. A rigorous analysis of the stability of the closed-loop systems presented here was conducted, which resulted in the design of sliding mode type control laws regulating the translational and expansional OF. Via nonlinear programming procedures, the optimal reference trajectory in terms of the fuel consumption was computed offline and used in the closed loop as feedforward terms for providing the OF and pitch control loops with reference signals. The guidance algorithm proposed here is designated as sub-optimal in terms of fuel expenditure since it provides the system with an optimal trajectory from the HG to the LG computed via nonlinear programming. The actual landing strategy is therefore sub-optimal since the optimal trajectory is computed offline only once. In view of the simulation results we can conclude that the strategy is close to the optimal behavior. Simulations with various initial conditions gave a clear picture of the performances of the present algorithm. The experimental results obtained confirmed that the G&C strategy developed here almost fulfilled the requirements in terms of the spacecraft's final position, velocity and fuel consumption. It is now proposed to conduct further research on the following lines. First, in order to do away with the use of bulky IMUs and gimbal systems, an observer based solely on the OF could be used to accurately estimate  $\omega_x, \omega_z$  and  $\theta$ . An initial study on an observer of this kind was recently presented in [22]. Secondly, although the final pitch angle estimates meet the objectives, an improvement could be made by designing a nonlinear control law regulating the pitch dynamics in order to avoid having to differentiate the

pitch error, which depends on the control signals.

### ACKNOWLEDGMENT

We are most grateful to S. Viollet, G. Jonniaux, E. Kervendal and E. Bornschlegl for their fruitful suggestions and comments during this study. We thank J. Blanc for improving the English manuscript. This research work was co-funded by CNRS Institutes (Life Science; Information Science; Engineering Science and Technology), the Aix-Marseille University, European Space Agency, the French Aerospace Lab (ONERA), and the French Aerospace Lab and Airbus Defense and Space under ESA's Networking/Partnering Initiative program (NPI) for advanced technologies for space.

### REFERENCES

- [1] A. E. Johnson and J. F. Montgomery, "Overview of terrain relative navigation approaches for precise lunar landing," in *Aerospace Conference, 2008 IEEE*. IEEE, 2008, pp. 1–10.
- [2] F. Ruffier and N. Franceschini, "Optic flow regulation: the key to aircraft automatic guidance," *Robotics and Autonomous Systems*, vol. 50, pp. 177–194, 2005.
- [3] B. Hérisse, T. Hamel, R. Mahony, and F. Russotto, "A terrain-following control approach for a VTOL Unmanned Aerial Vehicle using average optical flow," *Autonomous Robots*, vol. 29, no. 3–4, pp. 381–399, 2010. [Online]. Available: <http://dx.doi.org/10.1007/s10514-010-9208-x>
- [4] G. Barrows and C. Neely, "Mixed-mode VLSI optic flow sensors for in-flight control of a Micro Air Vehicle," in *SPIE : Critical technologies for the future of computing*, vol. 4109, San Diego, CA, USA, Aug. 2000, pp. 52–63.
- [5] S. Griffiths, J. Saunders, A. Curtis, B. Barber, T. McLain, and R. Beard, "Maximizing miniature aerial vehicles," *IEEE Robotics & Automation Magazine*, vol. 13, pp. 34–43, 2006.
- [6] F. Ruffier and N. Franceschini, "Aerial robot piloted in steep relief by optic flow sensors," in *IEEE/RSJ International Conference on Intelligent Robots and Systems (IROS)*. IEEE, 2008, pp. 1266–1273.
- [7] A. Beyeler, J. Zufferey, and D. Floreano, "OptiPilot: control of take-off and landing using optic flow," in *European Micro Aerial Vehicle Conference (EMAV)*, vol. 27, Delft, Netherlands, Sept. 2009.
- [8] F. Kendoul, K. Nonami, I. Fantoni, and R. Lozano, "An adaptive vision-based autopilot for mini flying machines guidance, navigation and control," *Autonomous Robots*, vol. 27, pp. 165–188, 2009.
- [9] B. Hérisse, T. Hamel, R. Mahony, and F.-X. Russotto, "Landing a VTOL Unmanned Aerial Vehicle on a Moving Platform Using Optical Flow," *IEEE Transactions on Robotics*, vol. 28, no. 1, pp. 77–89, Feb. 2012.
- [10] G. Sabiron, P. Chavent, T. Raharijaona, P. Fabiani, and F. Ruffier, "Low-speed optic-flow sensor onboard an unmanned helicopter flying outside over fields," in *IEEE International Conference on Robotics and Automation (ICRA)*, 2013.
- [11] F. Valette, F. Ruffier, S. Viollet, and T. Seidl, "Biomimetic optic flow sensing applied to a lunar landing scenario," in *International Conference on Robotics and Automation (ICRA)*, 2010, pp. 2253–2260.
- [12] V. Medici, G. Orchard, S. Ammann, G. Indiveri, and S. Fry, "Neuromorphic computation of optic flow data Bio-inspired landing using biomorphic vision sensors," ESA, Tech. Rep., 2010.
- [13] D. Izzo and G. de Croon, "Nonlinear model predictive control applied to vision-based spacecraft landing," in *Proceedings of the EuroGNC 2013, 2nd CEAS Specialist Conference on Guidance, Navigation & Control, Delft University of Technology, Delft, The Netherlands, Apr. 10-12 2013*, pp. 91–107.
- [14] D. Izzo, N. Weiss, and T. Seidl, "Constant-Optic-Flow Lunar Landing: Optimality and Guidance," *Journal of Guidance, Control, and Dynamics*, vol. 34, pp. 1383–1395, 2011.
- [15] D. Izzo and G. de Croon, "Landing with time-to-contact and ventral optic flow estimates," *Journal of Guidance, Control, and Dynamics*, vol. 35 (4), pp. 1362–1367, 2011.
- [16] G. Sabiron, T. Raharijaona, L. Burlion, E. Kervendal, E. Bornschlegl, and F. Ruffier, "Sub-optimal Lunar Landing GNC using Non-gimbaled Bio-inspired Optic Flow Sensors," *IEEE Transactions on Aerospace and Electronic Systems*, (in revision).
- [17] T. Jean-Marius and S. Trinh, "Integrated Vision and Navigation for Planetary Exploration - Final Report," Aérospatiale Espace & Défense, Tech. Rep. RM-TN-00-18-AS/M, 1999.
- [18] J. Koenderink and A. Doorn, "Facts on optic flow," *Biological Cybernetics*, vol. 56, pp. 247–254, 1987.
- [19] A. Argyros, D. Tsakiris, and C. Groyer, "Biomimetic centering behavior [mobile robots with panoramic sensors]," *Robotics Automation Magazine*, vol. 11, no. 4, pp. 21 – 30, 68, Dec. 2004.
- [20] P. Falugi, E. Kerrigan, and E. Van Wyk, *Imperial College London Optimal Control Software User Guide (ICLOCS)*, Department of Electrical Engineering, Imperial College London, London, UK, 2010.
- [21] H. K. Khalil and J. Grizzle, *Nonlinear systems*. Prentice hall Upper Saddle River, 2002, vol. 3.
- [22] G. Sabiron, L. Burlion, G. Jonniaux, E. Kervendal, E. Bornschlegl, T. Raharijaona, and F. Ruffier, "Backup State Observer Based on Optic Flow Applied to Lunar Landing," in *IEEE/RSJ International Conference on Intelligent Robots and Systems (IROS) (In press)*, 2014, pp. 2325 –2332.



# ARTICLE 5: BACKUP STATE OBSERVER BASED ON OPTIC FLOW APPLIED TO LUNAR LANDING

## CONTENTS

---

ABSTRACT . . . . .	135
I INTRODUCTION . . . . .	135
II LUNAR LANDER DYNAMICS AND OPTIC FLOW EQUATIONS . . . . .	136
III OPTIC FLOW FUSION AND LPV MODEL DEFINITION . . . . .	137
IV OBSERVER DESIGN FOR A CLASS OF LPV SYSTEMS AND APPLICATION TO A LUNAR LANDING SCENARIO . . . . .	138
V SIMULATION RESULTS WITH 3 OF SENSORS . . . . .	138
VI CONCLUSIONS . . . . .	141
ACKNOWLEDGMENT . . . . .	142
REFERENCES . . . . .	142



## Article 5: Backup State Observer Based on Optic Flow Applied to Lunar Landing

Art. 5. Backup State Observer Based on OF Applied to Lunar Landing

**Article published in 2014 in IEEE/RSJ International Conference on Intelligent Robots and Systems, pp 2325-2332, Chicago, USA, 14-18 September 2014.**

**Authors: G. Sabiron, L. Burlion, G. Jonniaux, E. Kervendal, E. Bornschlegl, T. Raharijaona, and F. Ruffier**

**S**ATISFIED with results obtained on the guidance and control strategies presented in chapters 3.2 and 3.3, we decided to investigate ways to reduce further the need for complementary sensors.

The following step would be to propose a vision-only type of GNC strategy using only visual motion sensors for optic flow sensing. In accordance with the literature and the industrial partners, the dependency on IMU might be seen as extremely critical. Attitude of the system is almost always assumed to be measured and thus, every stabilizing GNC strategy is built on this strong assumption. The inertial measurement unit becomes the mainstay of the entire GNC strategy. In case of IMU failure the usual way to ensure system's integrity is to use software and hardware redundancy which increases at the same time the embedded weight and the energy consumption.

The need for IMU-less solution is essential. As opposed to the IMU that can be embedded onboard UAVs on Earth and that weight only few milligrams, an IMU designed for space harsh environment can represent up to 20% of the dry mass of the lander. This explains why exploratory missions could use backup inertial systems avoiding the need for redundancy of this kind of bulky equipment.

An innovative way to tackle IMU dependency would be to extract attitude estimates from visual feedback.

Using cameras, several interesting solutions allow attitude estimation with horizon detection (Thurrowgood et al., 2009; Thurrowgood et al., 2010), sun's light polarization (Chahl and Mizutani, 2012) or stereo vision (Moore et al., 2009). Even so, the choice was made to focus on the use of minimalistic 6-pixels sensors to satisfy aerospace related constraints. Shabayek et al. (2012) presented a comprehensive review on vision based attitude estimation on UAV.

Looking at the non-gimbaled expression of the optic flow in planar motion:

$$\omega_{\Phi}(t) = \frac{V(t)}{D(t)} \sin(\Phi(t)) - q(t) \quad (3.4.1)$$

where  $\Phi(t) = \alpha + \theta(t) + \gamma(t)$ , and  $D = \frac{h(t)}{\sin(\alpha + \theta(t))}$ , one might feel that all required information are available (see Fig. A of the following paper for notations). We need to extract and separate each interesting component from this nonlinear expression using fusion from several sensors. For instance, the rotational component have the same influence on the measurement no matter the gazing direction meanwhile the translational component is directly dependent on the viewing direction.

In this paper we propose a new method to estimate ventral optic flow  $\omega_x = \frac{V_x}{h}$ , expansion optic flow  $\omega_z = \frac{V_z}{h}$ , and pitch angle  $\theta$  using only visual motion sensors attached to the lander structure. Even though we do not have knowledge of the state vector, we do have access to the reference trajectory supposed to be followed thorough the entire descent. Based on the assumption that the lander stays close enough to the reference trajectory at all time, we linearize the system around this trajectory to obtain an LPV system. We propose a Kalman-like linear observer based on findings presented in (Besançon, Bornard, and Hammouri, 1996). Thanks to a change of variable, we extend the class of nonlinear system to which this LPV observer could be applied.

Satisfactory results are obtained on PANGU-simulated images in terms of estimates of  $\omega_x$ ,  $\omega_z$ , and  $\theta$  using only three miniature optic flow sensors. A pre-processing step could be added on the raw optic flow measurement to smooth small magnitude noises and improve the overall estimation.

Author contributions:

G.S., L.B., E.K., E.B., T.R., F.R. designed research;

G.S. performed research;

G.S., L.B., G.J., F.R. contributed with technical and analytic tools;

G.S. , L.B., F.R. analyzed data;

and G.S., L.B., T.R., F.R. wrote the paper.

# Backup State Observer Based on Optic Flow Applied to Lunar Landing

Guillaume Sabiron<sup>1,2</sup>, Laurent Burlion<sup>2</sup>, Grégory Jonniaux<sup>3</sup>,  
Erwan Kervendal<sup>3</sup>, Eric Bornschlegl<sup>4</sup>, Thibaut Raharijaona<sup>1</sup>, and Franck Ruffier<sup>1</sup>

**Abstract**—The observer presented in this paper, which was based on the use of three minimalistic bio-inspired Visual Motion Sensors (VMS) detecting Optic Flow (OF) cues, states was intended as a backup solution in the case of Inertial Measurement Unit (IMU) failure. Contrary to most previous Guidance Navigation and Control (GNC) solutions for planetary landing, which have involved a sensor suite including an IMU, an innovative strategy is presented here for estimating states without any need for inertial measurements, based solely on information about the relative velocity of the images of the surrounding environment. A Linear Parameter Varying (LPV) observer designed on a LPV system linearized around a reference trajectory, estimates: the ventral OF, the expansion OF and the local pitch angle. A previously developed observer was applied here to a larger class of nonlinear systems by making an ingenious change of variable. Simulations performed on a lunar landing scenario yielded satisfactory performance and showed the robustness of the OF based observer to initial uncertainties and measurement noise.

## I. INTRODUCTION

In most previous systems designed for the autonomous navigation of robotic systems, pose and attitude parameters have usually been measured or estimated during planetary landing [5], [33], [16]. However, vision based sensors and algorithms which meet the stringent weight, size and power consumption requirements of spatial applications, have recently provided new means of controlling these complex systems. Two different vision based approaches have been widely studied by performing numerical simulations:

- The first approach was based on the use of images along with information provided by sensors of other kinds or embedded knowledge of the terrain to reconstruct classical states such as velocities, attitude angles and angular velocities [19], [28], [6], [8], [27], [11]. Once these states have been estimated, classical control theory can be used to bring the system autonomously to the

appropriate destination. However, these recent developments are often associated with a high computational cost, mainly due to the image processing algorithm extracting visual cues from the cameras output.

- In the second approach, the system was driven on the basis of relative information extracted from images of the environment. It has been established that flying insects use the Optic Flow (OF), which provides them with relative angular velocity and proximity information with respect to obstacles, to navigate swiftly in unknown complex environments. The authors of several robotic studies inspired by insects' behavior have used the OF to perform hazardous tasks such as taking off, terrain-following, and landing safely and efficiently [29], [14], avoiding frontal obstacles [2], [12], [30], [4], tracking a moving target [23] and hovering and landing on a moving platform [15]. OF based lunar landing has been addressed in several studies using either a nonlinear observer connected to a LQ controller to track a constant OF reference in [32] or PID type controllers to track constant OF references [26] or exponentially decreasing [17] or more recently, Model Predictive Control [18]. In all these studies, sensors oriented at constant angles of 90° and sometimes 135° were used to compute specific OF expressions [26] so that:

$$\begin{cases} \omega_x = \frac{V_x}{h} = \omega_{90^\circ} \\ \omega_z = \frac{V_z}{h} = \omega_{90^\circ} - 2\omega_{135^\circ} \end{cases} \quad (1)$$

Keeping (1) constant or near a slowly varying reference trajectory while  $h$  decreases ensures a soft touchdown of the closed loop system.

In other studies, OF measurements have been used as a means of estimating the usual states of the system along with other more classical sensors such as Inertial Measurement Units (IMUs), sonars, Global Positioning System (GPS), airspeed sensors and/or accelerometers [10], [22], [32], [9].

However, in all of these studies, the Inertial Measurement Unit (IMU) was the crucial cue: nowadays, an IMU is the corner stone of all the autopilots designed for vehicles of all kinds. For instance, in August 2012, the NASA scientists reported the occurrence of an IMU failure which caused the very advanced Morpheus lander prototype to crash while performing its first untethered flight [7]. IMU-less backup solutions are still urgently required in order to prevent accidents of this kind.

In the present paper, which focuses on the navigation part of the whole GNC strategy (observation issue), it is not

\* This research work is co-funded by CNRS Institutes (Life Science; Information Science; Engineering Science and Technology), the Aix-Marseille University, European Space Agency, ONERA the French Aerospace Lab and Astrium Satellites under ESA's Networking/Partnering Initiative program (NPI) for advanced technologies for space.

<sup>1</sup> G. Sabiron, T. Raharijaona and F. Ruffier are with Aix-Marseille University, CNRS, Institute of Movement Science, Biorobotics Dept., UMR7287, 13288, Marseille, France {Thibaut.Raharijaona, Franck.Ruffier}@univ-amu.fr.

<sup>2</sup> G. Sabiron, and L. Burlion are with the French Aerospace Lab (ONERA, Systems Control and Flight Dynamics -DCSD-), 31055 Toulouse, France {Guillaume.Sabiron, Laurent.Burlion}@onera.fr

<sup>3</sup> G. Jonniaux, E. Kervendal are with Airbus Defence and Space, 31400 Toulouse, France {Gregory.Jonniaux, Erwan.Kervendal}@astrium.eads.net

<sup>4</sup> E. Bornschlegl is with the European Space Agency (ESTEC), 2200 AG Noordwijk, The Netherlands Eric.Bornschlegl@esa.int



First the angle  $\Phi - \gamma$  was no longer constant, which ruled out simple calculations such as those performed in (1). Secondly, the rotational OF  $\omega_R = -q$  was included in the measurements. This component  $\omega_R$  was usually subtracted from the measured OF,  $\omega_{meas}$ , using IMU measurements: this operation is known as the derotation process (see [1]). Unfortunately, since the IMU was lost, it was no longer possible to perform the derotation process or to close the attitude control loop depending on pitch and angular pitch velocity measurements. We therefore used an OF based observer to estimate  $\omega_x$  and  $\omega_z$  during the descent as well as the pitch angle  $\theta$  without using any gimballed sensors, IMUs or velocity measurements. In the case of IMU failure, this solution could be used as a backup solution to feed control laws with accurate estimates and enable a small airborne vehicle to perform a soft landing.

### III. OPTIC FLOW FUSION AND LPV MODEL DEFINITION

A fusion scheme was applied to the OF measurements and the landers dynamics (2) were linearized around a reference trajectory so as to obtain a Linear Parameter Varying (LPV) state space model, which was used throughout to design the observer.

Let us take only  $N$  available measurements ( $\omega_{\alpha_1}; \dots; \omega_{\alpha_N}$ ) to estimate the pitch angle  $\theta$  and useful values of OF, namely the ventral OF,  $\omega_x$ , and the expansion OF,  $\omega_z$ :  $\begin{bmatrix} \omega_x(t) \\ \omega_z(t) \end{bmatrix} = \begin{bmatrix} \frac{V_x}{h(t)} \\ \frac{V_z}{h(t)} \end{bmatrix}$  from the available measurements.

Assuming that we are dealing with a practically flat ground (i.e.  $D = h / \cos(\frac{\pi}{2} - \Phi + \gamma)$ , where  $\gamma$  denotes the flight path angle (the orientation of the velocity vector with respect to the local horizontal),  $h$  denotes the ground height, and  $\Phi - \gamma$  denotes the angle between the gaze direction and the local horizontal) and using the notations presented on Fig. 1, we obtain the following general expression for the 2D OF:

$$\omega_{\Phi}(t) = \frac{V(t)}{D(t)} \sin(\Phi(t)) - q(t) \quad (4)$$

where  $\Phi(t) = \alpha + \theta(t) + \gamma(t)$ , and  $D = \frac{h(t)}{\sin(\alpha + \theta(t))}$   
Based on (1) this gives:

$$\omega_{\alpha + \theta}(t) = \frac{1}{2} \begin{pmatrix} 1 - c(2(\alpha + \theta(t))) \\ s(2(\alpha + \theta(t))) \\ -2 \end{pmatrix}^T \begin{bmatrix} \omega_x(t) \\ \omega_z(t) \\ q(t) \end{bmatrix} \quad (5)$$

where  $\sin(\gamma(t)) = \frac{V_z}{V}$  and  $\cos(\gamma(t)) = \frac{V_x}{V}$  and  $\alpha$ , the only time invariant parameter (time notations were dropped for the sake of clarity);  $s(\cdot)$  and  $c(\cdot)$  denotes the sine function and the cosine function.

Extracting a time invariant matrix depending on  $\alpha$  yields

$$\omega_{\alpha + \theta} = \begin{pmatrix} \frac{1}{2} \\ c(2\alpha) \\ s(2\alpha) \end{pmatrix}^T \begin{bmatrix} \omega_x - 2q \\ -c(2\theta)\omega_x + s(2\theta)\omega_z \\ s(2\theta)\omega_x + c(2\theta)\omega_z \end{bmatrix} \quad (6)$$

The following linear system can then be solved using  $N \geq 3$  measurements if  $H^T H$  is invertible:

$$\begin{bmatrix} \omega_x - 2q \\ -\cos(2\theta)\omega_x + \sin(2\theta)\omega_z \\ \sin(2\theta)\omega_x + \cos(2\theta)\omega_z \end{bmatrix} = H_{left}^{-1} \begin{pmatrix} \omega_{\alpha_1 + \theta} \\ \vdots \\ \omega_{\alpha_N + \theta} \end{pmatrix} \quad (7)$$

where the left inverse  $H_{left}^{-1}$  is defined as  $H_{left}^{-1} = (H^T H)^{-1} H^T$ , with  $H_{left}^{-1} H = I_n$ ,  $H \in M(m, n, \mathbb{R})$ ,  $m > n$  and  $H$  defined as follows:

$$H_N = \begin{pmatrix} 1 & \cos(2\alpha_1) & \sin(2\alpha_1) \\ \vdots & \vdots & \vdots \\ 1 & \cos(2\alpha_N) & \sin(2\alpha_N) \end{pmatrix}$$

**Remark** It should be noted that for  $N=3$  the matrix  $H$  matrix is a square matrix:

$$\begin{bmatrix} \omega_x - 2q \\ -c(2\theta)\omega_x + s(2\theta)\omega_z \\ s(2\theta)\omega_x + c(2\theta)\omega_z \end{bmatrix} = H^{-1} \begin{pmatrix} \omega_{\alpha_1 + \theta} \\ \omega_{\alpha_2 + \theta} \\ \omega_{\alpha_3 + \theta} \end{pmatrix} \quad (8)$$

with

$$H = \begin{pmatrix} \frac{1}{2} & \cos(2\alpha_1) & \sin(2\alpha_1) \\ \frac{1}{2} & \cos(2\alpha_2) & \sin(2\alpha_2) \\ \frac{1}{2} & \cos(2\alpha_3) & \sin(2\alpha_3) \end{pmatrix}$$

It has to be checked that the following condition is satisfied to ensure that  $H$  is invertible

$$s(2(\alpha_3 - \alpha_2)) + s(2(\alpha_1 - \alpha_3)) + s(2(\alpha_2 - \alpha_1)) \neq 0 \quad (9)$$

The result of the linear least squares calculation with  $N > 3$  (and the matrix inversion with  $N = 3$ ) gives a nonlinear system with three equations and four unknowns (i.e.  $\omega_x$ ,  $\omega_z$ ,  $\theta$  and  $q$ ) which it is impossible to solve analytically. We therefore had to make use of the knowledge available about the systems dynamics, which was done by designing an LPV observer for a linearized model of the lander's dynamics. Roughly speaking, we therefore linked together two unknowns  $\theta$  and  $q$ , since  $\theta = q$ . During space missions including entry, descent and landing phases, a reference trajectory has often been provided. This trajectory has to be followed during the actual landing to ensure the safety of the lander and reduce the fuel consumption (see [25], [34]). The reference trajectory can be expressed in terms of state trajectories, crater patterns, or a 2-D or 3-D image database [21]. In this study, we adopted a landing scenario with a computed offline reference trajectory which had to be followed. **Our main assumption was that we would stay sufficiently close to this reference trajectory to be able to derive and use an LPV model for the system around the reference trajectory defined by  $X^* = [h^*, \omega_x^*, \omega_z^*, \theta^*, q^*]^T$  involving the input control sequences  $u^* = [u_{th}^*, u_{\theta}^*]^T$  from the system dynamics (2) and the results of the linear least squares calculations (8).** Linearized outputs are given by

$$\begin{aligned}
 Y &= \begin{pmatrix} 1 & 0 & 0 \\ -c(2\theta^*) & s(2\theta^*) & 2\omega_x^*s(2\theta^*) + 2\omega_z^*c(2\theta^*) \\ s(2\theta^*) & c(2\theta^*) & 2\omega_x^*c(2\theta^*) - 2\omega_z^*s(2\theta^*) \end{pmatrix} \begin{pmatrix} \Delta\omega_x \\ \Delta\omega_z \\ \Delta\theta \end{pmatrix} \\
 &+ \begin{pmatrix} -2 \\ 0 \\ 0 \end{pmatrix} \Delta q + \begin{pmatrix} \omega_x^* - 2q^* \\ -c(2\theta^*)\omega_x^* + s(2\theta^*)\omega_z^* \\ s(2\theta^*)\omega_x^* + c(2\theta^*)\omega_z^* \end{pmatrix}
 \end{aligned} \quad (10)$$

Which was rewritten as follows

$$Y = C_1 \begin{pmatrix} \Delta h \\ \Delta q \end{pmatrix} + C_2 (X^*(t)) \begin{pmatrix} \Delta\omega_x \\ \Delta\omega_z \\ \Delta\theta \end{pmatrix} + Y^* \quad (11)$$

$$\text{where } C_1 = \begin{pmatrix} 0 & -2 \\ 0 & 0 \\ 0 & 0 \end{pmatrix}.$$

A linearized state space model around a reference trajectory is given by

$$\begin{cases} \Delta \dot{X} = \begin{pmatrix} \Delta \dot{h} \\ \Delta \dot{q} \\ \Delta \dot{\omega}_x \\ \Delta \dot{\omega}_z \\ \Delta \dot{\theta} \end{pmatrix} = A(\rho(t)) \Delta X + B(\rho(t)) \begin{pmatrix} \Delta u_{th} \\ \Delta u_{\theta} \end{pmatrix} \\ \Delta Y = C(\rho(t)) \Delta X = Y - Y^* \end{cases} \quad (12)$$

with

$$A = \begin{pmatrix} \omega_z^* & 0 & 0 & h^* & 0 \\ 0 & 0 & 0 & 0 & 0 \\ \frac{-s(\theta^*)u_{th}^*}{m_{ldr}h^{*2}} & 0 & -\omega_z^* & -\omega_x^* & \frac{c(\theta^*)u_{th}^*}{m_{ldr}h^*} \\ \frac{-c(\theta^*)u_{th}^*}{m_{ldr}h^{*2}} + \frac{gM_{\phi n}}{h^{*2}} & 0 & 0 & -2\omega_z^* & \frac{-s(\theta^*)u_{th}^*}{m_{ldr}h^*} \\ 0 & 1 & 0 & 0 & 0 \end{pmatrix} \quad (13)$$

$$B = \begin{pmatrix} 0 & 0 \\ 0 & R/I \\ \frac{s(\theta^*)}{m_{ldr}h^*} & 0 \\ \frac{c(\theta^*)}{m_{ldr}h^*} & 0 \\ 0 & 0 \end{pmatrix}; \quad C(\rho(t)) = (C_1 \quad C_2(\rho(t))) \quad (14)$$

The time varying vector  $\rho(t)$  depended on the reference trajectory, its associated input control signals and on the lander's mass so that  $\rho(t) = [h^*, \omega_x^*, \omega_z^*, \theta^*, q^*, u_{th}^*, m_{ldr}]^T$ .

An LPV system was obtained; an LPV observer will now be designed to estimate state deviations from the reference trajectory, assuming that these deviations are small.

#### IV. OBSERVER DESIGN FOR A CLASS OF LPV SYSTEMS AND APPLICATION TO A LUNAR LANDING SCENARIO

In this section, we present an LPV observer based on the solution proposed in [3], which was extended to include a larger class of nonlinear systems and applied to the lunar landing scenario adopted in this paper.

##### A. LPV Observer Design

Let us now consider an LPV system having the following form

$$\begin{cases} \dot{X}(t) = A(\rho(t))X + B(\rho(t))u(t) \\ y(t) = C(\rho(t))X(t) = (C_1 \quad C_2(\rho(t)))X(t) \end{cases} \quad (15)$$

where  $X \in \mathbb{R}^n$ ,  $\rho \in \mathbb{R}^m$ ,  $u \in \mathbb{R}^p$ ,  $y \in \mathbb{R}^r$ ,  $A: \mathbb{R}^m \rightarrow \mathcal{M}(n, n)$ ,  $B: \mathbb{R}^m \rightarrow \mathcal{M}(n, p)$ ,  $C: \mathbb{R}^m \rightarrow \mathcal{M}(r, n)$ ,  $C_1 \in \mathcal{M}(r, n-s)$ ,  $C_2: \mathbb{R}^m \rightarrow \mathcal{M}(r, s)$  where  $\mathcal{M}(k, l)$  denotes the space consisting of  $k \times l$  matrices with  $k$  rows and  $l$  columns with coefficients provided in  $\mathbb{R}$ .  $I_a$  denotes the identity matrix having the size  $a \times a$ .

It is worth noting that the system described by (11)-(12) belongs to this class of LPV systems.

**Lemma 1** *Let us consider the system (15) and assume that the parameter  $\rho(t)$  is measured and regularly persistent (see [3] for a definition) and the sub-matrix  $C_2(\rho(t))$  is invertible and differentiable with respect to time, then for all gain matrices  $\Theta > 0$ , the system:*

$$\dot{\hat{X}}(t) = \bar{A}\hat{X}(t) + \bar{B}u(t) - S^{-1}\bar{C}^T(\hat{y}(t) - y(t)) \quad (16)$$

$$\begin{aligned} \dot{S}(t) &= -\Theta S(t) - \bar{A}(\rho(t))^T S(t) \\ &\quad - S(t)\bar{A}(\rho(t)) + \bar{C}^T\bar{C} \end{aligned} \quad (17)$$

$$S(0) > 0$$

where

$$\bar{X}(t) = \begin{pmatrix} I_{n-s} & 0_{n-s,s} \\ 0_{s,n-s} & C_2(\rho(t)) \end{pmatrix} X(t) = M(\rho(t))X(t)$$

which yields

$$\bar{A} = \left( \dot{M}(\rho(t))M(\rho(t))^{-1} + M(\rho(t))A(\rho(t))M(\rho(t))^{-1} \right)$$

$$\bar{B} = M(\rho(t))B(\rho(t)); \quad \bar{C} = (C_1 \quad I_s)$$

is an observer for (12).

*Proof:* Let us now consider the new state vector resulting from the following change of variable  $\bar{X} = M(\rho(t))X$ : (12) becomes

$$\begin{aligned} \dot{\bar{X}} &= \left( \dot{M}(\rho(t))M(\rho(t))^{-1} + M(\rho(t))A(\rho(t))M(\rho(t))^{-1} \right) \bar{X} \\ &\quad + M(\rho(t))B(\rho(t))u \end{aligned}$$

and

$$y = \bar{C}\bar{X}$$

which corresponds to the class of systems covered by theorem 2.1 presented in [3] (additional proof can be found in [13]). ■

As previous authors have pointed out, with this observer, we ensure that  $\|\epsilon(t)\|^2 \leq ae^{-\lambda_{min}(\Theta)t}$  where  $\epsilon(t) = \hat{X}(t) - X(t)$  is the estimation error,  $\lambda_{min}(\Theta)$  is the smallest eigenvalue of  $\Theta$  and  $a$  is a constant depending on the initial errors,  $\Theta$  and  $u$ .

### B. Application to the lunar lander LPV state space model

Applying the change of variable to the system described in (11)-(12) gives the new state vector

$$\Delta\bar{X} = \begin{pmatrix} \Delta h \\ \Delta q \\ \Delta\bar{x}_1 \\ \Delta\bar{x}_2 \\ \Delta\bar{x}_3 \end{pmatrix} = \begin{pmatrix} I_2 & 0_{2,3} \\ 0_{3,2} & C_2(\rho(t)) \end{pmatrix} \Delta X$$

$$\Delta\dot{\bar{X}} = M(\rho(t)) \Delta X$$

where  $0_{a,b}$  denotes the null matrix having the size  $a \times b$ .

The measurement equation can then be written with a time invariant observation matrix  $\bar{C}$

$$Y = Y^* + (C_1 \quad I_3) \Delta\bar{X} = Y^* + \bar{C} \Delta\bar{X}$$

and the state equation can be written as follows

$$\Delta\dot{\bar{X}} = \begin{pmatrix} I_2 & 0_{2,3} \\ 0_{3,2} & \dot{C}_2 C_2^{-1} + C_2 A C_2^{-1} \end{pmatrix} \Delta\bar{X} + \begin{pmatrix} I_2 & 0_{2,3} \\ 0_{3,2} & C_2 \end{pmatrix} B \Delta u$$

with

$$\dot{C}_2 = \begin{pmatrix} 0 & 0 & 0 \\ 2q^*s(2\theta^*) & 2q^*c(2\theta^*) & C_{223} \\ 2q^*c(2\theta^*) & -2q^*s(2\theta^*) & C_{233} \end{pmatrix}$$

$$C_{223} = 2[2q^*c(2\theta^*)\omega_x^* + s(2\theta^*)\dot{\omega}_x^* - 2q^*s(2\theta^*)\omega_z^* + c(2\theta^*)\dot{\omega}_z^*]$$

$$C_{233} = 2[-2q^*s(2\theta^*)\omega_x^* + c(2\theta^*)\dot{\omega}_x^* - 2q^*c(2\theta^*)\omega_z^* - s(2\theta^*)\dot{\omega}_z^*]$$

By applying lemma (1), the observer can be expressed as follows:

$$\begin{aligned} \Delta\dot{\hat{X}} &= \begin{pmatrix} I_2 & 0_{2,3} \\ 0_{3,2} & \dot{C}_2 C_2^{-1} + C_2 A C_2^{-1} \end{pmatrix} \Delta\hat{X} \\ &+ \begin{pmatrix} I_2 & 0_{2,3} \\ 0_{3,2} & C_2 \end{pmatrix} B \Delta u - S^{-1} \bar{C}^T (\hat{Y} - Y) \\ &= \bar{A} \hat{X}(t) + \bar{B} u(t) - S^{-1} \bar{C}^T (\hat{Y}(t) - Y(t)) \end{aligned} \quad (18)$$

$$\dot{S} = -\Theta S - \bar{A}^T S - S \bar{A} + \bar{C}^T \bar{C}; \quad S(0) > 0 \quad (19)$$

$\Theta$  does influence the observers convergence time, but a high gain  $\Theta$  is liable to amplify any measurement noise present in the simulation involving virtual images of the lunar ground. We therefore used a trial and error method and engineering knowledge of the dynamics and sensors to define the  $S$  and  $\Theta$  matrices as follows:

$$S(0) = \begin{pmatrix} 1 & & & & \\ & 0.2 & & & \\ & & I_2 & & \\ & & & 0.2 & \\ & & & & 0.3 \end{pmatrix} \text{ and } \Theta = \begin{pmatrix} 20 & & & & \\ & 0.05 & & & \\ & & 20I_2 & & \\ & & & & 0.3 \end{pmatrix}$$

$\Theta$  is a tuning parameter which affects the rate of convergence of the estimated states.

### V. SIMULATION RESULTS WITH 3 OF SENSORS ( $N = 3$ )

The results of the simulation illustrate the performances of the LPV observer. We focused here on performing simulations based on real image processing rather than using methods based on the intentional corruption of signals by adding Gaussian noise. Simulations were run under open loop conditions to obtain realistic OF measurements using three sensors placed on the lander at random angles  $\alpha_1 = 90^\circ$ ,  $\alpha_2 = 120^\circ$  and  $\alpha_3 = 160^\circ$  in a range corresponding to the landing scenario adopted here, so that they remained ground oriented during the entire descent phase and the condition defined by (9) was satisfied.

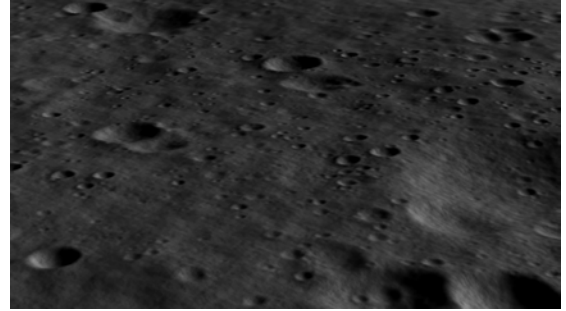


Fig. 2. Example of an image of the lunar ground obtained using PANGU software 2.70

PANGU software was used to generate images of the lunar surface, taking the position of the system, the elevation of the sun and the camera's properties into account. The simulated lunar surface was irregular and sometimes included craters up to 40 m deep. The images generated by PANGU contained 256 gray-scale levels and had a resolution of  $256 \times 256$  pixels. Each of the OF sensors (also called VMSs) included six photoreceptors: the visual axes of each pair of photoreceptors were separated by the inter-receptor angle  $\Delta\varphi = 0.1^\circ$ . The angular sensitivity of each photoreceptor obeyed a 2-D Gaussian function mimicking the angular sensitivity of the fly's photoreceptors with the acceptance angle (the angular width at half height)  $\Delta\rho = \Delta\varphi = 0.1^\circ$ . These small inter-receptor and acceptance angles make it possible to compute very low velocities. Since we have such a narrow field of view, even high spatial frequency contrasts will be detected by the photodiodes, which is extremely useful at low OF levels, where fewer contrasts occur in the sensor's line of sight. In the simulated VMS model, the photoreceptors' output was simulated at each time step by convolving the PANGU-generated lunar surface image with the 2-D Gaussian filter. The simulated 6-pixel VMSs based on the actual code implemented in the sensor then assessed the OF. Fig. 2 shows a simulated image of the lunar ground generated using PANGU. One can see various craters, boulders and shadows caused by the rims of craters and the elevation of the sun. Simulations were run in open loop with precomputed input control signals using a lunar landing scenario starting with  $h_0 = 1496m$ ,  $\omega_{x_0} = 2.18^\circ/s$ ,  $\omega_{z_0} =$

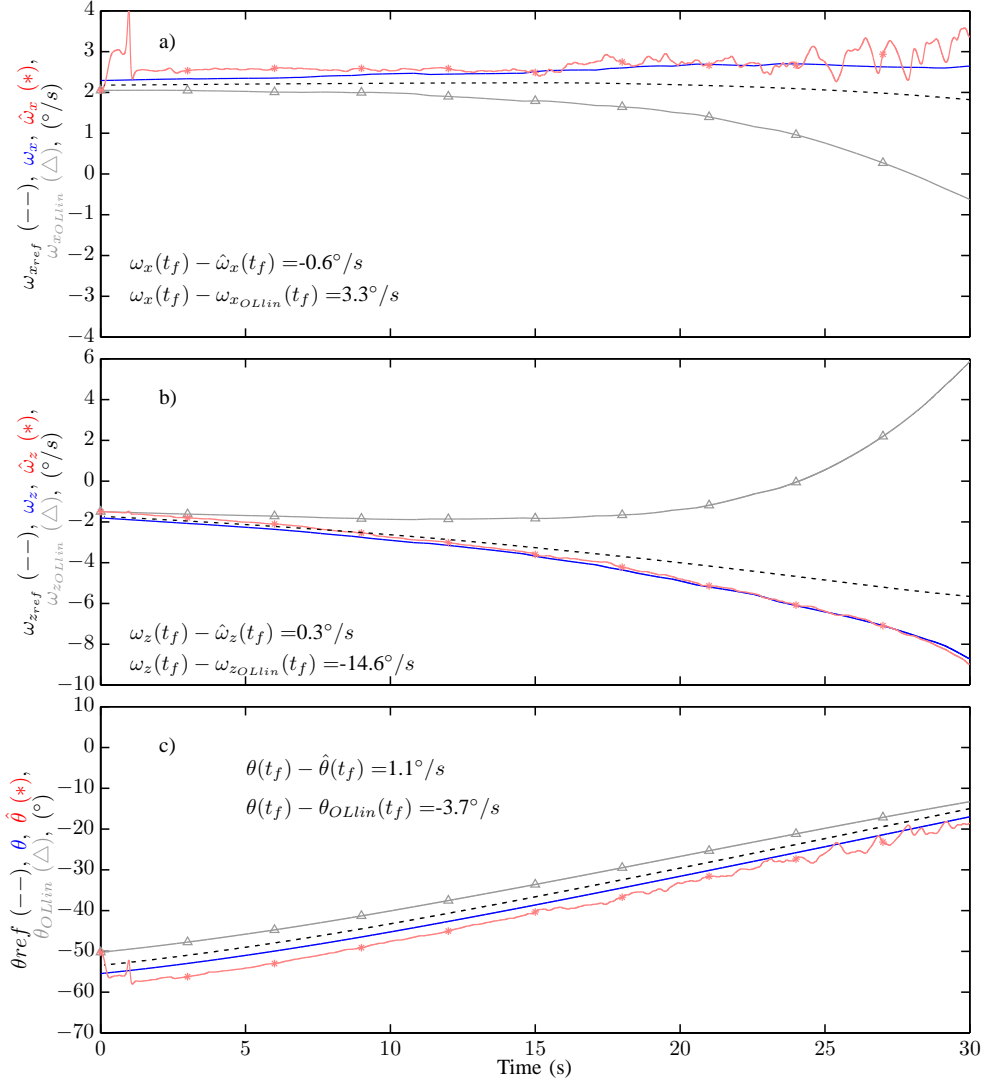


Fig. 3. Evolution of estimated  $\hat{\omega}_x$ ,  $\hat{\omega}_z$  and  $\hat{\theta}$  in the nonlinear system with the newly designed LPV observer. The three sub-figures show the actual state of the nonlinear system (blue line), the reference state (dashed black line), the open loop linearized system ( $\Delta$ -mark line) and the estimated states (\*-mark line). The open loop linearized system states correspond to a simulation where the linearized system is run in open loop from the same initial conditions as the observer (states are denoted  $\omega_{xOLlin}$ ,  $\omega_{zOLlin}$  and  $\theta_{OLlin}$ ). One can see that the estimated states converged quickly toward the actual states of the nonlinear system, which were deliberately intended not to follow the reference trajectory. It should be noted in addition that the open loop linearized system alone would not have sufficed to obtain an accurate state estimation. Estimated states were initialized, giving  $\Delta\hat{\omega}_{x_0} = -0.126^\circ/s$ ,  $\Delta\hat{\omega}_{z_0} = 0.23^\circ/s$ ,  $\Delta\hat{\theta}_0 = 3.23^\circ$ .

$-1.72^\circ/s$ ,  $\theta_0 = -53.43^\circ$ ,  $q_0 = -0.92^\circ/s$ ,  $m_{ldro} = 758kg$ . Initial states deviations from the reference trajectory were chosen so that  $\Delta h_0 = 100m$ ,  $\Delta\omega_{x_0} = -0.115^\circ/s$ ,  $\Delta\omega_{z_0} = -0.08/s$ ,  $\Delta\theta_0 = -2^\circ$ ,  $\Delta q_0 = -0.2^\circ/s$ . The estimated states were initialized, giving  $\Delta\hat{h}_0 = 60m$ ,  $\Delta\hat{\omega}_{x_0} = -0.126^\circ/s$ ,  $\Delta\hat{\omega}_{z_0} = 0.23/s$ ,  $\Delta\hat{\theta}_0 = 3.23^\circ$ ,  $\Delta\hat{q}_0 = -0.2^\circ/s$ . Fig. 3 and Fig.4 present simulations based on the state estimation technique presented here. In sub-figures 3.a-c, one can see the actual state (blue line), the reference state (dashed black line), the open loop linearized system ( $\Delta$ -mark line) and the estimated states (\*-mark line). In the sub-figures 4.c, one can see the actual outputs (blue line), the reference outputs (dashed black line), the linearized open loop outputs ( $\Delta$ -

mark line), the estimated outputs (\*-mark line) and the output given by the PANGU-based measurements ( $\nabla$ -mark line). The open loop linearized system states and outputs were obtained in simulation with the linearized system run in open loop from the same initial conditions as the observer (states are denoted  $\omega_{xOLlin}$ ,  $\omega_{zOLlin}$ ,  $\theta_{OLlin}$ ,  $h_{OLlin}$ ,  $q_{OLlin}$  and  $y_{OLlin}$ ).

As expected  $\hat{\omega}_x$ ,  $\hat{\omega}_z$  and  $\hat{\theta}$  converged quickly toward the actual states, and it is worth noting that we also obtained a raw estimates of  $h$  which took longer to converge but were not intended to be used in the future control scheme.  $\hat{q}$  seems to have been more sensitive to the simulated image-based measurements than the other estimates: this was due to the events created by the OF measurement techniques

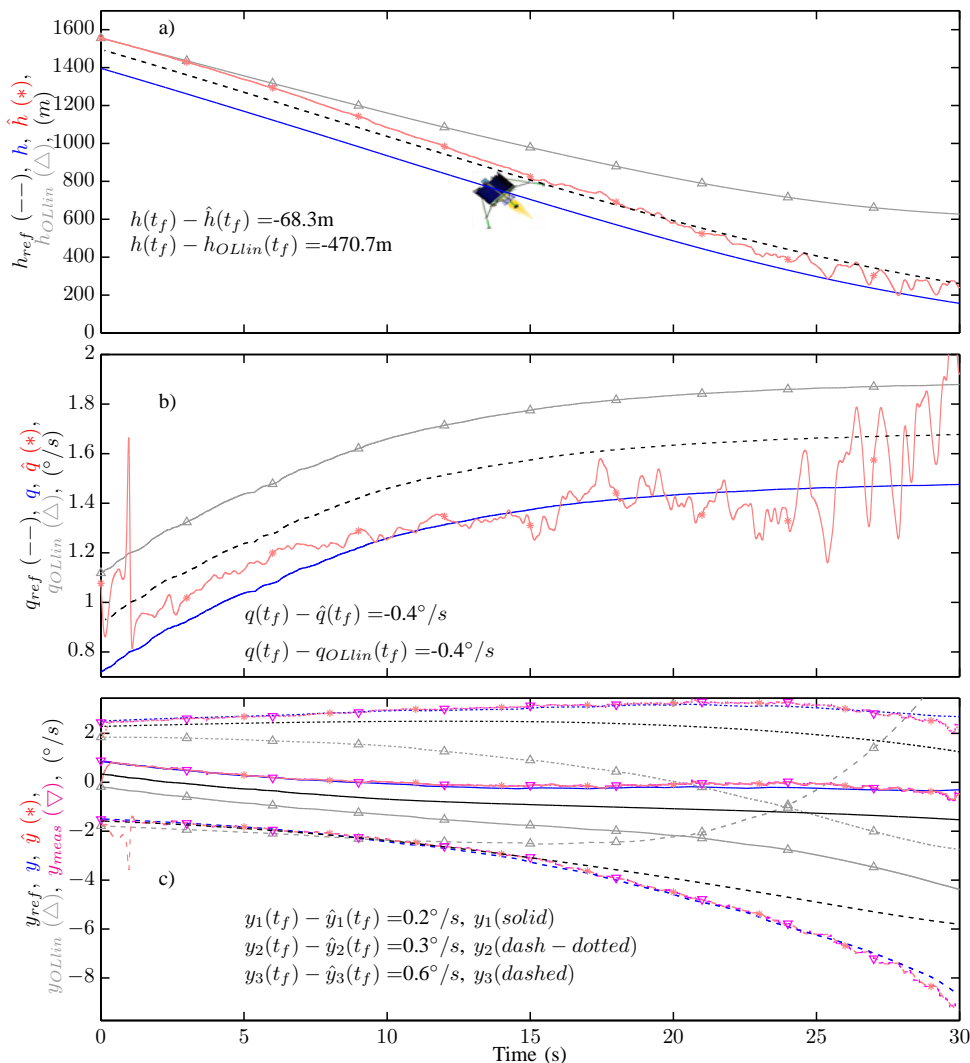


Fig. 4. Evolution of  $\hat{h}$ ,  $\hat{q}$  and the outputs of the observer  $\hat{Y} = [\hat{y}_1, \hat{y}_2, \hat{y}_3]^T$  in the nonlinear system equipped with an LPV observer. One can see from this figure that the estimated states gave good raw estimates of the actual states despite the intrinsic sensitivity of the system to noise during the last few seconds. The estimated outputs were very close to the actual outputs of the nonlinear system. The estimated states were initialized in such a way that  $\Delta\hat{h}_0 = 60\text{m}$ ,  $\Delta\hat{q}_0 = -0.2^\circ/s$ . The open loop linearized system states correspond to a simulation where the linearized system is run in open loop from the same initial conditions as the observer (states are denoted  $h_{OLin}$ ,  $q_{OLin}$  and  $y_{OLin}$ ).

as well as the noise in the measurements. Simulations with theoretical measurements were also run to check the validity of this statement (i.e.  $\hat{q} - q$  tended to 0 when the outputs were perfect). Open loop linearized system ( $\Delta$ -mark line) states (without the presence of an observer) did not converge toward true values, and even diverged with  $\omega_x$  and  $\omega_z$ .

## VI. CONCLUSIONS

This study addressed the state estimation problem by using OF sensors without any need for IMU measurements. In the novel LPV observer adapted from [3] to our class of nonlinear systems by making a change of variable, the measurements used required only three lightweight bio-inspired visual motion sensors hard-mounted onto the landers structure (i.e.  $\omega_{\alpha_1+\theta}$ ,  $\omega_{\alpha_2+\theta}$  and  $\omega_{\alpha_3+\theta}$ ). No inertial measurements (attitude, angular velocities, angular or linear

accelerations) or linear velocities or even altitudes were needed in this setup. The promising results obtained here showed the effectiveness of the observer in simulations based on software-generated images of the lunar ground. The ventral OF, expansion OF and pitch angle estimates were very near the actual states although substantial sensor noise and the estimated initial states were slightly inaccurate. Due to the extreme minimalism of the present OF sensors and the overall backup solution, the performances of the present observer are not comparable with the high-accuracy IMU devices available. However, the present observer was intended as a backup means of driving the lander safely toward the lunar surface based on the use of small, energy efficient sensors if major sensor failures of any kind (involving not only the IMU) should occur.

The next step will consist in designing the control laws,

taking  $\omega_x$ ,  $\omega_z$  and  $\theta$  as inputs to bring the lander safely to the ground while following a precomputed reference trajectory. To overcome the poor estimation of the pitch angular speed, two approaches could be used:

- controlling the lander's attitude only using pitch measurement (basically a position feedback),
- or combining the estimated angular pitch rate with the time derivative of the estimated pitch angle.

It would also be interesting to compare results obtained with the present LPV observer with traditional extended unscented Kalman filters, which are designed on very similar lines and are being increasingly used to meet challenges of this kind. The LPV observer was chosen because of its well-established success with nonlinear systems, and also because of the proof of convergence provided by the Lyapunov theory underlying Besançon, Bornard and Hammouri's observer [3]. A cost-minimization scheme could be developed in order to improve the settings of the observers matrices  $\Theta$  and  $S(0)$ . Further simulations will be performed in order to define the limitations of the solution proposed in terms of the initial errors and measurement noise.

#### ACKNOWLEDGEMENTS

We thank J. Blanc for improving the English manuscript. The authors would like to thank the three anonymous referees for their valuable comments and suggestions to improve the quality of the paper.

#### REFERENCES

- [1] A.A. Argyros, D.P. Tsakiris, and C. Groyer. Biomimetic centering behavior [mobile robots with panoramic sensors]. *Robotics Automation Magazine*, 11(4):21 – 30, 68, Dec. 2004.
- [2] G.L. Barrows and C. Neely. Mixed-mode VLSI optic flow sensors for in-flight control of a Micro Air Vehicle. In *SPIE : Critical technologies for the future of computing*, volume 4109, pages 52–63, San Diego, CA, USA, Aug. 2000.
- [3] G. Besançon, G. Bornard, and H. Hammouri. Observer synthesis for a class of nonlinear control systems. *European Journal of Control*, 2(3):176–192, 1996.
- [4] A. Beyeler, J.C. Zufferey, and D. Floreano. OptiPilot: control of take-off and landing using optic flow. In *European Micro Aerial Vehicle Conference (EMAV)*, volume 27, Delft, Netherlands, Sept. 2009.
- [5] M. Bryson and S. Sukkarieh. Vehicle model aided inertial navigation for a uav using low-cost sensors. In *Proceedings of the Australasian Conference on Robotics and Automation*, 2004.
- [6] T. Cheviron, T. Hamel, R. Mahony, and G. Baldwin. Robust nonlinear fusion of inertial and visual data for position, velocity and attitude estimation of uav. In *Robotics and Automation, 2007 IEEE International Conference on*, pages 2010–2016. IEEE, 2007.
- [7] J. Devolites, J.B. Olsan, and S. Munday. Morpheus 1.5 a lander failure investigation results. In *AIAA SPACE 2013 Conference and Exposition*, 2013.
- [8] G. Flandin, B. Polle, B. Frapard, P. Vidal, C. Philippe, and T. Voirin. Vision based navigation for planetary exploration. In *32nd Annual AAS Rocky Mountain Guidance and Control Conference*, 2009.
- [9] L. R. García Carrillo, A. E. Dzul López, R. Lozano, and C. Pégard. Combining stereo vision and inertial navigation system for a quadrotor uav. *Journal of Intelligent & Robotic Systems*, 65(1-4):373–387, 2012.
- [10] M.A. Garratt and J.S. Chahl. Vision-based terrain following for an unmanned rotorcraft. *Journal of Field Robotics*, 25:284–301, 2008.
- [11] V. Grabe, H.H. Bulthoff, and P.R. Giordano. On-board velocity estimation and closed-loop control of a quadrotor uav based on optical flow. In *Robotics and Automation (ICRA), 2012 IEEE International Conference on*, pages 491–497, May 2012.
- [12] S. Griffiths, J. Saunders, A. Curtis, B. Barber, T. McLain, and R. Beard. Maximizing miniature aerial vehicles. *IEEE Robotics & Automation Magazine*, 13:34–43, 2006.
- [13] H. Hammouri and J. de Leon Morales. Observer synthesis for state-affine systems. In *Decision and Control, 1990., Proceedings of the 29th IEEE Conference on*, pages 784–785. IEEE, 1990.
- [14] B. Hérisse, T. Hamel, R. Mahony, and F.X. Russotto. A terrain-following control approach for a vtol unmanned aerial vehicle using average optical flow. *Autonomous Robots*, 29(3-4):381–399, 2010.
- [15] B. Hérisse, T. Hamel, R. Mahony, and F.X. Russotto. Landing a VTOL unmanned aerial vehicle on a moving platform using optical flow. *IEEE Transactions on Robotics*, 28(1):77 –89, Feb. 2012.
- [16] M.D. Hua. Attitude estimation for accelerated vehicles using gps/ins measurements. *Control Engineering Practice*, 18(7):723–732, 2010.
- [17] D. Izzo and G. de Croon. Landing with time-to-contact and ventral optic flow estimates. *Journal of Guidance, Control, and Dynamics*, 35 (4):1362–1367, 2011.
- [18] D. Izzo and G. de Croon. Nonlinear model predictive control applied to vision-based spacecraft landing. In *Proceedings of the EuroGNC 2013, 2nd CEAS Specialist Conference on Guidance, Navigation & Control, Delft University of Technology*, pages 91–107, Delft, The Netherlands, Apr. 10-12 2013.
- [19] T. Jean-Marius and S.E. Strandmoe. Integrated vision and navigation for a planetary lander. Technical report, AEROSPATIAL, Espace et Défense, Les Mureaux-France. ESA, ESTEC, 1998.
- [20] T. Jean-Marius and S. Trinh. Integrated vision and navigation for planetary exploration - final report. Technical Report RM-TN-00-18-AS/M, Aérospatiale Espace & Défense, 1999.
- [21] A.E. Johnson and J.F. Montgomery. Overview of terrain relative navigation approaches for precise lunar landing. In *Aerospace Conference, 2008 IEEE*, pages 1–10. IEEE, 2008.
- [22] F. Kendoul, I. Fantoni, and K. Nonamib. Optic flow-based vision system for autonomous 3d localization and control of small aerial vehicles. *Robotics and Autonomous Systems*, 57:591–602, 2009.
- [23] F. Kendoul, K. Nonami, I. Fantoni, and R. Lozano. An adaptive vision-based autopilot for mini flying machines guidance, navigation and control. *Autonomous Robots*, 27:165–188, 2009.
- [24] J.J. Koenderink and A.J. Doorn. Facts on optic flow. *Biological Cybernetics*, 56:247–254, 1987.
- [25] X.L. Liu and G.R. Duan. Robust guidance and control of lunar lander using model reference approach. In *Proc. SPIE*, volume 5985, pages 856–860, 2005.
- [26] V. Medici, G. Orchard, S. Ammann, G. Indiveri, and S.N. Fry. Neuromorphic computation of optic flow data bio-inspired landing using biomorphic vision sensors. Technical report, ESA, 2010.
- [27] A.I. Mourikis, N. Trawny, S.I. Roumeliotis, A.E. Johnson, A. Ansar, and L. Matthies. Vision-aided inertial navigation for spacecraft entry, descent, and landing. *IEEE Transactions on Robotics*, 25(2):264 –280, Apr. 2009.
- [28] S. Parkes, M. Dunstan, D. Matthews, I. Martin, and V. Silva. LIDAR-based GNC for planetary landing: Simulation with PANGU. In R.A. Harris, editor, *Data Systems in Aerospace (DASIA)*, page 18.1, Prague, Czech Republic, Jun. 2003.
- [29] F. Ruffier and N. Franceschini. Optic flow regulation: the key to aircraft automatic guidance. *Robotics and Autonomous Systems*, 50:177–194, 2005.
- [30] F. Ruffier and N. Franceschini. Aerial robot piloted in steep relief by optic flow sensors. In *IEEE/RSJ International Conference on Intelligent Robots and Systems (IROS)*, pages 1266–1273. IEEE, 2008.
- [31] G. Sabiron, P. Chavent, T. Raharijaona, P. Fabiani, and F. Ruffier. Low-speed optic-flow sensor onboard an unmanned helicopter flying outside over fields. In *IEEE International Conference on Robotics and Automation (ICRA)*, 2013.
- [32] F. Valette, F. Ruffier, S. Viollet, and T. Seidl. Biomimetic optic flow sensing applied to a lunar landing scenario. In *International Conference on Robotics and Automation (ICRA)*, pages 2253–2260, 2010.
- [33] J. Wendel, O. Meister, Schlaile C., and G.F. Trommer. An integrated gps/mems-imu navigation system for an autonomous helicopter. *Aerospace Science and Technology*, 10(6):527 – 533, 2006.
- [34] J.Y. Zhou, K.L. Teo, D. Zhou, and G.H. Zhao. Optimal guidance for lunar module soft landing. *Nonlinear Dynamics and Systems Theory*, 10(2):189–201, 2010.

## CONCLUSION

This part developed the design of guidance navigation and control strategies for soft lunar landing based on optic flow and attitude measurement with a focus on the possibility to rely solely on optic flow.

In the first article (Sabiron et al., 2014c), we had to adapt the optic flow regulation background to this aerospace application to take into account the fuel consumption objective. It was done via non linear programming to compute a nominal sub-optimal reference trajectory to be tracked through the descent.

Track a pre-computed optimal trajectory could have led to a large fuel consumption if the lander would have oscillated at high frequency around the latest. Indeed a small correction when the lander is below the trajectory might lead to a small overshoot with respect to the trajectory and thus a small correction to reach the trajectory from above and so on. It can be noted that the large inertia of the lander brings a low pass dynamical behavior of the lander which filters out naturally this kind of over-correction. Indeed the lander's dynamics in rotation is slow preventing the correction when above the trajectory and, as observed in simulations, leading to a fuel consumption very close to the optimal scenario in closed loop.

Then, a navigation filter was designed in order to use optic flow sensors fixed to the lander structure giving a viewing direction depending on the current lander's attitude. Finally, two control laws (in (Sabiron et al., 2014b; Sabiron et al., 2014c)) were designed to ensure global asymptotical stability of the closed loop.

This innovative full GNC solution validated through extensive simulations gave interesting results and showed the potential of the optic flow visual cue for space applications. We used the richness of optic flow measurements to act on the different dynamics of the lander and reduce final velocities at the LG.

The next natural step was to reduce further the need for various sensors and get rid of the IMU. Optic flow before derotation not only features information about velocity, vicinity to obstacles but also attitude and angular rates. Instead of derotating the optic flow, the idea was to extract also the knowledge of attitude and angular rate.

(Sabiron et al., 2014a) presented a vision-only linear observer estimating ventral optic flow, expansion optic flow and pitch angle. Using image-based optic flow measurements obtained on an approach phase PANGU simulation were performed to validate the potential of the solution. As far as we know, for the first time a navigation solution allowing to extract attitude information from very lightweight vision sensors was proposed.

Successful results obtained here allow us to consider that an autonomous lunar landing based on optic flow measurement could be performed softly.

An interesting, but time consuming future step, could be to perform a PANGU-based simulation featuring:

- The linear observer to estimate  $\omega_x$ ,  $\omega_z$  and  $\theta$ ,
- The optimal reference trajectory computed via nonlinear programming,
- The inner attitude loop controlling the pitch dynamics,
- The outer loop controlling both  $\omega_x$  and  $\omega_z$  toward their respective reference trajectories.

# DISCUSSION AND OUTLOOK

# 4

## CONTENTS

---

4.1	ACCOMPLISHED WORK . . . . .	147
4.1.1	OF-BASED GNC STRATEGY DESIGN . . . . .	148
4.1.2	OPTIC FLOW SENSORS DEVELOPMENT AND CHARACTERIZATION . . . . .	150
4.1.3	SUMMARY OF THE MAIN CONTRIBUTIONS . . . . .	151
4.2	NEW LIMITS TO EXCEED . . . . .	151
4.2.1	FLAT TERRAIN HYPOTHESIS . . . . .	151
4.2.2	ILLUMINATION CONDITIONS . . . . .	152
4.2.3	6-DOF MOTION . . . . .	153
4.2.4	EVENT BASED CONTROL DESIGN . . . . .	153
4.2.5	ROBUSTNESS OF THE GNC STRATEGY TO INITIAL UNCERTAINTIES . . . . .	153
4.2.6	LINEARIZATION AROUND A REFERENCE TRAJECTORY . . . . .	154
4.3	FUTURE WORK . . . . .	155
4.3.1	FUTURE WORK ON THE OPTIC FLOW SENSORS . . . . .	155
4.3.2	FUTURE WORK ON THE GNC DESIGN . . . . .	156



**T**wo parallel objectives are currently driving planetary landing systems design.

- The first one concerns the need for miniaturized sensors to cope with stringent constraints associated with aerospace vehicles in terms of weight, cost and consumption. Each kilogram added to the lander requires the addition of several kilograms distributed onto the propulsion system and the fuel tanks for both the lander and the launcher.
- The second one is related to the need for light and energy efficient backup GNC strategies in case of main system failure. We need to be sure that the GNC algorithm will bring gently the lander to the planet's surface to ensure the integrity of both the scientific equipment and the lander. Once again the fuel efficiency is required to reduce as much as possible the required amount of fuel at launch.

Using the recent advances in control system theory which improved significantly the design, the tuning and the overall capabilities of feedback systems, vision based techniques have brought new means of controlling such space robotic systems. These efforts helped with the precision, the energy consumption and most of all the reliability of the GNC. In most cases these improvements came at the cost of weight and consumption of the overall system.

Another kind of drawback associated with current solutions is the fact that as soon as one or several sensors are lost, the nominal solution either requires sensor's redundancy or will eventually fail to land softly. The traditional solutions are thus not along the lines of the search for miniaturization.

Bio-inspired approaches that have been extensively studied in literature take the opposing view providing miniaturized sensors, ensuring reliability of the solution and reducing the need for complex and heavy sensor suite. Along with the project partners, we decided to investigate such solutions for planetary landing to validate if whether or not they could provide us a new framework worth considering.

The high-level goal of this project was to bring a proof of feasibility of optic flow-based lunar landing.

### **4.1 Accomplished work**

In this thesis, two main topics have been dealt with, while keeping as a principal motivation the mutual contribution brought by biorobotics to both biology and robotics. Emphasis was placed on the technology transfer from biology to robotics.

Taking inspirations from Nature to develop innovative solutions for planetary landing was the foundation of the scientific contribution. Here, we present and discuss the

results obtained regarding GNC design and simulation as well as development of the two optic flow sensors.

#### 4.1.1 OF-based GNC strategy design

Firstly, we defined a simplified but representative lunar lander model and agreed on the landing scenario to settle the scope of the application. Assumptions and simplifications were made in accordance with literature and industrial partners in order to stay as close as possible to the actual dynamical system and real trajectories to guarantee the representativeness of the simulations.

Once the system was described and the scenario chosen, we addressed the GNC design block after block to provide a full bio-inspired closed loop.

1. The guidance algorithm describes in chapter 3.2 provides an optimal trajectory from point A to point B (namely from HG to LG) with respect to the fuel consumption. Thanks to the nonlinear dynamics describing the lander's motion under physical constraints and scenario requirements, we defined an optimal control problem and solved it using nonlinear programming tools. This optimal trajectory is expressed in terms of lander's states. In order to be used by the optic flow and pitch control laws, this trajectory is then expressed in terms of high interest optic flow and attitude that is to say expansion ( $\omega_z = \frac{V_z}{h}$ ) and ventral ( $\omega_x = \frac{V_x}{h}$ ) optic flow, pitch angle  $\theta$ , and pitch angular rate  $q$ . It is worth noting that the optimal control problem is solved for a specific landing scenario but could be adapted to any kind of trajectory.
2. Two different navigation filters were proposed:
  - i The first one presented in chapter 3.2 fuses **N non-gimbaled measurements after the derotation process**. The IMU is used twice: for the derotation; and for the linear least square formulation which estimates accurately the expansion optic flow  $\omega_z$  and ventral optic flow  $\omega_x$ . For the first time to the best of our knowledge, an optic flow based navigation strategy with large attitude maneuvers ( $-66^\circ \leq \theta < 0^\circ$ ) was proposed with sensors fixed to the lander's body avoiding the requirements for bulky gimbal systems.
  - ii The second, more advanced, navigation filter described in chapter 3.4, fuses **N non-gimbaled measurements before the derotation process**. No IMU is required by the solution anymore. This navigation filter features a linear least square formulation coupled to an LPV observer. It estimates accurately the expansion and ventral optic flow but also the local pitch angle and gives raw

estimates of the height and pitch angular speed as long as the lander stay sufficiently close to the reference trajectory.

3. The control laws ensured the tracking of the optimal optic flow profiles by the estimated expansion and ventral optic flows.
  - i We presented a first nonlinear control design based on the Lyapunov theory in chapter 3.2. The control laws are similar to nonlinear dynamic inversion featuring feedforward terms, and classical PID elements. The global asymptotic stability not strictly proven with this control design. The proof ensured that either the velocities converged either the optic flows converged. This ambiguity was not an issue in the simulations performed but made us design an improved control scheme.
  - ii The second, more advanced, nonlinear control scheme designed in chapter 3.3 was also based on the Lyapunov theory. Control laws were similar to sliding mode control due the switching nature of the equations including absolute values and sign-dependent elements. A rigorous analysis of the closed loop using only optic flow and IMU measurements as feedback information brought proofs of convergence. The underlying trick that made this design possible was the propagated bounds on the altitude obtained via the integration of the expansion optic flow  $\omega_z$ .

Regarding attitude control (i.e. pitch angle and pitch angular velocity control in the 2-D plane), a PID controller was designed and validated through simulations. As for the relation between the attitude and optic flow control loops two strategies were tested.

- i In the first control design (chapter 3.2), the two loops were totally decoupled. Each of them followed their own pre-defined optimal reference trajectories. In the presence of high tracking errors, this might result in a desynchronization since the orientation of the control signal  $u_{th} = (u_x, u_z)^T$  might be shifted from the actual pitch angle  $\theta$ . For example, if the control signals resulting from a large error on the reference tracking gives  $u_{th} = (u_x, 0)^T$  (which correspond to an horizontal thrust of  $u_x$  N) but the pitch control loop regulate  $\theta$  around  $45^\circ$ : the actual thrust will be  $u_{th} = \frac{\sqrt{2}}{2} (u_x, u_x)^T$ .
- ii The second control design (chapter 3.3) provided a strategy to derive a pitch reference signal from the control signal  $u_{th} = (u_x, u_z)^T$ . The optic flow control laws compute  $u_x$  and  $u_z$  which result in the vector  $u_{th}$  defined by a norm  $u_{th} = \sqrt{u_x^2 + u_z^2}$  and an orientation  $\theta_{ref} = \arctan\left(\frac{u_x}{u_z}\right)$  (a small constant  $\varepsilon$  was

added to the denominator to avoid division by zero). Using this strategy, no desynchronization could occur anymore as long as the dynamics of the inner loop are faster than the outer loop (classical requirement for cascaded control).

Simulations performed to validate the GNC solution either integrated SIL capabilities (PANGU software and actual sensor's firmware) in chapter 3.2 and 3.4 or took into account sensor noise in chapter 3.3. SIL simulations were tedious to run due to the high computational requirements of image processing. A simulation including 20 optic flow sensors based on 5 LMSs run for 26 hours on a powerful computer. These times consuming simulations prevented us from running numerous PANGU-based validations. We could not validate the second control design with the second navigation strategy or even run Monte-Carlo simulations.

Another advantage of such distributed sensor solution that have not been investigated or discussed yet, is that in the case of sensor failure, we might expect reduced performances but the solution could keep ensuring soft landing. Indeed, the linear least squares algorithms used in the GNC scheme may give raw measurement even with few defective sensors. This ability is not possible in the case of unique main sensors.

Anyhow, bio-inspired sensors and principles allowed us to design innovative GNC strategies based solely on optic flow sensors fixed to the structure with low weight, size and consumption requirements while ensuring a soft and reliable lunar landing.

#### 4.1.2 Optic flow sensors development and characterization

Consequently we developed and tested these miniature sensors under real life conditions. The challenges addressed during this PhD were two-fold.

- In chapter 2.1, a study brought a two-directional measurement capability to the LMS. Using the LMSs, the optic flow can now be determined in two opposite directions which is extremely helpful in the case of a system rotating while moving forward. Once again, very interesting experimental results were obtained: optic flow was measured accurately in the  $[-350^\circ/s; -80^\circ/s] \cup [80^\circ/s; 350^\circ/s]$  range.
- In chapter 2.2, we had to adapt the measurement range to low speeds to cope with the optic flow range experienced during lunar landings. To do that, we modified the optics (tuned the interreceptor and acceptance angles), the filtering stages (modified cut-off frequencies for analog and digital filters) and the look-up-table to be able to detect high frequency contrasts and measure small optic flow values. Then outdoor tests were performed on-board an 80 kg helicopter. It raised the TRL of the sensors and gave promising results as for the applicability to a real landing scenario. We improved TRL of the LMSs to level 5-6 (Mankins, 1995).

The design of a second low speed optic flow sensor based on 5 LMSs showed the repeatability of the design in chapter 2.2.

### 4.1.3 Summary of the main contributions

One of the main advantages of the optic-flow based GNC framework presented in the thesis is that it could be applied to many different applications. We brought a methodology to compute a fuel efficient path to follow to get from point A to point B in terms of optic flow along with the tools to follow it: control laws and navigation algorithms. Different devices were developed and tested covering a large range of optic flow and thus a wide range of possible applications. Regarding experimental development of sensors, the workflow was introduced and could be repeated to adapt the device to an uncovered range since each steps were presented in details.

## 4.2 New limits to exceed

### 4.2.1 Flat terrain hypothesis

At the beginning of part 3, several assumptions adopted in our work are stated. Among them, one can find that we assume a flat terrain:

- i Moon's radius of curvature is considered infinite
- ii Hills, craters, boulders are not taken into account in the design phases but are included in the PANGU based simulations.

These assumptions might be seen both as limitations and a benefit of the solution.

1. As recently discussed in Ruffier and Franceschini (2014), the optic flow regulation principle allows to follow appropriately the unpredictable changes in the environment although no explicit knowledge of ground height and ground speed are provided. For instance, flying over a hill, will reduce the local height and thus increase the optic flow and thus the tracking error. The optic flow control will increase the braking force to reduce the speed even further. The aforementioned assumptions are thus a benefit of the optic flow regulation principle.
2. However, these hypothesis might become a pitfall when it comes to the measurements. For instance, pitch estimation on an uneven ground might result in large estimation errors since local pitch angle might be radically different from one area to another. Flying over craters could also deteriorate the measurements since we fuse optic flow measurements from several sensors oriented in various directions.

Indeed, few sensors might be oriented toward the crater and thus sense a low optic flow (due to the higher distance to ground) meanwhile sensors oriented before the rim of the craters could experience a much higher optic flow.

A solution to these drawbacks is discussed later on with the hazard avoidance techniques.

#### 4.2.2 Illumination conditions

One limitation about the LMS is the need for contrasts in the surrounding environment. The ESA Lunar Lander mission was designed to study the effects of the surface at the South Pole of the Moon on systems (robots and humans) and to demonstrate soft precision technologies with hazard avoidance (Neal, 2009; De Rosa et al., 2012; Carpenter et al., 2012). Such as usual cameras used for TRN, LMS are passive visual sensors and thus require enough illumination to assess the optic flow. On the one hand, South Pole of the moon offers quasi-continuous illumination conditions of several months. On the other hand illuminated areas are very limited in size and large shadows appear due to the low sun elevation (Bussey et al., 2010; Delaune, 2013) as observed on Fig. 4.1 from the Kaguya mission (see Kato, Sasaki, and Takizawa (2010) for more information about the Kaguya mission).



Figure 4.1 – Image of the Moon's surface near the South Pole taken by the HDTV onboard the KAGUYA at 12:07 p.m. on 11/07/07 (Japan Standard Time). Credit: JAXA/NHK.

Despite the large shadows, the illuminated areas of the lunar surface offers great measurements due to their high contrast as observed in simulations. High level contrasts appear at the lunar surface changing rapidly from strong dark to strong white areas giving noticeable contrasts edges and thus favorable conditions for LMS.

### 4.2.3 6-DOF motion

Unlike flying insects, LMSs feature a very low resolution with its 6 photodiodes. For example, *Drosophila melanogaster* possess a panoramic compound eye with up to 700 ommatidia (Floreano et al., 2013) each of them featuring several photoreceptors.

In this thesis we studied the first option: larger field of view with several 1-D sensors oriented in different viewing directions. With a sensor setup allowing 3D optic flow measurement, one might consider landing on planetary bodies with atmospheric disturbances such as wind gust. This kind of external disturbances might imply high lateral velocities if not taken into account by the GNC strategy (6-DOF motion). However, keeping  $\omega_y$  to 0 could prevent unwanted deviations from the nominal trajectory. Including a control of lateral motion ( $\omega_y$ -control) and an attitude controller for the roll and yaw motions makes the planar test case studied here representative of full 6-DOF performance.

### 4.2.4 Event based control design

We do not take advantage of the event based nature of the LMSs measurements. As long as a no new contrasts are detected, the last measure of optic flow is kept constant and the control signals are computed with a time varying reference signals. These results lead to unnecessary full expenditure. If the tracking error keep growing due to the absence of new measurement (constant output signal), the controller will keep increasing (or decreasing) accordingly the control signals even if the trajectory was successfully corrected. Event-based control theory provides tools to control such systems. Usually these three elements are associated: an event detector, an observer, and a control signal generator. Then, the control signals are computed and delivered to the actuators only when an event occurs (see Åström (2008) for more details on event based control).

### 4.2.5 Robustness of the GNC strategy to initial uncertainties

As discussed in chapters 3.2, 3.3 and 3.4, the guidance scheme presented in this thesis is based on a pre-computed optimal trajectory expressed in terms of optic flow (and pitch angle for the decoupled control strategy presented in the TAES paper). When the lander starts from the nominal conditions at the HG, the guidance provides a fuel efficient trajectory to follow (chapter 3.2 for a full description). Nonetheless, initial conditions may not be perfectly met when switching to our GNC strategy (errors on the initial conditions) which results in a reference trajectory no longer optimal. Two possible ways to deal with this issue could be explored:

- A bank of reference trajectories could be stored in memory. A selection algorithm

would then have to select the most suited trajectory to follow when the GNC solution is switched on. This solution is not an optimal guidance either even if it is better than a guidance based on a fixed and unique trajectory. Indeed, following the correct trajectory would lead to the same energy efficient landing as the one studied in this thesis. Furthermore, with the bank of reference trajectory coupled to the selection process, pinpoint landing could possibly be achieved. When processing the optimal trajectories, an additional constraint on the final downrange has to be added to the optimal control problem to ensure better precision at the LG no matter the initial conditions. Based on conducted simulations, we could expect a  $\pm 30\text{m}$  range of precision at the LG.

- A second improvement for the guidance strategy would be the use of advanced MPC and NMPC (the letter N in the acronym stands for Nonlinear) (Garcia, Prett, and Morari, 1989; Chemori and Marchand, 2008b; Chemori and Marchand, 2008a; Grüne and Pannek, 2011; Alamir, 2012; Camacho and Alba, 2013). These techniques avoid the need for a pre-computed trajectory since the optimization is done online at each time step. Despite the high computational requirements it does solve a cost minimizing control strategy which provides a reference trajectory generation block (see Singh and Fuller (2001) and De Doná et al. (2009)). In that case, the guidance strategy could be said to be optimal with respect to fuel expenditure.

It could be interesting to take into account the model of actuators (pulsed thrusters, saturations) in the stability analysis in the two control designs. Finally, robustness analysis may be performed to validate the full GNC solution. Several theories provide different tools to assess the robustness. One could use advanced analytic tools such as  $\mu$  analysis (Doyle, 1982; Ferreres, 1999), integral quadratic constraint (Megretski and Rantzer, 1997) or even Lyapunov theory (Khalil and Grizzle, 2002). Time domain analysis methods such as Monte-Carlo simulations are extensively used in all space programs (see for example Hanson and Beard (2010)). In order to run Monte-Carlo simulations the issue of the duration of PANGU-based simulations would have to be addressed first.

#### 4.2.6 Linearization around a reference trajectory

The navigation solution presented in chapter 3.4 linearize the lander's dynamics around the reference trajectory to get an LPV model of the lander and design the LPV observer. The hypothesis always associated with linearization around equilibrium is that the system has to stay sufficiently close to the equilibrium to be representative of the system. In the current setup, with a unique reference trajectory starting from the nominal HG,

initial conditions could be, in practice, quite far from the reference trajectory. These deviations could lead to the divergence of the LPV observer. However it is important to note that the simulations performed in chapter 3.4 with high initial deviations in height did not make the observer to diverge. With an improved guidance scheme featuring either a bank of reference trajectory or a MPC computed reference, the deviations at the HG could be greatly reduced and the estimation improved in terms of precision, robustness to measurement noise and observer's dynamics.

### 4.3 Future work

Following this PhD thesis, several ideas could be exploited to study further this optic flow based framework.

Firstly, some technical ideas are given and secondly we discuss potential applications.

#### 4.3.1 Future work on the optic flow sensors

We focused in this thesis on the approach phase from HG to LG to define a limited scope to work on. Interesting properties of the optic flow could be used to design GNC solution for the other phases of EDL for two main reasons:

1. As already mentioned, using a different kind of photoreceptor (matrix-shaped for instance) would allow the measurement of the optical flow vector field (2D-optic flow). An improved version of the LMS could allow vertical descent to be handled. Smooth vertical descent might be achieved by keeping all translational optic flow ( $\omega_x$  and  $\omega_y$ ) to zero and regulating the expansion optic flow ( $\omega_z$ ) around a reference. Furthermore de Croon et al. (2013) showed that flatness of the landing surface and the surface slope could be estimated using optic flow. This might be an interesting new feature to study in the hazard detection and avoidance system.
2. In the current firmware version of the LMS, the optic flow is assessed via a look up table containing the optic flow value for a certain time of travel with a fixed  $\Delta\phi$ . The fixed size look up table, imposed by the limited internal memory of the dsPIC, constraints the measured optic flow range. With an enhanced version of microcontroller, the look up table could be larger, widening *de facto* the measured optic flow range. As discussed in introduction, the "Time of travel" scheme computes a mean optic flow over  $\Delta t$  seconds. Innovative methods could be used to measure an optic flow more representative of the actual angular velocity of the images. With larger computational resources, other methods to determine the

time of travel could be used to improve the robustness of the output and enlarge the measurement range (see Kerhuel (2009) for an innovative example).

#### 4.3.2 Future work on the GNC design

As already mentioned in conclusion of part 3, it may be interesting to combine, the LPV observer presented in chapter 3.4 with the guidance proposed in chapter 3.2 and the improved control scheme described in chapter 3.3 in a simulator and assess the overall performances of the GNC strategy on PANGU-based simulations.

An unified GNC scheme from deorbit burn to touchdown could replace the time triggered EDL sequence demonstrated on MSL and thus avoid what could be seen as open loop critical events. Optic flow is a matter of scaling. The same sensor based on 5 LMSs could be used without any changes during another phase (for example with a faster speed and a proportionally higher altitude): it could result in the same experienced optic flow range.

Defining the GNC framework (i.e. providing new ways to bring the lander to the LG) paved the way for future research. Indeed, from a control systems point of view, this application is very interesting. It offers a challenging problem with a highly non-linear under-actuated system with actuators' saturations and very few measurements (state vector not measured). On top of that, in this thesis we made the assumption that the control signal was delivered as a continuous signal to the actuator meanwhile only quantized and sampled values are achievable due to the ON-OFF type of thrusters (see for instance Burlion (2007) for more details on sampled-data control). This makes room for many future studies to be performed from the GNC perspective as already stated:

- MPC techniques for the guidance algorithm,
- Kalman-like filters for state estimation,
- Nonlinear and/or robust nested control for the optic flow and pitch control loops,
- Nonlinear quantized and sampled-data control laws.

Hazard detection and avoidance algorithm issues have not been addressed in this work. However, optic flow regulators allow by definition either to keep a safe distance from obstacles or to reduce drastically the system's velocity as discussed by Serres et al. (2008a). Flying over an obstacle (for example a hill) will result in a decrease of the local height which will increase the measured optic flow and create a tracking error. This tracking error will result in an increase of the thrust (i.e. in the delivered control signals) which will reduce the lander's velocity. This obstacle avoidance behavior is intrinsic to

the optic flow regulators but it does not provide much information on potential hazard located on the predefined trajectory.

An interesting idea to anticipate frontal obstacles would be to use frontal mounted sensors and compare their outputs with expected output in the case of a planar terrain as studied by Ruffier and Franceschini (2008). As soon as a cliff, a crater, a mountain will appear in the field of view of the frontal mounted sensors, the residual errors between measurements and predicted output which indicate the presence of an obstacle will raise and could trigger an alarm. Then the avoidance strategy has to be developed to select another hazard free landing site and initiate the avoidance maneuver. The study performed by Zufferey (2005) (see chapter 5, Fig. 5.3) showed the optic flow amplitude along the equatorial of the vision sensor for various frontal approach of obstacle (at different approach angles). One can see that depending on the approach angle different behaviors might be observed which reinforce the idea of an obstacle avoidance strategy based on residual measurements assessed comparing nominal behavior with actual landing.

Another very critical space application concerns autonomous on orbit rendezvous capability, which is even more critical in the case of manned station. High precision requirements for docking have to be fulfilled. Active debris removal (ADR) is currently in extensively studied by all the space actors (Kaplan, 2009; Kervendal, Chabot, and Kanani, 2013). Some ADR strategies require autonomous on orbit rendezvous with non-cooperative target to catch it before initiating reentry. Optic flow regulation could also be used to ensure centering and low velocity approach for the proximity operations and docking (last tens of meters). Keeping the lateral optic flows ( $\omega_x$  and  $\omega_y$ ) to zero and the expansion optic flow close to a reference might ensure safe and precision docking.

Several other applications might also benefit from this interesting technology. Automotive industry could be of particular interest in such sensori-motor processing and associated sensors for autonomous driving tasks such as parking, centering or even obstacle avoidance. Finally, one can think of aeronautical applications: during the parking phase self-motion could be estimated thanks to optic flow integration at a known height.

To conclude, countless applications might be of interest to apply these bio-inspired principles developed for millions of years by nature to achieve such complex behaviors.



# BIBLIOGRAPHY

- Acikmese, B. and Ploen, S. R. (2007).  
“Convex programming approach to powered descent guidance for Mars landing”.  
In: *Journal of Guidance, Control, and Dynamics* 30.5, pp. 1353–1366.
- Alamir, M. (2012).  
“A framework for real-time implementation of low-dimensional parameterized NMPC”. In: *Automatica* 48.1, pp. 198–204.
- Amic, S. (2002).  
“Intégration des fonctions de détection de mouvements par le traitement parallèle des signaux visuels”. MA thesis. École Nationale Supérieure d'Électronique et de Radioélectricité de Grenoble.
- Anderson, B. D. and Moore, J. B. (2012).  
*Optimal filtering*. Courier Dover Publications.
- Argyros, A. A., Tsakiris, D. P., and Groyer, C. (2004).  
“Biomimetic centering behavior [mobile robots with panoramic sensors]”. In: *IEEE Robotics Automation Magazine* 11.4, pp. 21–30, 68. ISSN: 1070-9932. DOI: 10.1109/MRA.2004.1371612.
- Åström, K. J. (1996).  
“Automatic control: A perspective”. In: *Colloquium on Automatic Control*. Ed. by C. Bonivento, G. Marro, and R. Zanas. Vol. 215. Lecture Notes in Control and Information Sciences. Springer Berlin Heidelberg, pp. 1–26. ISBN: 978-3-540-76060-3.
- (2008).  
“Event based control”. In: *Analysis and design of nonlinear control systems*. Springer, pp. 127–147.
- Åström, K. J. and Kumar, P. (2014).  
“Control: A perspective”. In: *Automatica* 50.1, pp. 3–43. ISSN: 0005-1098.
- Åström, K. J. and Murray, R. M. (2010).  
*Feedback systems: an introduction for scientists and engineers*. Princeton university press.
- Aubépart, F. and Franceschini, N. (2007).  
“Bio-inspired optic flow sensors based on FPGA: Application to Micro-Air-Vehicles”. In: *Microprocessors and Microsystems* 31, pp. 408–419.
- Baird, E., Srinivasan, M., Zhang, S., Lamont, R., and Cowling, A. (2006).  
“Visual Control of Flight Speed and Height in the Honeybee”. In: *From Animals to Animats 9*. Ed. by S. Nolfi, G. Baldassarre, R. Calabretta, J. Hallam, D. Marocco, J.-A. Meyer, O. Miglino, and D. Parisi. Vol. 4095. Springer Berlin / Heidelberg, pp. 40–51. ISBN: 978-3-540-38608-7.

- Ball, A. J., Garry, J. R. C., Lorenz, R. D., and Kerzhanovich, V. (2007). *Planetary landers and entry probes*. Vol. 1. Cambridge University Press Cambridge, UK.
- Barron, A. and Srinivasan, M. V. (2006). "Visual regulation of ground speed and headwind compensation in freely flying honey bees (*Apis mellifera* L.)" In: *Journal of Experimental Biology* 209.5, pp. 978–984.
- Barron, J. L., Fleet, D. J., and Beauchemin, S. S. (1994). "Performance of optical flow techniques". In: *International journal of computer vision* 12.1, pp. 43–77.
- Barrows, G. L. and Neely, C. (2000). "Mixed-mode VLSI optic flow sensors for in-flight control of a Micro Air Vehicle". In: *SPIE : Critical technologies for the future of computing*. Vol. 4109. San Diego, CA, USA, pp. 52–63.
- Benson, R. and Delbrück, T. (1992). *Direction selective silicon retina that uses null inhibition*. Ed. by D. Touretzky. San Mateo, CA: Morgan Kaufman, pp. 756–763.
- Bertrand, S., Hamel, T., and Piet-Lahanier, H. (2008). "Stability analysis of an uav controller using singular perturbation theory". In: *Proceedings of the 17th IFAC world congress*, pp. 5706–5711.
- Besançon, G., Bornard, G., and Hammouri, H. (1996). "Observer synthesis for a class of nonlinear control systems". In: *European Journal of Control* 2.3, pp. 176–192.
- Besançon, G. (2007). "Nonlinear observers and applications". In:
- Beyeler, A., Zufferey, J. C., and Floreano, D. (2009a). "OptiPilot: control of take-off and landing using optic flow". In: *European Micro Aerial Vehicle Conference (EMAV)*. Vol. 27. Delft, Netherlands.
- (2009b). "Vision-based control of near-obstacle flight". In: *Autonomous robots* 27, pp. 201–219.
- Blanes, C. (1986). "Appareil Visuel élémentaire pour la navigation à vue d'un robot mobile autonome". (Advisor: N. Franceschini). Neurosciences, Univ. Aix-Marseille II.
- (1991). "Guidage visuel d'un robot mobile autonome d'inspiration bionique (Advisor: N. Franceschini)". PhD thesis. INP Grenoble.
- Bonin-Font, F., Ortiz, A., and Oliver, G. (2008). "Visual navigation for mobile robots: A survey". In: *Journal of intelligent and robotic systems* 53.3, pp. 263–296.
- Borst, A. (2000). "Models of motion detection". In: *Nature neuroscience* 3, pp. 1168–1168.
- Boyd, S. and Vandenberghe, L. (2009). *Convex optimization*. Cambridge university press.
- Brady, T. and Paschall, S. (2010). "The challenge of safe lunar landing". In: *IEEE Aerospace Conference, 2010*, pp. 1–14.

- Braun, R. D. and Manning, R. M. (2007).  
 “Mars exploration entry, descent, and landing challenges”. In: *Journal of spacecraft and rockets* 44.2, pp. 310–323.
- Bryson, A. E. (1975).  
*Applied optimal control: optimization, estimation and control*. CRC Press.
- Burkhart, P. D. and Casoliva, J. (2012).  
 “MSL DSENGS EDL analysis and operations”. In: *23rd International Symposium on Space Flight Dynamics (ISSFD), Pasadena, California, October 29–November 2, 2012*. Pasadena, CA: Jet Propulsion Laboratory, National Aeronautics and Space Administration, 2012.
- Burlion, L. (2007).  
 “Contribution à l’analyse et à la commande de systèmes non linéaires à commande échantillonnée”. PhD thesis. Université de Paris-Sud XI.
- Bussey, D., McGovern, J., Spudis, P., Neish, C., Noda, H, Ishihara, Y, and Sørensen, S.-A. (2010).  
 “Illumination conditions of the south pole of the Moon derived using Kaguya topography”. In: *Icarus* 208.2, pp. 558–564.
- Camacho, E. F. and Alba, C. B. (2013).  
*Model predictive control*. Springer.
- Carpenter, J., Fisackerly, R., Espinasse, S., and Lunar Exploration Definition Team, the (2010).  
*Lunar Exploration Definition Team Lunar Exploration Objectives and Requirements Definition*. Tech. rep. ESA Report. URL: [http://www.lpi.usra.edu/lunar/strategies/LunarLander\\_LERD\\_CDI\\_230512.pdf](http://www.lpi.usra.edu/lunar/strategies/LunarLander_LERD_CDI_230512.pdf).
- Carpenter, J. D., Fisackerly, R., De Rosa, D., and Houdou, B. (2012).  
 “Scientific preparations for lunar exploration with the European Lunar Lander”. In: *Planetary and Space Science* 74.1, pp. 208–223.
- Chahl, J. and Mizutani, A. (2012).  
 “Biomimetic attitude and orientation sensors”. In: *Sensors Journal, IEEE* 12.2, pp. 289–297.
- Chahl, J., Thakoor, S., Le Bouffant, N., Stange, G., Srinivasan, M. V., Hine, B., and Zornetzer, S. (2003).  
 “Bioinspired engineering of exploration systems: a horizon sensor/attitude reference system based on the dragonfly ocelli for mars exploration applications”. In: *Journal of Robotic Systems* 20.1, pp. 35–42.
- Chan, R., Mulla, A., and Stol, K. (2010).  
 “Characterisation of Low-cost Optical Flow Sensors”. In: *Proceedings of the IEEE of the Australasian Conference on Robotics and Automation (ACRA)*. Brisbane, Australia, pp. 1–8.
- Chaumette, F. and Hutchinson, S. (2006).  
 “Visual servo control. I. Basic approaches”. In: *IEEE Robotics & Automation Magazine* 13.4, pp. 82–90.
- Chaumette, F., Hutchinson, S., et al. (2007).  
 “Visual servo control, Part II: Advanced approaches”. In: *IEEE Robotics and Automation Magazine* 14.1, pp. 109–118.

- Chemori, A. and Marchand, N. (2008a).  
 "A prediction-based nonlinear controller for stabilization of a non-minimum phase PVTOL aircraft". In: *International Journal of Robust and Nonlinear Control* 18.8, pp. 876–889.
- (2008b).  
 "Global discrete-time stabilization of the pvtol aircraft based on fast predictive control". In: *Proceedings of the 17th World Congress The International Federation of Automatic Control*.
- Cheng, R. (1966).  
 "Surveyor Terminal Guidance". In: *Peaceful Uses of Automation in Outer Space*. Springer, pp. 499–514.
- Cheng, Y. and Ansar, A. (2005).  
 "Landmark Based Position Estimation for Pinpoint Landing on Mars". In: *IEEE International Conference on Robotics and Automation (ICRA)*, pp. 1573 –1578.
- Cheng, Y., Goguen, J., Johnson, A., Leger, C., Matthies, L., Martin, M., and Willson, R. (2004).  
 "The Mars exploration rovers descent image motion estimation system". In: *Intelligent Systems, IEEE* 19.3, pp. 13–21.
- Chin, G., Brylow, S., Foote, M., Garvin, J., Kasper, J., Keller, J., Litvak, M., Mitrofanov, I., Paige, D., Raney, K., et al. (2007).  
 "Lunar reconnaissance orbiter overview: The instrument suite and mission". In: *Space Science Reviews* 129.4, pp. 391–419.
- Cho, D.-H., Jeong, B., Lee, D., and Bang, H. (2009).  
 "Optimal perilune altitude of lunar landing trajectory". In: *International Journal of Aeronautical & Space Sciences* 10.1, pp. 67–74.
- Collett, T. and Land, M. (1975).  
 "Visual control of flight behaviour in the hoverfly *Syritta pipiens* L." In: *Journal of Comparative Physiology* 99.1, pp. 1–66.
- Conroy, J., Gremillion, G., Ranganathan, B., and Humbert, J. (2009).  
 "Implementation of wide-field integration of optic flow for autonomous quadrotor navigation". In: *Autonomous Robots* 27 (3), pp. 189–198. ISSN: 0929-5593.
- Coron, J.-M. (2009).  
*Control and nonlinearity*. 136. American Mathematical Soc.
- Crawford, I. A., Anand, M., Cockell, C., Falcke, H., Green, D., Jaumann, R., and Wic-zorek, M. (2012).  
 "Back to the Moon: The scientific rationale for resuming lunar surface exploration". In: *Planetary and Space Science* 74.1, pp. 3–14.
- David, C. T. (1982).  
 "Compensation for height in the control of groundspeed by *Drosophila* in a new, 'barber's pole' wind tunnel". In: *Journal of comparative physiology* 147.4, pp. 485–493.
- de Croon, G. and Izzo, D. (2012).  
 "Real-time landing based on optimality principles and vision". In: *23rd International Symposium on Space Flight Dynamics (ISSFD)*.

- de Croon, G., Izzo, D, and Schiavone, G (2011).  
 “Time-to-Contact Estimation in Landing Scenarios Using Feature Scales”. In: *International Joint Conference on Artificial Intelligence*. Advanced Concepts Team, European Space Agency.
- de Croon, G., Ho, H., De Wagter, C, Van Kampen, E, Remes, B, and Chu, Q. (2013).  
 “Optic-flow based slope estimation for autonomous landing”. In: *International Journal of Micro Air Vehicles* 5.4, pp. 287–298.
- De Doná, J., Suryawan, F, Seron, M., and Lévine, J. (2009).  
 “A flatness-based iterative method for reference trajectory generation in constrained NMPC”. In: *Nonlinear Model Predictive Control*. Springer, pp. 325–333.
- de Plinval, H. (2014).  
 “Commande référencée vision pour drones à décollages et atterrissages verticaux”. PhD thesis. Institut Supérieur de l’Aéronautique et de l’Espace.
- De Rosa, D., Bussey, B., Cahill, J. T., Lutz, T., Crawford, I. A., Hackwill, T., Gasselt, S. van, Neukum, G., Witte, L., McGovern, A., et al. (2012).  
 “Characterisation of potential landing sites for the European Space Agency’s Lunar Lander project”. In: *Planetary and Space Science* 74.1, pp. 224–246.
- Delaune, J. (2009).  
 “Guidance and Control for Lunar Descent and Landing”. MA thesis. Cranfield University.
- (2013).  
 “Navigation visuelle pour l’atterrissage planétaire de précision indépendante du relief”. PhD thesis. Institut Supérieur de l’Aéronautique et de l’Espace.
- Delaune, J., Le Besnerais, G., Sanfourche, M., Voirin, T., Bourdarias, C., and Farges, J.-L. (2012).  
 “Optical Terrain Navigation for Pinpoint Landing: Image Scale and Position-Guided Landmark Matching”. In: *Advances in the Astronautical Sciences* 144, pp. 627–643.
- Desai, P. N., Prince, J. L., Queen, E. M., Schoenenberger, M. M., Cruz, J. R., and Grover, M. R. (2011).  
 “Entry, Descent, and Landing Performance of the Mars Phoenix Lander”. In: *Journal of Spacecraft and Rockets* 48.5, pp. 798–808.
- Deutschmann, R. A. (1997).  
 “Analog VLSI Motion Sensors”. PhD thesis. Technische Universität München; California Institute of Technology.
- Douglass, J. K. and Strausfeld, N. J. (1996).  
 “Visual motion-detection circuits in flies: parallel direction-and non-direction-sensitive pathways between the medulla and lobula plate”. In: *The Journal of neuroscience* 16.15, pp. 4551–4562.
- Doyle, J. (1982).  
 “Analysis of feedback systems with structured uncertainties”. In: *IEE Proceedings D (Control Theory and Applications)*. Vol. 129. 6. IET, pp. 242–250.
- Draper, C. (1965).  
*Space Navigation Guidance and Control. Volume 1*. Tech. rep. R-500. Massachusetts Institute of Technology - Instrumentation Laboratory.

- Dubois-Matra, O., Parkes, S., and Dunstam, M. (2009).  
 “Testing and Validation of Planetary Vision-based navigation systems with PANGU”. In: *21st International Symposium on Space Flight Dynamics (ISSFD)*. Toulouse, France.
- Egelhaaf, M., Boeddeker, N., Kern, R., Kurtz, R., and Lindemann, J. (2012).  
 “Spatial vision in insects is facilitated by shaping the dynamics of visual input through behavioural action”. In: *Frontiers in Neural Circuits* 6.108. ISSN: 1662-5110.
- Expert, F. (2013).  
 “Flying robot inspired by insects: From optic flow sensing to visually guided strategies to control a Micro Aerial Vehicle”. PhD thesis. Université d’Aix-Marseille.
- Expert, F., Roubieu, F., and Ruffier, F. (2012).  
 “Interpolation based “time of travel” scheme in a Visual Motion Sensor using a small 2D retina”. In: *IEEE Sensors Conference 2012*, pp. 2231–2234.
- Expert, F. and Ruffier, F. (2012).  
 “Controlling docking, altitude and speed in a circular high-roofed tunnel thanks to the optic flow”. In: *IEEE/RSJ International Conference on Intelligent Robots and Systems (IROS)*. IEEE, pp. 1125–1132.
- Expert, F., Viollet, S., and Ruffier, F. (2011).  
 “Outdoor Field Performances of Insect-Based Visual Motion Sensors”. In: *Journal of Field Robotics* 28, pp. 529–541.
- Fantoni, I. and Lozano, R. (2002).  
*Non-linear control for underactuated mechanical systems*. Springer.
- Ferreres, G. (1999).  
*A practical approach to robustness analysis*. Springer.
- Floreano, D., Pericet-Camara, R., Viollet, S., Ruffier, F., Brückner, A., Leitel, R., Buss, W., Menouni, M., Expert, F., Juston, R., et al. (2013).  
 “Miniature curved artificial compound eyes”. In: *Proceedings of the National Academy of Sciences* 110.23, pp. 9267–9272.
- Forest, L. M., Kessler, L. J., and Homer, M. (2007).  
 “Design of a human-interactive autonomous flight manager (AFM) for crewed lunar landing”. In: *AIAA Infotech Aerospace, Rohnert Park, CA*, pp. 7–10.
- Franceschini, N. (1983).  
 “In-vivo microspectrofluorimetry of visual pigments.” In: *Symposia of the Society for Experimental Biology*. Vol. 36, p. 53.
- Franceschini, N. (1985).  
 “Early processing of colour and motion in a mosaic visual system”. In: *Neuroscience Research (Suppl. 2)*. Ed. by Elsevier, pp. 17–49.
- (2009).  
 “Towards automatic visual guidance of aerospace vehicles: from insects to robots”. In: *Acta Futura*. Vol. 3, pp. 15–34.
- Franceschini, N. (2014).  
 “Small Brains, Smart Machines: From Fly Vision to Robot Vision and Back Again”. In: *Proceedings of the IEEE* 102.5, pp. 751–781. ISSN: 0018-9219. DOI: 10.1109/JPROC.2014.2312916.

- Franceschini, N., Pichon, J., and Blanes, C. (1992).  
 "From insect vision to robot vision". In: *Philosophical Transactions of the Royal Society of London* 337, pp. 283–294.
- Franceschini, N., Riehle, A., and Nestour, A. (1989).  
 "Facets of vision". In: ed. by D. Stavenga and R. Hardie. Springer. Chap. Directionally selective motion detection by insect neurons, pp. 360–390.
- Franceschini, N., Ruffier, F., and Serres, J. (2007).  
 "A Bio-Inspired Flying Robot Sheds Light on Insect Piloting Abilities". In: *Current Biology* 17, pp. 329–335.
- Franceschini, N. (1975).  
 "Sampling of the visual environment by the compound eye of the fly: fundamentals and applications". In: *Photoreceptor optics*. Springer, pp. 98–125.
- Frapard, B and Mancuso, S (2006).  
 "Vision navigation for European landers and the NPAL project". In: *6th International ESA Conference on Guidance, Navigation and Control Systems, Loutraki, Greece. ESA (October 2005)*.
- Garcia, C. E., Prett, D. M., and Morari, M. (1989).  
 "Model predictive control: theory and practice - a survey". In: *Automatica* 25.3, pp. 335–348.
- Garratt, M. and Chahl, J. (2008).  
 "Vision-Based Terrain Following for an Unmanned Rotorcraft". In: *Journal of Field Robotics* 25, pp. 284–301.
- Gauthier, J.-P. and Kupka, I. (2001).  
*Deterministic observation theory and applications*. Cambridge University Press.
- Gianpaolo, C. and Patrick, D. (2009).  
 "Vision-based unmanned aerial vehicle navigation using geo-referenced information". In: *EURASIP Journal on Advances in Signal Processing* 2009.
- Gibson, J. (1950).  
 "The perception of the visual world". In: New York: Houghton Mifflin.
- Goswami, J. and Annadurai, M (2009).  
 "Chandrayaan-1: India's first planetary science mission to the moon". In: *Current Science* 96.4, pp. 486–491.
- Götz, K. (1964).  
 "Optomotorische untersuchung des visuellen systems einiger Augenmutanten der fruchtfliege *Drosophila*." In: *Biological Cybernetics* 2, pp. 77–92.
- Green, W., Oh, P., and Barrows, G. (2004).  
 "Flying insect inspired vision for autonomous aerial robot maneuvers in near-earth environments". In: *International Conference on Robotics and Automation (ICRA)*. Vol. 3, 2347–2352 Vol.3.
- Griffiths, S., Saunders, J., Curtis, A., Barber, B., McLain, T., and Beard, R. (2006).  
 "Maximizing miniature aerial vehicles". In: *IEEE Robotics & Automation Magazine* 13, pp. 34–43.

- Griffiths, S., Saunders, J., Curtis, A., Barber, B, McLain, T, and Beard, R (2007).  
 "Obstacle and terrain avoidance for miniature aerial vehicles". In: *Advances in Unmanned Aerial Vehicles*. Springer, pp. 213–244.
- Grotzinger, J. P., Crisp, J., Vasavada, A. R., Anderson, R. C., Baker, C. J., Barry, R., Blake, D. F., Conrad, P., Edgett, K. S., Ferdowski, B., et al. (2012).  
 "Mars Science Laboratory mission and science investigation". In: *Space Science Reviews* 170.1-4, pp. 5–56.
- Grüne, L. and Pannek, J. (2011).  
*Nonlinear model predictive control*. Springer.
- Guerrero-Castellanos, J.-F., Rifai, H., Marchand, N., and Poulin, G. (2009).  
 "Bounded attitude stabilization of rigid bodies without attitude estimation and velocity measurement". In: *IEEE International Conference on Robotics and Biomimetics, 2008. ROBIO 2008*. IEEE, pp. 2203–2209.
- Guizzo, G., Draï, R, Desprè, N, and Jurado, M. M. (2011).  
 "Flight Tests Results of the Precision Landing GNC Test Facility". In: *8th International ESA Conference on Guidance, Navigation & Control Systems*, Carlsbad, Czech Republic.
- Guo, J. and Han, C. (2009).  
 "Design of guidance laws for lunar pinpoint soft landing". In: *Advances in the Astronautical Sciences* 135.3, pp. 2133–2145.
- Hamel, J.-F., Neveu, D., and Lafontaine, J. de (2006).  
 "Feature matching navigation techniques for lidar-based planetary exploration". In: *AIAA Guidance, Navigation and Control Conference and Exhibit*.
- Hanson, J. and Beard, B. (2010).  
 "Applying monte carlo simulation to launch vehicle design and requirements analysis". In:
- Hargraves, C. R. and Paris, S. W. (1987).  
 "Direct trajectory optimization using nonlinear programming and collocation". In: *Journal of Guidance, Control, and Dynamics* 10.4, pp. 338–342.
- Harrison, R. R. (2000).  
 "An analog VLSI motion sensor based on the fly visual system". PhD thesis. California Institute of Technology.
- Harrison, R. R. and Koch, C. (1999).  
 "A Robust Analog VLSI Motion Sensor Based on the Visual System of the Fly". In: *Autonomous Robots* 7(3) (3), pp. 211–224. ISSN: 0929-5593.
- Harvey, B. (2007).  
*Russian planetary exploration: history, development, legacy and prospects*. Springer.
- Hateren, J. and Schilstra, C (1999).  
 "Blowfly flight and optic flow. II. Head movements during flight". In: *Journal of Experimental Biology* 202.11, pp. 1491–1500.
- Hausen, K. (1982).  
 "Motion sensitive interneurons in the optomotor system of the fly". In: *Biological Cybernetics* 45.2, pp. 143–156.

- Hengstenberg, R. (1988).  
 “Mechanosensory control of compensatory head roll during flight in the blowfly *Calliphora erythrocephala* Meig.” In: *Journal of comparative Physiology A* 163.2, pp. 151–165.
- Hérissé, B., Hamel, T., Mahony, R., and Russotto, F. (2010).  
 “A terrain-following control approach for a VTOL Unmanned Aerial Vehicle using average optical flow”. English. In: *Autonomous Robots* 29.3-4, pp. 381–399. ISSN: 0929-5593. DOI: 10.1007/s10514-010-9208-x. URL: <http://dx.doi.org/10.1007/s10514-010-9208-x>.
- (2012).  
 “Landing a VTOL Unmanned Aerial Vehicle on a Moving Platform Using Optical Flow”. In: *IEEE Transactions on Robotics* 28.1, pp. 77–89.
- Hérissé, B. (2010).  
 “Asservissement et Navigation Autonome d’un drone en environnement incertain par flot optique”. PhD thesis. Université Nice Sophia Antipolis.
- Hérissé, B., Russotto, F.-X., Hamel, T., and Mahony, R. (2008).  
 “Hovering flight and vertical landing control of a VTOL unmanned aerial vehicle using optical flow”. In: *IEEE/RSJ International Conference on Intelligent Robots and Systems, 2008*, pp. 801–806.
- Hérissé, B., Hamel, T., Mahony, R., and Russotto, F.-X. (2009).  
 “A nonlinear terrain-following controller for a VTOL unmanned aerial vehicle using translational optical flow”. In: *IEEE International Conference on Robotics and Automation, 2009*, pp. 3251–3257.
- Honegger, D., Meier, L., Tanskanen, P., and Pollefeys, M. (2013).  
 “An open source and open hardware embedded metric optical flow cmos camera for indoor and outdoor applications”. In: *IEEE International Conference on Robotics and Automation, 2013*, pp. 1736–1741.
- HorrIDGE, G. A. (1977).  
 “The compound eye of insects”. In: *Scientific American* 237, pp. 108–120.
- Hua, M.-D., Hamel, T., Morin, P., and Samson, C. (2009).  
 “A control approach for thrust-propelled underactuated vehicles and its application to VTOL drones”. In: *IEEE Transactions on Automatic Control* 54.8, pp. 1837–1853.
- (2013).  
 “Introduction to feedback control of underactuated VTOL vehicles: A review of basic control design ideas and principles”. In: *IEEE Control Systems* 33.1, pp. 61–75.
- Humbert, J. S., Conroy, J. K., Neely, C. W., and Barrows, G. (2010).  
 “Wide-field integration methods for visuomotor control”. In: *Flying Insects and Robots*. Springer, pp. 63–71.
- Humbert, J. and Hyslop, A. (2010).  
 “Bioinspired visuomotor convergence”. In: *IEEE Transactions on Robotics* 26.1, pp. 121–130.
- Hutchinson, S., Hager, G. D., and Corke, P. I. (1996).  
 “A tutorial on visual servo control”. In: *IEEE Transactions on Robotics and Automation* 12.5, pp. 651–670.

- Hyslop, A. and Humbert, J. (2010).  
 “Autonomous navigation in three-dimensional urban environments using wide-field integration of optic flow”. In: *Journal of guidance, control, and dynamics* 33.1, pp. 147–159.
- Hyslop, A., Krapp, H. G., and Humbert, J. S. (2010).  
 “Control theoretic interpretation of directional motion preferences in optic flow processing interneurons”. In: *Biological cybernetics* 103.5, pp. 353–364.
- Iida, F. (2001).  
 “Goal-directed navigation of an autonomous flying robot using biologically inspired cheap vision”. In: *Proceedings of the 32nd International Symposium on Robotics (ISR)*. Vol. 1404–1409. Seoul, South Korea, p. 21.
- Iida, F. (2003).  
 “Biologically inspired visual odometer for navigation of a flying robot”. In: *Robotics and Autonomous Systems* 44.3, pp. 201–208.
- Isidori, A. (1995).  
*Nonlinear control systems*. Vol. 1. Springer.
- Izzo, D. and de Croon, G. (2011).  
 “Landing with time-to-contact and ventral optic flow estimates”. In: *Journal of Guidance, Control, and Dynamics* 35 (4), pp. 1362–1367.
- (2013).  
 “Nonlinear model predictive control applied to vision-based spacecraft landing”. In: *Proceedings of the EuroGNC 2013, 2nd CEAS Specialist Conference on Guidance, Navigation & Control, Delft University of Technology*. Delft, The Netherlands, pp. 91–107.
- Izzo, D., Weiss, N., and Seidl, T. (2011).  
 “Constant-Optic-Flow Lunar Landing: Optimality and Guidance”. In: *Journal of Guidance, Control, and Dynamics* 34, pp. 1383–1395.
- Jabbari, E., Kim, D., Lee, L. P, and Ghaemmaghami, A., eds. (2014).  
*Handbook of Biomimetics and Bioinspiration: Biologically-Driven Engineering of Materials, Processes, Devices, and Systems*. World Scientific Publishing Company.
- Janschek, K., Tchernykh, V., and Beck, M. (2006).  
 “Performance Analysis for Visual Planetary Landing Navigation Using Optical Flow and DEM Matching”. In: *AIAA Guidance, Navigation, and Control Conference and Exhibit*.
- Johansen, T. and Fossen, T. (2013).  
 “Control allocation - A survey”. In: *Automatica* 49.5, pp. 1087–1103.
- Johnson, A. and Montgomery, J. (2008).  
 “Overview of terrain relative navigation approaches for precise lunar landing”. In: *Aerospace Conference, 2008 IEEE*. IEEE, pp. 1–10.
- Johnson, A., Willson, R., Cheng, Y., Goguen, J., Leger, C., Sanmartin, M., and Matthies, L. (2007).  
 “Design through operation of an image-based velocity estimation system for Mars landing”. In: *International Journal of Computer Vision* 74.3, pp. 319–341.
- Johnson, A. E., Klumpp, A. R., Collier, J. B., and Wolf, A. A. (2002).  
 “Lidar-based hazard avoidance for safe landing on Mars”. In: *Journal of guidance, control, and dynamics* 25.6, pp. 1091–1099.

- Kaplan, M. H. (2009).  
 "Survey of space debris reduction methods". In: *AIAA 6619*, p. 2009.
- Kato, M, Sasaki, S, Tanaka, K, Iijima, Y, and Takizawa, Y (2008).  
 "The Japanese lunar mission SELENE: Science goals and present status". In: *Advances in Space Research* 42.2, pp. 294–300.
- Kato, M., Sasaki, S., and Takizawa, Y. (2010).  
 "The Kaguya mission overview". In: *Space science reviews* 154.1-4, pp. 3–19.
- Kendoul, F., Fantoni, I, and Nonami, K. (2009).  
 "Optic flow-based vision system for autonomous 3D localization and control of small aerial vehicles". In: *Robotics and Autonomous Systems* 57, pp. 591–602.
- Kendoul, F., Nonami, K., Fantoni, I., and Lozano, R. (2009).  
 "An adaptive vision-based autopilot for mini flying machines guidance, navigation and control". In: *Autonomous Robots* 27 (3), pp. 165–188.
- Kendoul, F., Yu, Z., and Nonami, K. (2010).  
 "Guidance and nonlinear control system for autonomous flight of minirotorcraft unmanned aerial vehicles". In: *Journal of Field Robotics* 27.3, pp. 311–334.
- Kennedy, J. S. (1940).  
 "The visual responses of flying mosquitoes." In: *Proceedings of the Zoological Society of London*. Vol. 109. 4. Wiley Online Library, pp. 221–242.
- Kennedy, J. S. (1951).  
 "The migration of the desert locust (*Schistocerca gregaria* Forsk.). I. The behaviour of swarms. II. A theory of long-range migrations". In: *Philosophical Transactions of the Royal Society of London. Series B, Biological Sciences*, pp. 163–290.
- Kerhuel, L., Viollet, S., and Franceschini, N. (2010).  
 "Steering by gazing: An efficient biomimetic control strategy for visually guided micro aerial vehicles". In: *IEEE Transactions on Robotics* 26.2, pp. 307–319.
- Kerhuel, L. (2009).  
 "Capteurs optiques minimalistes & réflexes oculomoteurs biomimétiques. Application à la robotique aérienne". PhD thesis. Université Montpellier II-Sciences et Techniques du Languedoc.
- Kervendal, E., Chabot, T., and Kanani, K. (2013).  
 "GNC Challenges and Navigation Solutions for Active Debris Removal Mission". In: *Advances in Aerospace Guidance, Navigation and Control*. Springer, pp. 761–779.
- Keshavan, J, Gremillion, G, Escobar-Alvarez, H, and Humbert, J. (2014).  
 "A  $\mu$  analysis-based, controller-synthesis framework for robust bioinspired visual navigation in less-structured environments". In: *Bioinspiration & biomimetics* 9.2, p. 025011.
- Khalil, H. K. and Grizzle, J. (2002).  
*Nonlinear systems*. Vol. 3. Prentice hall Upper Saddle River.
- Kirchner, W. and Srinivasan, M. (1989).  
 "Freely flying honeybees use image motion to estimate object distance". In: *Naturwissenschaften* 76.6, pp. 281–282.

- Kirschfeld, K. (1976).  
 "The Resolution of Lens and Compound Eyes". English. In: *Neural Principles in Vision*. Ed. by F. Zettler and R. Weiler. Proceedings in Life Sciences. Springer Berlin Heidelberg, pp. 354–370. ISBN: 978-3-642-66434-2.
- Koenderink, J. and Doorn, A. (1987).  
 "Facts on optic flow". In: *Biological Cybernetics* 56, pp. 247–254.
- Kokotović, P. and Arcak, M. (2001).  
 "Constructive nonlinear control: a historical perspective". In: *Automatica* 37.5, pp. 637–662.
- Krapp, H. G. and Hengstenberg, R. (1996).  
 "Estimation of self-motion by optic flow processing in single visual interneurons". In: *Nature* 384.6608, pp. 463–466.
- Krøvel, T. (2005).  
 "Optimal tuning of PWPF modulator for attitude control". MA thesis. Norwegian University of Science and Technology.
- Krüger, H. and Theil, S. (2010).  
 "TRON-Hardware-in-the-loop test facility for lunar descent and landing optical navigation". In: *18th IFAC Symposium on Automatic Control in Aerospace*. IFAC.
- Kuenen, L. and Baker, T. (1982).  
 "Optomotor regulation of ground velocity in moths during flight to sex pheromone at different heights". In: *Physiological Entomology* 7.2, pp. 193–202.
- Kumakura, Y. (2000).  
 "Biomimetics—State of the art and its application to industry". In: *Mem. School BOST Kinki University* 6.1.
- Land, M. F. (1997).  
 "Visual Acuity In Insects". In: *Annual Review of Entomology* 42, pp. 147–177.
- Land, M. F. and Nilsson, D.-E. (2012).  
*Animal eyes*. Oxford University Press.
- Lee, D. N. et al. (1976).  
 "A theory of visual control of braking based on information about time-to-collision". In: *Perception* 5.4, pp. 437–459.
- Lepora, N. F., Verschure, P., and Prescott, T. (2013).  
 "The state of the art in biomimetics". In: *Bioinspiration & biomimetics* 8.1, p. 013001.
- Li, S. (2008).  
 "Computer Vision Based Autonomous Navigation for Pin-Point Landing Robotic Spacecraft on Asteroids". In: *Intelligent Robotics and Applications*. Springer, pp. 1115–1126.
- Liebe, C. C. (2002).  
 "Accuracy performance of star trackers—a tutorial". In: *Aerospace and Electronic Systems, IEEE Transactions on* 38.2, pp. 587–599.
- Liu, X.-L., Duan, G.-R., and Teo, K.-L. (2008).  
 "Optimal soft landing control for moon lander". In: *Automatica* 44.4, pp. 1097–1103.

- Loucks, M. et al. (2005).  
 “A comparison of lunar landing trajectory strategies using numerical simulations”.  
 In: *International Lunar Conference-September*.
- Ma, K. Y., Chirarattananon, P., Fuller, S. B., and Wood, R. J. (2013).  
 “Controlled flight of a biologically inspired, insect-scale robot”. In: *Science* 340.6132,  
 pp. 603–607.
- Mahony, R., Kumar, V., and Corke, P. (2012).  
 “Multirotor aerial vehicles: Modeling, estimation, and control of quadrotor”. In:  
*Robotics & Automation Magazine, IEEE* 19.3, pp. 20–32.
- Manecy, A., Viollet, S., and Marchand, N. (2012).  
 “Bio-inspired hovering control for an aerial robot equipped with a decoupled eye  
 and a rate gyro”. In: *IEEE/RSJ International Conference on Intelligent Robots and Sys-  
 tems, 2012*. IEEE, pp. 1110–1117.
- Manecy, A., Juston, R., Marchand, N., and Viollet, S. (2013).  
 “Decoupling the eye: a Key toward a Robust Hovering for sighted Aerial Robots”.  
 In: *Advances in Aerospace Guidance, Navigation and Control*. Springer, pp. 317–336.
- Mankins, J. C. (1995).  
 “Technology readiness levels”. In: *White Paper, April 6*.
- Marchand, N. and Hably, A. (2005).  
 “Global stabilization of multiple integrators with bounded controls”. In: *Automatica*  
 41.12, pp. 2147–2152.
- Marchand, N., Hably, A., and Chemori, A. (2007).  
 “Global stabilization with low computational cost of the discrete-time chain of in-  
 tegrators by means of bounded controls”. In: *IEEE Transactions on Automatic Control*  
 52.5, pp. 948–952.
- Mazarico, E., Rowlands, D., Neumann, G., Smith, D., Torrence, M., Lemoine, F., and  
 Zuber, M. (2012).  
 “Orbit determination of the lunar reconnaissance orbiter”. In: *Journal of Geodesy* 86.3,  
 pp. 193–207.
- McCrum, M, Parkes, S, Martin, I, and Dunstan, M (2010).  
 “Mars Visual Simulation for ExoMars Navigation Algorithm Validation”. In: *Proc. of*  
*i-SAIRAS*, pp. 283–290.
- Medici, V., Orchard, G., Ammann, S., Indiveri, G., and Fry, S. (2010).  
*Neuromorphic computation of optic flow data Bio-inspired landing using biomorphic vision*  
*sensors*. Tech. rep. ESA.
- Megretski, A. and Rantzer, A. (1997).  
 “System analysis via integral quadratic constraints”. In: *Automatic Control, IEEE*  
*Transactions on* 42.6, pp. 819–830.
- Metropolis, N. and Ulam, S. (1949).  
 “The monte carlo method”. In: *Journal of the American statistical association* 44.247,  
 pp. 335–341.
- Moeckel, R. and Liu, S.-C. (2007).  
 “Motion Detection Circuits for a Time-To-Travel Algorithm”. In: *IEEE International*  
*Symposium on Circuits and Systems (ISCAS)*, pp. 3079–3082.

- Moeckel, R. and Liu, S.-C. (2010).  
 "Motion detection chips for robotic platforms". In: *Flying Insects and Robots*. Springer, pp. 101–114.
- Moini, A. (2000).  
*Vision Chips: XA-NL*. Springer.
- Moore, R., Thurrowgood, S., Bland, D., Soccol, D., and Srinivasan, M. V. (2009).  
 "A stereo vision system for UAV guidance". In: *IEEE/RSJ International Conference on Intelligent Robots and Systems, 2009*. IEEE, pp. 3386–3391.
- Mourikis, A., Trawny, N., Roumeliotis, S., Johnson, A., Ansar, A., and Matthies, L. (2009).  
 "Vision-Aided Inertial Navigation for Spacecraft Entry, Descent, and Landing". In: *IEEE Transactions on Robotics* 25.2, pp. 264–280.
- Nalbach, G (1993).  
 "The halteres of the blowfly *Calliphora*". In: *Journal of Comparative Physiology A* 173.3, pp. 293–300.
- Neal, C. R. (2009).  
 "The Moon 35 years after Apollo: What's left to learn?" In: *Chemie der Erde-Geochemistry* 69.1, pp. 3–43.
- Netter, T. and Francheschini, N. (2002).  
 "A robotic aircraft that follows terrain using a neuromorphic eye". In: *IEEE/RSJ International Conference on Intelligent Robots and Systems, 2002*. Vol. 1, pp. 129–134.
- Ouyang, Z., Li, C., Zou, Y., Zhang, H., Lü, C., Liu, J., Liu, J., Zuo, W., Su, Y., Wen, W., et al. (2010).  
 "Primary scientific results of Chang'E-1 lunar mission". In: *Science China Earth Sciences* 53.11, pp. 1565–1581.
- Parkes, S., Martin, I., and Dunstan, M. (2004).  
 "Planet Surface Simulation with PANGU". In: *8th International Conference on Space Operations (2004)*. Montréal, Canada, pp. 1–10.
- Parkes, S., Dunstan, M., Matthews, D., Martin, I., and Silva, V. (2003).  
 "LIDAR-based GNC for Planetary Landing: Simulation with PANGU". In: *Data Systems in Aerospace (DASIA)*. Ed. by R. Harris. Prague, Czech Republic, p. 18.1.
- Parkes, S., Martin, I., and Dunstan, M. (2003).  
*Planet and Asteroid Natural Scene Generation Utility - Final Report*. Tech. rep. 11747/95/NL/JG. University of Dundee.
- Parkes, S. M. and Martin, I. (1999).  
 "Virtual lunar landscapes for testing vision-guided lunar landers". In: *IEEE International Conference on Information Visualization, 1999*. IEEE, pp. 122–127.
- Pichon, J.-M., Blanes, C., and Franceschini, N. (1989).  
 "Visual guidance of a mobile robot equipped with a network of self-motion sensors". In: *SPIE Conf. on Mobile Robots IV*. Ed. by W. Wolfe and W. Chun. Vol. 1195. Bellingham, U.S.A., pp. 44–53.
- Pichon, J.-M. (1991).  
*Guidage visuel d'un robot mobile autonome d'inspiration bionique*. Tech. rep. Grenoble, INPG.

- Ploen, S., Acikmese, B., and Wolf, A. (2006).  
 “A comparison of powered descent guidance laws for mars pinpoint landing”. In: *AIAA Guidance, Navigation, and Control Conference, Keystone, CO*.
- Pollard, B. D. and Sadowy, G. (2005).  
 “Next generation millimeter-wave radar for safe planetary landing”. In: *Aerospace Conference, 2005 IEEE*. IEEE, pp. 1213–1219.
- Portelli, G., Serres, J., Ruffier, F., and Franceschini, N. (2010).  
 “Modelling honeybee visual guidance in a 3-D environment”. In: *Journal of Physiology - Paris* 104, pp. 27–39.
- Portelli, G. (2011).  
 “Le pilotage visuel chez l’abeille: expériences et modèle”. PhD thesis. Université de Toulouse, Université Toulouse III-Paul Sabatier.
- Portelli, G., Ruffier, F., and Franceschini, N. (2010).  
 “Honeybees change their height to restore their optic flow”. In: *Journal of Comparative Physiology A* 196.4, pp. 307–313.
- Portelli, G., Ruffier, F., Roubieu, F. L., and Franceschini, N. (2011).  
 “Honeybees’ speed depends on dorsal as well as lateral, ventral and frontal optic flows”. In: *PloS one* 6.5, e19486.
- Pudas, M., Viollet, S., Ruffier, F., Kruusing, A., Amic, S., Leppävuori, S., and Franceschini, N. (2007).  
 “A miniature bio-inspired optic flow sensor based on low temperature co-fired ceramics (LTCC) technology”. In: *Sensors and actuators A: Physical* 133.1, pp. 88–95.
- Ramanan, R. and Lal, M. (2005).  
 “Analysis of optimal strategies for soft landing on the Moon from lunar parking orbits”. In: *Journal of earth system science* 114.6, pp. 807–813.
- Reichardt, W. (1969).  
 “Movement perception in insects”. In: *Processing of optical data by organisms and machines, International School of Physics “Enrico Fermi”: Course XLIII, 1968, Academic Press, New York, NY, USA*, pp. 465–493.
- Reichardt, W. (1957).  
 “Autokorrelationsauswertung als Funktionsprinzip des Zentralnervensystems”. In: *Zeitschrift Naturforschung Teil A* 12, p. 756.
- (1987).  
 “Evaluation of optical motion information by movement detectors”. In: *Journal of Comparative Physiology A* 161.4, pp. 533–547.
- Riehle, A and Franceschini, N (1984).  
 “Motion detection in flies: parametric control over ON-OFF pathways”. In: *Experimental Brain Research* 54.2, pp. 390–394.
- Rifaï, H., Marchand, N., and Poulin-Vittrant, G. (2012).  
 “Bounded control of an underactuated biomimetic aerial vehicle - Validation with robustness tests”. In: *Robotics and Autonomous Systems* 60.9, pp. 1165–1178.
- Rifaï, H., Guerrero-Castellanos, J.-F., Marchand, N., and Poulin-Vittrant, G. (2013).  
 “Biomimetic-based output feedback for attitude stabilization of a flapping-wing micro aerial vehicle”. In: *Robotica* 31.06, pp. 955–968.

- Robinson, M., Brylow, S., Tschimmel, M., Humm, D., Lawrence, S., Thomas, P., Denevi, B., Bowman-Cisneros, E., Zerr, J., Ravine, M., et al. (2010).  
 “Lunar reconnaissance orbiter camera (LROC) instrument overview”. In: *Space Science Reviews* 150.1-4, pp. 81–124.
- Roubieu, F. (2013).  
 “Réalisation d’un micro-robot autonome, inspiré du contrôle de vitesse et d’évitement d’obstacles observés chez l’abeille”. PhD thesis. Université d’Aix-Marseille.
- Roubieu, F., Expert, F., Boyron, M., Fuschlock, B., Viollet, S., and Ruffier, F. (2011).  
 “A novel 1-gram insect based device measuring visual motion along 5 optical directions”. In: *IEEE Sensors conference*. Limerick, Ireland, pp. 687–690.
- Roubieu, F., Serres, J., Franceschini, N., Ruffier, F., and Viollet, S. (2012).  
 “A fully-autonomous hovercraft inspired by bees: wall following and speed control in straight and tapered corridors”. In: *IEEE International Conference on Robotics and Biomimetics (ROBIO)*. IEEE, pp. 1311–1318.
- Roubieu, F., Expert, F., Sabiron, G., and Ruffier, F. (2013).  
 “Two-Directional 1-g Visual Motion Sensor Inspired by the Fly’s Eye”. In: *Sensors Journal, IEEE* 13.3, pp. 1025–1035. ISSN: 1530-437X. DOI: 10.1109/JSEN.2012.2230622.
- Roubieu, F. L., Serres, J. R., Colonnier, F., Franceschini, N., Viollet, S., and Ruffier, F. (2014).  
 “A biomimetic vision-based hovercraft accounts for bees’ complex behaviour in various corridors”. In: *Bioinspiration & biomimetics* 9.3, p. 036003.
- Rozas, P. and Cunningham, A. (1972).  
*Apollo Experience Report - Lunar Module Landing Radar and Rendezvous Radar*. Tech. rep. NASA.
- Ruderman, D. L. and Bialek, W. (1994).  
 “Statistics of natural images: Scaling in the woods”. In: *Physical review letters* 73.6, p. 814.
- Ruffier, F. (2004).  
 “Pilote automatique biomimétique - Système générique inspiré du contrôle visuo-moteur des insectes pour : le décollage, le suivi de terrain, la réaction au vent et l’atterrissage automatiques d’un micro-aéronef”. PhD thesis. INP Grenoble.
- Ruffier, F. and Expert, F. (2012).  
 “Visual motion sensing onboard a 50-g helicopter flying freely under complex VICON-lighting conditions”. In: *International Conference on Complex Medical Engineering*. Kobe, Japan, pp. 634–639.
- Ruffier, F. and Franceschini, N. (2003).  
 “OCTAVE, a bioinspired visuo-motor control system for the guidance of Micro-Air Vehicles”. In: *SPIE Conference on Bioengineered and Bioinspired Systems*. Ed. by A. Rodriguez-Vazquez, D. Abbott, and R. Carmona. Vol. 5119. Maspalomas, Spain, pp. 1–12.
- (2005).  
 “Optic flow regulation: the key to aircraft automatic guidance”. In: *Robotics and Autonomous Systems* 50, pp. 177–194.

- (2008).  
 “Aerial robot piloted in steep relief by optic flow sensors”. In: *IEEE/RSJ International Conference on Intelligent Robots and Systems (IROS)*. IEEE, pp. 1266–1273.
- Ruffier, F., Viollet, S., Amic, S., and Franceschini, N. (2003).  
 “Bio-inspired optical flow circuits for the visual guidance of micro air vehicles.” In: *IEEE International Symposium on Circuits and Systems (ISCAS)*. Vol. 3. Bangkok, Thailand, pp. 846–849.
- Ruffier, F. and Franceschini, N. (2014).  
 “Optic Flow Regulation in Unsteady Environments: A Tethered MAV Achieves Terrain Following and Targeted Landing Over a Moving Platform”. English. In: *Journal of Intelligent & Robotic Systems*, pp. 1–19. ISSN: 0921-0296.
- Rutishauser, D., Epp, C., and Robertson, E. (2012).  
 “Free-Flight Terrestrial Rocket Lander Demonstration for NASA’s Autonomous Landing and Hazard Avoidance Technology (ALHAT) System”. In: *Proc. of AIAA SPACE 2012*.
- Sabiron, G., Chavent, P., Raharijaona, T., Fabiani, P., and Ruffier, F. (2013).  
 “Low-speed optic-flow sensor onboard an unmanned helicopter flying outside over fields”. In: *IEEE International Conference on Robotics and Automation (ICRA)*, pp. 1742–1749.
- Sabiron, G., Burlion, L., Jonniaux, G., Kervendal, E., Bornschlegl, E., Raharijaona, T., and Ruffier, F. (2014a).  
 “Backup State Observer Based on Optic Flow Applied to Lunar Landing”. In: *IEEE/RSJ International Conference on Intelligent Robots and Systems (IROS)*, pp. 2325–2332.
- Sabiron, G., Burlion, L., Raharijaona, T., and Ruffier, F. (2014b).  
 “Optic Flow-Based Nonlinear Control and Sub-Optimal Guidance for Lunar Landing”. In: *IEEE International Conference on Robotics and Biomimetics (ROBIO) (Accepted)*.
- Sabiron, G., Raharijaona, T., Burlion, L., Kervendal, E., Bornschlegl, E., and Ruffier, F. (2014c).  
 “Sub-optimal Lunar Landing GNC using Non-gimbaled Bio-inspired Optic Flow Sensors”. In: *IEEE Transactions on Aerospace and Electronic Systems (in revision)*.
- Sane, S. P., Dieudonné, A., Willis, M. A., and Daniel, T. L. (2007).  
 “Antennal mechanosensors mediate flight control in moths”. In: *science* 315.5813, pp. 863–866.
- Santos-Victor, J., Sandini, G., Curotto, F., and Garibaldi, S. (1995).  
 “Divergent stereo in autonomous navigation: From bees to robots”. In: *International Journal of Computer Vision* 14.2, pp. 159–177.
- Serres, J., Dray, D., Ruffier, F., and Franceschini, N. (2008a).  
 “A vision-based autopilot for a miniature air vehicle: joint speed control and lateral obstacle avoidance”. In: *Autonomous Robots* 25.1-2, pp. 103–122.
- Serres, J., Masson, G., Ruffier, F., and Franceschini, N. (2008b).  
 “A bee in the corridor: centering and wall-following”. In: *Naturwissenschaften* 95(12), pp. 1181–1187.

- Shabayek, A. E. R., Démonceaux, C., Morel, O., and Fofi, D. (2012).  
 “Vision based uav attitude estimation: Progress and insights”. In: *Journal of Intelligent & Robotic Systems* 65.1-4, pp. 295–308.
- Shirai, Y. and Inoue, H. (1973).  
 “Guiding a robot by visual feedback in assembling tasks”. In: *Pattern recognition* 5.2, pp. 99–108.
- Singh, L. and Fuller, J. (2001).  
 “Trajectory generation for a UAV in urban terrain, using nonlinear MPC”. In: *Proceedings of the 2001 American Control Conference*. Vol. 3. IEEE, pp. 2301–2308.
- Singh, L. and Lim, S. (2008).  
 “On lunar on-orbit vision-based navigation: Terrain mapping, feature tracking driven EKF”. In: *AIAA Guidance, Navigation and Control Conference and Exhibit*, pp. 18–21.
- Singhose, W., Biediger, E., Okada, H., and Matunaga, S. (2006).  
 “Closed-form specified-fuel commands for on-off thrusters”. In: *Journal of guidance, control, and dynamics* 29.3, pp. 606–611.
- Sontag, E. D. (1998).  
*Mathematical control theory: deterministic finite dimensional systems*. Vol. 6. Springer.
- Spencer, D. A., Blanchard, R. C., Braun, R. D., Kallemeyn, P. H., and Thurman, S. W. (1999).  
 “Mars Pathfinder entry, descent, and landing reconstruction”. In: *Journal of Spacecraft and Rockets* 36.3, pp. 357–366.
- Srinivasan, M., Zhang, S., Lehrer, M., and Collett, T. (1996).  
 “Honeybee navigation en route to the goal: visual flight control and odometry”. In: *Journal of Experimental Biology* 199.1, pp. 237–244.
- Srinivasan, M. V. (1994).  
 “An image-interpolation technique for the computation of optic flow and egomotion”. In: *Biological Cybernetics* 71.5, pp. 401–415.
- Srinivasan, M. V., Chahl, J. S., Weber, K., Venkatesh, S., Nagle, M. G., and Zhang, S.-W. (1999).  
 “Robot navigation inspired by principles of insect vision”. In: *Robotics and Autonomous Systems* 26.2, pp. 203–216.
- Srinivasan, M. (2011).  
 “Honeybees as a Model for the Study of Visually Guided Flight, Navigation, and Biologically Inspired Robotics”. In: *Physiological Reviews* 91.2, pp. 413–460.
- Steltzner, A., Kipp, D., Chen, A., Burkhart, D., Guernsey, C., Mendeck, G., Mitcheltree, R., Powell, R., Rivellini, T., San Martin, M., et al. (2006).  
 “Mars Science Laboratory entry, descent, and landing system”. In: *Aerospace Conference, 2006 IEEE*. IEEE, 15–pp.
- Straw, A., Lee, S., and Dickinson, M. (2010).  
 “Visual Control of Altitude in Flying *Drosophila*”. In: *Current Biology* 20.17, pp. 1550–1556.
- Strother, J., Nern, A., and Reiser, M. (2014).  
 “Direct Observation of {ON} and {OFF} Pathways in the *Drosophila* Visual System”. In: *Current Biology* 24.9, pp. 976–983. ISSN: 0960-9822.

- Taylor, G. K. and Krapp, H. G. (2007).  
 “Sensory systems and flight stability: what do insects measure and why?” In: *Advances in insect physiology* 34, pp. 231–316.
- Thakoor, S., Chahl, J., Srinivasan, M. V., Young, L., Werblin, F., Hine, B., and Zornetzer, S. (2002).  
 “Bioinspired engineering of exploration systems for NASA and DoD”. In: *Artificial life* 8.4, pp. 357–369.
- Thurrowgood, S., Soccol, D., Moore, R., Bland, D., and Srinivasan, M. V. (2009).  
 “A vision based system for attitude estimation of UAVs”. In: *IEEE/RSJ International Conference on Intelligent Robots and Systems, 2009*. IEEE, pp. 5725–5730.
- Thurrowgood, S., Moore, R. J., Bland, D., Soccol, D., and Srinivasan, M. V. (2010).  
 “UAV attitude control using the visual horizon”. In: *Proc. Australasian Conference on Robotics and Automation, Brisbane, Australia*.
- Trawny, N., Mourikis, A. I., Roumeliotis, S. I., Johnson, A. E., and Montgomery, J. (2007).  
 “Vision-aided inertial navigation for pin-point landing using observations of mapped landmarks”. In: *Journal of Field Robotics* 24, pp. 357–378.
- Ulivi, P. and Harland, D. M. (2007).  
*Robotic Exploration of the Solar System: Part I: The golden age 1957-1982*. Springer and Praxis Publishing.
- (2008).  
*Robotic Exploration of the Solar System: Part 2: Hiatus and renewal, 1983-1996 (Springer Praxis Books/Space Exploration)*. Springer and Praxis Publishing.
- (2012).  
*Robotic Exploration of the Solar System: Part 3: Wos and Woes, 1997-2003*. Springer and Praxis Publishing.
- Valette, F., Ruffier, F., Viollet, S., and Seidl, T. (2010a).  
 “Biomimetic optic flow sensing applied to a lunar landing scenario”. In: *International Conference on Robotics and Automation (ICRA)*, pp. 2253–2260.
- Valette, F., Ruffier, F., Viollet, S., Seidl, T., Ampatzis, C., and Groote, K. (2010b).  
*Neuromorphic Computation of Optic Flow Data*. Tech. rep. ESA.
- Van Pham, B., Lacroix, S., and Devy, M. (2012).  
 “Vision-based absolute navigation for descent and landing”. In: *Journal of Field Robotics* 29.4, pp. 627–647.
- Voirin, T., Delaune, J., Le Besnerais, G., Farges, J., Bourdarias, C., and Krueger, H. (2013).  
 “Challenges of Pinpoint Landing for Planetary Exploration : the LION Absolute Vision-Based Navigation System Step-Wise Validation Approach”. In: *10th International Planetary Probe Workshop*.
- Wang, D., Huang, X., and Guan, Y. (2008).  
 “GNC system scheme for lunar soft landing spacecraft”. In: *Advances in Space Research* 42.2, pp. 379–385.
- Weiss, L. E. (1984).  
 “Dynamic visual servo control of robots : an adaptive image-based approach”. PhD thesis. Carnegie Mellon University.

- Weiss, L. E., Sanderson, A. C., and Neuman, C. P. (1987).  
 “Dynamic sensor-based control of robots with visual feedback”. In: *Robotics and Automation, IEEE Journal of* 3.5, pp. 404–417.
- Whiteside, T. C. and Samuel, G. (1970).  
 “Blur zone”. In: *Nature* 225, pp. 94–95. DOI: 10.1038/225094a0.
- Williams, J. G., Newhall, X., and Dickey, J. O. (1996).  
 “Relativity parameters determined from lunar laser ranging”. In: *Physical Review D* 53.12, p. 6730.
- Xu, P., Humbert, J., and Abshire, P. (2011).  
 “Analog VLSI Implementation of Wide-field Integration Methods”. In: *Journal of Intelligent & Robotic Systems* 64(3), pp. 465–487.
- Zhou, K., Doyle, J. C., Glover, K., et al. (1996).  
*Robust and optimal control*. Vol. 40. Prentice Hall New Jersey.
- Zufferey, J. C. and Floreano, D. (2006).  
 “Fly-inspired visual steering of ultralight indoor aircraft”. In: *IEEE Transactions on Robotics* 22(1), pp. 137–146.
- Zufferey, J., Beyeler, A., and Floreano, D. (2010).  
 “Autonomous flight at low altitude using light sensors and little computational power”. In: *International Journal of Micro Air Vehicles* 2(2), pp. 107–117.
- Zufferey, J.-C. (2005).  
 “Bio-inspired vision-based flying robots”. PhD thesis. École Polytechnique Fédérale de Lausanne.
- Zufferey, J.-C., Klapotocz, A., Beyeler, A., Nicoud, J.-D., and Floreano, D. (2007).  
 “A 10-gram vision-based flying robot”. In: *Advanced Robotics* 21.14, pp. 1671–1684.
- Zwaan, S. van der and Santos-Victor, J. (1999).  
 “An insect inspired visual sensor for the autonomous navigation of a mobile robot”. In: *Proc. of the Seventh International Symposium on Intelligent Robotic Systems (SIRS)*.





# **Résumé de thèse en français**



# TABLE DES MATIÈRES

TABLE DES MATIÈRES . . . . .	183
1 INTRODUCTION . . . . .	185
2 DÉVELOPPEMENT ET CARACTÉRISATION DE CAPTEURS DE FLUX OPTIQUE . . . . .	192
2.1 Développement d'un capteur de Flux Optique bidirectionnel . . . . .	192
2.2 Développement d'un capteur de Flux Optique dédié aux basses vitesses et testé en vol . . . . .	196
3 SYNTHÈSE D'ALGORITHMES DE GUIDAGE NAVIGATION ET COMMANDE POUR UN ATERRISSAGE LUNAIRE EN DOUCEUR . . . . .	201
3.1 Définition du scénario de référence . . . . .	201
3.2 Définition d'un stratégie GNC innovante . . . . .	202
3.3 Limites et améliorations de la stratégie GNC . . . . .	208
4 CONCLUSION . . . . .	214
RÉFÉRENCES . . . . .	216



## 1 INTRODUCTION

**D**ÉPUIS un certain nombre d'années, un regain d'intérêt apparaît envers l'atterrissage lunaire (ou alunissage) via de nombreuses missions (Chang'e 1, 2 et 3, Selene, Lunar Reconnaissance Orbiter ou encore Chandrayaan-1). Les missions Apollo ont fortement contribué à la connaissance de notre satellite naturel tant sur le plan de la science fondamentale que sur les prouesses techniques qui ont permis, par la suite, de réaliser des atterrissages sûrs et en douceur sur d'autres planètes. Cependant, notre exploration de ce plus proche voisin est encore loin d'être achevée. La mission "Lunar Lander" de l'Agence Spatiale Européenne (ESA pour *European Space Agency*) qui était prévue pour un lancement en 2018 suivi d'un atterrissage au pôle sud de la lune a été choisie comme mission de référence dans cette étude (voir CARPENTER et al. (2012) pour plus de détails sur cette mission).

Dans ces travaux, nous nous intéressons à l'utilisation de capteurs visuels de mouvement bio-inspirés et aux algorithmes de traitements associés comme dispositifs alternatifs (*backup*) permettant de réaliser un alunissage en douceur si le système principal venait à tomber en panne. En revanche, nous ne nous intéressons pas, dans cette première phase, aux autres objectifs qui peuvent être associés à ce genre de tâche tel que l'atterrissage de précision ou encore l'atterrissage sûr. Les algorithmes de Guidage, Navigation et Commande encore appelés GNC permettent de réaliser, entre autres, l'atterrissage autonome d'un véhicule spatial. À cette distance du centre de contrôle, une autonomie complète est nécessaire et les algorithmes GNC doivent être suffisamment robustes aux différentes incertitudes liées à l'environnement et au système considéré. La figure 1 présente une architecture GNC classique permettant de contrôler un système dynamique. Le guidage permet de fournir aux correcteurs la trajectoire de référence à suivre pour atteindre le site d'atterrissage. Cette trajectoire peut par exemple correspondre à une trajectoire précalculée optimale au sens de la consommation de carburant. L'algorithme de navigation permet d'estimer, si besoin, les états du système utilisés dans la commande et non mesurés par des capteurs. Enfin, la commande permet de corriger les erreurs de suivi entre la trajectoire de référence et la position actuelle du système fournie par le bloc de navigation.

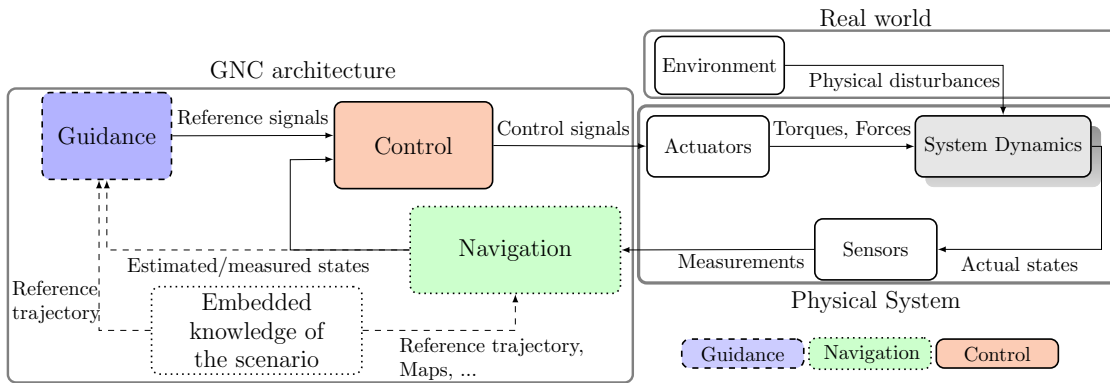


FIGURE 1 – Architecture GNC classique et différentes entrées sorties agissant sur un système physique. Les capteurs présents sur le système mesurent l'ensemble ou bien uniquement une partie des grandeurs physiques définissant la dynamique de ce dernier. Ces mesures sont ensuite transmises au bloc de navigation qui estime, à l'aide d'algorithmes de fusion de données ou bien d'observateurs, les grandeurs nécessaires à la correction de la trajectoire. Le guidage fournit aux correcteurs les signaux de référence à suivre. Enfin la commande détermine l'action que doivent réaliser les actionneurs physiques afin que les données fournies par la navigation suivent, au mieux, la trajectoire de référence déterminée par le guidage.

De nombreux capteurs basés sur des technologies très différentes existent pour mesurer les différents états du système. On retrouve par exemple les centrales inertielles (IMU pour *Inertial Measurement Unit*) qui mesurent les positions, vitesses et accélérations angulaires du système ainsi que les accélérations linéaires. Les capteurs altimétriques Laser, Radar ou encore Lidar permettent de connaître avec plus ou moins de précision la hauteur locale, ou bien, la topologie du terrain d'atterrissage. Enfin, on retrouve de plus en plus régulièrement des capteurs extéroceptifs tels que des caméras qui utilisent la vision pour naviguer dans un environnement complexe et inconnu. Les caméras sont des capteurs passifs n'émettant aucun signal ce qui leur confère un large champ d'opération non limité par la distance aux obstacles comme avec des capteurs altimétriques classiques.

Les contraintes de taille, de poids et de consommation poussent les scientifiques à développer de nouveaux concepts et matériels permettant de répondre à ces exigences toujours plus drastiques.

La robotique s'appuie largement sur la *vision par ordinateur* pour proposer des alternatives aux solutions classiques et utiliser la richesse d'information contenue dans les images du monde qui nous entoure. Cependant, ces algorithmes sont généralement gourmands en ressources calculatoires car le traitement de plusieurs milliers, voire millions de pixels nécessite de lourds calculs afin d'en extraire l'information utile.

Dans cette course à la miniaturisation, deux approches sont généralement envisagées. La première consiste à miniaturiser les technologies développées par l'homme depuis des décennies pour répondre aux contraintes d'embarquabilité toujours plus

strictes. La seconde, en revanche, s'appuie sur l'observation et la compréhension du vivant proposant des techniques spécialisées et des dispositifs miniatures, résultats d'une évolution commencée il y a plusieurs centaines de millions d'années. L'avantage de cette approche bio-inspirée permet d'éviter un effort considérable de miniaturisation et de concentrer nos travaux sur le perfectionnement de ces solutions.

La biorobotique s'inspire du vivant pour tenter de répondre à ce genre de problématiques. Par exemple, les insectes volants passionnent les scientifiques par leurs capacités maintes fois démontrées à naviguer de manière autonome dans des environnements inconnus, avec une agilité encore jamais égalée sur des aéronefs créés par la main de l'homme. Malgré leur faible poids, leurs faibles ressources calculatoires (moins d'un million de neurones chez l'abeille (STRAUSFELD, 1976; MENZEL et GIURFA, 2001)) ces animaux sont capables de contrôler leur hauteur, leur vitesse, d'éviter des obstacles, et de réaliser des tâches hautement complexes à reproduire technologiquement telles que l'atterrissage sur une plateforme mobile (telle que les fleurs). Le robot (*Robobee*) présenté par MA et al. (2013) est un robot de la taille d'un insecte qui pèse uniquement 80 milligrammes (sans alimentation) et qui est capable de se stabiliser en vol et de réaliser quelques manœuvres basiques. Cette réalisation impressionnante réalisée par l'équipe de Robert J Wood montre le réel potentiel de ce genre d'approches bio-inspirées pour répondre aux problématiques de la robotique aérienne actuelle. Nous nous intéressons en particulier au système visuel des insectes volants basé sur des yeux composés offrant un champ de vision quasi-panoramique. La figure 2 présente une photo des yeux composés de la mouche bleue (*Calliphora vomitoria*). Les caractéristiques optiques (GÖTZ, 1964; HORRIDGE, 1977; FRANCESCHINI, 1975; LAND, 1997), anatomiques (FRANCESCHINI, 1983) et neuronales (HAUSEN, 1982; FRANCESCHINI, 1985; FRANCESCHINI, RIEHLE et NESTOUR, 1989; DOUGLASS et STRAUSFELD, 1996; KRAPP et HENGSTENBERG, 1996) de l'œil composé traitent les signaux visuels en différentes étapes pour permettre finalement d'obtenir le champ vectoriel du flux optique dans une grande partie de la scène environnante. Le flux optique correspond au défilement des images contrastées sur la rétine de l'agent ce qui génère une vitesse angulaire propre au mouvement du système et fournit des informations sur les vitesses angulaires et linéaires ainsi que la proximité des obstacles.

Il convient à présent de définir l'expression mathématique du flux optique dans un environnement 3D :

$$\Omega(\Psi, \Theta) = -\frac{T - (T \cdot d(\Psi, \Theta) d(\Psi, \Theta))}{D(\Psi, \Theta)} - R \times d(\Psi, \Theta) \quad (1)$$

où  $\cdot$  représente le produit scalaire et  $\times$  le produit vectoriel (KOENDERINK et DOORN, 1987).  $\Omega(\Psi, \Theta)$  correspond à la vitesse relative d'un objet situé à une distance  $D(\Psi, \Theta)$



FIGURE 2 – Portrait d'une mouche bleue (*Calliphora vomitoria*) présentant deux larges yeux composés constitués chacun plusieurs centaines de facettes. Photographie de JJ Harrison sous licence © BY-SA.

dans la direction  $d(\Psi, \Theta)$  lorsque l'agent se déplace en translation selon le vecteur  $T$  et en rotation selon le vecteur  $R$ . Les différentes notations utilisées pour définir le flux optique sont présentées sur la figure 3. Le flux optique observé est toujours tangent à la sphère unitaire centrée à la position du capteur visuel. On distingue deux composantes dans l'expression complète du flux optique. Une composante translationnelle notée  $\Omega_T$  qui dépend de la vitesse ainsi que de la distance aux obstacles et une composante rotationnelle notée  $\Omega_R$  qui ne dépend que de la direction de visée et de la vitesse angulaire de l'agent.

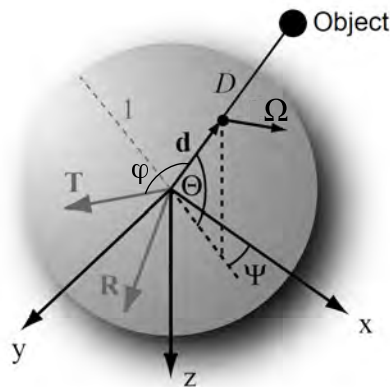


FIGURE 3 – Présentation des différentes notations permettant de définir le flux optique dans un environnement 3D. D'après ZUFFEREY et FLOREANO (2005)

La vision du mouvement semble être une information largement exploitée chez les insectes via des mécanismes sensorimoteurs leur permettant de contrôler leur vol. SRINIVASAN (2011) présente un travail de synthèse très complet sur les techniques de navigation visuelle chez les abeilles. On retrouve dans la littérature deux types d'études

complémentaires permettant de mieux appréhender le traitement de la vision chez les insectes volant :

- Premièrement, des études neurophysiologiques ont permis d’observer et de modéliser certaines fonctions de vision du mouvement présentes chez les insectes ailés. Basées sur les travaux de Franceschini et ses collègues, plusieurs versions de détecteurs élémentaires de mouvement (EMD pour *Elementary Motion Detector*) ont été développées. Ces capteurs minimalistes contenant uniquement 2 pixels permettent de mesurer le flux optique dans la direction du mouvement (voir FRANCESCHINI, PICHON et BLANES (1992), RUFFIER et FRANCESCHINI (2004), FRANCESCHINI, RUFFIER et SERRES (2007), EXPERT, VIOLLET et RUFFIER (2011), RUFFIER et EXPERT (2012) et FLOREANO et al. (2013) pour diverses implémentations). Par la suite ces capteurs ont été appelés capteurs locaux de mouvement (LMS pour *Local Motion Sensor*).

Dans la section 2 de cette étude, nous nous intéressons au développement et au perfectionnement de ce type de capteurs basés sur le principe du “temps de passage” (ou “*Time of Travel*” en anglais). Ce principe permet de déterminer la vitesse angulaire locale en calculant le temps de parcours d’un contraste depuis l’axe optique d’un premier photorécepteur jusqu’à l’axe optique d’un second, l’angle séparant les deux axes optiques étant connu. On obtient alors le flux optique comme étant le rapport de l’angle sur le temps de parcours. La figure 4 présente schématiquement le principe du “temps de passage”.

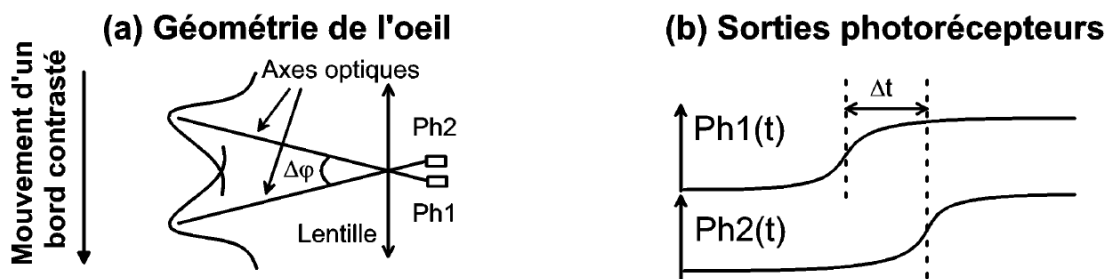


FIGURE 4 – Présentation du principe du “temps de passage”. a) Un contraste en mouvement va croiser successivement les axes optiques des deux photodiodes séparés d’un angle  $\Delta\varphi$  (angle inter-récepteur) créant ainsi un retard  $\Delta t$  inversement proportionnel à la vitesse angulaire de déplacement. b) Le “temps de passage”  $\Delta t$  est déterminé grâce au retard temporel présent entre les signaux électriques des deux photodiodes. Le flux optique  $\omega$  est alors calculé de la façon suivante  $\omega = \Delta\varphi / \Delta t$ . D’après RUFFIER (2004)

- Deuxièmement, des études éthologiques ont permis de comprendre comment cette mesure de flux optique est utilisée à des fins de navigation chez les insectes ailés (REICHARDT, 1969 ; SRINIVASAN et BERNARD, 1975 ; COLLETT et LAND, 1975 ;

HENGSTENBERG, 1988 ; SRINIVASAN et al., 1996 ; HATEREN et SCHILSTRA, 1999 ; BARRON et SRINIVASAN, 2006 ; BAIRD et al., 2006 ; PORTELLI et al., 2010 ; STRAW, LEE et DICKINSON, 2010). Le principe de régulation du flux optique a été observé, modélisé puis implémenté sur divers robots leur permettant de réaliser de nombreuses tâches complexes telles que le décollage, le suivi de terrain, l’atterrissage autonome ou encore l’évitement d’obstacle (RUFFIER, 2004 ; RUFFIER et FRANCESCHINI, 2005 ; FRANCESCHINI, RUFFIER et SERRES, 2007). La figure 5 présente plusieurs robots développés par l’équipe biorobotique. Tous ces robots utilisent le flux optique pour réaliser des tâches de navigation autonome.

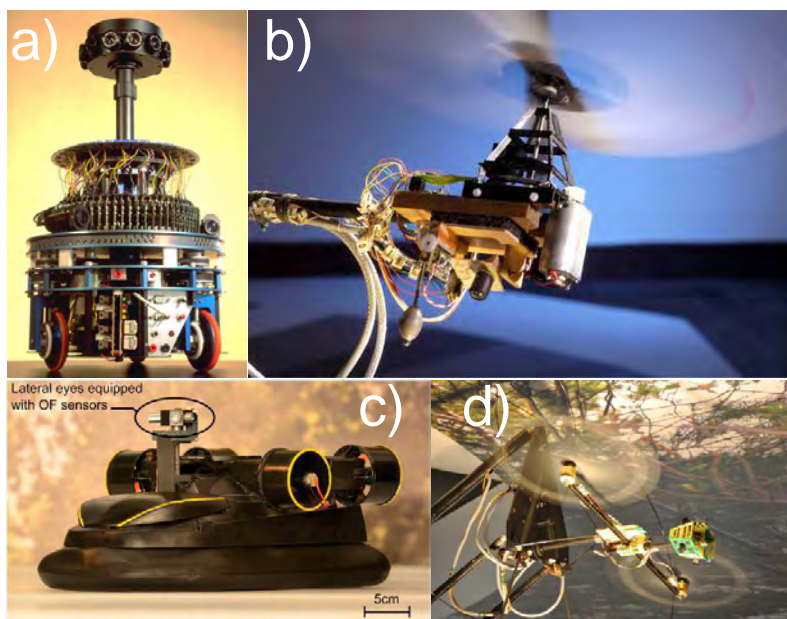


FIGURE 5 – a) Robot mouche capable de naviguer de manière autonome grâce à un réseau de seulement 118 pixels (FRANCESCHINI, PICHON et BLANES, 1992 ; PICHON, BLANES et FRANCESCHINI, 1989). b) Le robot OCTAVE (Optic flow based Control sysTem for Aerial VEhicles) est un robot volant autonome à trois degrés de liberté intégrant un unique détecteur élémentaire de mouvement (RUFFIER et FRANCESCHINI, 2003 ; RUFFIER et FRANCESCHINI, 2004 ; RUFFIER et FRANCESCHINI, 2005 ; RUFFIER et FRANCESCHINI, 2014). c) Aéroglisseur intégrant le pilote automatique appelé LORA III (Lateral Optic flow Regulation Autopilot) et utilisant 4 capteurs visuels de mouvement (ROUBIEU et al., 2014). d) Récemment le développement du BeeRotor a permis de montrer sa capacité à naviguer de manière autonome sur la base des flux optiques ventraux et dorsaux. Le BeeRotor nécessite uniquement 4 capteurs visuels de mouvement orientés vers le plafond et le sol ainsi qu’un gyromètre (EXPERT et RUFFIER, 2012).

Dans la section 3 de cette étude, nous nous intéressons donc à l’applicabilité de ces principes pour l’atterrissage lunaire. Le principe fondamental derrière cette régulation du flux optique s’appuie sur le fait que le flux optique lors d’une translation pure s’exprime par le rapport entre la vitesse et la distance à l’obstacle. En maintenant ce rapport constant, on assure la proportionnalité entre vitesse et altitude.

Plusieurs thèses présentent en français et en détails le fonctionnement du système visuel des insectes ainsi que les différents processus qui leur permettent de naviguer de manière autonome dans un environnement complexe et inconnu (RUFFIER, 2004 ; PORTELLI, 2011 ; ROUBIEU, 2013).

D'autres équipes se sont également intéressés à la régulation du flux optique pour réaliser des tâches de navigation autonome à bord de drones aériens (GREEN, OH et BARROWS, 2004 ; ZUFFEREY et FLOREANO, 2006 ; GRIFFITHS et al., 2006 ; GARRATT et CHAHL, 2008 ; BEYELER, ZUFFEREY et FLOREANO, 2009 ; KENDOUL et al., 2009 ; CONROY et al., 2009 ; ZUFFEREY, BEYELER et FLOREANO, 2010 ; HUMBERT et HYSLOP, 2010 ; HÉRISSE et al., 2012).

Concernant l'atterrissage lunaire basé sur la mesure du flux optique, il convient d'évoquer certains auteurs ayant posé les fondations de cette étude.

L'équipe biorobotique (ISM UMR AMU/CNRS) à Marseille a étudié lors d'un contrat ESA Ariadna (voir VALETTE et al. (2010b) pour le rapport final). VALETTE et al. (2010a) présente pour la première fois une stratégie d'atterrissage lunaire en douceur basée sur la régulation du flux optique en utilisant le logiciel PANGU avec un simple capteur local de mouvement (2 pixels). A l'aide d'une commande linéaire quadratique, et d'un observateur non linéaire les auteurs ont réalisé diverses simulations pour montrer la faisabilité d'une telle solution. Dans cette première approche, le tangage suivait une trajectoire prédéfinie en boucle ouverte sous la forme d'une fonction linéaire ou bien exponentielle. Les auteurs en concluent qu'une boucle de contrôle de l'attitude est nécessaire pour améliorer les performances et la robustesse.

Une autre étude ESA Ariadna a été présentée par MEDICI et al. (2010). Les auteurs ont étudié la régulation du flux optique à l'aide de différents types de commandes telles que les correcteurs PID, la commande prédictive non linéaire, la linéarisation par retour de sortie, la commande par mode glissant.

Un aspect important dans tout système embarqué concerne l'optimalité de la solution en termes de consommation de carburant. IZZO, WEISS et SEIDL (2011) ont réalisé une étude de l'optimalité d'un atterrissage à flux optique constant du point de vue de la consommation de carburant. Ils ont conclu qu'une trajectoire optimale en tangage était également nécessaire pour limiter la pénalité de consommation apportée par la contrainte de flux optique constant. Suite à cette étude les auteurs ont proposé une stratégie de régulation du flux optique associée à une régulation du temps avant impact (*time-to-contact* TTC) qui permet de contrôler directement la dynamique verticale (IZZO et DE CROON, 2011). DE CROON et IZZO (2012) présentent une solution proche de la commande prédictive type *model predictive control* sur un modèle sur-actionné. Il est intéressant de remarquer que les profils du flux optique dans cette descente optimale ne

sont pas constants. Plus récemment, IZZO et DE CROON (2013) ont étendu ces principes sur des modèles non linéaires sous actionnés.

## 2 DÉVELOPPEMENT ET CARACTÉRISATION DE CAPTEURS DE FLUX OPTIQUE

Jusqu'à présent, les diverses versions de détecteurs élémentaires de mouvement avaient été embarquées en intérieur sur des robots roulants ou aériens avec un nombre de degrés de liberté limités. Cela a permis d'obtenir de nombreux résultats très intéressants du point de vue de l'autonomie de ces derniers. Cependant, afin d'embarquer ces capteurs innovants sur des plateformes à six degrés de liberté sujettes à des mouvements complexes incluant de fortes rotations ainsi que des translations, il convient de s'intéresser à la possibilité de mesurer des valeurs positives et négatives du flux optique et également d'être en mesure d'adapter la gamme de mesure à l'application visée. Dans cette section nous nous intéressons à ces deux problématiques en proposant deux nouvelles versions du capteur. La première permet de déterminer le flux optique dans une large gamme de mesure centrée en zéro avec une précision et un taux de rafraichissement très satisfaisant. La seconde, en revanche, démontre la possibilité d'adapter la gamme de mesure aux faibles flux optiques tels qu'ils peuvent apparaître sur des drones à voilure tournante volant à faible altitude ou encore lors d'un alunissage en douceur.

### 2.1 Développement d'un capteur de Flux Optique bidirectionnel

Premièrement, nous avons développé un nouveau capteur de flux optique basé sur l'algorithme du "temps de passage". Il présente des caractéristiques intéressantes du point de vue de sa faible taille ( $23,3 \times 12,3mm$ ), son faible poids ( $< 1$  g optique incluse) et sa faible consommation ( $< 0,23$  W). La figure 6 présente ce nouveau capteur miniature.

La première innovation réside dans l'utilisation d'un réseau de photorécepteurs contenant 6 pixels (soit 5 paires de 2 pixels) associé à une fusion basée sur l'opérateur médian ce qui permet d'améliorer grandement la précision et le taux de rafraichissement de la sortie. Nous avons montré que ce capteur améliore l'écart type de l'erreur d'un facteur de 1,7 le diminuant ainsi de  $17^\circ/s$  pour un seul détecteur élémentaire (2 pixels) à  $11^\circ/s$  pour la sortie fusionnée de 5 détecteurs élémentaires de mouvement. Le taux de rafraichissement de la sortie fusionnée passe quant à lui de 15,7Hz à 67Hz. Les expériences ont été menées en intérieur en mesurant le flux optique sur des bandeaux déroulants représentant des scènes naturelles d'intérieur et d'extérieur. La figure 7 pré-

sente l'intérêt de la fusion (par opérateur médian) de la mesure de flux optique basés sur le principe du "temps de passage".

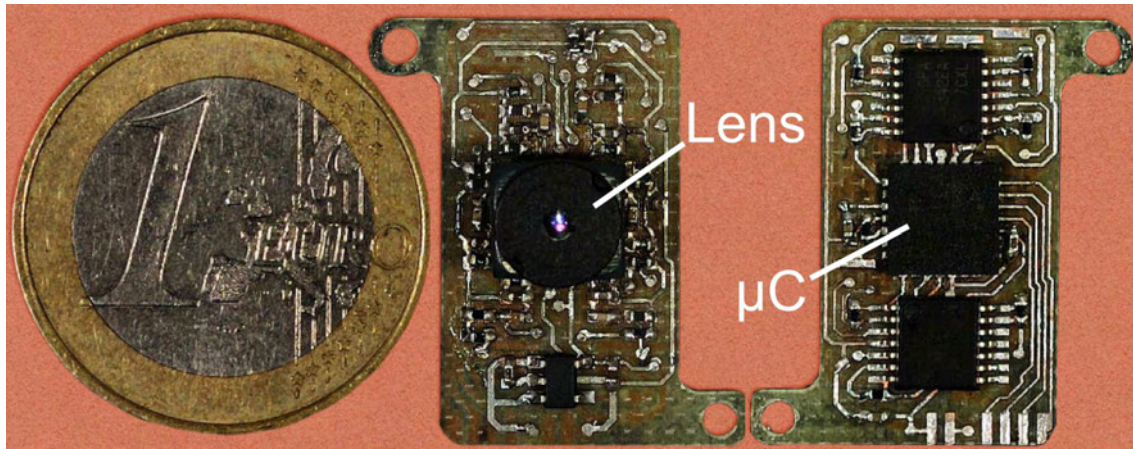


FIGURE 6 – Photo de face (au centre) et de dos (à droite) du capteur de flux optique pesant seulement 1g (taille : 23,3 × 12,3mm). Ce capteur est composé d'une lentille (distance focale : 2mm) placée devant une rétine LSC (6 pixels) et d'un microcontrôleur 16 bits le tout sur un PCB de 0.4mm d'épaisseur. D'après ROUBIEU et al. (2013).

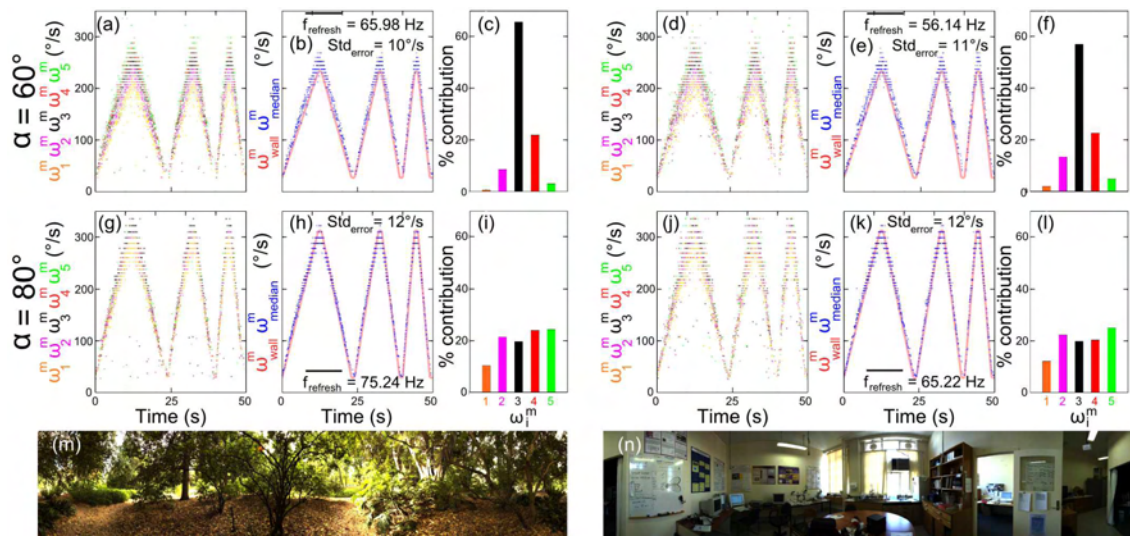


FIGURE 7 – Réponse dynamique du capteur visuel de mouvement et comparaison des sorties des 5 détecteurs élémentaires de mouvement à la sortie fusionnée grâce à l'opérateur médian. Le capteur est placé à une distance de 24cm d'un bandeau déroulant composé de contrastes naturels (scène extérieure et scène intérieure - voir sous-figure m. et n.). La réponse du capteur est obtenue pour deux orientations différentes (60° et 80° entre l'axe principal du capteur et l'orientation du bandeau). Le bandeau est contrôlé en vitesse via un moteur à courant continu qui applique des rampes de 27° /s à 230° /s (pour 60°) et 28° /s à 312° /s (pour 80°). Les sous figures a), d), g) et j) présentent les réponses de chaque détecteur élémentaire de mouvement. Etant donné leurs inclinaisons légèrement différentes par rapport au bandeau, les réponses de chacun diffèrent légèrement. Les sous figures a), d), g) et j) présentent la réponse fusionnée grâce à l'opérateur médian ce qui a pour effet d'améliorer grandement le taux de rafraichissement de la mesure et de diminuer également la dispersion. Enfin les sous-figures c), f) i), et l) affichent le pourcentage de contribution de chaque détecteur élémentaire de mouvement à la valeur médiane. D'après ROUBIEU et al. (2013).

La seconde innovation de cette étude porte sur la capacité du capteur à déterminer le flux optique non plus dans une seule direction mais dans deux directions opposées. Comme évoqué par BLANES (1991), en plaçant deux détecteurs élémentaires de mouvement dans deux directions opposées, celui qui fournit la mesure la plus élevée indique également le sens. Grâce à la rétine composée de 6 pixels appelée LSC, 10 détecteurs élémentaires de mouvements sont alors implémentés : l'opérateur maximum fournit le signe de la mesure, l'opérateur médian fournit une mesure précise et régulièrement rafraîchie du flux optique et une logique algorithmique conserve les mesures vraisemblables.

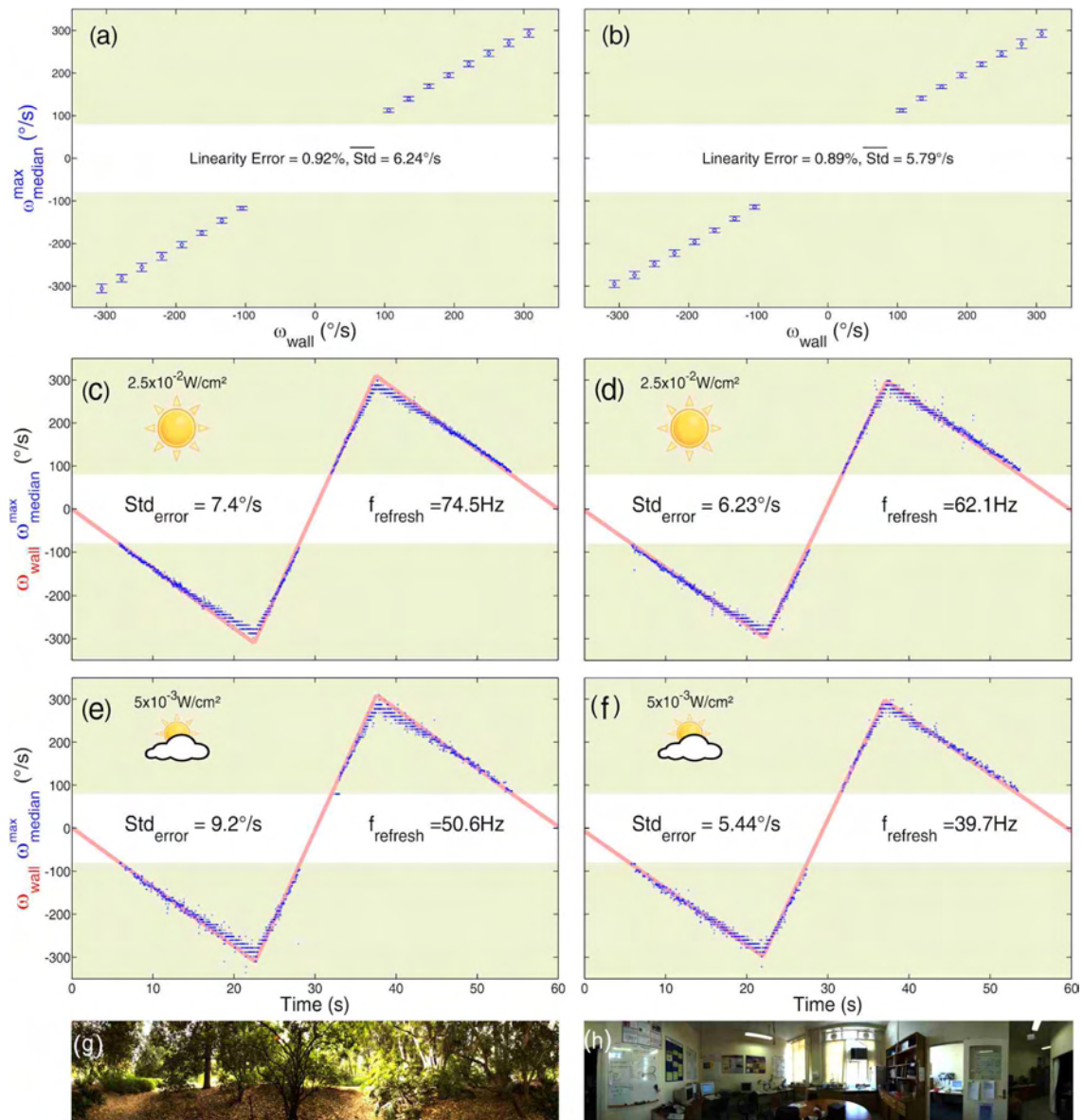


FIGURE 8 – Réponses statiques et dynamiques du capteur visuel de mouvement mesurant le flux optique dans la gamme  $[-350^{\circ}/s; -80^{\circ}/s] \cup [80^{\circ}/s; 350^{\circ}/s]$ . Le capteur est placé à une distance de 24cm d'un bandeau déroulant composé de contrastes naturels (scène extérieure et scène intérieure - voir sous-figure g. et h.). La réponse statique du capteur est obtenue en appliquant des paliers de 15s par pas de  $30^{\circ}/s$  dans la gamme  $[-315^{\circ}/s; -105^{\circ}/s] \cup [105^{\circ}/s; 315^{\circ}/s]$ . La faible erreur de linéarité pour chaque pas ainsi que la faible dispersion des mesures montrent la grande linéarité du capteur ainsi que sa grande précision. La réponse dynamique est obtenue en mesurant le flux optique sur des rampes allant de  $-300^{\circ}/s$  à  $300^{\circ}/s$  pour deux illuminations différentes. On constate que la réponse est encore une fois précise avec un haut taux de rafraichissement de la sortie. Il est important de remarquer que le signe de la mesure est déterminé sans aucune erreur sur l'ensemble de la gamme de mesure du capteur. D'après ROUBIEU et al. (2013).

Pour conclure, le développement de ce capteur a permis d'augmenter les capacités des capteurs de flux optique basés sur le principe du "temps de passage". Cela grâce à l'amélioration des caractéristiques en termes de précision de mesure et de fréquence

de rafraîchissement ainsi qu'à l'ajout d'une détermination sans erreur du signe du flux optique dans la large gamme  $[-315 \text{ }^\circ/\text{s}; -105 \text{ }^\circ/\text{s}] \cup [105 \text{ }^\circ/\text{s}; 315 \text{ }^\circ/\text{s}]$ . En effet, les excellentes performances démontrées de ce capteur de moins d'un gramme (dont tout le traitement a été optimisé pour être embarqué sur un unique microcontrôleur 16 bits) en font un candidat potentiel pour des applications robotiques d'évitement d'obstacle, de suivi de terrain, de décollage et d'atterrissage autonome.

## 2.2 Développement d'un capteur de Flux Optique dédié aux basses vitesses et testé en vol

Suite aux résultats pertinents obtenus en laboratoire avec le capteur décrit précédemment, nous nous sommes penchés sur une autre problématique qui est celle de la mesure de faibles flux optiques. En effet, la gamme de mesure perçue dans une application est propre à la dynamique du système en question. Par exemple pour des robots miniatures se déplaçant en intérieur dans un environnement encombré, le flux optique perçu peut être de l'ordre de plusieurs centaines de degrés par secondes (EXPERT, 2013 ; ROUBIEU et al., 2014). En revanche, lors d'un alunissage de type Apollo, le flux optique perçu est beaucoup plus faible. Il était donc important de vérifier que les capteurs visuels de mouvement basés sur le principe du "temps de passage" sont en mesure de déterminer de très faibles vitesses. La difficulté réside dans le fait que pour de faibles vitesses, peu de contrastes se déplacent dans le champ de vision étroit du capteur et donc par conséquent moins d'information utile est disponible. Cette diminution de l'information utile nécessite une précision accrue de la mesure et la capacité à distinguer davantage de contrastes en dépit de la vision floutée de ce type de capteurs. Nous proposons donc ici d'adapter les traitements optiques, analogiques et numériques afin de maintenir pour de faibles vitesses, une mesure précise et régulièrement rafraîchie.

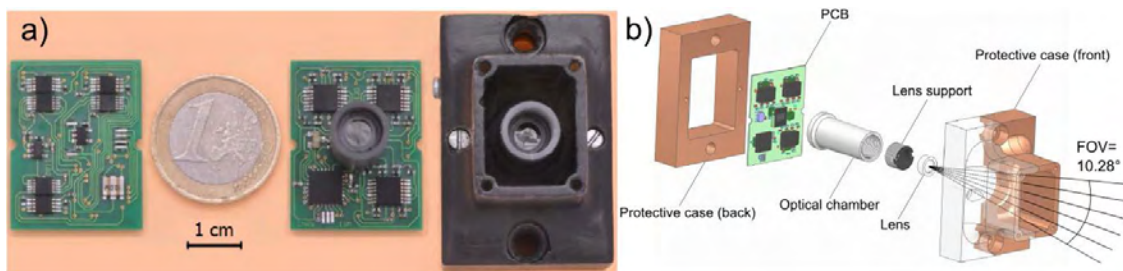


FIGURE 9 – a) Photo du capteur visuel de mouvement dédié aux basses vitesses, vue de face (centre) et de dos (gauche) de la carte électronique (taille :  $33 \times 40\text{mm}$ ) et vue de face du boîtier de protection (droite). b) Vue explosée de l'assemblage complet composé du boîtier de protection, de la carte électronique et de l'assemblage optique (lentille, support de la lentille, chambre optique). D'après SABIRON et al. (2013).

La figure 9 présente le nouveau capteur dédié aux basses vitesses avec son optique

contenant une lentille asphérique en plastique CAX183 de Thorlabs (longueur focale 18,33 mm, ouverture 4,07). Une grande longueur focale permet d'obtenir des angles d'acceptance (notés  $\Delta\rho$  et correspondant à la largeur à mi-hauteur de la fonction de sensibilité) et des angles inter-récepteurs (notés  $\Delta\varphi$  et correspondant à l'angle séparant deux axes optiques adjacents) suffisamment fins avec une fonction de sensibilité de type Gaussienne pour l'ensemble des photorécepteurs. En effet, une plus grande directivité des photorécepteurs permet de distinguer des contrastes à plus haute fréquence spatiale et donc d'augmenter la bande passante du capteur. Nous avons obtenu un réglage tel que les angles d'acceptance soient du même ordre de grandeur que les angles inter-récepteurs comme cela a été observé chez l'insecte diurne (LAND, 1997). On obtient alors  $\Delta\varphi = \Delta\rho \approx 1,5^\circ$ . Une fois les composants optiques réglés, nous avons également modifié les étapes de filtrage analogique et numérique afin d'isoler le signal utile se situant dans des fréquences plus basses que pour des capteurs de haut flux optique. De plus, étant donné que les tests préalables sont réalisés sur un drone à voilure tournante de type hélicoptère, à propulsion par moteur thermique, nous avons ajouté un filtre coupe bande du second ordre à virgule fixe dont la fréquence de coupure est centrée sur la fréquence du rotor principal.

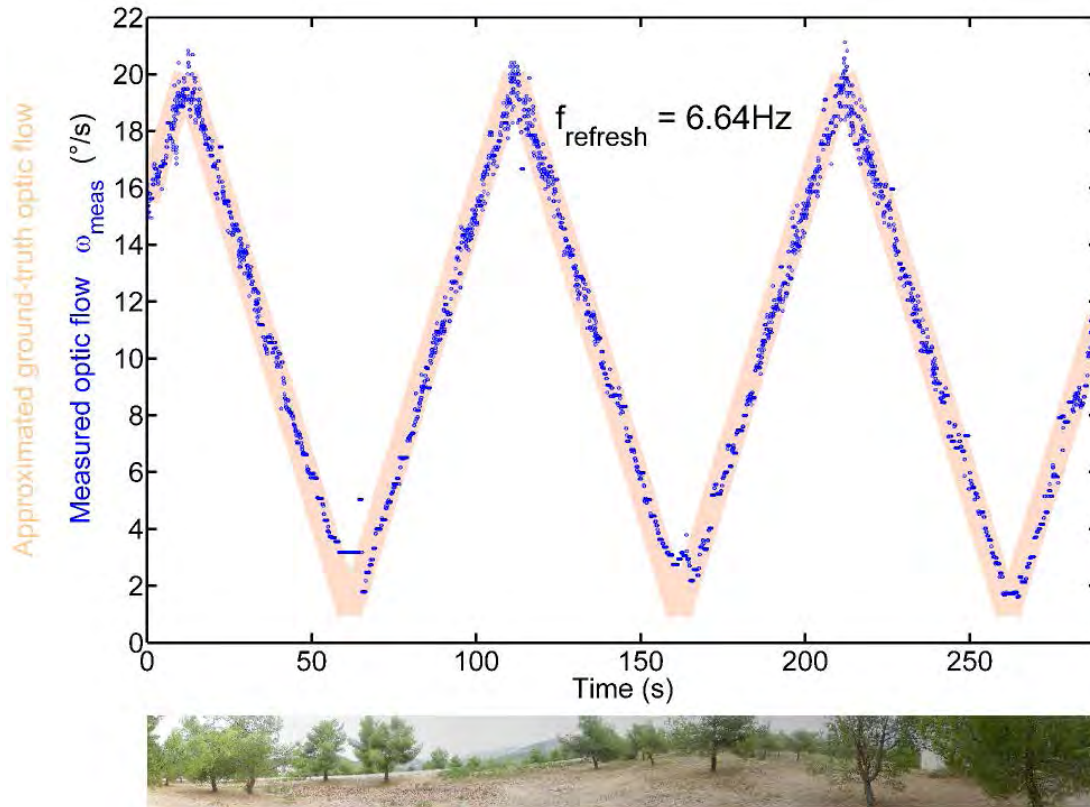


FIGURE 10 – Comparaison de la réponse dynamique du capteur visuel de mouvement dédié aux basses vitesses en environnement extérieur (bleu), avec le flux optique réel appelé "ground truth optic flow" et noté  $\omega_{\text{grd-trh}}$  (rose). Dans cette expérience, le capteur est entraîné en rotation à l'aide d'une courroie reliée à un moteur pas à pas (103H5208-0440 de Sanyo-Denki) (EXPERT, VIOLLET et RUFFIER, 2011). Les vitesses de rotation sont comprises entre  $1^\circ/\text{s}$  et  $20^\circ/\text{s}$  pour un capteur ayant une gamme de mesure comprise entre  $1,5^\circ/\text{s}$  et  $25^\circ/\text{s}$ . Conformément à ce qui est attendu, la mesure de flux optique correspond précisément à la valeur réelle avec un taux de rafraîchissement observé de 6,64 Hz. La dispersion n'est pas affichée car la synchronisation des signaux a été réalisée de manière qualitative et quelques dixièmes de seconde de décalage peuvent être encore présents ce qui donnerait une mesure faussée. D'après SABIRON et al. (2013).

Une fois le capteur développé et adapté aux basses vitesses, une caractérisation au sol a été réalisée. En entraînant le capteur en rotation pure autour d'un axe contrôlé en vitesse par un moteur pas-à-pas, nous avons pu vérifier le comportement de la sortie du capteur pour des vitesses allant de  $1^\circ/\text{s}$  à  $20^\circ/\text{s}$ . La figure 10 présente le résultat de la caractérisation dynamique du capteur en conditions extérieures non contrôlées (illumination et contrastes). Suite aux très bons résultats obtenus lors de cette caractérisation au sol, l'étape suivante concerne le test en vol sur une plateforme à six degrés de liberté. Pour cela, nous avons choisi le drone hélicoptère thermique ReSSAC (Recherche et Sauvetage par Système Autonome Coopérant) de l'Onera (modèle : Yamaha RMAX) qui est un drone de 80kg dont l'enveloppe de vol permet de générer en translation un flux optique représentatif d'un atterrissage lunaire. Le capteur visuel de mouvement dédié aux basses vitesses a donc été intégré à la plateforme de test sous le nez de l'appareil

avec un champ de vision dégagé. Une liaison série permet d'enregistrer les données en vol et de les synchroniser temporellement avec les autres données accessibles (attitude du robot, positions, et vitesses) sur la charge utile. Une interface de communication a également été développée permettant ainsi d'ajuster, en cas de besoin, les gains programmables des signaux visuels ou encore d'adapter le seuil utilisé par l'algorithme de détermination du "temps de passage".

La figure 11 présente les résultats obtenus lors d'un vol de 350 secondes réalisé à Caylus dans le sud-ouest de la France au-dessus d'un village de combat. Une trajectoire à hauteur constante de forme parallélogramme a été suivie passant au-dessus de divers obstacles tels que des maisons et des arbres ayant pour but de modifier brusquement la hauteur locale. On constate que malgré la trajectoire complexe le flux optique mesuré suit précisément la référence de flux optique. Il est à noter que la référence de flux optique a été reconstruite grâce aux données GPS, Lidar et d'attitude et contient donc elle-même des bruits provenant des différents capteurs utilisés. On observe que lorsque la hauteur locale diminue brusquement, le flux optique mesuré augmente en conséquence. De la même manière, lors d'un fort mouvement de tangage qui génère un fort flux optique de rotation, le capteur de flux optique dédié aux basses vitesses mesure efficacement ce court et intense pic de défilement. Enfin, lors de l'atterrissage manuel, on constate que le capteur fonctionne bien et offre des caractéristiques intéressantes en termes de précision et de rafraîchissement dans toute sa gamme de mesure  $[1,5 \text{ }^\circ/\text{s}; 25 \text{ }^\circ/\text{s}]$ .

Pour conclure, nous avons montré que l'algorithme du "temps de passage" permet également de mesurer de faibles flux optiques représentatifs de la phase d'approche d'un atterrissage lunaire. Ces tests ont été réalisés en extérieur dans un environnement contrasté naturel et dans des conditions d'illuminations non contrôlées sur une plateforme à six degrés de liberté sujette à de nombreuses perturbations (rotor principal et rotor de queue, bourrasques de vents, et mouvements non souhaités de roulis, tangage et lacet). De plus, nous avons augmenté le niveau de maturité technologique de ce type de capteur en l'intégrant sur l'application visée en conditions réelles de fonctionnement. Ces résultats encourageants montrent que ce capteur est parfaitement adapté pour des applications de navigation autonome de systèmes aéronautiques et aérospatiaux dont la gamme de flux optique perçue évolue de  $1,5 \text{ }^\circ/\text{s}$  à  $25 \text{ }^\circ/\text{s}$ . L'étape suivante consistera à tester le comportement de plusieurs capteurs avec un algorithme GNC sur ce type de plateforme pour valider le comportement en boucle fermée.

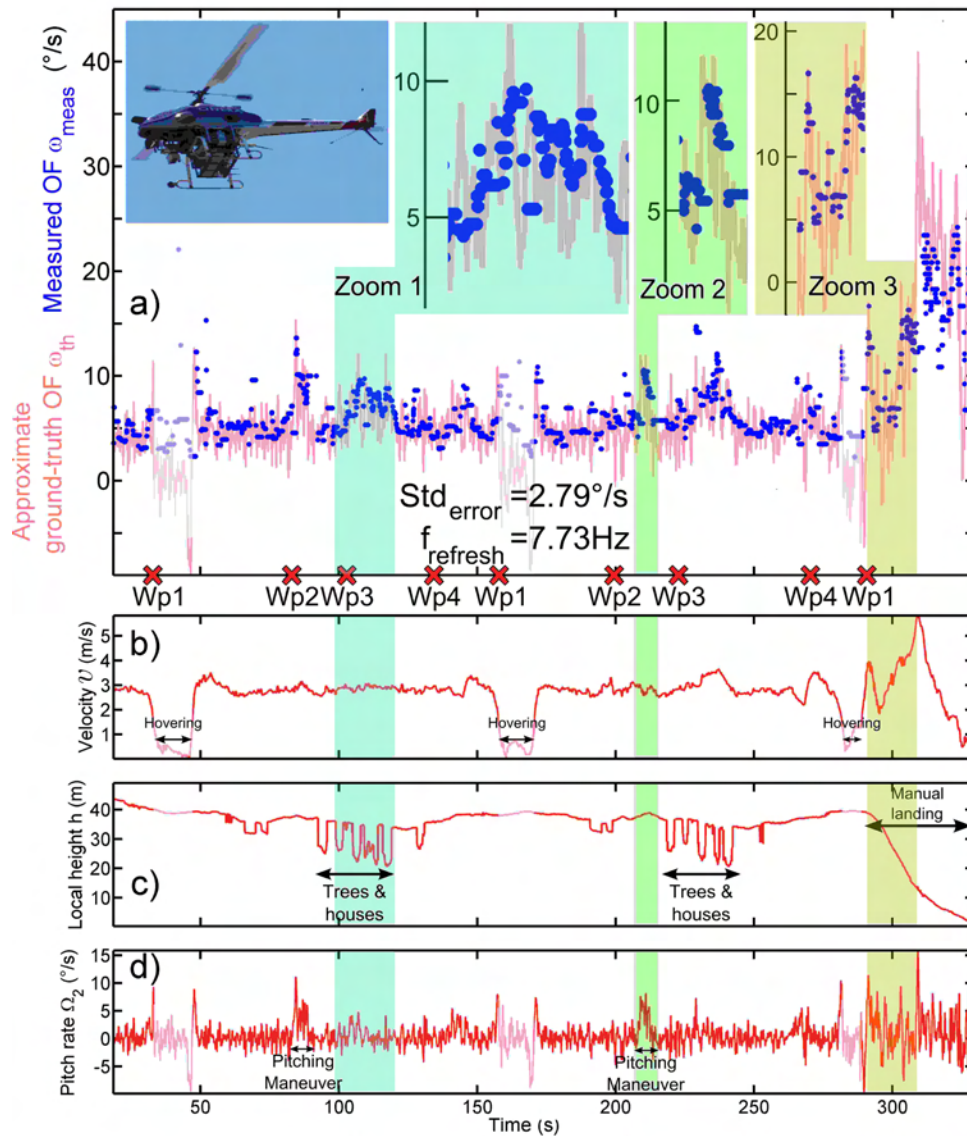


FIGURE 11 – Réponse du capteur visuel de mouvement dédié aux basses vitesses (bleu) lors d'une expérimentation en vol sur le drone hélicoptère ReSSAC et données de vol associées. a) Comparaison du flux optique mesuré (bleu) avec le flux optique reconstruit à l'aide des mesures GPS, IMU et Lidar (rouge). Malgré les fortes variations dues aux vibrations et à l'enveloppe de vol de l'appareil, la sortie suit précisément la référence avec une faible dispersion de  $2,79^\circ/s$  et un taux de rafraîchissement de  $7,73\text{Hz}$ . La première zone mise en avant montre l'effet d'une diminution de la hauteur locale sur la mesure. On constate que le flux optique augmente lorsque la hauteur locale diminue (à cause du survol d'une série de maisons et d'arbres). On peut également remarquer un fort mouvement en tangage après le point de passage 2 (WP2) lors du second tour qui est bien reporté sur la sortie du capteur. Enfin, lors de l'atterrissage manuel le flux optique augmente fortement ce qui permet de montrer que le capteur fonctionne de manière précise dans l'ensemble de la gamme  $[1,5^\circ/s; 25^\circ/s]$ . b) Norme du vecteur vitesse. c) Hauteur locale obtenue par combinaison des données GPS et Lidar. La hauteur moyenne était de  $40\text{m}$  mais cette dernière subit de fortes variations locales dues au relief du village de combat survolé. d) Vitesse angulaire en tangage du drone hélicoptère. D'après SABIRON et al. (2013).

### 3 SYNTHÈSE D'ALGORITHMES DE GUIDAGE NAVIGATION ET COMMANDE POUR UN ATERRISSAGE LUNAIRE EN DOUCEUR

La seconde étape principale de cette étude concerne le développement d'algorithmes de guidage navigation et commande pour permettre à terme d'utiliser le flux optique comme unique source d'information pour réaliser un atterrissage lunaire en douceur. Dans nos travaux, nous développons les blocs technologiques de guidage, navigation et commande pour contrôler un atterrisseur lunaire en utilisant dans un premier temps des capteurs de flux optique et une centrale inertielle. Dans un second temps, nous proposons une solution de navigation redondante (solution de secours en cas de défaillance des capteurs principaux) qui n'utilise pas de mesures inertielles et qui garantit les mêmes objectifs à l'atterrissage.

#### 3.1 Définition du scénario de référence

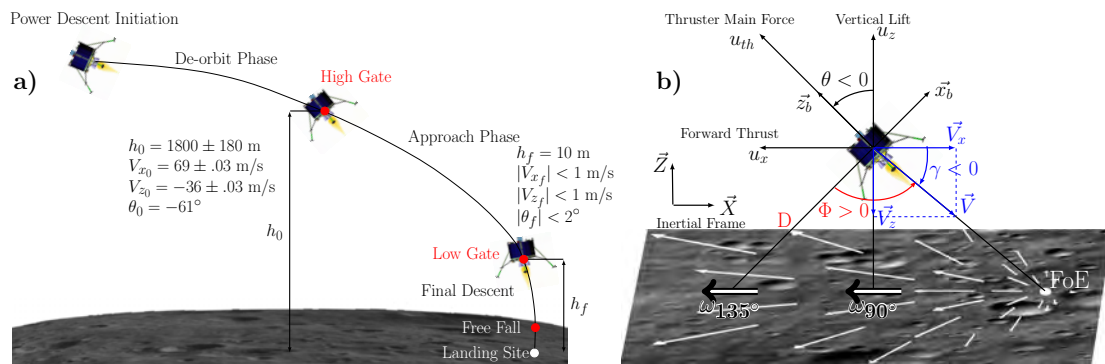


FIGURE 12 – Scénario de référence lors d'un alunissage et notations associées (dessin de l'atterrisseur, source : Airbus Defence and Space). a) La phase de l'alunissage étudiée dans cette étude concerne la phase d'approche qui est définie de la porte haute (hauteur à laquelle le site d'atterrissage devient visible) jusqu'à la porte basse (hauteur à partir de laquelle la poussière soulevée par les propulseurs empêche l'utilisation de capteurs basés vision). b) Schéma de l'atterrisseur lunaire dans un mouvement planaire (2D) avec le repère inertiel  $(\vec{X}, \vec{Z})$ , le vecteur vitesse  $\vec{V}$ , la poussée principale  $u_{th}$  et ses projections associées dans le repère vertical-local vertical-horizontal. Deux flux optiques spécifiques sont représentés à la surface de la lune  $\omega_{90^\circ}$  et  $\omega_{135^\circ}$ . D'après SABIRON et al. (2014a).

On s'intéresse à la phase d'approche définie de la porte haute (hauteur à laquelle le site d'atterrissage devient visible) jusqu'à la porte basse (hauteur à partir de laquelle la poussière soulevée par les propulseurs empêche l'utilisation de capteurs basés vision), il s'agit principalement d'une phase de freinage pendant laquelle le véhicule se redresse à la verticale (diminue son angle de tangage). La définition du scénario d'atterrissage est une étape importante permettant de déterminer la gamme de flux optique à mesurer et les conditions initiales et finales à atteindre pour la définition de la trajectoire optimale.

Cependant, il est important de noter que grâce à la nature du flux optique, cette application numérique pourrait être adaptée à d'autres phases d'atterrissage moyennant l'adaptation de la gamme de mesure du capteur ainsi qu'une nouvelle résolution du problème de commande optimale. La figure 12 présente les différentes conditions initiales et finales de la phase d'approche ainsi que les principales notations utilisées dans ce travail de thèse. L'objectif est d'atteindre la porte basse située à une hauteur sol de 10 m avec des vitesses horizontales et verticales inférieures à 1m/s en valeur absolue et avec un angle de tangage compris entre  $-2^\circ$  et  $2^\circ$ . Il est intéressant de remarquer que le flux optique est toujours nul dans la direction du vecteur vitesse et que ce pôle du flux optique est appelé foyer d'expansion.

### 3.2 Définition d'une stratégie GNC innovante

Suite aux recherches réalisées sur les insectes volants, de nombreuses études ont vu le jour proposant diverses techniques innovantes et inspirées des comportements observés. Par exemple, la régulation du flux optique autour d'une valeur constante présentée avec le robot OCTAVE (RUFFIER et al., 2003) s'appuie sur les observations réalisées chez les insectes par SRINIVASAN et al. (1996). Le maintien du système de vision en pure translation afin d'annuler le flux optique de rotation a également été observé chez l'insecte. Ce dernier a tendance à garder la tête droite lors d'une rotation suivant l'axe de roulis, ou encore à effectuer des saccades avec la tête pour ne pas avoir à mesurer du flux optique de rotation lors de larges mouvements en lacet. Cependant, comme le fait remarquer HÉRISSE et al. (2012), le rapport de la masse sur la traînée est très différent entre les insectes et les robots volants. Les stratégies de commande observées sur des systèmes biologiques ne se généralisent peut-être pas directement aux véhicules aériens ayant une forte inertie et un faible coefficient de traînée. Voilà pourquoi la synthèse d'algorithmes GNC pour un atterrisseur lunaire (coefficient de traînée considéré nul) a nécessité de modifier les principes de régulation du flux optique afin de satisfaire les fortes contraintes aérospatiales de poids, de prix et de consommation. Par exemple, concernant le guidage, des auteurs ont montré qu'il n'est pas optimal du point de vue de la consommation énergétique de maintenir un flux optique constant (IZZO, WEISS et SEIDL, 2011). Nous avons donc proposé de suivre une trajectoire optimale au sens de la consommation de carburant exprimée en flux optique. Le problème de commande optimale sous contraintes est résolu hors-ligne afin de déterminer la trajectoire optimale permettant de relier la porte haute à la porte basse. Nous avons pour cela pris en compte les contraintes associées à la dynamique du système, aux actionneurs de ce dernier, ainsi que les conditions finales souhaitées et les conditions initiales imposées. Le

suivi de cette trajectoire optimale est la première adaptation des principes bio-inspirés précédemment observés.

Concernant la boucle de pilotage, nous avons proposé des correcteurs non-linéaires qui assurent la stabilité globale asymptotique. Les preuves de stabilité utilisant la théorie de Lyapunov assurent la convergence soit des vitesses linéaires soit des flux optiques.

La figure 13 présente la trajectoire suivie lors d'une simulation d'alunissage en boucle fermée avec 2 capteurs visuels de mouvement placés sur des plateformes stabilisées en attitude grâce aux mesures de la centrale inertielle ce qui permet de garder les capteurs orientés dans des directions spécifiques (systèmes appelés cardans) indépendantes du tangage de l'atterrisseur. Les deux capteurs sont orientés à  $90^\circ$  et  $135^\circ$  par rapport à l'horizontale locale ce qui permet d'estimer directement les flux optiques d'expansion et ventraux utilisés par la commande. En effet on trouve :

$$\omega_x = \frac{V_x}{h} = \omega_{90^\circ} \quad (2)$$

$$\omega_x = \frac{V_z}{h} = \omega_{90^\circ} - 2\omega_{135^\circ} \quad (3)$$

On peut voir que les conditions finales sont quasiment remplies excepté pour la vitesse horizontale légèrement supérieure à 1 m/s comme escompté. Il est important de noter que la consommation obtenue est très proche de la consommation optimale ce qui valide par conséquent l'intérêt de notre approche. Cependant, la stabilisation des capteurs à l'aide de cardans n'est pas une solution viable étant donné le faible poids des capteurs et le besoin d'un système électromécanique supplémentaire. Il n'est pas souhaitable de les intégrer sur un mécanisme complexe qui risque de peser plus lourd que les capteurs eux-mêmes. Il convient alors de trouver une solution pour se passer de ces cardans.

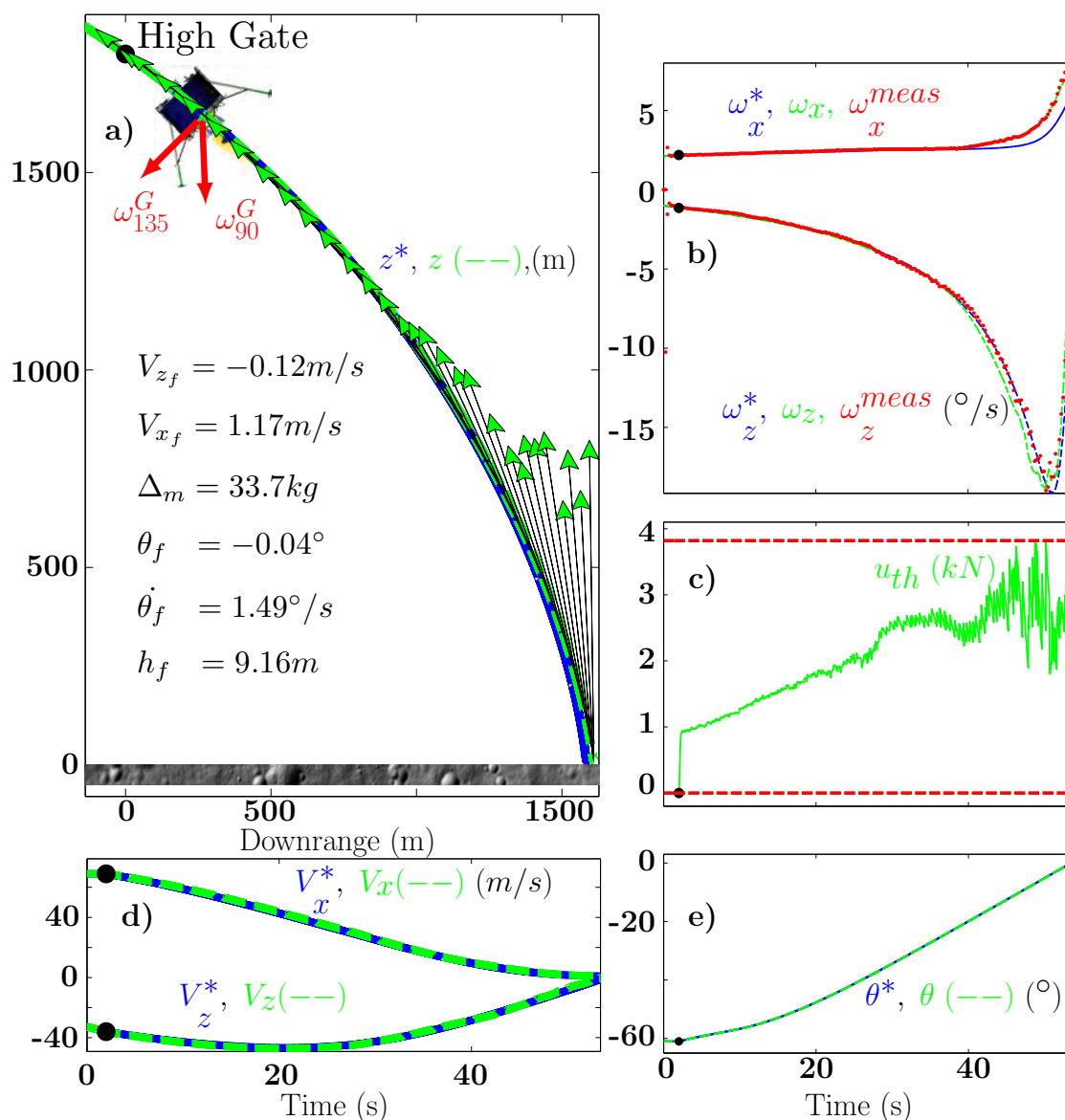


FIGURE 13 – Réponse en boucle fermée depuis la porte haute à la porte basse obtenue lors d’une simulation avec intégration du code du capteur et le logiciel PANGU avec 2 capteurs visuels de mouvement montés sur des plateformes stabilisées en attitude. a) Hauteur en fonction de la distance parcourue, orientation et amplitude normalisée de la poussée et conditions finales. b)-c) Flux optiques ventraux et d’expansion mesurés (pointillés bleus), réel (rouge), et optimaux (tirets noirs). d) Signaux de commande  $u_{th}$  (vert),  $u_x$  (bleu) et  $u_z$  (rouge). e) Profils des vitesses verticales et horizontales réelles (tirets verts) et optimales (bleu). f) Profil de tangage réel (tirets bleus) et optimal (rouge). D’après SABIRON et al. (2014c).

La seconde modification des principes bio-inspirés présentés dans la littérature concerne l’utilisation de capteurs fixés à la structure de l’atterrisseur. Contrairement au fait que les insectes gardent leur tête stable afin de ne mesurer que du flux optique de translation, nous avons décidé de fixer les capteurs à la structure de l’atterrisseur pour mesurer à la fois le flux optique de translation qui renseigne sur le rapport de la vitesse du système par rapport à sa proximité aux obstacles environnants et le flux op-

tique de rotation qui renseigne uniquement sur la vitesse angulaire du système. Toutes les informations nécessaires à une navigation autonome et sûre dans un environnement inconnu étant contenu dans ce flux optique complet, cela nous a permis de développer une solution GNC utilisant des capteurs fixés sur le véhicule ainsi qu'une centrale inertielle.

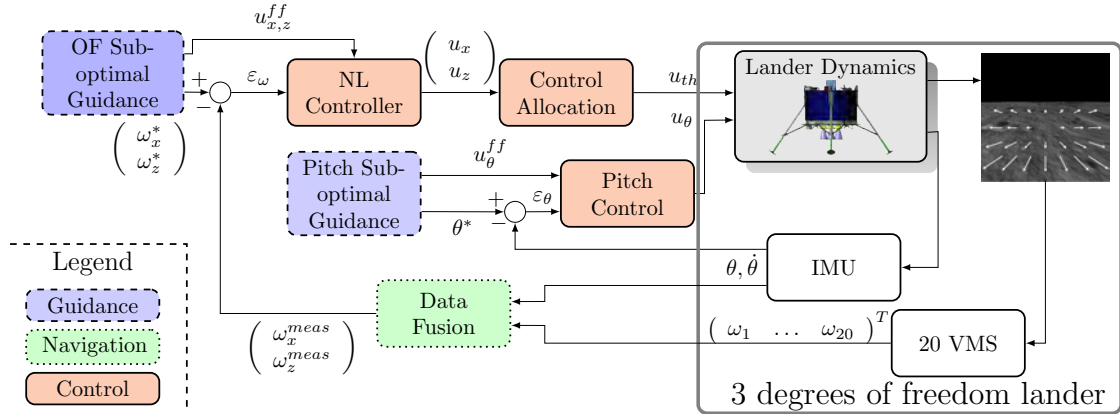


FIGURE 14 – Schéma bloc de la solution GNC proposé dans cette thèse. 20 capteurs fixés à la structure du véhicule ainsi qu'une centrale inertielle constituent l'ensemble des capteurs disponibles qui nourrissent l'algorithme de navigation. Ce bloc de fusion de données fourni aux correcteurs les estimations des flux optique spécifiques  $\omega_x = V_x/h$  et  $\omega_z = V_z/h$  déterminés grâce à un algorithme des moindres carrés linéaire. Les correcteurs calculent alors les commandes de freinage à appliquer au système pour annuler l'erreur de suivi qui peut exister entre les estimations de la navigation et les références fournies par le guidage. Le bloc d'allocation de commande détermine la norme du vecteur de commande défini par  $(u_x \ u_z)^T$ . La boucle interne de contrôle d'attitude délivre la commande de couple  $u_\theta$  aux actionneurs d'attitude grâce à un correcteur linéaire de retour de sortie et à la référence optimale de tangage fournie par le guidage sous-optimal. D'après SABIRON et al. (2014c).

La figure 14 présente l'architecture GNC globale de la solution proposée. On y retrouve le guidage sous-optimal en flux optique et en tangage qui nourrissent les correcteurs avec les références optimales calculées hors-ligne. La navigation est assurée par un algorithme des moindres carrés qui assure la fusion des sorties de 20 capteurs de flux optique fixés à la structure du véhicule à l'aide des mesures inertielles.

La différence est faite entre le calcul d'une trajectoire optimale au sens de la consommation de carburant et le guidage qui lui est sous-optimal. La trajectoire de référence est déterminée hors-ligne et n'est pas réajustée lors de la descente ce qui peut amener l'algorithme de guidage à faire suivre une trajectoire proche de l'optimale mais nécessitant une consommation de carburant supplémentaire. Cependant, la trajectoire déterminée via des outils de programmation non linéaire est optimale pour ce scénario en particulier.

Un effort particulier a été fait afin d'augmenter au maximum le réalisme des simulations. En effet, au lieu de réaliser des simulations théoriques (prenant en compte un

modèle de bruit de mesure), le code du capteur a été intégré en aval du logiciel PANGU qui permet de simuler des images virtuelles du sol lunaire. Le simulateur fournit à PANGU la position du véhicule ainsi que l'orientation et les paramètres intrinsèques des capteurs afin qu'il génère les portions d'images observées par les capteurs. Une fois ces images générées, le simulateur effectue le traitement visuel selon le principe du "temps de passage" et délivre des mesures de flux optique dépendant de la direction du mouvement. Ces simulations présentent un avantage certain du point de vue de la validation d'algorithmes de navigation visuelle relative. En revanche, un long temps de calcul est nécessaire ce qui empêche la réalisation d'un grand nombre de ces simulations.

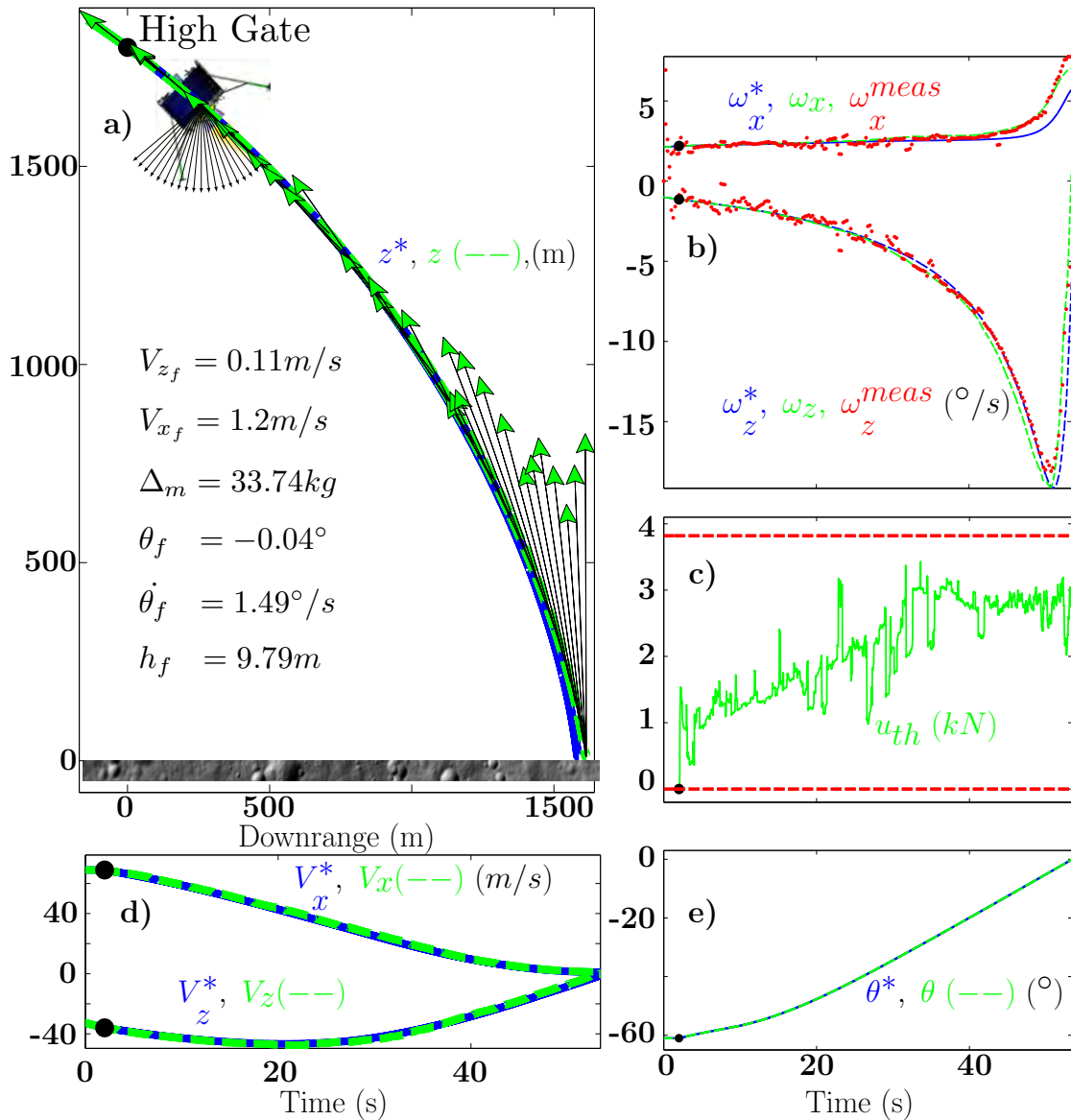


FIGURE 15 – Réponse en boucle fermée depuis la porte haute à la porte basse obtenue lors d’une simulation avec intégration du code du capteur et le logiciel PANGU avec 20 capteurs visuels de mouvement. a) Hauteur en fonction de la distance parcourue, orientation et amplitude normalisée de la poussée et conditions finales. b)-c) Flux optiques ventraux et d’expansion mesurés (pointillés bleus), réels (rouge), et optimaux (tirets noirs). d) Signaux de commande  $u_{th}$  (vert),  $u_x$  (bleu) et  $u_z$  (rouge). e) Profils des vitesses verticales et horizontales réelles (tirets verts) et optimales (bleu). f) Profil de tangage réel (tirets bleus) et optimal (rouge). D’après SABIRON et al. (2014c).

La figure 15 présente la trajectoire suivie lors d’une simulation d’alunissage en boucle fermée avec 20 capteurs visuels de mouvement. On peut voir que les conditions finales sont quasiment remplies excepté pour la vitesse horizontale légèrement supérieure à 1m/s. Il est important de noter que la consommation obtenue est encore une fois très proche de la consommation optimale ce qui valide par conséquent l’intérêt de notre approche.

### 3.3 Limites et améliorations de la stratégie GNC

Les résultats obtenus avec l'algorithme GNC utilisant le flux optique bien qu'ils soient très prometteurs ont toutefois quelques limitations :

1. Les correcteurs de flux optique développés précédemment ont été construits sur la base d'une inversion dynamique, d'une commande par action directe (*feedforward*<sup>1</sup> en anglais) et de correcteurs proportionnels. En utilisant la théorie de Lyapunov, on n'a pas à proprement parlé prouvé la stabilité asymptotique globale du système en boucle fermée mais on a obtenu un résultat plus surprenant. En effet, nous avons prouvé que ces correcteurs assurent (i) soit la convergence des vitesses vers leurs références respectives (ii) soit la convergence des flux optiques vers leurs références respectives.
  - i Les correcteurs assurent que les vitesses convergent asymptotiquement vers leurs références quand  $\text{sign}(h^* - h) = \text{sign}(V_x - V_x^*)$  (et respectivement  $\text{sign}(h^* - h) = \text{sign}(V_z - V_z^*)$ ),
  - ii Les correcteurs assurent que les flux optiques convergent asymptotiquement vers leurs références quand  $\text{sign}(h^* - h) \neq \text{sign}(V_x - V_x^*)$  (et respectivement  $\text{sign}(h^* - h) \neq \text{sign}(V_z - V_z^*)$ ).

Où la fonction signe est définie telle que :  $\text{sgn}(X) = \begin{cases} 1 & X \geq 0 \\ -1 & X < 0 \end{cases}$ .

Les signes des erreurs de suivi pourraient changer régulièrement ce qui pourrait perturber la convergence. Dans la pratique, nous avons observé que cela ne se présente pas. L'étape suivante serait alors de développer des lois de commande plus avancées qui permettraient d'assurer la stabilité globale asymptotique de la boucle fermée sans aucune condition de signe et fonction des états du système.

2. Le découplage entre la boucle interne de commande du tangage et la boucle externe de commande du flux optique pourrait entraîner de larges erreurs de suivi de consigne en cas de conditions initiales éloignées des conditions nominales. En effet, le correcteur de flux optique génère deux consignes de poussée :  $u_x$  et  $u_z$  qui définissent la norme du vecteur de poussée  $u_{th}$  ainsi que l'orientation souhaitée de ce dernier. Or la boucle de commande du tangage est uniquement utilisée pour suivre la trajectoire optimale de tangage sans tenir compte des sorties du régulateur de flux optique. L'étape logique suivante serait donc de lier ces deux boucles par le biais d'une commande cascadée qui fournirait comme précédemment les

<sup>1</sup>Une action *feedforward* permet de nourrir directement les signaux de commande sans passer par la boucle de rétroaction et donc sans tenir compte des mesures.

deux consignes de poussée ainsi qu'un angle de tangage qui servira de référence au correcteur d'attitude.

3. Enfin, une centrale inertielle est utilisée pour deux opérations. Premièrement afin d'effectuer la dérotation<sup>2</sup> des mesures de flux optique provenant de capteurs fixés à la structure (et donc sujet au flux optique de rotation), deuxièmement la régression linéaire réalisée sur les mesures au sens des moindres carrés nécessite la connaissance de l'orientation des capteurs dans le repère lié au centre de gravité de l'atterrisseur (valeurs connues) mais également dans le repère inertiel ce qui est fourni par la centrale inertielle. La prochaine étape serait de faire évoluer cet algorithme de navigation qui permet pour le moment d'estimer les flux optiques ventraux et d'expansion (notés respectivement  $\omega_x$  et  $\omega_z$ ) à partir de plusieurs capteurs de flux optique fixés au véhicule et d'une centrale inertielle. En utilisant un observateur linéaire à paramètres variants, nous verrons dans la suite que la connaissance du modèle dynamique du système et de la trajectoire de référence peut permettre de se passer complètement de capteurs inertiels.

Par la suite, nous avons proposé une loi de commande non-linéaire améliorée qui assure la stabilité globale asymptotique de la boucle fermée et la convergence asymptotique des flux optiques ventraux et d'expansion. Ces nouvelles lois de commande uniquement basées flux optique ont une structure de type mode glissant. Un intervalle calculé dynamiquement au cours de la descente permet de borner l'estimation de la hauteur locale. C'est grâce à cet intervalle obtenu par l'utilisation du flux optique d'expansion ( $\omega_z$ ) que ces correcteurs ont été synthétisés et que les preuves de stabilité ont été obtenues en se basant une fois de plus sur la théorie de Lyapunov. La seconde limitation concernant le découplage des deux boucles fermées a également été traitée dans cette synthèse améliorée. La référence fournie au correcteur de tangage ne provient plus du guidage optimal (qui fournit une trajectoire précalculée indépendamment de la trajectoire réellement suivie) mais des signaux de commandes synthétisés qui fournissent aux tuyères une force de freinage et au correcteur de tangage une consigne d'attitude. La figure 16 présente le schéma bloc de la stratégie GNC modifiée avec les deux boucles interne et externe cascades. Le guidage sous-optimal de tangage est uniquement utilisé en tant qu'action *feedforward*.

---

<sup>2</sup>La dérotation du flux est une opération qui consiste à soustraire la composante liée au flux optique de rotation grâce aux mesures d'attitudes provenant de l'IMU (ARGYROS, TSAKIRIS et GROVER, 2004)

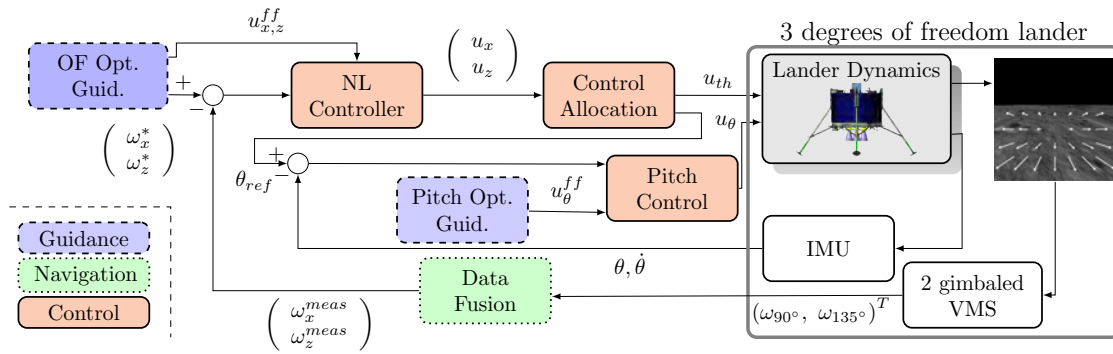


FIGURE 16 – Schéma bloc de l'architecture GNC modifiée. On retrouve ici les blocs de guidage sous-optimaux dont celui de tangage qui fournit une action feedforward au correcteur. La référence de tangage est fournie par l'orientation du vecteur de poussée calculée par les correcteurs de flux optique. Dans l'article duquel est tiré cette figure, l'attention est portée sur la partie commande et guidage ce qui explique pourquoi uniquement deux capteurs visuels de mouvement stabilisés en attitude sont considérés. L'un des deux est orienté selon la verticale locale et le second selon une direction orientée à  $135^\circ$  de la locale horizontale. Ces deux mesures de flux optique de translation permettent de déterminer directement  $\omega_x = \omega_{90^\circ}$  et  $\omega_z = \omega_{90^\circ} - 2\omega_{135^\circ}$ . D'après SABIRON et al. (2014b).

Les simulations réalisées avec cette nouvelle version de l'architecture GNC ont permis de démontrer les performances et la robustesse de la solution lors d'alunissage avec des conditions initiales éloignées des conditions nominales (voir figure 17 pour les simulations). Les objectifs de la porte basse sont quasiment atteints : seule la vitesse verticale finale est légèrement supérieure à la valeur attendue. Il est intéressant de remarquer que grâce à la régulation de flux optique, lorsque la hauteur initiale est plus faible, les vitesses (verticale et horizontale) ont tendance à être plus faibles tout au long de la descente (voir les courbes en rouge foncé et en noir sur la figure 17 pour des simulations avec une hauteur initiale plus faible :  $\Delta h(t_0) < -100m$ ).

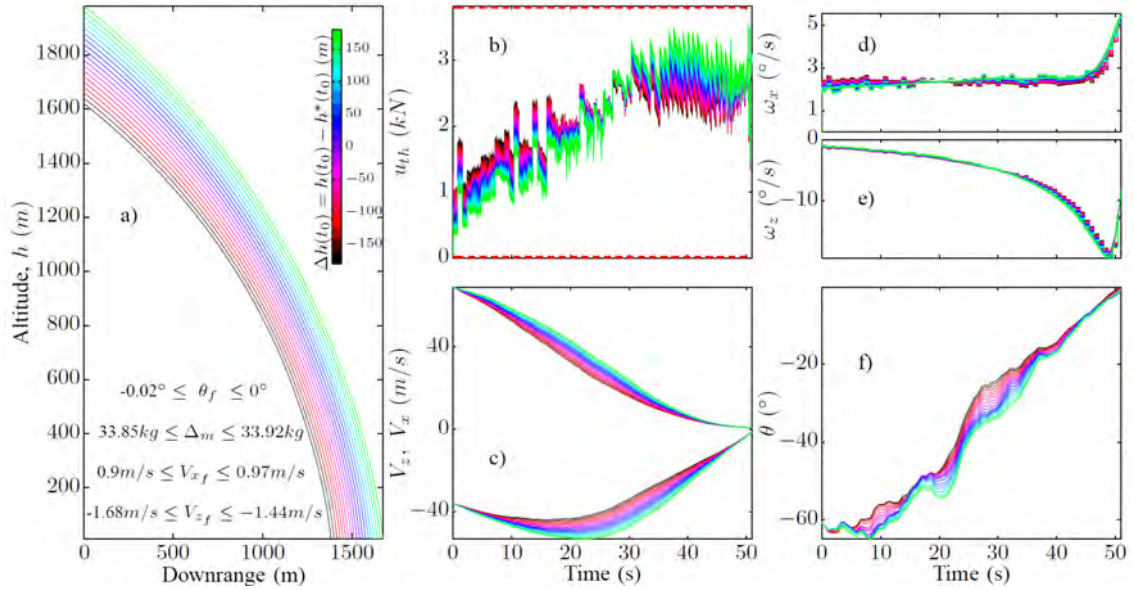


FIGURE 17 – Réponse en boucle fermée depuis la porte haute jusqu'à la porte basse pour  $h(t_0) \in [h^*(t_0) - 180, h^*(t_0) + 180]$ . a) Hauteur en fonction de la distance parcourue. b) Signal de commande  $u_{th}$ . Les actionneurs permettent de délivrer une commande telle que  $0 \text{ N} \leq u_{th} \leq 3820 \text{ N}$ . c) Vitesses verticale et horizontale en fonction du temps. d)-e) Flux optique ventral et flux optique d'expansion. f) Attitude en tangage  $\theta$  en fonction du temps. D'après SABIRON et al. (2014b).

La seconde amélioration a été apportée à l'algorithme de navigation afin de se passer de l'utilisation de la centrale inertielle. Afin d'alléger, de rendre moins coûteux et moins consommateur d'énergie les architectures GNC, nous avons montré que les informations contenues dans le flux optique permettent d'estimer des grandeurs d'attitude telle que le tangage. La centrale inertielle est un élément souvent essentiel et critique dans tous les systèmes GNC. Elle permet de stabiliser l'attitude d'un aéronef. Il a été observé que les insectes ailés possèdent un réflexe vestibulo-oculaire permettant de maintenir leur tête droite lors d'un mouvement en roulis du thorax. Pour de fortes variations, les insectes utilisent pour cela leur propre centrale inertielle appelée balanciers et sensibles aux vitesses de rotations mécaniques exercées sur le thorax selon 3 axes (lacet, tangage et roulis). Des études ont montré que les insectes utilisent également la vision pour détecter leur vitesse angulaire pour de faibles valeurs de vitesse de rotation. En observant la définition mathématique du flux optique, on se rend compte que toutes les informations nécessaires sont contenues dans cet indice visuel très riche. Il contient en effet des informations de vitesse, de proximité, de vitesse angulaire mais également de position angulaire.

Nous avons alors proposé une méthode d'estimation des flux optiques ventraux et d'expansion ainsi que du tangage basée sur l'utilisation de plusieurs capteurs visuels de mouvement fixés à la structure de l'atterrisseur. Un observateur linéaire à paramètres variant (LPV) a été synthétisé en s'appuyant sur la théorie présentée par BESANÇON,

BORNARD et HAMMOURI (1996). Grâce à un changement de variable, la classe des systèmes non-linéaires couverts par cet observateur a pu être élargie pour couvrir la représentation LPV d'un atterrisseur planétaire autour de sa trajectoire de référence.

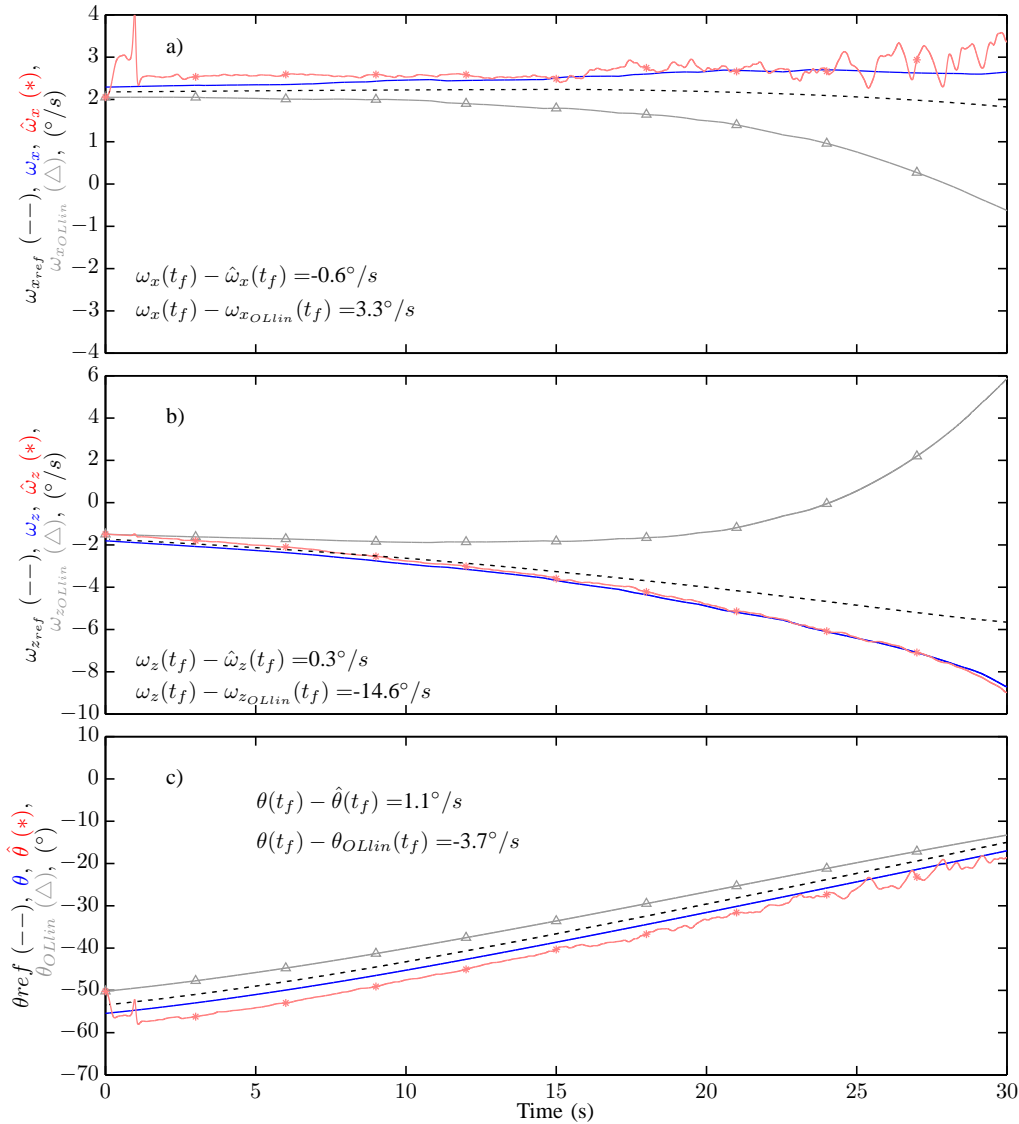


FIGURE 18 – Evolution des estimations du flux optique ventral  $\omega_x$ , du flux optique d'expansion  $\omega_z$  et du tangage sur le système non linéaire avec l'observateur LPV lors d'une simulation avec des données PANGU. Les trois sous-figures présentent les états du système (courbes bleues), les états de références (noir pointillé), les états du système linéarisé sans observateur (gris avec le marqueur  $\triangle$ ) et les états estimés (rouge avec le marqueur  $*$ ). Les états du système linéarisé sans observateur correspondent à une simulation du système non-linéaire partant des conditions initiales en boucle ouverte (notés  $\omega_{x,OLin}$ ,  $\omega_{z,OLin}$  et  $\theta_{OLin}$ ). On peut voir que les états estimés convergent rapidement vers les états réels volontairement éloignés de la trajectoire de référence. On peut également noter que les états du système linéarisé en boucle ouverte ne permettent pas d'avoir une précision d'estimation suffisante. D'après SABIRON et al. (2014a).

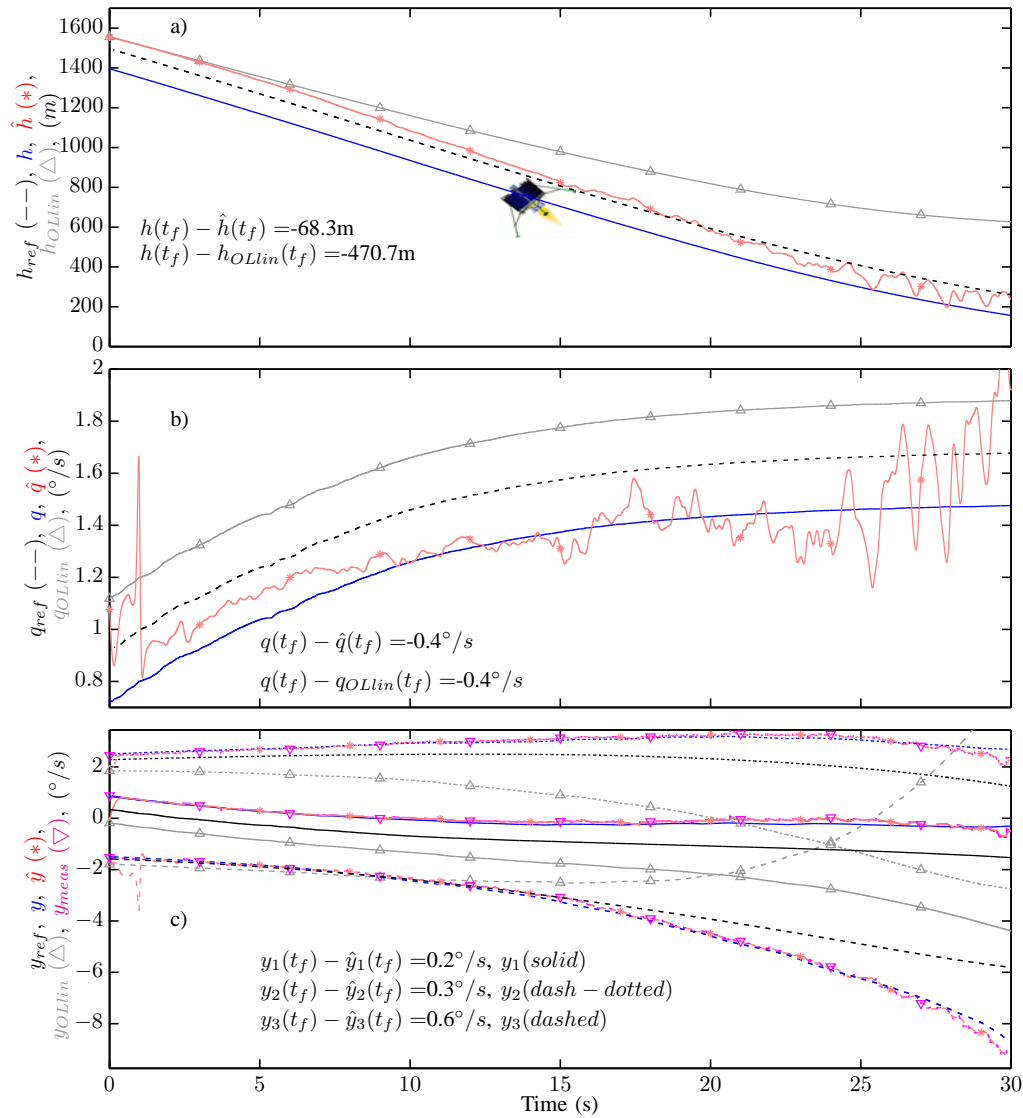


FIGURE 19 – Evolution des estimations de hauteur, de vitesse angulaire en tangage et des sorties sur le système non linéaire avec l'observateur LPV lors d'une simulation avec des données PANGU. Les trois sous-figures présentent les états du système (courbes bleues), les états de référence (noir pointillé), les états du système linéarisé sans observateur (gris avec le marqueur  $\triangle$ ) et les états estimés (rouge avec le marqueur  $*$ ). Les états du système linéarisé sans observateur correspondent à une simulation du système non-linéaire partant des conditions initiales en boucle ouverte (notés  $h_{xOLlin}$ ,  $q_{zOLlin}$  et  $y_{OLlin}$ ). On peut voir que les états estimés convergent rapidement vers les états réels volontairement éloignés de la trajectoire de référence. On peut également noter que les états du système linéarisé en boucle ouverte ne permettent pas d'avoir une précision d'estimation suffisante. D'après SABIRON et al. (2014a).

La figure 18 présente les résultats de l'estimation lors d'un scénario d'atterrissage lunaire en boucle ouverte sur le logiciel PANGU. En utilisant uniquement trois capteurs de flux optique fixés au véhicule, l'observateur LPV estime de manière précise les flux optiques ventraux et d'expansion ainsi que le tangage lors de la descente. Dans cette simulation, il est important de noter que les conditions initiales du système sont fortement éloignées des conditions nominales définies par la trajectoire de référence.

La linéarisation du système autour de la trajectoire de référence fournit une bonne approximation du système non linéaire et, malgré des conditions initiales éloignées des conditions initiales nominales, l'observateur réussit parfaitement à converger et à fournir des estimations qui seraient utilisables dans une boucle fermée (moyennant une dernière étape de filtrage passe bas). La figure 19 montre que l'observateur fournit également une estimation grossière de la hauteur et de la vitesse angulaire en tangage ne pouvant cependant pas être utilisée directement dans une boucle de régulation. Cette dernière montre également les sorties  $y_1$ ,  $y_2$ , et  $y_3$  ce qui met en avant la nécessité de l'observateur afin de suivre les états réels du système mais également la sensibilité de l'observateur. En effet, les faibles déviations qui existent entre les sorties estimées (courbes en violet) et les sorties réelles (courbes en bleu) ont un impact fort sur l'estimation des états.

Cette solution peut être présentée comme une solution de secours dans un mode dégradé par exemple lors de la perte d'un ou plusieurs capteurs principaux.

Pour conclure, nous avons proposé dans cette section des solutions nouvelles en guidage/pilotage et navigation. Elles pourraient dans le futur être appropriées à un système redondant d'atterrissage sans IMU.

## 4 CONCLUSION

Dans ces travaux, deux études complémentaires ont été menées avec pour objectif principal de montrer l'applicabilité de principes utilisés aujourd'hui en robotique aérienne et inspirés des insectes volants pour faire atterrir de manière autonome un robot sur le sol lunaire. Ces techniques bio-inspirées étudiées depuis de nombreuses années ont mené au développement de capteurs visuels de mouvement basés sur le principe du "temps de passage" permettant de déterminer le flux optique ainsi qu'au développement d'algorithmes de régulation du flux optique. Nous avons proposé premièrement de perfectionner ce type de capteurs afin de l'adapter aux contraintes liées à l'atterrissage planétaire. Les tests réalisés en intérieur ont permis de montrer la grande précision de mesure atteignable sur des contrastes naturels pour mesurer des flux optiques positifs et négatifs. Par la suite, les expérimentations en vol sur un drone hélicoptère ont démontré la capacité des capteurs visuels de mouvement à déterminer précisément les flux optiques faibles pouvant être mesurés lors de la phase d'approche d'un atterrissage lunaire. Enfin la seconde contribution de ces travaux a été d'apporter les outils nécessaires à la synthèse d'un algorithme GNC basé uniquement sur la mesure du flux optique. Sans utiliser de capteurs inertiels ni de capteurs actifs, il paraît désormais possible d'atteindre la porte basse avec des vitesses acceptables du point de vue du scénario

#### 4. CONCLUSION

---

de référence défini en accord avec nos partenaires industriels. Pour la première fois à notre connaissance, une solution alternative pouvant servir de solution de secours lors de la perte des capteurs principaux a été proposée pour effectuer un atterrissage en douceur. Les lois de commande développées corrigent l'écart entre la trajectoire réelle et la trajectoire de référence (précalculée par un algorithme d'optimisation) en utilisant uniquement une vingtaine de capteurs de flux optiques de quelques grammes fixés sur la structure du véhicule.

## RÉFÉRENCES

- ARGYROS, A. A., TSAKIRIS, D. P. et GROVER, C. (2004).  
 “Biomimetic centering behavior [mobile robots with panoramic sensors]”. In : *IEEE Robotics Automation Magazine* 11.4, p. 21–30, 68. ISSN : 1070-9932. DOI : 10.1109/MRA.2004.1371612.
- BAIRD, E., SRINIVASAN, M., ZHANG, S., LAMONT, R. et COWLING, A. (2006).  
 “Visual Control of Flight Speed and Height in the Honeybee”. In : *From Animals to Animats 9*. Sous la dir. de S. NOLFI, G. BALDASSARRE, R. CALABRETTA, J. HALLAM, D. MAROCCO, J.-A. MEYER, O. MIGLINO et D. PARISI. T. 4095. Springer Berlin / Heidelberg, p. 40–51. ISBN : 978-3-540-38608-7.
- BARRON, A. et SRINIVASAN, M. V. (2006).  
 “Visual regulation of ground speed and headwind compensation in freely flying honey bees (*Apis mellifera* L.)” In : *Journal of Experimental Biology* 209.5, p. 978–984.
- BESANÇON, G., BORNARD, G. et HAMMOURI, H. (1996).  
 “Observer synthesis for a class of nonlinear control systems”. In : *European Journal of Control* 2.3, p. 176–192.
- BEYELER, A., ZUFFEREY, J. C. et FLOREANO, D. (2009).  
 “Vision-based control of near-obstacle flight”. In : *Autonomous robots* 27, p. 201–219.
- BLANES, C. (1991).  
 “Guidage visuel d’un robot mobile autonome d’inspiration bionique (Advisor : N. Franceschini)”. Thèse de doct. INP Grenoble.
- CARPENTER, J. D., FISACKERLY, R., DE ROSA, D. et HOUDOU, B. (2012).  
 “Scientific preparations for lunar exploration with the European Lunar Lander”. In : *Planetary and Space Science* 74.1, p. 208–223.
- COLLETT, T. et LAND, M. (1975).  
 “Visual control of flight behaviour in the hoverfly *Syriffa pipiens* L.” In : *Journal of Comparative Physiology* 99.1, p. 1–66.
- CONROY, J., GREMILLION, G., RANGANATHAN, B. et HUMBERT, J. (2009).  
 “Implementation of wide-field integration of optic flow for autonomous quadrotor navigation”. In : *Autonomous Robots* 27 (3), p. 189–198. ISSN : 0929-5593.
- DE CROON, G. et IZZO, D. (2012).  
 “Real-time landing based on optimality principles and vision”. In : *23rd International Symposium on Space Flight Dynamics (ISSFD)*.

DOUGLASS, J. K. et STRAUSFELD, N. J. (1996).

“Visual motion-detection circuits in flies : parallel direction-and non-direction-sensitive pathways between the medulla and lobula plate”. In : *The Journal of neuroscience* 16.15, p. 4551–4562.

EXPERT, F. (2013).

“Flying robot inspired by insects : From optic flow sensing to visually guided strategies to control a Micro Aerial Vehicle”. Thèse de doct. Université d’Aix-Marseille.

EXPERT, F. et RUFFIER, F. (2012).

“Controlling docking, altitude and speed in a circular high-roofed tunnel thanks to the optic flow”. In : *IEEE/RSJ International Conference on Intelligent Robots and Systems (IROS)*. IEEE, p. 1125–1132.

EXPERT, F., VIOLLET, S. et RUFFIER, F. (2011).

“Outdoor Field Performances of Insect-Based Visual Motion Sensors”. In : *Journal of Field Robotics* 28, p. 529–541.

FLOREANO, D., PERICET-CAMARA, R., VIOLLET, S., RUFFIER, F., BRÜCKNER, A., LEITEL, R., BUSS, W., MENOUNI, M., EXPERT, F., JUSTON, R. et al. (2013).

“Miniature curved artificial compound eyes”. In : *Proceedings of the National Academy of Sciences* 110.23, p. 9267–9272.

FRANCESCHINI, N. (1983).

“In-vivo microspectrofluorimetry of visual pigments.” In : *Symposia of the Society for Experimental Biology*. T. 36, p. 53.

FRANCESCHINI, N. (1985).

“Early processing of colour and motion in a mosaic visual system”. In : *Neuroscience Research (Suppl. 2)*. Sous la dir. d’ELSEVIER, p. 17–49.

FRANCESCHINI, N., PICHON, J. et BLANES, C. (1992).

“From insect vision to robot vision”. In : *Philosophical Transactions of the Royal Society of London* 337, p. 283–294.

FRANCESCHINI, N., RIEHLE, A. et NESTOUR, A. (1989).

“Facets of vision”. In : sous la dir. de D. STAVENGA et R. HARDIE. Springer. Chap. Directionally selective motion detection by insect neurons, p. 360–390.

FRANCESCHINI, N., RUFFIER, F. et SERRES, J. (2007).

“A Bio-Inspired Flying Robot Sheds Light on Insect Piloting Abilities”. In : *Current Biology* 17, p. 329–335.

- FRANCESCHINI, N. (1975).  
“Sampling of the visual environment by the compound eye of the fly : fundamentals and applications”. In : *Photoreceptor optics*. Springer, p. 98–125.
- GARRATT, M. et CHAHL, J. (2008).  
“Vision-Based Terrain Following for an Unmanned Rotorcraft”. In : *Journal of Field Robotics* 25, p. 284–301.
- GÖTZ, K. (1964).  
“Optomotorische untersuchung des visuellen systems einiger Augenmutanten der fruchtfliege *Drosophila*.” In : *Biological Cybernetics* 2, p. 77–92.
- GREEN, W., OH, P. et BARROWS, G. (2004).  
“Flying insect inspired vision for autonomous aerial robot maneuvers in near-earth environments”. In : *International Conference on Robotics and Automation (ICRA)*. T. 3, 2347–2352 Vol.3.
- GRIFFITHS, S., SAUNDERS, J., CURTIS, A., BARBER, B., MCLAIN, T. et BEARD, R. (2006).  
“Maximizing miniature aerial vehicles”. In : *IEEE Robotics & Automation Magazine* 13, p. 34–43.
- HATEREN, J. et SCHILSTRA, C (1999).  
“Blowfly flight and optic flow. II. Head movements during flight”. In : *Journal of Experimental Biology* 202.11, p. 1491–1500.
- HAUSEN, K. (1982).  
“Motion sensitive interneurons in the optomotor system of the fly”. In : *Biological Cybernetics* 45.2, p. 143–156.
- HENGSTENBERG, R. (1988).  
“Mechanosensory control of compensatory head roll during flight in the blowfly *Calliphora erythrocephala* Meig.” In : *Journal of comparative Physiology A* 163.2, p. 151–165.
- HÉRISSÉ, B., HAMEL, T., MAHONY, R. et RUSSOTTO, F. (2012).  
“Landing a VTOL Unmanned Aerial Vehicle on a Moving Platform Using Optical Flow”. In : *IEEE Transactions on Robotics* 28.1, p. 77 –89.
- HORRIDGE, G. A. (1977).  
“The compound eye of insects”. In : *Scientific American* 237, p. 108–120.
- HUMBERT, J. et HYSLOP, A. (2010).  
“Bioinspired visuomotor convergence”. In : *IEEE Transactions on Robotics* 26.1, p. 121–130.

IZZO, D. et DE CROON, G. (2011).

“Landing with time-to-contact and ventral optic flow estimates”. In : *Journal of Guidance, Control, and Dynamics* 35 (4), p. 1362–1367.

— (2013).

“Nonlinear model predictive control applied to vision-based spacecraft landing”. In : *Proceedings of the EuroGNC 2013, 2nd CEAS Specialist Conference on Guidance, Navigation & Control, Delft University of Technology*. Delft, The Netherlands, p. 91–107.

IZZO, D., WEISS, N. et SEIDL, T. (2011).

“Constant-Optic-Flow Lunar Landing : Optimality and Guidance”. In : *Journal of Guidance, Control, and Dynamics* 34, p. 1383–1395.

KENDOUL, F., NONAMI, K., FANTONI, I. et LOZANO, R. (2009).

“An adaptive vision-based autopilot for mini flying machines guidance, navigation and control”. In : *Autonomous Robots* 27 (3), p. 165–188.

KOENDERINK, J. et DOORN, A. (1987).

“Facts on optic flow”. In : *Biological Cybernetics* 56, p. 247–254.

KRAPP, H. G. et HENGSTENBERG, R. (1996).

“Estimation of self-motion by optic flow processing in single visual interneurons”. In : *Nature* 384.6608, p. 463–466.

LAND, M. F. (1997).

“Visual Acuity In Insects”. In : *Annual Review of Entomology* 42, p. 147–177.

MA, K. Y., CHIRARATTANANON, P., FULLER, S. B. et WOOD, R. J. (2013).

“Controlled flight of a biologically inspired, insect-scale robot”. In : *Science* 340.6132, p. 603–607.

MEDICI, V., ORCHARD, G., AMMANN, S., INDIVERI, G. et FRY, S. (2010).

*Neuromorphic computation of optic flow data Bio-inspired landing using biomorphic vision sensors*. Rapp. tech. ESA.

MENZEL, R. et GIURFA, M. (2001).

“Cognitive architecture of a mini-brain : the honeybee”. In : *Trends in cognitive sciences* 5.2, p. 62–71.

PICHON, J.-M., BLANES, C. et FRANCESCHINI, N. (1989).

“Visual guidance of a mobile robot equipped with a network of self-motion sensors”. In : *SPIE Conf. on Mobile Robots IV*. Sous la dir. de W. WOLFE et W. CHUN. T. 1195. Bellingham, U.S.A., p. 44–53.

- PORTELLI, G., SERRES, J., RUFFIER, F. et FRANCESCHINI, N. (2010).  
“Modelling honeybee visual guidance in a 3-D environment”. In : *Journal of Physiology - Paris* 104, p. 27 –39.
- PORTELLI, G. (2011).  
“Le pilotage visuel chez l’abeille : expériences et modèle”. Thèse de doct. Université de Toulouse, Université Toulouse III-Paul Sabatier.
- REICHARDT, W. (1969).  
“Movement perception in insects”. In : *Processing of optical data by organisms and machines, International School of Physics “Enrico Fermi” : Course XLIII, 1968, Academic Press, New York, NY, USA*, p. 465 –493.
- ROUBIEU, F. (2013).  
“Réalisation d’un micro-robot autonome, inspiré du contrôle de vitesse et d’évitement d’obstacles observés chez l’abeille”. Thèse de doct. Université d’Aix-Marseille.
- ROUBIEU, F., EXPERT, F., SABIRON, G. et RUFFIER, F. (2013).  
“Two-Directional 1-g Visual Motion Sensor Inspired by the Fly’s Eye”. In : *Sensors Journal, IEEE* 13.3, p. 1025–1035. ISSN : 1530-437X. DOI : 10 . 1109 / JSEN . 2012 . 2230622.
- ROUBIEU, F. L., SERRES, J. R., COLONNIER, F., FRANCESCHINI, N., VIOLLET, S. et RUFFIER, F. (2014).  
“A biomimetic vision-based hovercraft accounts for bees’ complex behaviour in various corridors”. In : *Bioinspiration & biomimetics* 9.3, p. 036003.
- RUFFIER, F. (2004).  
“Pilote automatique biomimétique - Système générique inspiré du contrôle visuo-moteur des insectes pour : le décollage, le suivi de terrain, la réaction au vent et l’atterrissage automatiques d’un micro-aéronef”. Thèse de doct. INP Grenoble.
- RUFFIER, F. et EXPERT, F. (2012).  
“Visual motion sensing onboard a 50-g helicopter flying freely under complex VICON-lighting conditions”. In : *International Conference on Complex Medical Engineering*. Kobe, Japan, p. 634–639.
- RUFFIER, F. et FRANCESCHINI, N. (2003).  
“OCTAVE, a bioinspired visuo-motor control system for the guidance of Micro-Air Vehicles”. In : *SPIE Conference on Bioengineered and Bioinspired Systems*. Sous la dir. d’A. RODRIGUEZ-VAZQUEZ, D. ABBOTT et R. CARMONA. T. 5119. Maspalomas, Spain, p. 1–12.

- (2004).  
 “Visually guided micro-aerial vehicle : automatic take off, terrain following, landing and wind reaction”. In : *IEEE International Conference on Robotics and Automation (ICRA)*. T. 3, p. 2339–2346.
- (2005).  
 “Optic flow regulation : the key to aircraft automatic guidance”. In : *Robotics and Autonomous Systems* 50, p. 177–194.
- RUFFIER, F., VIOLLET, S., AMIC, S. et FRANCESCHINI, N. (2003).  
 “Bio-inspired optical flow circuits for the visual guidance of micro air vehicles.”  
 In : *IEEE International Symposium on Circuits and Systems (ISCAS)*. T. 3. Bangkok, Thailand, p. 846–849.
- RUFFIER, F. et FRANCESCHINI, N. (2014).  
 “Optic Flow Regulation in Unsteady Environments : A Tethered MAV Achieves Terrain Following and Targeted Landing Over a Moving Platform”. English. In : *Journal of Intelligent & Robotic Systems*, p. 1–19. ISSN : 0921-0296.
- SABIRON, G., CHAVENT, P., RAHARIJAONA, T., FABIANI, P. et RUFFIER, F. (2013).  
 “Low-speed optic-flow sensor onboard an unmanned helicopter flying outside over fields”. In : *IEEE International Conference on Robotics and Automation (ICRA)*, p. 1742–1749.
- SABIRON, G., BURLION, L., JONNIAUX, G., KERVENDAL, E., BORNSCHLEGL, E., RAHARIJAONA, T. et RUFFIER, F. (2014a).  
 “Backup State Observer Based on Optic Flow Applied to Lunar Landing”. In : *IEEE/RSJ International Conference on Intelligent Robots and Systems (IROS)*, p. 2325 – 2332.
- SABIRON, G., BURLION, L., RAHARIJAONA, T. et RUFFIER, F. (2014b).  
 “Optic Flow-Based Nonlinear Control and Sub-Optimal Guidance for Lunar Landing”. In : *IEEE International Conference on Robotics and Biomimetics (ROBIO) (Accepted)*.
- SABIRON, G., RAHARIJAONA, T., BURLION, L., KERVENDAL, E., BORNSCHLEGL, E. et RUFFIER, F. (2014c).  
 “Sub-optimal Lunar Landing GNC using Non-gimbaled Bio-inspired Optic Flow Sensors”. In : *IEEE Transactions on Aerospace and Electronic Systems (in revision)*.
- SRINIVASAN, M., ZHANG, S., LEHRER, M. et COLLETT, T. (1996).  
 “Honeybee navigation en route to the goal : visual flight control and odometry”. In : *Journal of Experimental Biology* 199.1, p. 237–244.

- SRINIVASAN, M. V. et BERNARD, G. D. (1975).  
“The effect of motion on visual acuity of the compound eye : a theoretical analysis”.  
In : *Vision research* 15.4, p. 515–525.
- SRINIVASAN, M. (2011).  
“Honeybees as a Model for the Study of Visually Guided Flight, Navigation, and Biologically Inspired Robotics”. In : *Physiological Reviews* 91.2, p. 413–460.
- STRAUSFELD, N. J. (1976).  
*Atlas of an insect brain*. Springer-Verlag Berlin, Heidelberg, New York.
- STRAW, A., LEE, S. et DICKINSON, M. (2010).  
“Visual Control of Altitude in Flying *Drosophila*”. In : *Current Biology* 20.17, p. 1550–1556.
- VALETTE, F., RUFFIER, F., VIOLLET, S. et SEIDL, T. (2010a).  
“Biomimetic optic flow sensing applied to a lunar landing scenario”. In : *International Conference on Robotics and Automation (ICRA)*, p. 2253–2260.
- VALETTE, F., RUFFIER, F., VIOLLET, S., SEIDL, T., AMPATZIS, C. et GROOTE, K. (2010b).  
*Neuromorphic Computation of Optic Flow Data*. Rapp. tech. ESA.
- ZUFFEREY, J. C. et FLOREANO, D. (2006).  
“Fly-inspired visual steering of ultralight indoor aircraft”. In : *IEEE Transactions on Robotics* 22(1), p. 137–146.
- ZUFFEREY, J.-C. et FLOREANO, D. (2005).  
“Toward 30-gram autonomous indoor aircraft : Vision-based obstacle avoidance and altitude control”. In : *IEEE International Conference on Robotics and Automation (ICRA)*. IEEE, p. 2594–2599.
- ZUFFEREY, J., BEYELER, A. et FLOREANO, D. (2010).  
“Autonomous flight at low altitude using light sensors and little computational power”. In : *International Journal of Micro Air Vehicles* 2(2), p. 107–117.

## **Synthèse d'une Solution GNC basée sur des Capteurs de Flux Optique Bio-inspirés adaptés à la mesure des basses vitesses pour un Atterrissage Lunaire Autonome en Douceur**

Dans cette thèse, nous nous intéressons au problème de l'atterrissage lunaire autonome et nous proposons une méthode innovante amenant une alternative à l'utilisation de capteurs classiques qui peuvent se révéler encombrants, énergivores et très onéreux. La première partie est consacrée au développement et à la construction de capteurs de mouvement inspirés de la vision des insectes volants et mesurant le flux optique. Le flux optique correspond à la vitesse angulaire relative de l'environnement mesurée par la rétine d'un agent. Dans un environnement fixe, les mouvements d'un robot génèrent un flux optique contenant des informations essentielles sur le mouvement de ce dernier. En utilisant le principe du « temps de passage », nous présentons les résultats expérimentaux obtenus en extérieur avec deux versions de ces capteurs. Premièrement, un capteur mesurant le flux optique dans les deux directions opposées est développé et testé en laboratoire. Deuxièmement un capteur adapté à la mesure des faibles flux optiques similaires à ceux pouvant être mesurés lors d'un alunissage est développé, caractérisé et enfin testé sur un drone hélicoptère en conditions extérieures. Dans la seconde partie, une méthode permettant de réaliser le guidage, la navigation et la commande (GNC pour Guidance Navigation and Control) du système est proposée. L'innovation réside dans le fait que l'atterrissage en douceur est uniquement assuré par les capteurs de flux optique. L'utilisation des capteurs inertiels est réduite au maximum. Plusieurs capteurs orientés dans différentes directions de visée, et fixés à la structure de l'atterrisseur permettent d'atteindre les conditions finales définies par les partenaires industriels. Les nombreuses informations décrivant la position et l'attitude du système contenues dans le flux optique sont exploitées grâce aux algorithmes de navigation qui permettent d'estimer les flux optiques ventraux et d'expansion ainsi que le tangage. Nous avons également montré qu'il est possible de contrôler l'atterrisseur planétaire en faisant suivre aux flux optiques estimés une consigne optimale au sens de la consommation d'énergie. Les simulations réalisées durant la thèse ont permis de valider le fonctionnement et le potentiel de la solution GNC proposée en intégrant le code du capteur ainsi que des images simulées du sol de la lune.

**Mots-clés :** Flux optique, Robotique Bio-Inspirée, Capteurs Visuels de Mouvement, Alunissage Autonome, Atterrissage Basé Vision, Guidage, Navigation, Commande Non-Linéaire, Drone Hélicoptère ReSSAC

### **Design of a GNC Solution based on Bio-Inspired Optic Flow Sensors adapted to low speed measurement for an Autonomous Soft Lunar Landing**

In this PhD thesis, the challenge of autonomous lunar landing was addressed and an innovative method was developed, which provides an alternative to the classical sensor suites based on RADAR, LIDAR and cameras, which tend to be bulky, energy-consuming and expensive. The first part is devoted to the development of a sensor inspired by the fly's visual sensitivity to optic flow (OF). The OF is an index giving the relative angular velocity of the environment sensed by the retina of a moving insect or robot. In a fixed environment (where there is no external motion), the self-motion of an airborne vehicle generates an OF containing information about its own velocity and attitude and the distance to obstacles. Based on the "Time of Travel" principle we present the results obtained for two versions of 5 LMSs based optic flow sensors. The first one is able to measure accurately the OF in two opposite directions. It was tested in the laboratory and gave satisfying results. The second optic flow sensor operates at low velocities such as those liable to occur during lunar landing was developed. After developing these sensors, their performances were characterized both indoors and outdoors, and lastly, they were tested onboard an 80-kg helicopter flying in an outdoor environment. The Guidance Navigation and Control (GNC) system was designed in the second part on the basis of several algorithms, using various tools such as optimal control, nonlinear control design and observation theory. This is a particularly innovative approach, since it makes it possible to perform soft landing on the basis of OF measurements and as less as possible on inertial sensors. The final constraints imposed by our industrial partners were met by mounting several non-gimbaled sensors oriented in different gaze directions on the lander's structure. Information about the lander's self-motion present in the OF measurements is extracted by navigation algorithms, which yield estimates of the ventral OF, expansion OF and pitch angle. It was also established that it is possible to bring the planetary lander gently to the ground by tracking a pre-computed optimal reference trajectory in terms of the lowest possible fuel consumption. Software-in-the-loop simulations were carried out in order to assess the potential of the proposed GNC approach by testing its performances. In these simulations, the sensor firmware was taken into account and virtual images of the lunar surface were used in order to improve the realism of the simulated landings.

**Keywords :** Optic flow, Bio-inspired robotics, Visual Motion Sensors, Autonomous lunar landing, Vision based landing, Guidance, Navigation, Nonlinear Control, Unmanned Aerial Vehicle, ReSSAC UAV